UNIVERSITÀ
POLITECNICA
DELLE MARCHE

Facoltà di Ingegneria

Ph.D. Course in Information Engineering

Neuromuscular Control Modeling: from Physics to Data-Driven Approaches

Candidate:

Andrea Tigrini

Advisor:

Prof. Sandro Fioretti

Coadvisor:

Federica Verdini, Ph.D.

Alessandro Mengarelli, Ph.D.

Academic Year 2020-2021

UNIVERSITÀ
POLITECNICA
DELLE MARCHE

Facoltà di Ingegneria

Ph.D. Course in Information Engineering

Neuromuscular Control Modeling: from Physics to Data-Driven Approaches

Candidate:

Andrea Tigrini

Advisor:

Prof. Sandro Fioretti

Coadvisor:

Federica Verdini, Ph.D.

Alessandro Mengarelli, Ph.D.

Academic Year 2020-2021

Università Politecnica delle Marche

Facoltà di Ingegneria

Ph.D. Course in Information Engineering

Via Brecce Bianche – 60131 Ancona (AN), Italy

A Benedetta

Abstract

This thesis focuses on the neuromuscular control modeling from two different perspectives which can be encountered in many engineering applications. Indeed, the characterization of the motor control constitutes the ground for a deeper understanding of the central nervous system (CNS), but also for the design of systems that permit to opportunely interact with the human being in tasks ranging from clinical diagnostics to rehabilitation and human-machine interaction.

In this framework, the biomechanics and the neural control of the human stance was investigated starting from a physical point of view. In particular, based on the recent findings reported in the literature, the intermittent motor control paradigm was investigated with the aim of understanding how such paradigm mirrors in the center of pressure (COP) trajectories. In other words, a first objective of this study is to find possible perspectives to link model based approaches to the more classical field of posturography. Following this line, a first contribution given in this work of thesis regards the analysis of COP generated from intermittent controlled inverted pendulum through the extended detrended fluctuation analysis, which was recently introduced in the literature. It has been found that the long-term correlation and inohmogeniety properties of the COP time series strictly depend on the derivative gain term of the intermittent controller and on the degree of intermittency of the control action. This opened to the possibility of interpreting COP descriptors used in posturography under a model based perspective. Thus, under this view, another contribution provided in this work of thesis regards the use of a more complex biomechanical model of the stance, e.g. a double-link inverted pendulum intermittently controlled at the ankle, to infer how two populations, young and elderly healthy adults, are described by the aforementioned model. In terms of novelty, it deserves to be pointed out the results regarding the mechanical modeling of the COP for a multi-link structure, and the assessment of its physiological plausibility through state of the art COP features.

Hence, rather than developing the analysis upon the more commonly employed sway

angle time-course, focus was given to the COP, which is the most direct measure that one can perform in posturography. On the other hand, when the perturbed posture motor task was taken into account, there was the need to enlarge the perspective, integrating kinematic, dynamic and muscle activity data. The idea of employing different sources of information to develop models of the CNS represents an important element that was investigated using tools related to hybrid system identification theory. This permitted to exclude linearization hypotheses that may limit the description of the control action, nor to implement too restrictive and cumbersome experimental setups for the data acquisition. Indeed, subjects underwent to impulsive support base translations in three different conditions: considering eyes open, closed, and performing mental counting. Although such data were essentially analyzed through a data-driven approach, the identified models guaranteed physical interpretations of the role played by the CNS in the three different conditions, without the need of external devices that injected random external forces at the lower or upper trunk levels.

The second main core of this thesis regards the characterization of the motor control using the surface electromyographic (sEMG) signals. This was motivated by the fact that modern technologies can exploit the sEMG signals not only for the analysis, but also for the design of architectures that, based on a certain amount of information, permit for instance to properly interact with a machine in many rehabilitation contexts. Thus, a first contribution given in this work regarded the muscle onset detection considering low SNR scenarios. In this framework, energy operators such as the Teager-Kaiser energy operator (TKEO) and its extended version (ETKEO) were investigated as signal preconditioning steps before the application of state of the art onset detection algorithms. The latter have been significantly boosted when ETKEO was used with respect to TKEO. It deserves to be pointed out that the use of extended energy operators for the sEMG signal preprocessing constitutes a novel element in this field that can be also further investigated in future studies.

Despite the knowledge of muscle onset activity constitutes a valuable source of information, modern technologies could require more structured forms of the information itself. Indeed, from the sEMG muscle one can also predict which movement the subject is going to perform by analyzing multiple sources of muscle activity. This aspect can be enclosed in the motion intention detection (MID) field. In this thesis a MID problem was investigated by taking into account two important aspects: as first the study was centered on the shoulder joint movements, since such joint plays a key role in many rehabilitation tasks of the upper

limb, although it was less studied from a kinesiological point of view. Secondly, the MID problem was faced under a pattern recognition perspective. This allowed to verify whether methodologies encountered in the myoelectric hand gesture recognition can be transferred in the affine field of MID. In particular, it was investigated both the time and frequency domain features since the latter have not been yet studied for solving EMG base MID problems. Moreover, in contrast to what reported in the literature, where MID problems generally consider only few movements, in this work of thesis up to eight shoulder movements have been investigated.

In a similar fashion, myoelectric pattern recognition architectures were also used in the assessment of the ten hand-written digits, i.e. 0,1,...,9. Indeed, despite the handwriting can be considered a hand movement that involves fine muscular control actions, it has not been consistently investigated in the field of sEMG based hand gesture recognition. Hence, the study performed in this work aims to verify the possibility to recognize the written digits from the sEMG muscle activity. Further, since the literature supports the change from forearm to wrist in order to acquire EMG data for hand gesture recognition, it was investigated whether such exchange can be performed when a challenging classification task, as the handwriting recognition has to be performed. The present results highlight that only when a proper spatial covering of the forearm and wrist muscles, in terms of EMG electrodes, is reached, the trained pattern recognition architectures can provide satisfactory performances.

In brief, this work of thesis focuses on the possibility to study aspects of neuromuscular control, i.e. related to balance maintenance and upper limb motion recognition and intent detection. Hence, the thesis is organized as follows:

- Chapters one and two take into account the investigation of the CNS control modeling in static and perturbed posture.
- Chapter three involves study of surface EMG signals in terms of onset detection and temporal characterization of motor control in lower and upper limb motor tasks.
- Chapter four and five focus on the characterization of upper limb movements with data-driven approaches through sEMG data, introducing more advanced aspects related to the myoelectric pattern recognition control in MID and handwriting recognition.

Contents

Glossary

- **AP**, Anterior-Posterior;
- **ARX**, AutoRegressive with eXogenous input;
- **CNS**, Central Nervous System;
- **COM**, Center Of Mass;
- **COP**, Center Of Pressure;
- **D**, Derivative;
- **DB**, Davies Bouldin index;
- **DFA**, Detrended Fluctuation Analysis;
- **DIP**, Double link Inverted Pendulum;
- **DL**, Deep Learning;
- **DT**, Dual Task;
- **DTW** Dynamic Time Warping;
- **EC**, Eyes Closed;
- **ECOC**, Error-Correcting Output Codes
- **EDFA**, Extended Detrended Fluctuation Analysis;
- **ED**, Extensor Digitorum;
- **EEG**; Electroencephalography;
- **EMG**, Electromyography;
- **EO**, Eyes Open;

- **ETKEO**, Extended Teager-Kaiser Energy Operator;
- **FD**, Frequency Domain;
- **FCR**, Flexor Carpi Radialis;
- **GA**, Gastrocnemius;
- **GAL**, Genetic Algorithm;
- **ICP**, Intermittent Controller Parameters
- **IP**, Inverted Pendulum;
- **IQR**, Interquartile Range;
- **LDA**, Linear Discriminant Analysis;
- **MID**, Motion Intention Detection;
- **ML**, Maxiumum Likelihood;
- **MLR**, Multiclass Logistic Regression;
- **MOD**, Muscle Onset Detection;
- **MSA**, Mean Semi-principal Axis;
- **NN**,Neural Network;
- **NRMSE**, Normalized Root Mean Square Error;
- **P**, Proportional;
- **PCA**, Principal Component Analysis;
- **PDF**, Probability Density Function;
- **PLM** Profile Likelihood Maximization;
- **PR**, Pattern Recognition;
- **PRA**, Pattern Recognition Architecture;
- **PRC**, Pattern Recognition Control;
- **PSD**, Power Spectrum Density;

- **PWARX**, Piecewise Affine AutoRegressive with eXogenous input
- **QSVM**, Quadratic Support Vector Machine;
- **SDA**, Sway Diffusion Analysis;
- **SI**, Separability Index
- **SVM**, Support Vector Machine;
- **SR**, Sway Range;
- **SVD**, Singular Value Decomposition;
- **TA**, Tibialis Anterior;
- **TD**, Time Domain;
- **TKEO**, Teager-Kaiser Energy Operator;
- **TP**, Threshold and Post-processor;
- **VIP**, Virtual Inverted Pendulum;
- **WLT**, Wavelet Transform;
- **WSA**, Within Subject Accuracy;

Chapter 1

Quiet posture: the mechanics of the stance and the intermittent control paradigm

1.1 Introduction

Balance maintenance of human upright stance constitutes a research area where different disciplines, ranging from biomechanics to robotics and neuroscience, found applications [1, 2, 3]. Indeed, despite each discipline carries its own perspective, all of them agree on the importance of understanding the hidden neuromuscular control mechanisms that the central nervous system (CNS) implements to maintain body balance. In robotics for instance, biological inspired control policies are crucial since they can be embodied in legged robots to efficiently maintain the stance [4, 5], whereas, in biomechanics and neuroscience, the analysis of postural adjustment strategies is particularly useful to better understand how pathologies affecting CNS may impact on the motor control performances [6, 7].

Although many different methodological approaches can be encountered in the literature to study the upright balance maintenance in unperturbed conditions, two general ways are clearly recognized. From one side, the model-based analyses make extensively use of the single link or multi-link inverted pendulum (IP) to model the mechanics of the stance [8, 9, 10]. Hence, the CNS acts as a controller that modulates the control torque at the joints in order to maintain stability and reject the toppling torque. The latter is induced by the gravity field and by the internal postural noise,wich is due to hemodynamics and respiration [11, 12]. In this view, the stance maintenance is treated as a cybernetic problem,

where the mechanics of the body affects and coexists with the processes that CNS is engaged to solve, i.e. sensory information fusion, motor commands generation and delivery [8, 13]. Indeed, the presence of an active control modulation injected in the feedback loop by the CNS was demonstrated in [12, 14], where it was highlighted that muscle stiffness, due to the basal muscle tone and tendon mechanical properties, is not sufficient *per se* to provide stance regulation.

A second way commonly recognized in the literature to study human balance maintenance makes use of data analysis methods and it is commonly referred as posturography. In such perspective, kinematic and dynamic postural time-series such as the trajectories of center of mass (COM) and center of pressure (COP) are commonly taken into account. In particular, the latter is one of the most employed since the COP is easily measurable through force plates. As a matter of fact, literature shows a wide spectrum of timeseries analysis approaches either specifically developed for COP [2, 15], or coming from non-linear signal processing field [7, 16, 17, 18]. Moreover, many important studies in posturography employed descriptors coming from the two above-mentioned lines in order to characterize the COP properties of healthy and pathological populations [19, 20, 21].

It is interesting to observe that some seminal works did not shrink from merging mechanical model-based and data-driven analyses [22, 10, 9, 23]. Indeed, despite the two aforementioned perspectives are different [23], the need for a unified view results of great importance when one would obtain highly explainable models. Indeed, in [23] the aforementioned approaches were combined through the approximate bayesian computation, in order to infer the parameters of the intermittent controller from posturographic data. This makes more underpinned the interpretation of the results if compared to models obtained through black box identification procedures, where high fidelity data fitting could be counterbalanced by a limited interpretability. This constitutes a recent example of a joined perspective manifested above. However, one can find older works in literature where the need of a profound model interpretation was pointed out through combination of model and data analyses. In [10] for instance, sway diffusion analysis (SDA) proposed by Collins and De Luca [2], was applied to simulated COP data obtained through an IP model under a continuous control paradigm. The control gains were varied within a feasible range, and the relations between the latter and the SDA parameters were pointed out [10]. Also in [9], the IP was used to model the stance, but the control policy employed shows an intermittent nature [9]. Such model was used to simulate sway data and changes in the controller parameters were related to changes

in the power spectral density properties of the sway signals.

It emerges from the previous paragraph, that the single link IP was particularly employed to mimic the human upright stance mechanics, whereas behind the CNS control action, debate regarding the actual strategy employed by the nervous system is still open. As anticipated, the ankle stiffness model proposed by Winter cannot be sufficient to stabilize the posture [24, 14]. For this reason, an active control torque that models the CNS role at the ankle is injected in the IP dynamics. Such torque was in general thought as a feedback law based on the delayed information of the sway angle ad its time derivative. Indeed, despite different speculative studies concerning the synthesis of the neural controller through optimal control theory can be found[25, 26], proportional (P) and derivative (D) delayed feedback law injected continuously or intermittently seemed to produce COM and COP data that coherently shares common properties with real data [10, 9, 8, 27, 28].

It is important to note that, as suggested by Asai and colleagues [9], and further confirmed in [29, 23, 13], an intermittent control can be more energetically efficient than a continuous one, since the controller can exploit the saddle type equilibrium point of the IP mechanics. Indeed, although the global IP dynamic is unstable, two manifolds, one stable and one unstable are potentially available to bound the sway around the equilibrium point. This can be obtained by steering the state close to the stable manifold [9], obtained through an unstable delay-induced dynamics that produces, in the state space, spiraling trajectories able to lead the state closer to the stable manifold. Thus, despite the two sub-dynamics are *per se* unstable, they can be orchestrated in a manner, i.e. by opportunely switching between them, in order to obtain a bounded stability with limit cycle. Hence, an intermittent control strategy seems more physiologically plausible with respect to a continuous regulation. This aspect was highlighted also in [2], where a similar conclusion was pointed out through SDA over real data.

The recent literature confirmed again the validity of the IP model intermittently controlled at the ankle [8, 30]. However, from a mechanical point of view, the multi-link nature of the human-body unavoidably rises questions regarding the role of the upper joints. In particular, it was observed that the hip can contribute to the stance stabilization when the posture is challenged by additional forces acting on the body [31]. Moreover as shown in [32], the range of motion around the hip is not negligible also in quiet stance, suggesting the use of a double-link IP (DIP) for the upright stance mechanical model [29]. Indeed, the velocity and acceleration around the hip showed significant greater values than those observed at the

ankle [33, 34]. This may indicate that some regulatory strategy acts at the hip in order to regulate the stance also in unperturbed conditions.

Frequency analysis supported the above stated hypothesis [34], showing that the lower and upper trunk segments of the body move in phase at frequencies below 0.5 Hz, whereas, for frequencies greater than 0.9 Hz, the character of the coordination between the upper and lower body segments becomes anti-phase. The nature of such coordination was investigated through a modeling perspective in [29, 8]. Specifically, Morasso and colleagues [8], highlighted that the hip can contribute through a passive mechanism, that is, a stiffness model as that proposed by Winter, whereas at the ankle, an intermittent control law based on a lumped sway information was employed [8, 13]. Such model can be refereed as the DIP/VIP, where VIP denotes the virtual inverted pendulum that can be obtained from any multi-link IP structure and that can be employed in quiet stance to describe an internal model exploited by the CNS to develop a control action [8, 27].

The physiological plausibility of the DIP/VIP model was assessed through the analysis of kinematic sway data, indeed, the upper and lower trunk oscillation showed the in-phase and counter-phase patterns respectively for the frequencies ranges lower that 0.5 Hz and greater than 0.9 Hz [8]. However, the model should also be able to reproduce plausible COP patterns as those observed in real data. This for two main reasons: as first, for any human balancing task, two variables, i.e. COM and COP, are of great physical importance, in particular,the COP encompasses the control action at ankle and upper joints [30, 13]. The second reason lies on the fact that COP time course constitutes a variable that can be effectively employed to merge classical posturography and model-based postural analysis [13].

Incidentally, investigating the plausibility of COP data obtained from DIP/VIP should require the use of meaningful descriptors that can be "robbed" from posturography, since they can be related to the neural controller parameters to infer whether the physical model is able to provide a good description of the actual process. Moreover, as observed in [27, 13], the COP of a DIP has to be mathematically formulated considering the multi-link nature of the mechanical structure. Indeed, the COP formulation from a single-link IP may mask the mechanical meaning of the aforementioned variable, rendering misleading the analysis of real COP data.

Hence in this chapter, particular attention was given to the descrption of the upright stance maintenance both from a physical modeling and data analysis point of view. Regarding the biomecanics of the stance the simple IP and DIP are introduced, then to investigate

the role played by the CNS, the intermittent control paradigm is reviewed both for the IP and for the DIP/VIP [9, 8]. Some posturographic analysis techniques such as SDA and the detrended fluctuation analysis (DFA) with its extension (EDFA), are reported. A public available dataset containing COP of young and elderly adults was employed in this thesis. In particular, the COP descriptors obtained by varying the control gains of the DIP/VIP were compared with those characterizing the two aforementioned population in order to further investigate whether the DIP/VIP model can be used to describe possible rearrangements of balance motor control due to aging [13, 27].

1.2 Methods

1.2.1 Single-link and double-link inverted pendulum for modeling the upright stance

In this section the two principal models for the description of the stance mechanics commonly encountered in the literature are reported. These models, namely the IP and DIP previously introduced (chapter 1), model the dynamics of the stance in the sagittal plane [9, 8]. Thus, one could wonder whether a description of such motor task is of interest also in the frontal plane. It should be noted that the sagittal plane encompasses the description in the anterior-posterior direction (AP), while the frontal plane takes into account the medial-lateral direction (ML) [35, 36]. However, from a physical point of view, in quiet conditions, the gravity-pull mainly impacts on the dynamics of the stance in the sagittal plane. This is due to the natural constraints enforced by the feet, limbs and joints shapes. This is confirmed by the greater variations of the COP in the AP if compered with respect to what observed in the ML [35]. Although such aspect could be trivial, one should observe that in ML important regulatory mechanisms take place at the hip when the feet are slightly disaligned on the support base [35]. The importance of ML and thus of the frontal plane in modeling the stance can be observed also in the gait initiation [37], or more in general when the COP displacement is physically constrained by the nature of the motor task in the AP direction [30].

Hence, despite the modeling of balance maintenance in the frontal plane can carry additive information regarding the control mechanisms actuated at the lower limb joints [30], in this work of thesis attention was given to the stance in sagittal plane following the modeling perspective commonly encountered in the literature [24, 14, 10, 9, 29, 38, 28, 23, 39]. Let

thus introduce the single inverted pendulum model, which constitutes a fundamental block also in the modeling of more articulated motor tasks [40, 41].

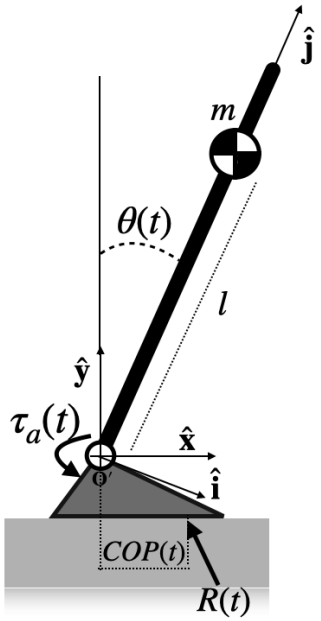

Figure 1.1: Schematic representation of the single-link inverted pendulum used to model the body stance mechanics.

Figure 1.1 shows the IP with its fundamental kinematic and dynamic quantities. The sway angle $\theta(t)$ represents the angular displacement of the COM around the ankle, assumed that the COM is rigidly linked to the aforementioned joint by means of a rod with no inertia. The total torque at the ankle is expressed through $\tau_a(t)$ and, in quiet condition, it mirrors all the dynamics of the pendulum, that is the destabilizing mechanisms induced by the postural noise, the gravity pull, and the regulatory actions due to passive and active control policies. It is important to observe that the global ankle torque is generated by the ground reaction force $R(t)$ exchanged between the body and the ground through the feet at a certain distance from the joint center. Such distance varies in time and can be represented by the COP time-course since the height of the ankle center with respect to the support base remains invariant static balance maintenace.

In quiet stance, the intrinsic non-linear dynamics of the pendulum can be linearized with respect to the unstable equilibrium point $\theta = 0$, this was corroborated by experimental data [24, 42], resulting in a widely accepted and employed modeling assumption [9, 29, 23, 43, 28].

Hence, the IP dynamics can be written as follows:

$$I\ddot{\theta} = mgl\sin\theta + \tau_a \tag{1.1}$$

or in a linearized form:

$$I\ddot{\theta} = mgl\theta + \tau_a \tag{1.2}$$

where I is the moment of inertia of the pendulum, that in this case corresponds to $I = ml^2$. The sway angle is θ and is defined with respect to the vertical axis, m is the total body mass of the subject, l is the distance between the ankle center and the COM, g is the gravity acceleration whereas τ_a is the ankle torque. Despite the model (1.2) is a simple second-order mechanical system, it is able to capture important aspects of the stance mechanics coherently with what observed from real posturographic data [8]. It should be stressed, that the equilibrium point $\theta = 0$ corresponding to the alignment of the link with the vertical axis (figure 1.1) is unstable and of the saddle type, i.e. there are two directions where the state evolves in a straigth line, moving away from the equilibrium point, or apporaching the latter in the other case. The two directions are given by the eigenvector of the IP dynamics [9]. This aspect is of great importance, and it is recalled in the next sections to explain the idea behind the intermittent control paradigm.

On the other hand, since the link is thought rigidly connected with the feet, and they are in equilibrium with the ground, the reaction force can be applied directly to the COM. Hence, as highlighted in [44, 13], the following equation holds:

$$m\begin{bmatrix}\ddot{x}_g\\ \ddot{y}_g\end{bmatrix} + mg\begin{bmatrix}0\\1\end{bmatrix} = \mathbf{R} = \begin{bmatrix}R_x\\R_y\end{bmatrix} \tag{1.3}$$

where $\ddot{x}_g$ and $\ddot{y}_g$ are the components of the COM acceleration vector, whereas R_x and R_y are the components of the ground reaction force $\mathbf{R}$. Moreover, for the feet the following torque equilibrium relation can be written:

$$\tau_a = mgx_g - COP(t)R_y - l_aR_x \tag{1.4}$$

where l_a is the vertical distance between the ground and the ankle joint center. It should be noted that $R_x \ll R_y$, $R_y \approx mg$. Thus the contribution given by R_x in (1.4) can be neglected.

It follows that the center of pressure can be written as

$$COP(t) = \frac{mgx_g - \tau_a}{mg} \tag{1.5}$$

since from the pendulum dynamics (1.2) the left-side term, namely the inertial term, is proportional to τ_a and under the linerization hypothesis one can write $I\ddot{\theta} = ml\ddot{x}_g$, by substituting in (1.5) the relation $\ddot{x}_g = \frac{l}{g}(x_g - COP)$ holds [12, 36]. Further from (1.5), it emerges the nature of COP as a lumped measure that accounts for both the gravity pull and the total ankle momentum τ_a which encloses the control and the postural noise torques [13].

Let now focus the attention to a double-link description of the stance. As already mentioned in section 2.1, a DIP description of the stance is encouraged by the fact that hip showed CNS-mediated regulatory mechanisms in perturbed posture [31] and possibly passive stiffness mechanisms in quiet stance maintenance [8, 45]. The dynamic equations of the DIP can

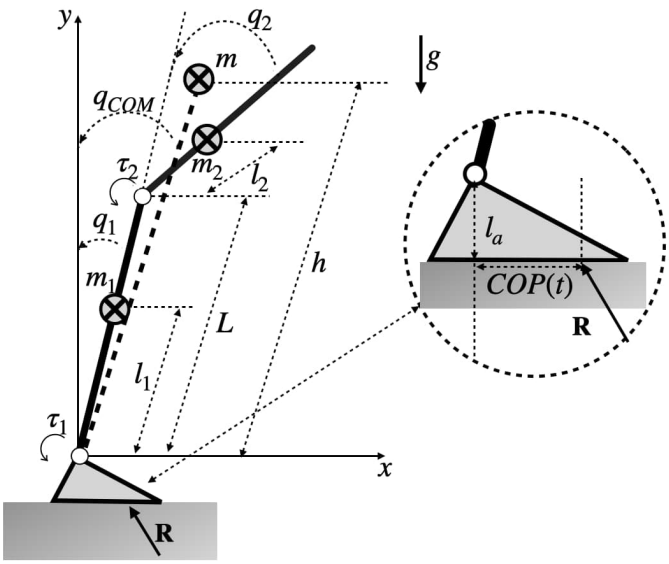

Figure 1.2: Schematic representation of the DIP and its VIP lumped from the overall mechanical structure.

be retrieved by using the lagrangian formulation [46, 8], one can notice that for the DIP shown in figure 1.2, the system equations resemble to the common two-link manipulator equations [46]. Hence, given the two generalized coordinates q_1 and q_2, representing the angles between the lower body segment and the vertical axis, and between the lower and upper body segments respectively, one can write them in a compact notation introducing

$\mathbf{q} = \begin{bmatrix} q_1 & q_2 \end{bmatrix}^T$. Hence the resulting equations of the system are:

$$\mathbf{M}(\mathbf{q})\ddot{\mathbf{q}} + \mathbf{C}(\mathbf{q}, \dot{\mathbf{q}})\dot{\mathbf{q}} + \mathbf{G}(\mathbf{q}) = \boldsymbol{\tau} \tag{1.6}$$

where $\mathbf{M}(\mathbf{q})$, $\mathbf{C}(\mathbf{q}, \dot{\mathbf{q}})$, $\mathbf{G}(\mathbf{q})$ are the inertial matrix, the generalized Coriolis term, and the gravity dependent torque respectively. The sum of the torques applied at the two joints is represented by $\boldsymbol{\tau}$. The above mentioned matrices for the DIP and the generalized coordinates reported in figure 1.2 assumes the following form :

$$\mathbf{M}(\mathbf{q}) = \begin{bmatrix} M_{11} & M_{12} \\ M_{21} & M_{22} \end{bmatrix} \tag{1.7}$$

$$\mathbf{C}(\mathbf{q}, \dot{\mathbf{q}}) = \begin{bmatrix} C_{11} & C_{12} \\ C_{21} & 0 \end{bmatrix} \tag{1.8}$$

$$\mathbf{G}(\mathbf{q}) = -g \begin{bmatrix} G_1 \\ G_2 \end{bmatrix} \tag{1.9}$$

with

$$\begin{cases} M_{11} = I_1 + I_2 + m_1 l_1^2 + m_2(L^2 + l_2^2 + 2Ll_2 \cos q_2) \\ M_{12} = M_{21} = I_2 + m_2(l_2^2 + Ll_2 \cos q_2) \\ M_{22} = I_2 + m_2 l_2^2 \end{cases} \tag{1.10}$$

$$\begin{cases} C_{11} = -m_2 L l_2 \dot{q}_2 \sin q_2 \\ C_{12} = -m_2 L l_2 (\dot{q}_1 + \dot{q}_2) \sin q_2 \\ C_{21} = m_2 L l_2 \dot{q}_2 \sin q_2 \end{cases} \tag{1.11}$$

$$\begin{cases} G_1 = (m_1 l_1 + m_2 L) \sin q1 + m_2 l_2 \sin(q_1 + q_2) \\ G_2 = m_2 l_2 \sin(q_1 + q_2) \end{cases} \tag{1.12}$$

where m_1, I_1 and m_2, I_2 are the mass and the moment of inertia of the lower and upper trunk respectively, l_1 represents the distance between the ankle and the lower limb COM, l_2 is the distance between the hip and the COM of the upper trunk, whereas L is the distance between the ankle and the hip joint.

As done for the IP model, DIP can be linearized as in [29], however, as numerically evaluated in [8, 13], the intermittent control paradigm is able to stabilize the system given in a nonlinear form. Moreover, the mechanical linearization of the DIP cancel out the term $\mathbf{C}(\mathbf{q}, \dot{\mathbf{q}})$ which shows physical coupling effects between the lower and upper segment. Hence, hereon the DIP dynamics refers to the nonlinear system reported in (1.6).

As already mentioned, an IP description can be obtained starting from the DIP or more in general by an multi-link structure [44]. Then, such IP can be used as an internal model for computing control action as done in the DIP/VIP model [8, 13]. To obtain the virtual IP, one can observe that from a mechanical point of view, the center of gravity can be retrieved from the upper and lower limb masses, indeed, for the DIP (see figure 1.2) one can write:

$$\begin{bmatrix} x_g \\ y_g \end{bmatrix} = \begin{bmatrix} m_1 l_1 \sin q_1 + m_2 (L + l_2) \sin(q_1 + q_2) / (m_1 + m_2) \\ m_1 l_1 \cos q_1 + m_2 (L + l_2) \cos(q_1 + q_2) / (m_1 + m_2) \end{bmatrix} \tag{1.13}$$

and the variable q_{COM} can be computed as:

$$q_{COM} = \arctan\left(\frac{x_g}{y_g}\right) \tag{1.14}$$

where q_{COM} is the sway angle of the virtual IP with respect to the vertical. Under the hypothesis that the DIP is in equilibrium, the relations expressed through (1.3),(1.4),(1.5) hold [44, 13, 27]. However, it is interesting to observe that the multi-link nature of the DIP suggests a more profound investigation behind the physical meaning of the COP [13]. Actually, the net ankle moment τ_a expressed in (1.5) is the time derivative of the angular momentum at the ankle joint [44, 47], more precisely, by introducing σ_a as the angular momentum of the DIP around the ankle, it follows that $\tau_a \equiv \dot{\sigma}_a$. The angular momentum σ_a by definition is linear with respect to the angular velocities and it can be obtained by deriving the lagrangian of the DIP $\mathcal{L}(\mathbf{q}, \dot{\mathbf{q}})$ with respect to q_1 [13]:

$$\sigma_a = \frac{\partial}{\partial \dot{q}_1} \mathcal{L}(\mathbf{q}, \dot{\mathbf{q}}) = \mathbf{N}(\mathbf{q}) \dot{\mathbf{q}} \tag{1.15}$$

where $\mathbf{N}(\mathbf{q})$ can be obtained directly by computing the partial derivative of the lagrangian. However, as observed in [47], one can exploit the fact that only the kinetic energy term of the lagrangian depends on $\dot{\mathbf{q}}$. This is convenient since one can easily obtain a form for $\mathbf{N}(\mathbf{q})$

[13]:

$$\sigma_a = \begin{bmatrix} M_{11} & M_{12} \end{bmatrix} \dot{\mathbf{q}} = \mathbf{N}(\mathbf{q})\dot{\mathbf{q}} \tag{1.16}$$

hence $\mathbf{N}(\mathbf{q})$ corresponds to the first row of the DIP inertia matrix. The time derivative of the angular momentum can be performed numerically, however it is interesting to notice that, when one differentiates (1.15) with respect to time and substitutes in such time derivatives the DIP dynamics, it realizes that COP lumps all the control actions developed at the ankle and hip joints, spanning both passive and active mechanisms [13, 44]. Thus, it can be hypothesized that, if the postural control mechanisms at the considered joints are physiologically plausible, one should obtain COP time-series that, under some opportune descriptors, resemble the characteristics observed through real data posturographic analysis [13, 27].

1.2.2 Modeling the CNS active role in balance maintenance: the intermittent control paradigm

In the previous section, the mechanical models commonly encountered for describing the kinetic quantities involved in balance maintenance have been introduced. However, a biomechanical perspective of the regulatory processes that take place at the body joints cannot avoid the formalization of the active role played by the CNS in sensing and delivering postural adjustment commands.

As mentioned in 2.1, the role of the CNS in regulating the stance is not limited to the mere muscle tone maintenance, but on the contrary, the literature highlighted that the CNS actively contributes to the stance maintenance through feedback control strategies [12, 2]. Moreover, the idea that such control action is characterized by an intermittent nature kept particular attention from the scientific community. Indeed, as reported in the seminal work of Collins and De Luca[2], the CNS could monitor the postural fluctuations at the joints through interoception, acting when the sway overcomes some threshold. However, such intuition of "act when needed" was better formalized through the use of opportune variable structure control policies by Asai and colleagues [9]. In this thesis, the intermittent control employed for modeling the active role provided by the CNS is referred to the one proposed in [9]. This choice was motivated by two reasons: firstly the model presents physiological and physical plausible basis as confirmed in [9, 8, 30, 13], secondly the sway data of the global models, i.e. stance mechanics plus control, seem able to reproduce patterns observed in real data, supporting the validity of such active control model for the CNS [23].

Let now consider the stabilization the IP model seen in section 1.2.1 whose dynamics can be described through (1.2) as in [9, 23]. The torque τ_a can be thought as the sum of three contributions:

$$\tau_a = \tau_s + \tau_{\text{act}} + \tau_n \tag{1.17}$$

where τ_s is the stiffness control torque due to basal muscle tone and ligaments mechanical properties, this control mechanism can contribute to the balance maintenance but it is not sufficient to provide full stabilization without an additive contribution [12, 14]. A linear feedback made by a proportional (P) and derivative (D) contributions with respect to the angle sway variable can capture consistently this stiffness properties of the muscles [12], thus for τ_s a the following model can be employed:

$$\tau_s = -K\theta(t) - B\dot{\theta}(t) \tag{1.18}$$

where K and B are essentially a passive spring and damping components which model the aforementioned muscle and ligaments resistance to the body inertia. The intermittent active control modeling the CNS contribution is expressed through τ_a, and presents a switching nature. In order to describe this term in (1.17), a phase space partitioning is required to inject the input in the system when the system-state latter enters or remains within a specific portion of the aforementioned space. As in [9, 23], the regions in the state space for which the active control is turned on or off is shown in figure 1.3. Actually, switching controllers can be obtained by thresholding quantities of interest such as the sway angle and its time derivatives [28], this leads to rectangle-like on-off regions in the state space, however more complicated geometries for describing S_off as that employed in [9, 29, 8] were supported by other approaches based on reinforcement learning for stabilizing inverted pendulum [48]. A further aspect that deserves to be recalled is that the feedback loop provided by the active control generally accounts for a delay term that models the nervous fibers transmission and commands computation. Such delay in the feedback loop is taken in consideration regardless the use of a continuous or intermittent motor control paradigm [9, 28, 43]. However, while in the continuous paradigm the delay implies a fine P and D parameter tuning to get the IP stabilization, the intermittent control accepts lower values for the two above mentioned controller gains, exploiting the spiraling delay-induced instability of the system in the S_{on} region to steer the state close to the unique stable manifold of the pendulum [23]. Thus it is possible to proof through Poincaré maps that a bounded stability with limit cycle can be

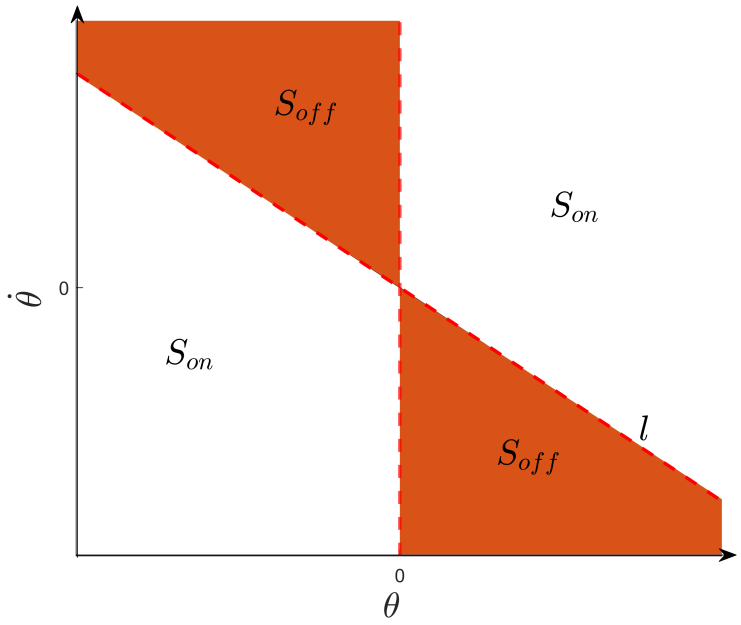

Figure 1.3: Phase space partitioning for the intermittent control model. Active control is turned on when system state is in the S_{on} regions and is turned on in the S_{off} one

obtained [9]. Hence, the active control law employed can be mathematically expressed as follows:

$$\begin{cases} \tau_{\text{act}} = P\theta_{\Delta} + D\dot{\theta}_{\Delta}; & \text{if } \theta_{\Delta}(\dot{\theta}_{\Delta} - l\theta_{\Delta}) > 0 \\ \tau_{\text{act}} = 0; & \text{otherwise} \end{cases} \tag{1.19}$$

where P and D are the proportional and derivative control gains of the active controller, θ_{Δ} and $\dot{\theta}_{D}elta$ expresses the sway angle and its time derivative delayed of a quantity of time Δ, whereas α is the slope of the line that defines the S_{on} region (figure 1.3). As highlighted in [23], the switching activity is driven by the portion of the phase plane where the active controller is turned on with respect to the whole phase plane (figure 1.3). This quantity can be defined as ρ and it is formally equivalent to [23]:

$$\rho = \frac{S_{on}}{S_{on} + S_{off}} \equiv 0.5 - \frac{\arctan(\alpha)}{\pi} \tag{1.20}$$

To be noted, if the active controller is continuously turned on, the S_{off} area is equal to zero ($\rho = 1$), and the model generalizes the continuous motor control paradigm [23]. For a non-null S_{off} the active controller is turned on and off ($\rho < 1$) and the motor control paradigm is the intermittent one. Eventually, if the S_{on} area is zero ($\rho = 0$), the active

controller never turns on and the pendulum stabilization can be reached only through the passive components of τ_a.

The idea of extending this active control policy to a DIP structure was introduced in [29], where a linearized VIP was employed. Also in that case, a specific partition of the state space was proposed, and the switching criteria were ruled out. However, one can wonder if there is the need of an active control component at the hip. However, since the hip presents gross ligament and muscles, it might contribute through a stiffness mechanism in the stabilization of the body. The latter principle was followed by Morasso and co-workers in [8], where the DIP/VIP described in section 1.2.1 was introduced. This perspective is confirmed also by [45], where hip muscle activity presents no correlation with the oscillations of the upper trunk. This can be translated in the modeling framework assuming that hip stiffness is over-critical. Thus, given the hip stiffness K_h, the condition $K_h > m_2 g l_2$ holds (figure 1.2) [8], which means that in quiet stance the hip behaves as a non actuated joint which stiffs the upper trunk. Under this assumption, the control law expressed through 1.19 was used to active control the DIP only at the ankle. Recalling the torque vector $\boldsymbol{\tau}$ in the DIP dynamics (1.6), it can be viewed as the sum of three components resembling what observed for the IP:

$$\boldsymbol{\tau} = \boldsymbol{\tau}_s + \boldsymbol{\tau}_{\text{act}} + \boldsymbol{\tau}_n \tag{1.21}$$

the $\boldsymbol{\tau}_s$ represents the stiffness torque modeled as in (1.4), more specifically:

$$\boldsymbol{\tau}_S = \begin{bmatrix} K_a q_1 + B_a \dot{q}_1 \\ K_h q_2 + B_h \dot{q}_2 \end{bmatrix} \tag{1.22}$$

where K_a and K_h model the stiffness at the ankle and the hip, whereas B_a and B_h account for the intrinsic damping properties of the muscles. Concerning the active torque $\boldsymbol{\tau}_{\text{act}}$ in the DIP/VIP framework, one can observe that it can be modeled as:

$$\boldsymbol{\tau}_{\text{act}} = \begin{cases} \begin{bmatrix} -(P q_{COM_\Delta} + D \dot{q}_{COM_\Delta}) \\ 0 \end{bmatrix} & \text{if } q_{COM_\Delta}(\dot{q}_{COM_\Delta} - \alpha q_{COM_\Delta}) > 0 \\ \begin{bmatrix} 0 \\ 0 \end{bmatrix} & \text{otherwise} \end{cases} \tag{1.23}$$

to be noticed, the control laws (1.19) and (1.23) are of the same form since they consider the

same state space partition and the same joint of actuation, however, in this case, the state variable employed is the one obtained by the VIP internal model, namely q_{COM} which lumps the information of the overall DIP mechanical structure. As observed through numerical simulations [8, 13], the system can be stabilized within the control gains ranges proposed in [8]. The last term that have to be described in (1.4) and in (1.21) is the postural noise, i.e. τ_n and $\boldsymbol{\tau}_n$ for IP and DIP respectively, and it can be modeled through additive gaussian noise with null mean and standard deviation that commonly ranges between 0.2 and 0.5 Nm.

The two above mentioned models, that is IP and DIP/VIP, can be used in a variety of ways, ranging from simulation to parameter identification and inference [8, 23, 13]. In the following sections these two models will be used respectively in two contexts. In the first case, the IP intermittently controlled is analyzed in order to understand how long-term correlation and inhomogeneity properties of the simulated COP time-series changes with respect to changes in the active controller parameters. On the contrary DIP/VIP is used to evaluate whether differences between COP descriptors of healthy young and elderly adults can be mirrored in changes in controller parameters. However, before to enter in the details of the two experiments, it is important to describe the COP analysis techniques used in this work of thesis.

1.2.3 Time-series analysis perspective of COP data

The annalysis of posturographic data, in particular of COP time course in both AP and ML directions received great attention through the years [19]. Many different descriptors have been proposed to synthetically describe the process of balance maintenance and its alteration from real data. A consistent number of geometrical and frequency domain descriptors were proposed in [20], however spatial features highlighted by Prieto et. al [20] for instance, do not take into account the correlation properties of the COP time-series, which on the contrary can highlight different aspects regarding the regulatory mechanisms involved in the upright stance maintenance [49]. In this view, nonlinear timeseries analysis approaches focusing on timeseries self-similarity, disorder state and attractor in phase space revealed to be particularly useful in characterizing the COP data [50, 7, 49, 17, 51]. Moreover, literature highlights analysis tools that were developed for the COP[2, 16, 15].

1.2.4 SDA

Among the tools properly developed for COP, Collins and De Luca proposed the sway diffusion analysis (SDA) [2], Zatsiorsky and Duarte formulated the rambling and trembling COP decomposition , whereas Jacono et al. developed the sway density curve [15]. However, in the latter, descriptors are extracted from an aggregated timeseries that combines both AP and ML information [15], while rambling and trembling decomposition requires that COP data are opportunely combined with ground reaction force time-course [16]. Thus, despite such techniques permit a deep understanding of the posturography dataset one deals with, they need multiple timeseries fusion. Although SDA can be performed upon the bidimensional COP data to obtain a global description, one can also treat the single AP and ML components separately[2]. This is particularly convenient in those cases where one would study the effects of control parameters changes in a model that describes the stance maintenance in one direction [10, 27, 13].

The steps required to perform the SDA are reported in [2] and they are here recalled. Given the COP time course, one can compute the square of the COP displacements Δr between all pairs of points separated in time by a specific time interval Δt, the square displacements were then averaged over the number of samples m spanned by a given Δt [2]:

$$\langle \Delta r^2 \rangle_{\Delta t} = \frac{\sum_{i=1}^{N-m} (\Delta r_i^2)}{N-m} \tag{1.24}$$

The plot of COP mean square displacement versus time interval Δt is referred to as a *stabilogram-diffusion plot* (figure 1.4). From the latter representation one can compute different parameters, in particular the two diffusion coefficients D_{rs} and D_{rl} of the short and long-term region respectively, obtained through linear interpolation as in figure 1.4. Another important feature is the critical time T_{CR} which describes the time scale for which a distinction between the two aforementioned regions takes place. Such kind of analysis resulted particularly useful to discriminate among group of subjects since it permits to highlight differences in the typical two regions encountered in the stabilogram diffusion plot obtained for COP data [52, 7]. However, it is remarkable that the SDA descriptors should be interpreted under the feedback control theory [21], in this perspective the long-term region should mirror the sign of the modulatory activity carried by the CNS, whereas the "open-loop" control strategy defined by Collins and De Luca should be prevailed by the passive stabilization mechanisms. Moreover, it can be observed that the SDA can be classified

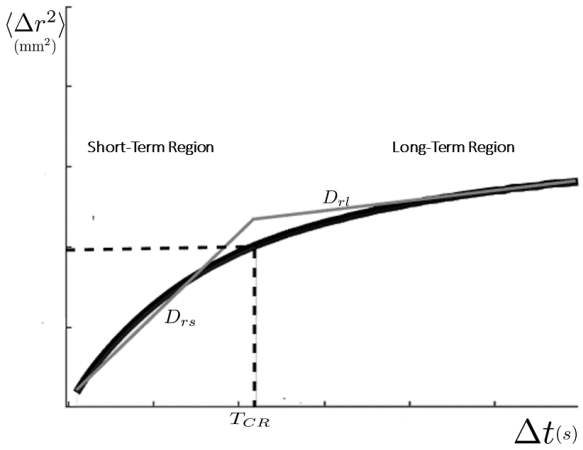

Figure 1.4: Schematic representation of the stabilogram diffusion plot. The T_{CR} is obtained as the time interval at which the intersection between the two fitting lines, respectively characterized by D_{rs} and D_{rl} slope coefficients, occurs.

as a multi-scale fractal analysis technique [53, 49]. However, also a global fractal analysis performed over the time-series can provide meaningful interpretation of the posturographic data as shown in [7, 13, 54, 51].

1.2.5 EDFA

A typical approach to perform fractal time-series fractal analysis is the detrended fluctuation analysis (DFA). Such technique was originally developed by Peng et al. [55, 56], and it was used to deal with a variety of biological timeseries, ranging from heart-rate to electroencephalographic activity and COP data [56, 57, 54, 7]. More in detail, given a time series $x(i)$ of length N, the DFA involves the transformation of $x(i)$ in its profile $y(i)$ through an integration after mean removal [56, 58]:

$$y(k) = \sum_{i=1}^{k} [x(i) - \langle x \rangle], \quad \langle x \rangle = \sum_{i=1}^{N} x(i) \tag{1.25}$$

The resulting profile or random walk undergoes to non-overlapping segmentations of equal length n. Then, for each segment of the profile, a local trend $y_n(k)$ is computed through a linear fit in a least square sense [59, 56]. When local trend is available, one can proceed by computing the fluctuation, or standard deviation of the signal profile around the local trend

as:

$$F(n) = \sqrt{\frac{1}{N}\sum_{k=1}^{N}[y(k) - y_n(k)]^2} \tag{1.26}$$

The process is iterated for different segment size (n) in order to obtain $F(n)$ over a possible large number of scales. In general, $F(n)$ presents a power law behavior of the type:

$$F(n) \sim n^{\alpha} \tag{1.27}$$

where the α parameter can be estimated through the log-log representation of $F(n)$ versus n and it is generally referred as the Hurst exponent [58, 56, 7].

What reported until now are the basic steps of the DFA. However, as highlighted in [59], the inhomogeneity of the data, which can be due to multiple dynamics interactions, can lead to a consistent variability of the profile fluctuations around the local trend among the different signal epoch sizes (n). This can produce a departure from model (1.27), rendering more challenging the interpretation of the classical DFA. To mitigate this aspect, in [60, 59] the authors proposed a DFA extension, namely EDFA, that takes care of the heterogeneity in the RMS fluctuations. Hence, in addition to the canonical DFA, one can consider the following quantity:

$$dF(n) = max[F_{loc}(n)] - min[F_{loc}(n)] \tag{1.28}$$

where $dF(n)$ is the difference between the maximum and minimum local RMS fluctuations $F_{loc}(n)$ [59]. Here, the local RMS fluctuations of the signal profile $y(k)$ from the trend $y_n(k)$ depends on the epoch length (n). As observed in [59], also $dF(n)$ could change with n, following a power-law dependence with another scaling exponent β:

$$dF(n) \sim n^{\beta} \tag{1.29}$$

In this view, β can be used in conjunction with the Hurst exponent (HE) obtained through the classical DFA in order to enrich the description of the data, hence considering not only the persistent or anti-persistent behavior of the time-series, but also evaluating the local inhomogeneity of the latter [59]. Moreover, it is important to note that a relation between the sample or time scale (n)and the information content of the signal in the frequency domain

exists [54]. In particular a relation of the following type holds:

$$n(f) = \frac{f_s}{f} \tag{1.30}$$

where f_s is the sampling frequency and f is considered frequency that one would investigate. Hence, the larger is the time scale (n) the lower is the frequency one is considering. Despite this could appear trivial, it is important to remember that the sign of CNS modulation in balance control is manifested at low-band frequency ranges of 0.5-0.1 Hz (LB) [54, 19].

1.2.6 Long-term correlation and inhomogeneity of the inverted pendulum COP data under the intermittent control

A first aspect that deserves to be investigated is the study of the global long-term correlation of the sway data generated by the IP model when it is controlled intermittently (see section 1.2.2). Following what proposed in [9], the stiffness term K in (1.18) was set at the 80% of mgh. In this way, a low level of intermittency is always required. One thousand stable simulations of 60 s were run sampling (P, D, ρ) from opportune uniform distributions, whereas the other parameters of the model were fixed as reported in table 1.1. For each simulation, the COP with respect to the ankle joint was obtained following the relation proposed in 1.5.

Table 1.1: Table shows the model parameters and the intermittent controller parameters used to simulate the model. P, D and ρ were sampled from uniform distributions in plausible ranges [8, 23, 29]

m (kg)	I (kg·m^2)	h (m)	B (N·m·s/rad)	K (N·m/rad)	g (m/s^2)	Δ (s)	σ (N·m)	P (N·m/rad)	D (N·m·s/rad)	ρ
60	60	1	4.0	471	9.81	0.2	0.2	$\mathcal{U}_{[294;\,471]}$	$\mathcal{U}_{[0;\,400]}$	$\mathcal{U}_{[0.3;\,1]}$

Then, EDFA was performed and both Hurst and β exponents were calculated in order to understand how intermittent controller parameters affects the complexity of the COP time-course. Moreover, as reported in 1.2.2, the parameter ρ guides the level of intermittency of the control low. Thus, since $\rho \simeq 0.6$ has been reported for a typical intermittent control model whereas for $\rho \to 1$ the control policy approaches a continuous behavior [23], two different windows of ρ values have been investigated, with respect to the relationship between ρ itself, the control gains (P and D), and the EDFA exponents (α and β). When ρ ranges from 0.3 to 0.6 one can consider a full intermittent control regime, whereas for ρ greater than 0.6, one can refer to a shift toward a continuous control policy.

1.2.7 DIP/VIP kinetic plausibility

As it would be emerged in section 2.1, a further aspect investigated in this work of thesis was the evaluation of the kinetic plausibility of the DIP/VIP model[13]. To do this a public available dataset presented in [61] was employed to compare real COP characteristics with the ones obtained by simulated COP. In particular, posturogrpahic data of thirty subjects were taken into account: fifteen belonging to a healthy adults group, representing a young cohort (Y) with an age not greater than 36.9 years and fifteen to an elderly group (O), presenting an age greater than 60.0 years [13]. Data were sampled at 100 Hz for 60 s, filtered at 10 Hz with a zero-phase second order low-pass filter, and detrended. Only the anterior-posterior component (AP) of COP was considered for further analysis in order to maintain coherency with the DIP/VIP model description of the upright stance.

Three COP descriptors were selected to evaluate the DIP/VIP kinetic plausibility. Such descriptors were selected among a set of six, based on their ability in highlighting significant differences between the Y and O groups. The initial feature set embraced the only two universal indexes in AP direction presented in [19]: the frequency at which COP presents the 50% (PF50) of its whole power spectrum density (PSD) [19, 20], and the slope of the PSD in the low frequency band 0.1 - 0.5 Hz (SLOPE-L) [9, 19]. Moreover, two features related to sway amplitude, i.e. the mean distance (MD) and the sway range (SR) [20, 6] were taken into account, whereas HE and T_{CR} were considered as complexity time-series descripotrs since they demonstrated their discriminative power in other studies [62, 63]. Each feature was computed for both the two aforementioned groups, and they were group-compered as in [13] to asses which feature could provide insight decription of the changes in control mechanisms between Y and O.

It resulted that PF50, T_{CR} and HE were able to discriminate between Y and O groups, hence they were used for the evaluation of COP time-series obtained as output of the DIP/VIP. The anthropometric characteristics required to fill the latter were computed as the average among the subjects and they are reported in table 1.2 [13]. In this case, the

Table 1.2: Table shows the anthropometric values used to fill the DIP/VIP model in the simulation steps.

L (m)	l_1 (m)	l_2 (m)	m_1 (kg)	m_2 (kg)	I_1 (kg·m^2)	I_2 (kg·m^2)	K_a (N·m/rad)	K_h (N·m/rad)	B_a (N·m·s/rad)	B_h (N·m·s/rad)
0.87	0.39	0.45	19.3	40.7	2.9	7.9	366.0	246.0	22.0	22.0

coefficient α in (1.23) was set equal to 0.4 s^{-1} in accordance with [8], in the same way a delay value of $\Delta = 0.2$ s was chosen [8, 9], whereas the $\boldsymbol{\tau}_n$ was modeled through white noise with standard deviation of 0.2 N·m [8, 29].

Concerning the intermittent control gains, based on the results provided by [8], P varied between $0.3 \cdot mgh$ and $0.9 \cdot mgh$ N·m, and D between 0 to 200 $N \cdot m \cdot s/rad$ [8]. Such range of values were linearly spaced forming a parameter space used to parametrized the intermittent controller for the simulation of COP from the DIP/VIP model. The P-D grids representation was limited to those values for which the model provided stable and physiologically plausible outputs. For each combination of P-D parameters, 10 COP time-series were generated [13].

Thus, PF50, T_{CR} and HE were computed for each simulated COP, providing the dependency of each metric upon P and D combinations. For both populations , i.e. Y and O groups, it was assumed a plausible range for each of the above-mentioned metric (PMR), defined as the mean population value ± standard deviation (see section 1.3). Eventually, a series of grids was built to obtain P and D ranges for which all the three COP descriptors were coherent with synthetic and real data at the same time. Therefore, those P-D values for which the feature maps fell within the PMR-Y and PMR-O at least one time among the ten COP realizations and for all of the three features were selected [13, 27].

1.3 Results

1.3.1 On the long-term correlation properties and inhomogeneity of sway data under the intermittent control paradigm

In Figure 1.5 the mean trends among all the simulated time series of both F and dF are shown in the log-log scale. The fluctuations manifest a greater variability at the higher time

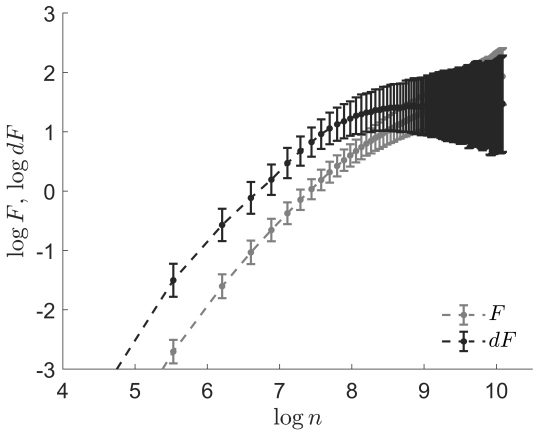

Figure 1.5: Log-log representation of the EDFA fluctuations in mean and standard deviation; the latter was computed over the 1000 synthetic COP time-series generated by the model.

scales, suggesting that changes in the active controller parameters mainly impacts at the lower frequency ranges. Indeed, focusing at LB range (figure1.6), one can appreciate that both type of fluctuations are affected by the aforementioned parameters (see 1.2.6). In particular, dF showed a greater level of variability at all the (n) with respect to F, likely indicating that dF responds to the same control parameters changes by greater modifications of its value. As reported in section 1.3.1, the three intermittent controller parameters (ICP) P, D and ρ guide the dynamics of the IP, hence in figure 1.7, 1.8, and 1.9 are reported the relations between the Hurst exponent α, and the inhomogeneity coefficient β, with respect to the three aforementioned ICP when considered over their range of variation (table 1.1). Globally, P does not appear related to neither the long term correlation nor to the inhomogeneity properties of the simulated COP time-series, as showed by the poor correlation obtained between P, α, and β (figure 1.7). The same can be observed for the ρ parameters (figure 1.9), although the scattered data points seem to reveal a nonlinear relation between the variables taken into account (figure 1.9). On the contrary, the derivative gain term D presents a strong relation observed with both the EDFA coefficients, e.g. $r = -0.83$ and $r = -0.63$, $p <0.0001$,

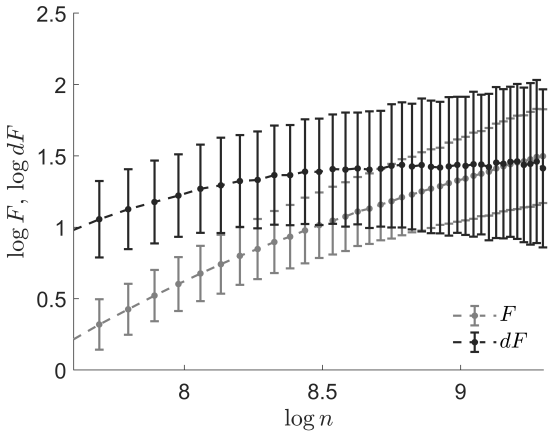

Figure 1.6: Log-log representation of the EDFA fluctuations in mean and standard deviation. Focus on the time scales that maps the frequency band 0.5-0.1 Hz.

for α and β respectively.

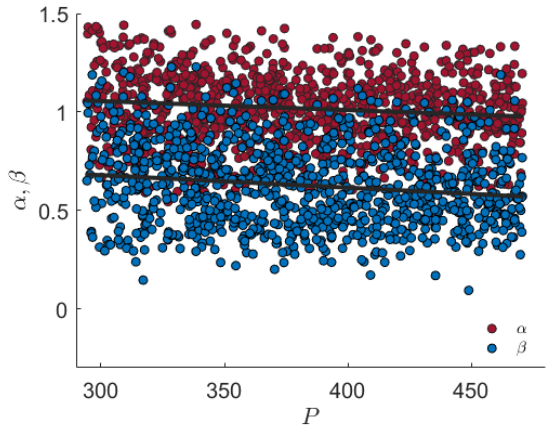

Figure 1.7: EDFA coefficients α and β obtained for the simulated COP time series and scattered in relation to P parameter. The correlation coefficients results $r = -0.12$ and -0.15, for α and β respectively. Figure shows also the linear trend between P and the coefficients.

The role of D in affecting the long term correlation and inhomogeneity properties of COP time-series, at least globally, is strengthened by considering separately $\alpha - D$ and $\beta - D$ relations (figures 1.10 and 1.11). In both cases, it appears that the inter-dependence between D and EDFA coefficients can be fitted with two straight lines characterized by different slopes, highlighting the possible existence of two different relationships, depending upon D values. In order to test this hypothesis, both the $\alpha - D$ and $\beta - D$ were fitted through a least-square spline approach [64], testing respectively the existence of three models, described by one, two, and three polynomials of order 1. The criterion used for assessing the best

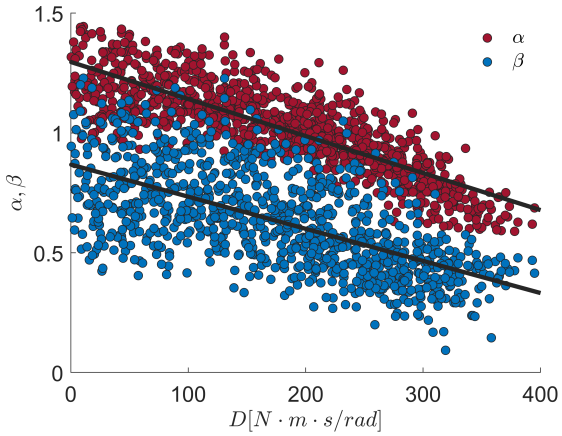

Figure 1.8: EDFA coefficients α and β obtained for the simulated COP time series and scattered in relation to D parameter. The correlation coefficients results $r = -0.83$ and -0.63, for α and β respectively. Figure shows also the linear trend between D and the coefficients.

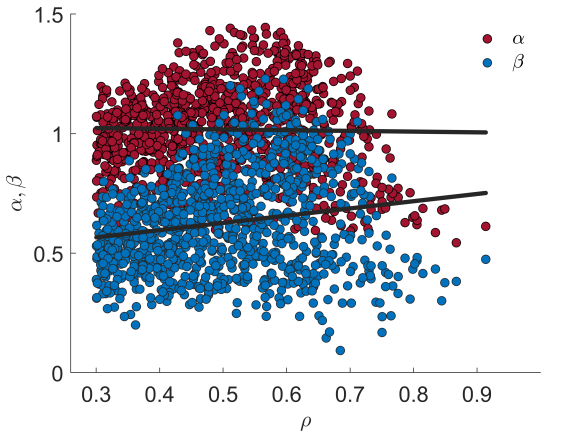

Figure 1.9: EDFA coefficients α and β obtained for the simulated COP time series and scattered in relation to ρ parameter. The correlation coefficients result $r = -0.019$ and 0.17, for α and β respectively. Figure shows also the lines fitted through least mean square analysis between ρ and the coefficients α and β.

model was the normalized Akaike's information criterion (nAIC) [65], for which the most accurate model presents the lowest nAIC.

For both $\alpha - D$ and $\beta - D$ data distributions, the best fitting model is that with a single knot point and thus with two lines: in this case the nAIC resulted equal to -4.67 versus -4.57 (one line) and -4.40 (three lines) for $\alpha - D$. Similarly, for $\beta - D$ the two-lines model presented a nAIC of -3.67 versus -3.60 (one line) and -3.52 (three lines). In addition, in both cases the crossing point between the two lines (the knot), presents the same value, i.e. D =243 $N \cdot m \cdot s \cdot rad^{-1}$ (Figs. 1.10 and 1.11).

This suggests that ρ ad P data can be partitioned in relation to the knot point identified for D. Therefore, those P and ρ values for which the correspondent D gain is respectively $<243\ N \cdot m \cdot s \cdot rad^{-1}$ and $\geq 243\ N \cdot m \cdot s \cdot rad^{-1}$ are separately consider to better highlight the possible relations that the two aforementioned parameters may present with respect to the EDFA coefficients. The P gain does not show any significant correlation neither with α ($r = -0.36$ and $r = -0.19$, for $D < 243N \cdot m \cdot s \cdot rad^{-1}$ and $D \geq 243N \cdot m \cdot s \cdot rad^{-1}$ respectively), nor with β ($r = -0.32$ and $r = -0.11$, for $D < 243N \cdot m \cdot s \cdot rad^{-1}$ and $D \geq 243N \cdot m \cdot s \cdot rad^{-1}$ respectively). On the contrary, ρ presents a different behavior with respect to α and β depending on the values assumed by the derivative gain. When D is lower than 243 $N \cdot m \cdot s \cdot rad^{-1}$, both α and β showed a significant (p <0.0001) correlation with ρ (r =0.44 and 0.61, respectively, figure. 1.12), whereas for D greater than 243 $N \cdot m \cdot s \cdot rad^{-1}$, the relations between ρ and the two EDFA coefficients completely disappears (figure 1.13), showing poor correlation coefficients,e.g. $r = -0.0021$ for $\alpha - \rho$ and $r = -0.14$ for $\beta - \rho$. This aspect supports what previously reported regarding the particular shape of the data cluster shown in 1.9, hence revealing a more profound relation among the ICP and the characteristics of COP time-course.

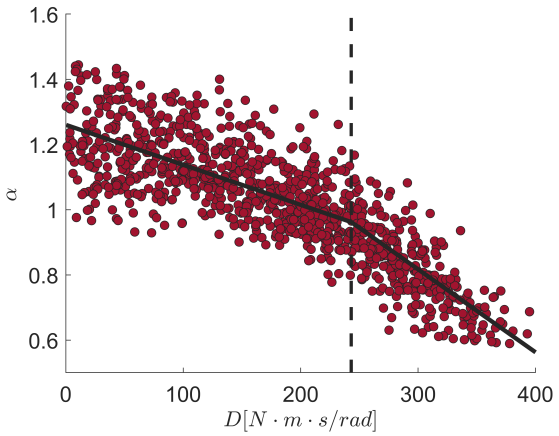

Figure 1.10: EDFA α coefficient scattered against D parameter. The two lines of the best fitting model are reported in black and the knot point is indicated with the dashed, vertical line.

1.3.2 Regarding the DIP/VIP kinetic plausibility

The average PSD, reported in a log-log scale (see figure 1.14, panel a) shows a higher power content at the lower frequency range for the Y group and a statistically significant lower PF50 (figure 1.14 panel b). This was further confirmed by the PMR obtained through the

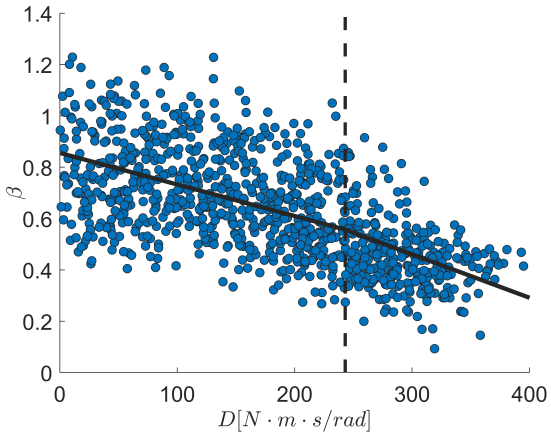

Figure 1.11: EDFA β coefficient scattered against D parameter. The two lines of the best fitting model are reported in black and the knot point is indicated with the dashed, vertical line.

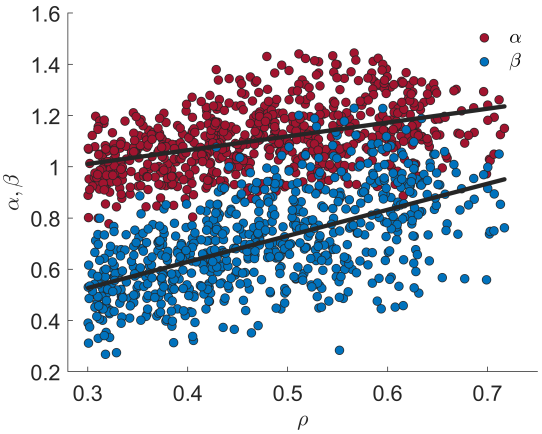

Figure 1.12: EDFA coefficients α and β obtained for the simulated COP time series and scattered in relation to ρ parameter for D <243 $N \cdot m \cdot s \cdot rad^{-1}$. Figure shows also the linear trend between ρ and the coefficients.

analysis reported in section 1.2.7 and listed in table 1.3.

Table 1.3: Table shows PMR for the three parameters and for both populations.

	PMR		
Group	PF50 (Hz)	T_{CR} (s)	HE
Y	0.09±0.06	1.63±0.59	1.32±0.12
O	0.16±0.13	1.12±0.32	1.17±0.13

Moreover, for the Y group, the mean SDP (figure 1.14, panel c) increased less than the O

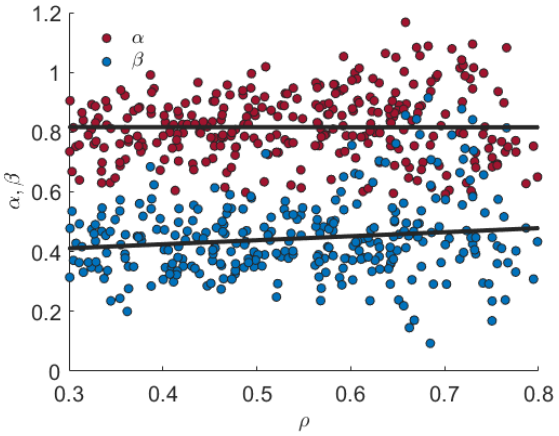

Figure 1.13: EDFA coefficients α and β obtained for the simulated COP time series and scattered in relation to ρ parameter for $D \geq 243\ N \cdot m \cdot s \cdot rad^{-1}$. Figure shows also the lines fitted through least mean square analysis between ρ and the coefficients α and β.

at the lower time scales. This contributes to the higher T_{CR} (Table 1.3), since the SDP slope in its first part heavily impacts on the T_{CR} estimation [2], the statistical analysis performed additionally showed that the T_{CR} resulted able to discriminate between Y and O (figure 1.14, panel d). Eventually, the HE exhibited a strong significant difference between the two groups (figure 1.14, panel f), confirming the discriminant power of this feature [7]. This can be appreciated also from the remarkable change in the average regression lines slope between Y and O groups (figure 1.14, panel e, and Table 1.3). The three COP descriptors were also computed for the synthetic COP data. Gray-maps (figure 1.15) describe how PF50, T_{CR} and HE vary with respect to the active control parameterization. PF50 seems to be more sensitive to the variations of D when P was $\approx$ 300 N·m/rad (figure 3a), and greater PF50 excursions were found for low P values[13]. On the opposite, T_{CR} (figure 1.15, panel b) seemed to better mirror changes in the P parameter when D was low (between 0 and 50 N·m·s/rad). The HE instead presented a smoothed trend, radially decreasing when both P and D increase (figure 1.15, panel c). Eventually, the ranges obtained for the two groups were reported in table 1.4 and their average$\pm$ standard deviation values are reported as shaded areas in figure 1.15. Larger P and D values were admissible to obtain COP having characteristics in line with the O group with respect to the Y population. On the contrary, the Y group admitted narrower P and D ranges [13].

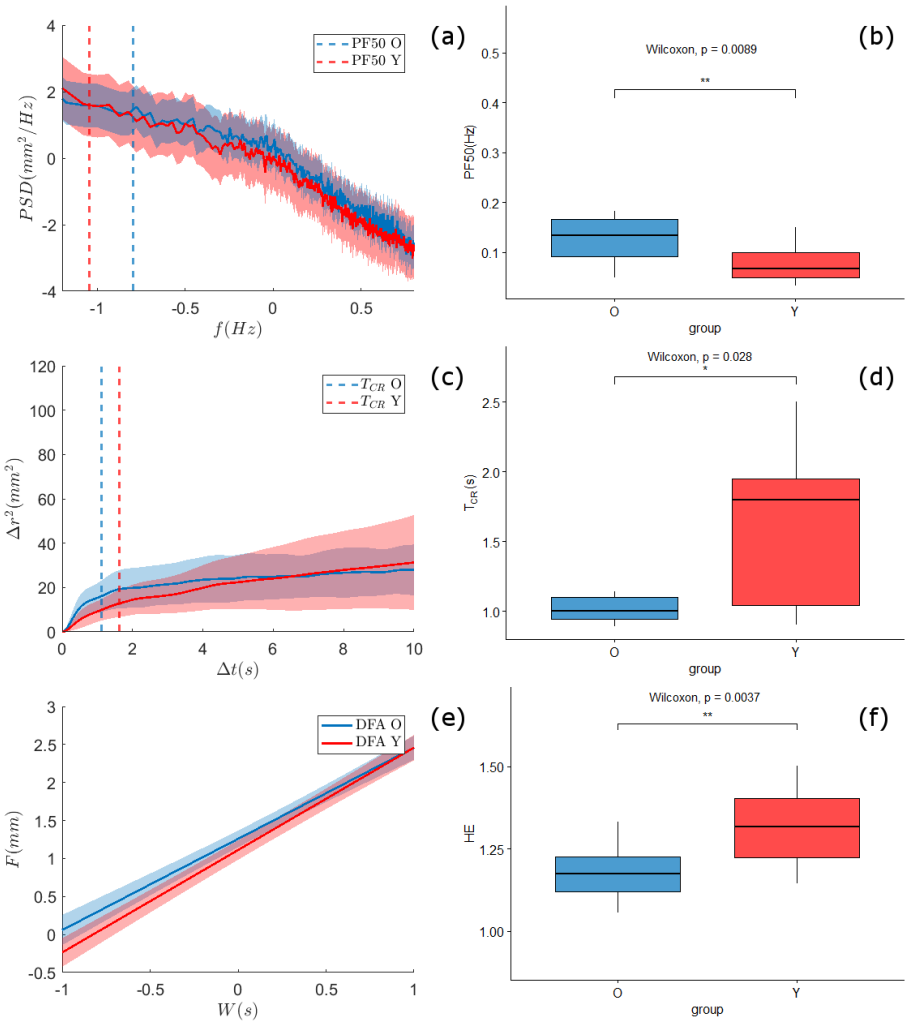

Figure 1.14: Left panels (a, c) show PSD and SDP averaged values for Y (red) and O (blue) populations. Standard deviations are represented by shaded areas. In panel a, vertical dashed lines indicate mean PF50 values for both groups. Vertical dashed lines in panel a and c represent respectively mean PF50 and mean T_{CR} for Y and O groups. The average regression lines obtained from DFA analysis are presented in panel e. Shaded areas stand for the standard deviations. In panels a and e, both axes are expressed in common logarithmic scale. Right panels (b, d, f) show Y (red) and O (blue) groups comparisons for PF50, T_{CR}: and HE. ** indicates p<0.01 and * stands for p<0.05.

Table 1.4: Table shows the considered P and D ranges for the grids.

Group	P (N·m/rad)	D (N·m·s/rad)
Y	257.36÷322.38	0÷49.47
O	257.36÷463.25	0÷74.21

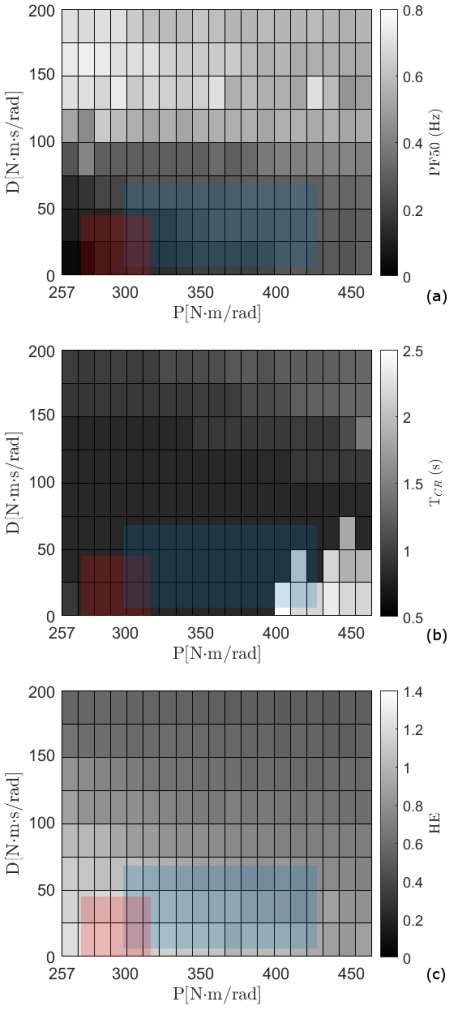

Figure 1.15: Panel a shows how PF50 varied with respect to the P and D parameters. Colormap was obtained computing PF50 from the synthetic COP time-series, obtained for each point of the P-D grid. T_{CR} and HE were computed with the same line and shown in panel b and c respectively.Shaded boxes, for Y (red) and O (blue) populations, are centered in the average P-D values (289.9 – 24.7 for Y and 360.3 - 37.1 for O), while the areas account for the standard deviation (23.4 – 20.1 for Y and 64.1 – 31.9 for O).

1.4 Discussion

In this chapter, the study of balance maintenance under the intermittent control paradigm was investigated. The first experiment (see section 1.2.6 and 1.3.1) took into account the study of the postural data generated through the single-link IP model proposed by Asai at al. [9]. This was done to understand the correlation properties of the COP data generated by the model, and at the same time, investigate whether such properties changes in relation to the intermittent controller parameters. In the second experiment (see section 1.2.7 and 1.3.2),

HE obtained by DFA and other COP descriptors were used to verify the kinetic palusbility of the DIP/VIP model [13, 8]. Moreover, the latter was used to possibly explain a remapping of the control activity due to aging by comparing the COP descriptors of the real and simulated data[13].

1.4.1 Long term correlation and inhomogeneity properties of the COP under the intermittent control paradigm

Concerning the simulation study proposed in 1.2.6, the results confirm that the intermittent control policy is a suitable paradigm to model the active role played by the CNS in modulating the stance. Indeed the fluctuation F and dF showed grater variability at greater time-scales (figure 1.5), this means that changes in the active control policy induced by changes in the three ICP, affect the COP time course at the LB (figure 1.6), coherently with what reported in the literature regarding the frequency bands at which neural modulation mirrors on COP data. Indeed, for instance, part of such neural modulation due to the visuo-vestibular information should be mirrored in COP time-series at frequency lower than 0.5 Hz [54]. Further confirmations on the COP frequency band at which the control neural activity manifests itself can be found in [19], where the universal COP descriptors were related with the COP at frequency between 0.04 Hz and 0.5 Hz.

Moreover the dF fluctuations presented greater sensitivity to the controller parametric changes if compared to those shown by F in the LB range (figure 1.6), suggesting a greater variability of the β coefficients obtained from the simulated COP data. This confirms from one hand the capability of the inhomogeneity coefficient β to be a further useful parameters for the description of COP data, and on the other hand, it suggests that such COP descriptors account for the disorder state of the time-series, and represent useful way to investigate the neural strategy behind the human balance maintenance [49]. Indeed, the β coefficient was introduced in [59] to take into account for the local transient that can be found in a non-stationary time-series [60]. Hence, the investigation of the inhomogeneity coefficient β as a possible state disorder metric such as the sample entropy or fuzzy entropy should be carefully assessed in future studies [49, 50].

Although the fluctuations F and dF were able to highlight concise aspects on how active controller changes affected the posturographic data, a more detailed analysis for each ICP was carried out in order to quantify the long term correlation and inhomogeinety properties

of the simulated COP time-series in relation to the active controller characteristics, since the latter strongly impacts on the stability and sway of the IP model [23]. From a global perspective, the P parameter did not appear related to neither the long term correlation properties, nor to the inhomogeneity of the simulated COP time-series as highlighted in section 1.3.1.This confirms that when P is large enough to compensate the portion of the gravitational toppling torque not counteracted by the passive muscles properties (K and B), a wide range of values is admissible for P and thus, with respect to D, its role becomes less crucial for the control model [8, 9]. The latter aspect aligns with the strong relation observed between both EDFA coefficients and D (figure 1.8) which showed significant correlations (section 1.3.1). Incidentally the $\alpha - D$ relation (figure 1.8) points out that the higher is D, the lower is the long-term correlation of the COP time-series, in agreement with previous studies that reported lower values of α in elderly populations, where a degraded motor control can be assumed [52, 13]. A similar interpretation was pointed out by Suzuki et al. [23], where it was observed that patients affected by Parkinson's disease showed higher D values if compared to healthy elderly. In fact, control schemes that involve large derivative gains constitutes an energetically inefficient control scheme, with inflexible and non-reactive stabilizing mechanisms, marked b lower Hurst exponents [23].

A decreasing trend was also observed in the $\beta - D$ relation (figure 1.8), highlighting that the inhomogeneity of the COP timeseries decreases for progressively higher values of D (Fig. 1.8). The coefficient β was defined to indicate departure from the power law behavior (1.27), since the standard deviation of the profile from the local trend (1.26) can vary significantly among the different segments [60]. A reduction of inhomogeneity implies COP timeseries characterized by regular oscillatory fluctuations, closer to a stationary behavior. Hence as highlighted above, the β coefficient can provide additional information regarding the organization of the biological signals in terms of *complexity* [60]. The lower β values observed for increasing derivative gains appears in agreement also with the *loss of complexity* paradigm [66]. This hypothesis essentially states that healthy physiological systems produce responses that are complex in the sense of non linear correlations and long-term dynamics, while a functions' breakdown, due to aging or disease, leads to less complex outputs that mirror a reduced ability in producing an adaptive set of responses when facing motor, cognitive or neurological needs [67, 68]. Thus, the reduction of β coefficient highlights a loss of fine-structures in COP epochs and it suggests a reduced capability to cope with balance demands, relying on a set of few and repeatable postural patterns with a limited physiological

adaptability. Hence, a lower degree of inhomogeneity could reflect a rearrangement in the CNS motor control schemes due to certain pathologies, resembling an inefficient tuning of the IP active controller [23, 69].

The last parameter analyzed was ρ, which as happened for P, it did not show significant correlation neither with α nor with β (figure 1.9). However, the analysis performed through correlation coefficients on the global set, i.e. considering all the realizations (figure 1.9), could not highlight possible local linear trends in the ρ-α and ρ-β relations, deserving focused investigations related to the limits of the intermittent control paradigm. This suggests that, despite the significant role of ρ in defining the exchange between the ON and OFF sub-dynamics (section 1.2.2), it appears to be not directly related with the stochastic properties of the COP time-series quantified through the EDFA. In addition, it deserves to be noted that, within the range of P and D values selected in this study (Table 1.1), stable simulations were obtained for ρ up to $\simeq$0.9, although ρ was free to vary with the upper bound set to 1 (Table 1.1). This indicates that the condition for a fully continuous control (ρ =1) was not able to provide a stable simulation among the one thousand stable obtained. Hence, the findings of this experiment are limited to an intermittent control regime.

From the discussion above, it emerges the dominant role of D, among the three ICP, in determining the long-term correlation and inhomogeneity properties of the COP data. This aspect was also supported by considering a more fine analysis regarding $\alpha - D$ and $\beta - D$ relations. Indeed, as shown in the 1.3.1, both of them were optimally fitted, under nAIC criterion, by two lines with a knot point at D =243 $N \cdot m \cdot s \cdot rad^{-1}$.To be noted, such D value was obtained directly from the above mentioned data-driven analysis and thus it cannot be claimed that it represents a critical value for the intermittent control scheme. Its possible physical meaning, however, deserves to be carefully investigated in future studies, also in relation to the other ICP. Incidentally, the analysis performed by dividing the data for D lower and greater than 243 $N \cdot m \cdot s \cdot rad^{-1}$ highlighted that the intermittent control law employed in this study can influence COP time-series properties also through more subtle features that deserve to be pointed out. As a matter of fact, ρ parameter becomes more crucial for lower D values, showing significant correlation with α and β (figure 1.12).

1.4.2 Physiological interpretation of the intermittent control

From the discussion reported above, it emerges that the stochastic behavior and the inhomogeneity of a timeseries, quantified by the EDFA coefficients, manifest a direct relationship

with the intermittent nature of balance control when D assumes typical values for this control strategy [23]. In addition, this is also in agreement with ρ values that not overcome $\simeq$ 0.7, which permits to exploit the two main characteristics of the intermittent control that actually make intelligent such kind of policy : as first, the fact that the active controller exploits the saddle equilibrium point of the passive IP with its stable manifold. Hence, from a kibernetic perspective, this can be viewed as a smart agent that knows the plant and use its properties. Secondly, since the neural delay is unavoidable, the controller makes use of typical state steering patterns induced by the presence of the delay admitting lower control gains. This choice of reaching stability by switching between two unstable dynamics rather than continuously supervising the process, can be viewed as an ecologic strategy of the CNS for producing motor commands that guarantees robustness of the system with respect to parametric changes [70].This eventually permits to obtain limit cycle stability without the need of greater control efforts [23, 9].

Finally, it is interesting to note that the α coefficient maintains in any case values quite close to 1 (Fig. 1.12), possibly referring to an attempt to maintain the output of the balance regularization, i.e. the COP, close to a $1/f$ process. Indeed, the latter is frequently encountered in different physiological time-series, characterizing a healthy motor control [54, 71, 72]. On the other hand, the β coefficient covered a larger set of values (Fig. 1.12), pointing out that the simulated COP timeseries exhibited different degrees of irregularity in their local structures [59, 60]. The latter can be associated with the complexity of the physiological system generating the data[60], which in healthy conditions is commonly characterized by a higher complexity [72, 73], leading in turn to an enhanced robustness and adaptability of the response [73, 74].

When $D \geq 243\ N \cdot m \cdot s \cdot rad^{-1}$, the correlation between ρ and the EDFA coefficients, completely disappears (figure 1.13). A possible explanation for this behavior can be proposed considering that, for such range of D values, the S_{on} dynamics can stabilize the IP process *per se* [23], without the need for switching between sub-dynamics, since with this range of D values ($\geq 243\ N \cdot m \cdot s \cdot rad^{-1}$) the (P, D) of the ON-subsystem is located inside the stability region reported by Suzuki et al. [23]. In this context, the control policy mimics a stabilizing delayed continuous control [23] and thus it is reasonable to assume that ρ becomes less crucial within this control scheme, loosing its relations with EDFA coefficients. In passing, the relations highlighted between α and the two ICP parameters D and ρ in section 1.3.1, aligns with the the findings of Yamamoto et al. [19], who reported that the slope of the PSD

at the LB range of the COP signals, which is a universal posturogrpahic index, is related to the Hurst exponent α of the DFA [75]. Hence the α coefficient seems to be particular suitable in highlighting the neural modulation of the CNS that affects the COP time-course.

1.4.3 Further insights on the intermittent control: the DIP/VIP.

The simulation experiments and the analysis proposed in the first part essentially aimed to investigate the intermittent control model in a posturography scenario where time-series analysis approaches were commonly encountered [7, 2, 49]. This has constituted a first attempt to merge model-based and data-driven analysis, however the bio-mechanical model of the stance used was a single-link IP, which can be a limiting assumption also in virtue of the findings proposed in [29, 8], although as shown in section 1.3.1, it was able to capture also complex dynamics typical of what observed in real data. In the second experiment (section 1.2.7) the study was thus enlarged both in terms of mechanical model complexity and posturographic descriptors employed to evaluate the physiological plausibility of the intermittent control model by means of the DIP/VIP. Let thus consider the investigation proposed in 1.2.7.

The P-D grids in section 1.3.2 (figure 1.15) confirmed the sensitivity of synthetic COP to different parametrization of the active controller, highlighting the possibility to obtain COP time-series whose descriptors lie within the PMR observed in both Y and O populations [13]. In particular, both P and D admitted greater values for the O group compared to the Y one (table 1.4). Such result should indicate the functional rearrangement of the CNS control recognized in the elderly [76, 52], which can be mapped through the tuning of the intermittent controller and mirrored by the COP. Incidentally, greater P and D values were associated with lower HE in the O group 1.15, hence suggesting an enhanced anti-persistent behavior in the COP time-series of the latter. This aspect aligns with the findings in [7, 52] and it indicates that greater regulatory efforts are needed to achieve postural stabilization [52], eventually resulting in a more energetically expensive control [9].

A similar point of view can be reached by analyzing the PF50 (see figure 1.14, panel a). Indeed, such descriptor quantifies the spreading of the COP spectrum towards the higher frequencies, i.e. the greater is the PF50, the larger is the amount of power of faster dynamics, possibly associated with an augmented level of stochasticity [19, 2]. Moreover, from its physical meaning, COP encompasses both the active and passive control activity at the lower joints as observed in section 1.2.2, thus reflecting also the motor commands modulated by

muscles activity and their mechanical characteristics [21]. Therefore, an enhanced stochastic COP behavior might refer to a stiffer muscular strategy recognizable in the elderly [52] that may have altered the mechanical muscle properties or the neuromodulatory changes [13]. Confirmations of such hypothesis can be found in the PSD slope at the lower frequencies (SLOPE-L) [19, 23, 9]. Indeed, a nearly flat SLOPE-L indicates a body stiffness that tends to be overcritical, i.e. $\gg mgh$, whereas a consistent negative value of the slope generally refers to an optimal stiffness tuning [23, 9]. This agree with the greater P values for the O population and is also supported by the SLOPE-L computed over the real data that resulted higher for the O subjects (-0.95±0.84) with respect to the Y group (-1.62±1.15) [13].

The T_{CR} descriptor appears less sensitive to changes in the P-D parameters. As a matter of fact, form the grids in figure 1.15 one can appreciate that T_CR has a uniform trend and limited variations for a large set of the controller parametrizations [13]. This could be misinterpreted since it could appear that DIP/VIP is not able to capture the physiological regulatory mechanisms behind balance maintenance. Indeed, literature highlights that T_{CR} and more in general SDA can be highly descriptive of the different control dynamics exhibited in both healthy individuals and populations presenting a wide spectrum of balance disorders [62, 63]. However, one should recall that the SDA approach is a postural data assessment framework that grounds the basis on the time-series analysis perspective, hence it might not be necessarily exploited by a mechanistic model, whenever accurate as the DIP/VIP used in this study [21, 2]. It is therefore desirable to investigate in the future the possible role of SDA in the analysis of variable structure balance control model. Indeed despite the two lines in [2, 9] seem different, they convey both on the idea that multiple dynamics contribute to the regularization of the stance.

Moreover, as highlighted in [13], one should notice that the choice of a set of COP features already successfully used for investigating COP timeseries in young and elderly subjects [7, 52, 20] further supports the validity of the DIP/VIP model from a kinetic viewpoint. Eventually, it deserves to be stressed that the investigation of the active controller parameters was limited to P and D gains, while α, and thus ρ, was set at a fixed value (section 1.2.7). This could represent a partial limitation of the study, since the findings reported in the first experiment highlight that the role of α could be predominant at least in certain regions of the active controller parameter space. However, it should be also recalled that the DIP mechanical structure may require a more refined partition of the state space in order to maintain the stability, thus this aspect need to be adequately examined in focused studies.

Undoubtedly, one can have glimpsed the tendency present in modern posturography, which would infer active controller parameters using data from different populations [23, 77, 78]. This is generally achieved, in unperturbed conditions, using features derived from COM, even if COP measures are the most common data used in classical posturography [8, 29, 30]. However, there are some reasons that suggest the opportunity to use COP rather than COM. As first, COP is a directly measurable quantity that can be obtained from force plates, whereas the COM can be estimated in different ways, i.e. stereophotogrammetric-based procedures or by processing of COP data [42, 79, 80]. However, although such procedures are commonly employed to highlight kinesiological aspects of the balance maintenance, they could lead to a loss of information, that can be instead captured through different identification procedures [23, 69]. In fact, the COP time-course represents a meaningful source of information of the descending neural control and of the mechanical actuation provided by the musculoskeletal system [21]. Hence, the use of COP time-series represents a more preferable choice when human stance is investigated from a neuromuscular perspective.

However, the use of multi-link structure renders more challenging the COP modeling, whereas defining COP from a single link IP is somewhat straightforward [81]. Thus, despite the parametric identification is not the primary aim of the study, the approach followed in section 1.2.1 for the modeling of the COP from DIP structures constitute a useful contribution toward the integration of physiological data and mechanical models of balance. This renders the methodological aspects faced in this study potentially appealing in the identification of multi-input, multi-output models of the stance.

The additional value of using a DIP/VIP or in general multi-link models can be appreciated also considering that this allows to investigate whether changes in the neural control modulations are mirrored in how CNS manages the intrinsic body redundancy of the quiet stance [29, 82]. Indeed, a detrimental condition that affects the CNS capacity in managing the body redundancy can be a sign of functional rearrangement due to neurological disorders [69]. The key role of COP in accounting for mechanical redundancy is fundamental also in other applications, e.g. bipedal legged robotics. In this context, the COP can be treated through the more general concept of zero moment point [83], which has to encompass the multi-link structure in its formulation in order to properly control both the standing and dynamic phase of gait [44, 47]. Therefore, an inefficient regulatory activity can be recognized by considering COP characteristics [1]. This could hold also for the human system, where a degraded regulatory activity, due to a disease, can affect the management of multi-link

structure from a balance maintenance point of view [82, 13].

Findings of the present study support the plausibility of DIP/VIP model of the stance [8], here enriched by the kinetic perspective [13]. Hence, both the mechanics and the control policy can be suitable for modeling the cybernetic problem previously introduced (see section 2.1). The hybrid policy employed for managing the body redundancy through the VIP part of the model resulted to drive the synthetic COP characteristics [13]. Indeed, since a physiological coherent model of the control action at the two joints was employed, human-like patterns were observed in the simulated COP time-series [27]. As highlighted in (1.5), COP spans non linearly the torque vector $\boldsymbol{\tau}$ over σ_a. Thus, both passive and active effects at the hip and ankle were mirrored in the COP, which encompasses the information about the stability of the mechanical structure [13].

1.4.4 The role of COP in balance maintenance

Hence, from the two experiments conducted in this thesis, emerges that COP encompasses information regarding the dynamic stabilization process of the stance, which unavoidably account for the passive biomechanical structure of the skeletal systems within the gravity filed, and the neural modulation or active control. Thus, from a physiological point of view, one can wonder whether such information can be exploited by the CNS to strength the control output in the ordinary balancing tasks dealt by any subject during the daily life. Confirmations regarding the plausibility of this assumption were reached also in [1], were the COP, being proportional to the torque, can be used as a feedback information in the balance control loop, making the system robust with respect to external perturbation,e.g. support base movements or external impacts [1, 84]. Moreover, as reported in [13], also quiet stance is subject to internal and external stimuli such as hemodynamics and gravity pull [75, 11]. Thus, COP can represents itself a valuable source of information that can be used by the CNS for tuning balance control strategies in either perturbed or unperturbed conditions.

Despite one can wonder about the existence of an internal model of the COP within the CNS [8], there is no doubt regarding the existence of an integration process of tactile and proprioceptive sensors of the feet [85], that makes plausible the existence of COP information within the balance control schemes [8]. This suggests a more profound picture regarding the nature of the COP. Indeed, as for certain balancing tasks, CNS must switch the role between COP and COM information in the motor control paradigm [30]. Thus, although classical literature [36] agreed in viewing the COM as the controlled variable and COP as the control

variable, it could be a limiting assumption for studying possible rearrangements in the motor control with respect to neurological disorders. This aspect can be further investigated in future studies, where kinematic and kinetic simultaneous measures are available [61], in order to better clarify the relationship between COP and COM in this kind of modeling framework.

Bibliography

[1] Robert J Peterka. Comparison of human and humanoid robot control of upright stance. *Journal of Physiology-Paris*, 103(3-5):149–158, 2009.

[2] James J Collins and Carlo J De Luca. Open-loop and closed-loop control of posture: a random-walk analysis of center-of-pressure trajectories. *Experimental brain research*, 95(2):308–318, 1993.

[3] M. Popovic. *Biomechanics and robotics*. 2013.

[4] Vittorio Lippi. Prediction in the context of a human-inspired posture control model. *Robotics and Autonomous Systems*, 107:63–70, 2018.

[5] Thomas Mergner and Karim Tahboub. Neurorobotics approaches to human and humanoid sensorimotor control. *Journal of physiology, Paris*, 103(3-5):115–118, 2009.

[6] JW Błaszczyk, R Orawiec, D Duda-Kłodowska, and G Opala. Assessment of postural instability in patients with parkinson's disease. *Experimental Brain Research*, 183(1):107–114, 2007.

[7] Hassan Amoud, Mohamed Abadi, David J Hewson, Valérie Michel-Pellegrino, Michel Doussot, and Jacques Duchêne. Fractal time series analysis of postural stability in elderly and control subjects. *Journal of neuroengineering and rehabilitation*, 4(1):12, 2007.

[8] Pietro Morasso, Amel Cherif, and Jacopo Zenzeri. Quiet standing: The single inverted pendulum model is not so bad after all. *PloS one*, 14(3):e0213870, 2019.

[9] Yoshiyuki Asai, Yuichi Tasaka, Kunihiko Nomura, Taishin Nomura, Maura Casadio, and Pietro Morasso. A model of postural control in quiet standing: robust compensation of delay-induced instability using intermittent activation of feedback control. *PLoS One*, 4(7):e6169, 2009.

[10] Robert J Peterka. Postural control model interpretation of stabilogram diffusion analysis. *Biological cybernetics*, 82(4):335–343, 2000.

[11] Silvia Conforto, Maurizio Schmid, Valentina Camomilla, Tommaso D'Alessio, and Aurelio Cappozzo. Hemodynamics as a possible internal mechanical disturbance to balance. *Gait & posture*, 14(1):28–35, 2001.

[12] Pietro G Morasso and Marco Schieppati. Can muscle stiffness alone stabilize upright standing? *Journal of neurophysiology*, 82(3):1622–1626, 1999.

[13] Andrea Tigrini, Federica Verdini, Sandro Fioretti, and Alessandro Mengarelli. Center of pressure plausibility for the double-link human stance model under the intermittent control paradigm. *Journal of Biomechanics*, 128:110725, 2021.

[14] Pietro G Morasso and Vittorio Sanguineti. Ankle muscle stiffness alone cannot stabilize balance during quiet standing. *Journal of neurophysiology*, 88(4):2157–2162, 2002.

[15] Marco Jacono, Maura Casadio, Pietro G Morasso, and Vittorio Sanguineti. The sway-density curve and the underlying postural stabilization process. *Motor control*, 8(3):292–311, 2004.

[16] Vladimir M Zatsiorsky and Marcos Duarte. Rambling and trembling in quiet standing. *Motor control*, 4(2):185–200, 2000.

[17] Luigi Ladislao and Sandro Fioretti. Nonlinear analysis of posturographic data. *Medical & biological engineering & comPuting*, 45(7):679–688, 2007.

[18] Alice Nicolaï, Myrto Limnios, Alain Trouvé, and Julien Audiffren. A langevin-based model with moving posturographic target to quantify postural control. *IEEE Transactions on Neural Systems and Rehabilitation Engineering*, 29:478–487, 2021.

[19] Tomohisa Yamamoto, Charles E Smith, Yasuyuki Suzuki, Ken Kiyono, Takao Tanahashi, Saburo Sakoda, Pietro Morasso, and Taishin Nomura. Universal and individual characteristics of postural sway during quiet standing in healthy young adults. *Physiological reports*, 3(3):e12329, 2015.

[20] Thomas E Prieto, Joel B Myklebust, Raymond G Hoffmann, Eric G Lovett, and Barbara M Myklebust. Measures of postural steadiness: differences between healthy young and elderly adults. *IEEE Transactions on biomedical engineering*, 43(9):956–966, 1996.

[21] Luigi Baratto, Pietro G Morasso, Cristina Re, and Gino Spada. A new look at posturographic analysis in the clinical context: sway-density versus other parameterization techniques. *Motor control*, 6(3):246–270, 2002.

[22] Alessandra Bottaro, Youko Yasutake, Taishin Nomura, Maura Casadio, and Pietro Morasso. Bounded stability of the quiet standing posture: an intermittent control model. *Human movement science*, 27(3):473–495, 2008.

[23] Yasuyuki Suzuki, Akihiro Nakamura, Matija Milosevic, Kunihiko Nomura, Takao Tanahashi, Takuyuki Endo, Saburo Sakoda, Pietro Morasso, and Taishin Nomura. Postural instability via a loss of intermittent control in elderly and patients with parkinson's disease: A model-based and data-driven approach. *Chaos: An Interdisciplinary Journal of Nonlinear Science*, 30(11):113140, 2020.

[24] David A Winter, Aftab E Patla, Francois Prince, Milad Ishac, and Krystyna Gielo-Perczak. Stiffness control of balance in quiet standing. *Journal of neurophysiology*, 80(3):1211–1221, 1998.

[25] Xingda Qu, Maury A Nussbaum, and Michael L Madigan. A balance control model of quiet upright stance based on an optimal control strategy. *Journal of biomechanics*, 40(16):3590–3597, 2007.

[26] Kamran Iqbal. Optimal time-varying postural control in a single-link neuromechanical model with feedback latencies. *Biological Cybernetics*, 114(4):485–497, 2020.

[27] Andrea Tigrini, Alessandro Mengarelli, Sandro Fioretti, and Federica Verdini. Anterior-posterior center of pressure analysis for the dip/vip balance maintenance model: Formalization and preliminary results. In *2021 10th International IEEE/EMBS Conference on Neural Engineering (NER)*, pages 832–835. IEEE, 2021.

[28] John Milton and Tamas Insperger. Acting together, destabilizing influences can stabilize human balance. *Philosophical Transactions of the Royal Society A*, 377(2153):20180126, 2019.

[29] Yasuyuki Suzuki, Taishin Nomura, Maura Casadio, and Pietro Morasso. Intermittent control with ankle, hip, and mixed strategies during quiet standing: a theoretical proposal based on a double inverted pendulum model. *Journal of Theoretical Biology*, 310:55–79, 2012.

[30] Pietro Morasso. Centre of pressure versus centre of mass stabilization strategies: the tightrope balancing case. *Royal Society open science*, 7(9):200111, 2020.

[31] Fay B Horak and Lewis M Nashner. Central programming of postural movements: adaptation to altered support-surface configurations. *Journal of neurophysiology*, 55(6):1369–1381, 1986.

[32] Yu Aramaki, Daichi Nozaki, Kei Masani, Takeshi Sato, Kimitaka Nakazawa, and Hideo Yano. Reciprocal angular acceleration of the ankle and hip joints during quiet standing in humans. *Experimental brain research*, 136(4):463–473, 2001.

[33] Yuanfen Zhang, Tim Kiemel, and John Jeka. The influence of sensory information on two-component coordination during quiet stance. *Gait & posture*, 26(2):263–271, 2007.

[34] Robert Creath, Tim Kiemel, Fay Horak, Robert Peterka, and John Jeka. A unified view of quiet and perturbed stance: simultaneous co-existing excitable modes. *Neuroscience letters*, 377(2):75–80, 2005.

[35] Nicolas Termoz, Suzanne E Halliday, David A Winter, James S Frank, Aftab E Patla, and François Prince. The control of upright stance in young, elderly and persons with parkinson's disease. *Gait & posture*, 27(3):463–470, 2008.

[36] David A Winter. *Biomechanics and motor control of human gait: normal, elderly and pathological*. 1991.

[37] Yun-Ju Lee, Jing Nong Liang, Bing Chen, and Alexander S Aruin. Characteristics of medial-lateral postural control while exposed to the external perturbation in step initiation. *Scientific reports*, 9(1):1–10, 2019.

[38] John Milton, Ryan Meyer, Max Zhvanetsky, Sarah Ridge, and Tamás Insperger. Control at stability's edge minimizes energetic costs: expert stick balancing. *Journal of The Royal Society Interface*, 13(119):20160212, 2016.

[39] Gergely Gyebrószki, Gábor Csernák, John G Milton, and Tamás Insperger. The effects of sensory quantization and control torque saturation on human balance control. *Chaos: An Interdisciplinary Journal of Nonlinear Science*, 31(3):033145, 2021.

[40] Pietro Morasso, Taishin Nomura, Yasuyuki Suzuki, and Jacopo Zenzeri. Stabilization of a cart inverted pendulum: improving the intermittent feedback strategy to match the limits of human performance. *Frontiers in computational neuroscience*, 13:16, 2019.

[41] Nadia Sultan, Muhammad Najam ul Islam, and Asif Mahmood Mughal. Nonlinear postural control paradigm for larger perturbations in the presence of neural delays. *Biological Cybernetics*, 115(4):397–414, 2021.

[42] Pietro G Morasso, Gino Spada, and Roberto Capra. Computing the com from the cop in postural sway movements. *Human Movement Science*, 18(6):759–767, 1999.

[43] Robert J Peterka. Sensory integration for human balance control. *Handbook of clinical neurology*, 159:27–42, 2018.

[44] Christine Chevallereau, Dalila Djoudi, and Jessy W Grizzle. Stable bipedal walking with foot rotation through direct regulation of the zero moment point. *IEEE Transactions on Robotics*, 24(2):390–401, 2008.

[45] Mark Saffer, Tim Kiemel, and John Jeka. Coherence analysis of muscle activity during quiet stance. *Experimental Brain Research*, 185(2):215–226, 2008.

[46] Bruno Siciliano, Lorenzo Sciavicco, Luigi Villani, and Giuseppe Oriolo. *Robotics: modelling, planning and control*. Springer Science & Business Media, 2010.

[47] Eric R Westervelt, Jessy W Grizzle, Christine Chevallereau, Jun Ho Choi, and Benjamin Morris. *Feedback control of dynamic bipedal robot locomotion*. CRC press, 2018.

[48] Kenjiro Michimoto, Yasuyuki Suzuki, Ken Kiyono, Yasushi Kobayashi, Pietro Morasso, and Taishin Nomura. Reinforcement learning for stabilizing an inverted pendulum naturally leads to intermittent feedback control as in human quiet standing. In *2016 38th Annual International Conference of the IEEE Engineering in Medicine and Biology Society (EMBC)*, pages 37–40. IEEE, 2016.

[49] Alessandro Mengarelli, Andrea Tigrini, Sandro Fioretti, and Federica Verdini. Postural dynamics and loss of complexity in diabetic patients with and without neuropathy. *Human Movement Science (Under Review)*, 2022.

[50] Ling Tang, Huiling Lv, Fengmei Yang, and Lean Yu. Complexity testing techniques for time series data: A comprehensive literature review. *Chaos, Solitons & Fractals*, 81:117–135, 2015.

[51] Andrea Tigrini, Federica Verdini, Sandro Fioretti, and Alessandro Mengarelli. Long term correlation and inhomogeneity of the inverted pendulum sway time-series under the

intermittent control paradigm. *Communications in Nonlinear Science and Numerical Simulation*, 2022.

[52] JJ Collins, CJ De Luca, A Burrows, and LA Lipsitz. Age-related changes in open-loop and closed-loop postural control mechanisms. *Experimental Brain Research*, 104(3):480–492, 1995.

[53] Nikita Kuznetsov, Scott Bonnette, Jianbo Gao, and Michael A Riley. Adaptive fractal analysis reveals limits to fractal scaling in center of pressure trajectories. *Annals of biomedical engineering*, 41(8):1646–1660, 2013.

[54] Pierre Gilfriche, Véronique Deschodt-Arsac, Estelle Blons, and Laurent M Arsac. Frequency-specific fractal analysis of postural control accounts for control strategies. *Frontiers in physiology*, 9:293, 2018.

[55] C-K Peng, Sergey V Buldyrev, Shlomo Havlin, Michael Simons, H Eugene Stanley, and Ary L Goldberger. Mosaic organization of dna nucleotides. *Physical review e*, 49(2):1685, 1994.

[56] C-K Peng, Shlomo Havlin, H Eugene Stanley, and Ary L Goldberger. Quantification of scaling exponents and crossover phenomena in nonstationary heartbeat time series. *Chaos: an interdisciplinary journal of nonlinear science*, 5(1):82–87, 1995.

[57] Jong-Min Lee, Dae-Jin Kim, In-Young Kim, Kwang-Suk Park, and Sun I Kim. Detrended fluctuation analysis of eeg in sleep apnea using mit/bih polysomnography data. *Computers in biology and medicine*, 32(1):37–47, 2002.

[58] ON Pavlova and AN Pavlov. Scaling features of intermittent dynamics: Differences of characterizing correlated and anti-correlated data sets. *Physica A: Statistical Mechanics and its Applications*, 536:122586, 2019.

[59] AN Pavlov, AI Dubrovsky, AA Koronovskii Jr, ON Pavlova, OV Semyachkina-Glushkovskaya, and Jürgen Kurths. Extended detrended fluctuation analysis of electroencephalograms signals during sleep and the opening of the blood–brain barrier. *Chaos: An Interdisciplinary Journal of Nonlinear Science*, 30(7):073138, 2020.

[60] Alexey N Pavlov, Arkady S Abdurashitov, AA Koronovskii Jr, Olga N Pavlova, OV Semyachkina-Glushkovskaya, and Jürgen Kurths. Detrended fluctuation anal-

ysis of cerebrovascular responses to abrupt changes in peripheral arterial pressure in rats. *Communications in Nonlinear Science and Numerical Simulation*, 85:105232, 2020.

[61] Damiana A Santos and Marcos Duarte. A public data set of human balance evaluations. *PeerJ*, 4:e2648, 2016.

[62] Nima Toosizadeh, Jane Mohler, David G Armstrong, Talal K Talal, and Bijan Najafi. The influence of diabetic peripheral neuropathy on local postural muscle and central sensory feedback balance control. *PloS One*, 10(8):e0135255, 2015.

[63] Vera Novak, Mareile Haertle, Peng Zhao, Kun Hu, Medha Munshi, Peter Novak, Amir Abduljalil, and David Alsop. White matter hyperintensities and dynamics of postural control. *Magnetic Resonance Imaging*, 27(6):752–759, 2009.

[64] Xinchen Zhang and Jeffrey G Andrews. Downlink cellular network analysis with multi-slope path loss models. *IEEE Transactions on Communications*, 63(5):1881–1894, 2015.

[65] L Ljung. *System identification-theory for the user 2nd edition ptr prentice-hall*. 1999.

[66] Lewis A Lipsitz. Dynamics of stability: the physiologic basis of functional health and frailty. *The Journals of Gerontology Series A: Biological Sciences and Medical Sciences*, 57(3):B115–B125, 2002.

[67] Ary L Goldberger, C-K Peng, and Lewis A Lipsitz. What is physiologic complexity and how does it change with aging and disease? *Neurobiology of Aging*, 23(1):23–26, 2002.

[68] M Costa, AA Priplata, LA Lipsitz, Z Wu, NE Huang, Ary L Goldberger, and C-K Peng. Noise and poise: enhancement of postural complexity in the elderly with a stochastic-resonance–based therapy. *EPL (Europhysics Letters)*, 77(6):68008, 2007.

[69] Maria Letizia Corradini, Sandro Fioretti, Tommaso Leo, and Roberto Piperno. Early recognition of postural disorders in multiple sclerosis through movement analysis: a modeling study. *IEEE Transactions on Biomedical Engineering*, 44(11):1029–1038, 1997.

[70] Pietro Morasso and Vishwanathan Mohan. The body schema: neural simulation for covert and overt actions of embodied cognitive agents. *Current Opinion in Physiology*, 19:219–225, 2021.

[71] Chunjiang Fu, Yasuyuki Suzuki, Pietro Morasso, and Taishin Nomura. Phase resetting and intermittent control at the edge of stability in a simple biped model generates 1/f-like gait cycle variability. *Biological cybernetics*, 114(1):95–111, 2020.

[72] Jeffrey M Hausdorff. Gait dynamics in parkinson's disease: common and distinct behavior among stride length, gait variability, and fractal-like scaling. *Chaos: An Interdisciplinary Journal of Nonlinear Science*, 19(2):026113, 2009.

[73] Stefan Thurner, Christian Mittermaier, and Klaus Ehrenberger. Change of complexity patterns in human posture during aging. *Audiology and Neurotology*, 7(4):240–248, 2002.

[74] Brad Manor, Madalena D Costa, Kun Hu, Elizabeth Newton, Olga Starobinets, Hyun Gu Kang, CK Peng, Vera Novak, and Lewis A Lipsitz. Physiological complexity and system adaptability: evidence from postural control dynamics of older adults. *Journal of Applied Physiology*, 109(6):1786–1791, 2010.

[75] Taishin Nomura, Shota Oshikawa, Yasuyuki Suzuki, Ken Kiyono, and Pietro Morasso. Modeling human postural sway using an intermittent control and hemodynamic perturbations. *Mathematical Biosciences*, 245(1):86–95, 2013.

[76] JHJ Allum, MG Carpenter, F Honegger, AL Adkin, and BR Bloem. Age-dependent variations in the directional sensitivity of balance corrections and compensatory arm movements in man. *The Journal of Physiology*, 542(2):643–663, 2002.

[77] Kevin L McKee and Michael C Neale. Direct estimation of the parameters of a delayed, intermittent activation feedback model of postural sway during quiet standing. *PloS one*, 14(9):e0222664, 2019.

[78] A Tietäväinen, MU Gutmann, E Keski-Vakkuri, J Corander, and E Hæggström. Bayesian inference of physiologically meaningful parameters from body sway measurements. *Scientific reports*, 7(1):1–14, 2017.

[79] JJ Eng and DA Winter. Estimations of the horizontal displacement of the total body centre of mass: considerations during standing activities. *Gait & Posture*, 1(3):141–144, 1993.

[80] Timo Tossavainen. *Virtual reality and posturography applied to postural control research.* Tampere University Press, 2006.

[81] IM Schut, JH Pasma, JMB Roelofs, V Weerdesteyn, H van der Kooij, and AC Schouten. Estimating ankle torque and dynamics of the stabilizing mechanism: no need for horizontal ground reaction forces. *Journal of Biomechanics*, page 109813, 2020.

[82] Hendrik Reimann and Gregor Schöner. A multi-joint model of quiet, upright stance accounts for the "uncontrolled manifold" structure of joint variance. *Biological cybernetics*, 111(5):389–403, 2017.

[83] Miomir Vukobratović and Branislav Borovac. Zero-moment point—thirty five years of its life. *International journal of humanoid robotics*, 1(01):157–173, 2004.

[84] Vadakkepat Prahlad, Goswami Dip, and Chia Meng-Hwee. Disturbance rejection by online zmp compensation. *Robotica*, 26(1):9, 2008.

[85] Frederic JF Viseux. The sensory role of the sole of the foot: Review and update on clinical perspectives. *Neurophysiologie Clinique*, 50(1):55–68, 2020.

Chapter 2

Perturbed Posture: a modeling perspective

2.1 Introduction

In the previous chapter, the problem of human upright stance maintenance was faced considering the unperturbed case, where the only external force that challenges the central nervous system (CNS) in regulating the stance is the toppling effects induced by the gravity field [1]. At the same time, different internal factors supplied by the internal postural noise or due to changes in the visual field can potentially impact on the balance maintenance, but they can be still mentioned under the static balance maintenance [2, 3].

On the other hand, perturbed posture refers to those tasks or experiments where additive eternal disturbances such as external forces, torques and vibrations are employed in perturbing the upright stance [4, 5, 6]. Despite many different experimental protocol have been developed for assessing the postural responses to such disruptive events, it is important to highlight that the support base translational movements were taken into account in the milestone work of Horak and Nashner [4]. Such form of perturbations continues to be still appealing as demonstrated in recent works where the problem of balance maintenance is studied also in relation to cortical information processes [7, 8]. A possible reason behind this may lie on the capability of support base translational movements to mimic potential events that can be encountered in the daily living [4, 5, 9]. Additionally, other sources of perturbations i.e. visual sensory deprivation, or cognitive load, can be employed in conjunction with support base movements in order to elicit CNS motor responses [10]. This can be obtained respectively by asking the subjects to close their eyes or perform mental counting while they undergo the

experiment [10].

The experimental data employed to evaluate the postural adjustments able to counteract the aforementioned perturbations are those mentioned in the previous chapter. e.g. the center of pressure (COP), and the kinematic sway angles at the ankle and at the hip [4]. However, also muscular activity has to be cited as a valuable source of information for this motor task, since the muscles can provide a stereotyped activation patterns [4]. Moreover, evidences confirm that evoked postural responses to external perturbations, such as support base movements, can involve higher control cortical centers of the brain [11]. This recently supports the use of electroencephalography as an additive source of information that can be adopted in perturbed posture analysis [8, 7]. However, as highlighted in the previous chapter, a modeling perspective that accounts for biomechanical quantities as those above mentioned, can be considered fundamental for a better comprehension of the CNS actuated control mechanisms [12, 13, 14, 1, 15].

In passing, it should be noted that the kinematic and kinetic data are used either for comparison with the corresponding quantities simulated by the model in order to verify the biological plausibility [16, 17], or to identify models directly form the data through specific identification procedures [18, 19, 20]. The latter aspect is of fundamental importance to enrich meaningful descriptions of the control dynamics elicited by a subject or a given population. In this context, one can encounter different methodological procedures that differ depending on the data one deals with. As reported in [19], the identification procedures applied to retrieve CNS control model are in open or closed loop form, and they can be performed in the time or frequency domains. However, also the indirect identification [20], which views at the system in closed loop form as an autonomous system, obtained remarkable results [20]. A similar approach was used in [21, 22], where a sliding mode control model of the CNS was proposed, and controller gains were identified through an indirect identification procedure. The hypothesis that CNS uses a sliding variable to control voluntary movements was investigated in the fascinating paper of Hanneton et al. [23], where visuo-manual tracking tasks were analyzed. Such idea was not far from what proposed in [24], where the authors advanced the hypothesis of switching dynamics to model the human manual control. Moreover other studies dealing with the modeling of unperturbed balance maintenance supported the idea of using sliding mode control paradigm to describe the role played by the CNS that should track the reference position of vertical equilibrium of the pendulum, hence rejecting all possible disturbance injected by internal or external noise [15, 25].

This approach gave good results in tracking sway data in unperturbed posture [15], but also in stabilizing the double-link inverted pendulum (IP), hence rejecting the disturbance induced by the acceleration of the platform [21, 22]. Indeed, the sway angles of the lower and upper trunk of the double link IP reproduced what observed in real data [22]. Moreover, the indirect identification procedure performed allowed to characterize the controller parameters, identifying the complement role of ankle and hip strategies, although the *a posteriori* interpretation of the model is far to be trivial. By using linearity assumptions behind the structure of the controller, it was possible to get more explainable model of the CNS as done in [19, 6, 20, 26]. This eventually led to use well acknowledge procedures as those described in [27].

Another important aspect that literature highlights is the source and type of disturbance. In [6], for instance, an experimental device was presented and used for neuromuscular control identification purposes. Such device perturbed the stance by impinging forces at the lower and upper trunk of the human body rather than accelerate or tilt the support base, hence highlighting the importance of challenging balance maintenance with external forces. A relation between torques (controller output) and sway angles was estimated following [28], which essentially made use of the partial coherence to estimate the neuromuscular frequency response function. Hence, the experimental protocol and the device employed in [6] was specifically designed and realized to obtain disturbance time-series minimally correlated to joint torques, which represent the output of the balance regulatory activity. However, for the reasons stated above in the clinical scenario, support base movement still represents the most common choice for investigating upright stance maintenance after external perturbations [29, 30, 31], but from a modeling point of view, surface translations present some issues that need to be highlighted. Indeed, the acceleration of the platform induces an inertial disturbance at the center of mass (COM) that cannot be independent with respect to the control torques simply from mechanical reasons as it is described in the next section. Moreover, the magnitude of the perturbation may render the linear approximations used for modeling the neural controller not pertinent since the mechanics of the stance can reveal its intrinsic non-linear nature [21].

A possible way to deal with such nonlinearity is the use of discontinuous control architectures [1, 32]. Indeed many physiological evidences suggest a discontinuous or hybrid nature of the postural control as already observed in the first chapter of this thesis. Additionally, as observed in previous studies [4, 7], the muscles act as bursting agents that suddenly

come into play to reject the disturbances and restore the balance maintenance. These physiological aspects have been given less consideration in the modeling perspective of balance maintenance in perturbed conditions [33, 20, 19]. However, the literature manifested an increasing interest for hybrid system identification and different methodologies have been developed [34]. Hence, investigating whether a hybrid control policy can be employed to model the physiological control mechanism in perturbed balance maintenance may be a valuable research line. Moreover, the idea of modeling neural controllers with hybrid properties directly form the data constitutes an element of novelty of the present work.

From the control perspective, hybrid systems are characterized by dynamics that arises from the interaction between continuous and discrete dynamics, and they can be used to model physical phenomena characterized by a discontinuous behavior [35, 36]. Piece Wise Affine (PWA) models represent hybrid systems obtained by the partition of the state-input domain into non-overlapping polyhedral regions and then considering affine sub-systems for each region. Such kind of models are suitable for deriving hybrid descriptions from the data, capturing nonlinear characteristics among them [35, 36]. In particular, the piecewise affine autoregressive with exogenous input models (PWARX), was selected as a proper model family since it resulted an acceptable trade-off between the complexity of the data that have to be fitted and the degree of interpretability that such models allow [35, 37].

Therefore, the PWARX was used to build different models of the neuromuscular control action played by the CNS. It should be noted that a data-driven approach like the one selected can take into account of multiple and different sources of information [34, 38], resulting in a good opportunity to explore the physiological mechanisms behind the stance maintenance in perturbed conditions. This has found confirmations also in other studies related with the balance maintenance [18, 39], although different experimental conditions held and simpler autoregressive models were employed. A further aspect that deserves to be pointed out is the physics of the process under examination. This agrees with the line followed in the first chapter, and it permits to consciously determine the time-series needed to obtain a good model description of the CNS. For this reason in the following section, in addition to the tools needed for the PWARX identification, it is described the experimental protocol that involved also visuo-deprivation and cognitive load. Attention was given to the formulation of the stance mechanics since only through mechanics one can comprehend the nature of the disturbance and how it affects the process [40].

2.2 Methods

2.2.1 Experimental Protocol

In this study, ten healthy subjects were recruited. None of them was affected by musculoskeletal or neurological disorders that potentially could affect their abilities in maintaining the stance. Participants gave their written informed consent after being informed on each step of the experimental procedure. The study was undertaken in compliance with the ethical principles of the Helsinki Declaration and was approved by the local ethics committee.

In order to acquire the kinematic data, each subject was instrumented with 26 reflective markers placed on anatomical landmarks following the guidelines given by Leardini et al. [41] (Figure 2.1). Additional markers were placed on the platform corners to track the translational movements. A six cameras optical motion analysis system (BTS Elite, Italy) was opportunely calibrated and used to capture the kinematic data for all the experiments, whereas, a Kistler force platform was employed for recording the dynamic data, e.g COP and ground reaction force. Further, muscles activity was collected through surface electromyography (sEMG). The signals were recorded bilaterally from the tibialis anterior (TA) and the gastrocnemius medialis (GA). All data were synchronously recorded: kinematics was acquired with a sampling frequency of 100 Hz, while sEMG and force plate data at 1000 Hz.

Once instrumented, participants stood on a servo-controlled movable platform, waiting for the rise of the external disturbance. Each perturbation consisted of a backward horizontal displacement (5 cm) of the base of support, with a time duration of 0.3 s. Each subject underwent two-stages experiment. In the first stage, the participants performed ten trials with eyes open to avoid the first trial effect and account for the habituation rate [42]. Then, in the second stage, three further trials were performed: the first one with eyes open (EO), the second one with eyes closed (EC), while in the third each subject stood on the platform with eyes open counting back from 100. This latter is referred to as dual task (DT) and was designed to investigate how the postural control reflex may change in the presence of a cognitive task. The time at which the platform motion starts remained unknown for the subject in both stages of the experiment. Each trial was accepted whether the subject maintained both feet on the platform for the entire duration of the record, without step responses. Otherwise, the trial was discharged and repeated.

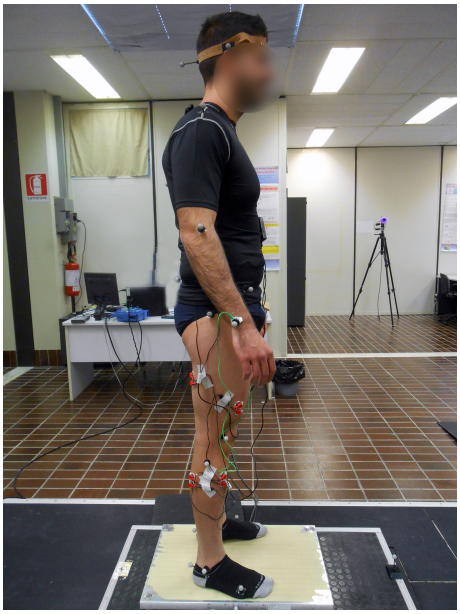

Figure 2.1: Example of a subject that underwent to the experimental protocol. One can appreciate the experimental setup constituted by a Kistler platform positioned over a translating base. Marker placement and sEMG probes on GA and TA are also visible. All the data were acquired in the Movement Analysis Laboratory at Università Politecnica delle Marche.

2.2.2 Perturbed stance mechanics: the role of the support base acceleration

As it was clarified in the first chapter related to the unperturbed balance maintenance, a fundamental core in the study of neuromuscular control strategies lies on the mechanics of the stance. Therefore, also in the case of perturbed posture the mechanical stimuli that are induced by external actions need to be carefully analyzed and taken into account in the description of the task. In [6] for instance; the perturbing device can apply direct forces to the human subject, on the contrary, in support base-shift this does not happen. Indeed, the support base acceleration generates to the human body an inertial force coupled with the gravity pulling. Such ensemble of forces provokes disturbance torques at the lower limb joints, eventually perturbing the human upright stance. It is possible to model the physics mentioned above in the sagittal plane employing of a multi-link inverted pendulum on a moving platform [21]. However, as highlighted in the previous section, the magnitude of the disturbance employed, and the subjects training phase, permitted to assume that the balancing response was mainly based on the ankle strategy [4], enforcing the validity of a single-link inverted pendulum model for describing the biomechanics of the motor task. As

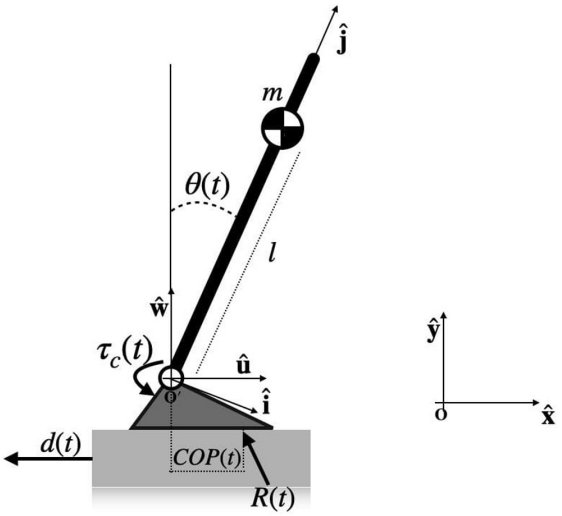

Figure 2.2: Biomechanical model of the upright stance. The generalized coordinates and the reference frames are also reported, together with the external forces acting on the system and the internal control torque, modeled as a lumped control action acting at the ankles.

shown in figure 2.2, the inverted pendulum model was used to describe the mechanics of the stance, indeed, the whole body is considered as a unique rigid rod hinged at the level of the ankle, whereas the feet are modeled with no inertia and assumed to be fixed with the platform. More in detail, let assume the three reference frames: $R_g = \{O, \quad \hat{x}, \quad \hat{y}\}$ representing the global one; $R_p = \{O', \quad \hat{u}, \quad \hat{w}\}$ the platform RF whose origin coincides with the ankle joint (O'), and R_b denotes the pendulum RF with the origin in O'. The entire mechanical system presents two degrees of freedom given by $\mathbf{q}(t) = [x(t) \quad \theta(t)]$, where $x(t)$ represents the backward displacement along the horizontal axis (Fig. 2.2), such degree of freedom was used to inject a disturbance rather than model a control action as done in other works [43, 44]. The $\theta(t)$ is the sway angle of the rod with respect to the vertical axis $\hat{w}$, providing information regarding the COM sway and representing the controlled variable for the process. As for the unperturbed stance modeling the mass m of the subject can be considered concentrated in the COM.

In order to derive the equation of the system, conservation of the angular momentum can be applied:

$$\frac{d\mathbf{L}}{dt} = \sum_{k=1}^{n} \mathbf{M}_{k/O} \tag{2.1}$$

where the term $\frac{d\mathbf{L}}{dt}$ is the rate of change of the angular momentum of the mechanical system and $\sum_{k=1}^{n} \mathbf{M}_{k/O}$ represents the sum of all moments generated by external forces with respect to the origin of R_g. In this case $n = 2$, since the moments acting on the system are: $\mathbf{M}_g$ caused by gravitational field acting on the center of mass m and the global torque applied at the ankle, generated by the ground reaction force $\mathbf{R}$ applied at the CoP (Fig. 2.2). Then, it is possible to obtain the equation of the single inverted pendulum:

$$M_a(t) = ml^2\ddot{\theta}(t) - mglsin(\theta(t)) + \dot{d}(t)mlsin(\theta(t))\dot{\theta}(t) - \ddot{d}(t)mlcos(\theta(t)) \tag{2.2}$$

where $M_a(t)$ represents the total torque generated at the ankle, which depends on the linear displacement $d(t)$, angular displacement $\theta(t)$ and their time derivatives. The linear acceleration $\ddot{d}(t)$ acts as an input that generates the inertial disturbance for the system. Another source of disturbance is given by the Coriolis term, which is the element in (2.2) that depends on the linear velocity $\dot{d}(t)$ and angular velocity $\dot{\theta}(t)$. It should be noticed that the net torque measured $M_a(t)$contains the sign of the active control due to CNS and the torque due to the disturbance. Hence, to retrieve the control torque at the ankle, the following decomposition has been taken into account:

$$\begin{cases} \tau_d(t) & = -mglsin(\theta(t)) + \dot{d}(t)mlsin(\theta(t))\dot{\theta}(t) - \ddot{d}(t)mlcos(\theta(t)) \\ \tau_c(t) & = M_a(t) - \tau_d(t) \end{cases} \tag{2.3}$$

where $M_a(t)$ is the external ankle torque, obtained as the cross product between position vector of the $CoP(t)$ with respect to the ankle joint and the ground reaction force $\mathbf{R}(t)$ (figure 2.2). $\tau_d(t)$ is the torque generated by the disturbances while $\tau_c(t)$ is the internal control torque modeled as the difference between the measured $M_a(t)$ and the disturbance torque $\tau_d(t)$, derived by the model. The aforementioned mechanical perspective permitted a better interpretation of how data were related each other in the experiment. Moreover the disturbance torque in (2.3) clearly shows that the disturbance is coupled with the sway angle $\theta(t)$, challenging the identification of generalized models of the CNS in perturbed posture. For this reason, some procedures used for mitigate such drawback are reported in the following.

2.2.3 Data preparation

For each subject, data series of 1 s were considered, starting from the beginning of the perturbation for the EO, EC and DT conditions. This was motivated, by the aim of examining the control dynamics taking place during the transient phase of the response, avoiding the possible voluntary control effects arising whether greater temporal epochs are taken into account. This assumption appears in agreement with other studies dealing with the same topic [42, 45, 46, 29]. The kinematic data were filtered with a second order zero-phase low-pass filter with 10 Hz cut-off frequency, whereas the kinetic data were low-pass filtered at 15 Hz, then detrended and down-sampled at 100 Hz.

The inverse dynamics and the decomposition 2.3 were used to retrieve $\tau_c(t)$ as the difference between $M_a(t)$ and the disturbance torque $\tau_d(t)$. An example of the control torque $\tau_c(t)$ of a representative subject, for the three considered conditions, e.g. EO, EC, DT, are reported in figure 2.3.

For what concernes sEMG data, the GA and TA signals of the dominant leg are taken into account and band pass filtered between 30 and 450 Hz. After that, the root mean square (RMS) is computed and down-sampled at 100 Hz. to obtain coherent temporal representation among all the data types. At the end of such step, for each subject and for each condition 4 time series made by 100 samples were obtained, that is, the control torque $\tau_c(t)$, the sway angle $\theta(t)$, and the RMS of GA and TA. Such data were used in the identification procedure to retrieve a model of the neuromuscular control.

2.2.4 Identification Procedure and Analysis

In this work, the piecewise affine (PWA) paradigm was used to model the time-series behind the neuromuscular control. Such models are a representation of hybrid systems which can be obtained as first by partitioning the regression space into a finite number of non-overlapping convex polyhedral regions, then by identifying linear/affine subsystems within each of the partitions [35]. As highlighted by [34], one can arbitrarily select a number of finite partitions in order to approximate, with a certain degree of precision, the relations between the regressors and the outputs. Hence, such PWA models have been employed to approximate a nonlinear continuous behavior by a collection of linear or affine sub-models, each of them valid only in a certain portion of the data space. In the following, the mathematical tools needed for describing such models are reported. As first let consider a system in the input-output (I/O)

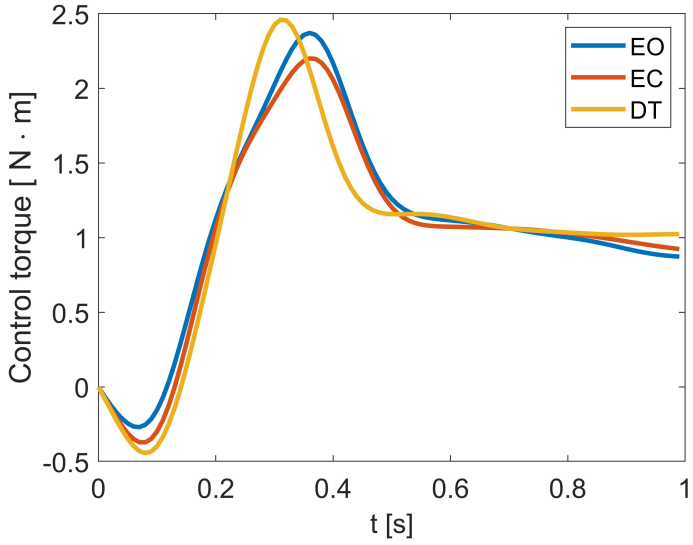

Figure 2.3: Control torque $\tau_c(t)$ for a representative subject measured in the three experimental conditions.

form:

$$\boldsymbol{y}_k = \boldsymbol{f}(\boldsymbol{x}_k, \boldsymbol{e}_k) \tag{2.4}$$

where $\boldsymbol{y}_k \in \mathbb{R}^p$ is the output vector, $\boldsymbol{x}_k \in \mathbb{R}^{n_d}$ is the regression vector, and $\boldsymbol{e}_k \in \mathbb{R}^p$ is the noise vector, which includes lagged values of the input $\boldsymbol{u}_{k-i}$ and the output $\boldsymbol{y}_{k-i}$. Following this representation, for a hybrid system the following holds[40, 34]:

$$\boldsymbol{y}_k = \boldsymbol{f}_{\sigma(k)}(\boldsymbol{x}_k, \boldsymbol{e}_k) \tag{2.5}$$

where $\boldsymbol{y}_k$, $\boldsymbol{x}_k$, $\boldsymbol{e}_k$ are as in (2.4), and the discrete state $\sigma(k) \in \{1, \ldots, s\}$ selects the active sub-model $\{\boldsymbol{f}_j\}_{j=1}^s$ at time k, where s is the number of sub-models. The discrete state $\sigma(k)$ depends on the regression vector $\boldsymbol{x}_k$, i.e., $\sigma(k) = j$ if $\boldsymbol{x}_k \in \mathcal{X}_j$, where $\mathcal{X}_j$'s are regions that form a partition of the whole regression space $\mathcal{X}$. Hybrid system identification, in the form given by (2.5) requires a parameterization in order to identify an opportune I/O data relation. Hence, (2.5) becomes [34, 40]:

$$\boldsymbol{y}_k = \boldsymbol{f}_{\sigma(k)}(\boldsymbol{x}_k[\boldsymbol{\theta}_{\sigma(k)}], \boldsymbol{e}_{\sigma(k)}, \boldsymbol{\theta}_{\sigma(k)}) \tag{2.6}$$

which implies the determination of all the parameter vectors $\{\boldsymbol{\theta}_j\}_{j=1}^s$ and the number of sub-models s constituting the system. In passing, it is also necessary to solve a classification

problem: it is required to classify which part of data is described by a sub-model rather than another one [40, 37]. To be noted, the form given in (2.6) is yet a general representation in which the functions $\boldsymbol{f}_{\sigma(k)}$ can assume also a non-linear relation with respect to their arguments. However, as highlighted in [37, 34, 40] linear sub-models made by autoregressive with exogenous input (ARX) systems provided remarkable results in describing also complex dynamics [34, 36, 37]. Literature defined the structure of (2.6) made by ARX sub-systems as piecewise affine autoregressive with exogenous input (PWARX) model.

The general form of PWARX can be found in many works [35, 36, 34, 37, 40]:

$$\boldsymbol{y}_k = \begin{cases} \boldsymbol{\theta}_1^\top \begin{bmatrix} \mathbf{x}_k \\ 1 \end{bmatrix} + \boldsymbol{e}_k, & if \quad \boldsymbol{x}_k \in \mathcal{X}_1 \\ \boldsymbol{\theta}_2^\top \begin{bmatrix} \mathbf{x}_k \\ 1 \end{bmatrix} + \boldsymbol{e}_k, & if \quad \boldsymbol{x}_k \in \mathcal{X}_2 \\ \vdots & \\ \boldsymbol{\theta}_s^\top \begin{bmatrix} \mathbf{x}_k \\ 1 \end{bmatrix} + \boldsymbol{e}_k, & if \quad \boldsymbol{x}_k \in \mathcal{X}_s \end{cases} \tag{2.7}$$

for $(k = 1 \dots N)$, where $\boldsymbol{y}_k \in \mathbb{R}^p$ is the output vector and $\boldsymbol{e}_k \in \mathbb{R}^p$ is the noise at time k. The regression vector $\boldsymbol{x}_k \in \mathbb{R}^{n_d}$ can assume the following form:

$$\boldsymbol{x}_k = \begin{bmatrix} \mathbf{y}_{k-1}^\top & \dots & \mathbf{y}_{k-n_y}^\top & \mathbf{u}_{k-1}^\top & \dots & \mathbf{u}_{k-n_u}^\top \end{bmatrix}^\top \tag{2.8}$$

where $\mathbf{u}_k \in \mathbb{R}^m$ is the input vector and $n_d = pn_y + mn_u$, with non-negative integers n_y and n_u representing, respectively, the output and input lag order [37]. Let $\mathcal{X} \subseteq \mathbb{R}^{n_d}$ be the regression space, and $\mathcal{X}_i$, $(i = 1, 2, \dots, s)$ represents a convex polyedral subset of $\mathcal{X}$. Each polyedron $\mathcal{X}_i$ is assumed to satisfy $\mathcal{X}_i = \{ \boldsymbol{x}_k \in \mathcal{X} : \mathscr{H}_i [\boldsymbol{x}_k \quad 1]^\top \leq \mathbf{0} \}$, $(i = 1, 2, \dots, s)$, $\mathcal{X}_i \neq \emptyset \quad \forall i \in \{1, 2, \dots, s\}, \mathcal{X}_i \cap \mathcal{X}_j = \emptyset \quad \forall i, j \in \{1, 2, \dots, s\}$, $i \neq j$, and $\bigcup_{i=1}^{s} \mathcal{X}_i = \mathcal{X}$ [35, 34]. Each row of $\mathscr{H}_i$ defines a separating hyperplane between $\mathcal{X}_j$ and the other regions [34]. Indeed, if the PWA map is assumed to be continuous, the model parameters and the partition

of the domain are not independent. At the switching surface between two modes, it must hold that [34]:

$$\theta_i^\top [\boldsymbol{x}_k \quad 1]^\top = \theta_j^\top [\boldsymbol{x}_{k+1} \quad 1]^\top, \quad 1 \leq j < i \leq s \tag{2.9}$$

To be noticed, assuming the presence of only two sub-dynamics for the PWARX model, the state points $\mathbf{x}_k$ belong either to $\mathcal{X}_1$ or $\mathcal{X}_2$ with just one separating hyperplane characterized by the normal vector $\mathscr{H}_1$. Hence, in this case, when the condition $\mathscr{H}_1 [\boldsymbol{x}_k \quad 1]^\top \leq \mathbf{0}$ holds, the dynamics is driven by the first subsystem. When the latter condition does not hold, a switching to the second subsystem occurs and the system evolves accordingly.

The identification of a PWARX model for the neuromuscular control required firstly to define the dimension of the regression space n_d and the lag orders n_u and n_y for the input and output data respectively. This could be a not trivial aspect when no information is available regarding the order and the dynamics of the neural controller. Hypothetically. Such kind of information should be retrieved form the data in order to parsimoniously select a model structure that provides high generalization properties of the model without disregarding the fitting quality of the data themselves. Moreover, while the output is $\tau_c(t)$, the exogenous inputs that could be relevant to build the model are the sway angle $\theta(t)$ and the muscles RMS data. This great amount of exogenous information can further challenge the selection of the model structure. Thus, as suggested in [47], one can take advantage from the minimum redundancy maximum relevance principle (mRMR) to select the exogenous inputs, their lags, and the lags relative to the autoregressive part of the model. The mRMR selection algorithm was formulated by Ding and Peng [48], and further explained in [49]. Despite the mRMR was originally developed for categorical target variables, it was extended in an efficient manner for continuous target variables [50], rendering mRMR feature selection procedures appealing also for time-series modeling [47]. This constitute an element of novelty for the procedures adopted, that certainly merits future studies. However, it deserves to be highlighted that in modern system identification, data-driven algorithms inspired by statistical approaches (i.e. LASSO penalized regression) provided promising results to optimally select and identify the model from the data [51, 52]. This justified the methodological perspective investigated in this work, that required the selection of an opportune space upon which identifies the ARX sub-models.

Thus, the following pipeline was considered: for each subject and trial, a large regression space was generated delaying the input and output time-series by a lag limit value equal

to 20. Three large regression spaces, made by data relative to 7 subjects, were created for training as follows: seven of ten regression spaces were concatenated for trials, namely EO, EC and DT, by preserving the lag-coordinates. This corresponds to training-testing dataset split of 70-30%. Each training set was shrunk with the mRMR algorithm to the five most relevant components for predicting the torques τ_c at the current time. Thus, by means of mRMR, the original large n_d training dataset were reduced to spaces with $n_d = 5$, where the lags selection of the autoregressive (AR) and the exogenous (X) components was driven directly by the data [40]. In order to test the reliability of the identification procedure and the capability of the model in generalizing the dataset split of 60-40% and 50-50% were considered as reported in [40]. When regression space was defined, it was possible to proceed by analyzing how many partitions the datasets contained. This was done through the spectral clustering, whereas the optimal number of clusters was evaluated through the silhouette method [53]. Spectral clustering was employed to overcome the limitation of a parametric clustering approach, such as the Gaussian Mixture models used in [37], where the data are assumed to be a mixture of gaussian distributions, by relying on a geometric approach [54]. This can be particularly useful when the latter approach permit a better description of the data rather than the typical distribution based evaluation.

After clustering, data are labeled and employed to identify the polyedral regions that partition the regression space. In order to do this, soft margin support vector machine (SVM) was used, as in [37]. The last step was to identify the ARX sub-models. Possible data points lying on the hyperplanes were discharged and the closed form least mean square estimation based on pseudo-inverse matrix was employed to recover the parameters of each sub-model [37, 27]. Normalized root mean square error metric (NRMSE) was used to quantify the fitting goodness of the three identified models. Such measure will be referred as fit percentage:

$$fit_{\%} = 100\left(1 - \frac{\| y - \hat{y} \|}{\| y - \mu_y \|}\right) \tag{2.10}$$

where y is the data output, $\hat{y}$ is the output produced by the model and μ_y indicates the mean value of y.

2.3 Results

Table 2.1 shows the I/O structure built through the selection of $n_d = 5$ and the use of mRMR algorithm. In EC and DT conditions, mRMR does not report the RMS of TA in the first five most relevant components (Table 2.1), likely indicating that the information provided through TA in the regression scheme plays a secondary role if compared with GA. It deserves to be noted that in DT condition mRMR selected three time lags of the control torque in the first five most significant components, suggesting a more autoregressive scheme rather than those employed in the other two cases.

Table 2.1: The five ARX components selected by the mRMR algorithm for the three regression spaces namely EO, EC, DT, in terms of time-series lags chosen.

Condition	AR		X	
	τ_c	θ	GA	TA
EO	{1;20}	12	20	17
EC	{1;20}	19	{17;20}	
DT	{1;4;20}	18	19	

In all experimental conditions, the silhouette criterion suggested an optimal number of cluster equal to 2 (figure 2.4). This indicates that the data can be described by two sub-dynamics, e.g. two ARX components and one boundary hyperplane dividing the two clusters. Hence, for each experimental condition the identified systems are reported in Table 2.2.

Table 2.2: Regression vector ($\mathbf{x}_k$), estimated boundary hyperplane ($\hat{\mathscr{H}}_{12}$), and sub-models coefficients ($\hat{\boldsymbol{\theta}}_1$ and $\hat{\boldsymbol{\theta}}_2$) for the identified models in the three conditions, i.e. EO, EC, and DT.

EO				EC				DT			
$\mathbf{x}_k$	$\hat{\mathscr{H}}_{12}$	$\hat{\boldsymbol{\theta}}_1$	$\hat{\boldsymbol{\theta}}_2$	$\mathbf{x}_k$	$\hat{\mathscr{H}}_{12}$	$\hat{\boldsymbol{\theta}}_1$	$\hat{\boldsymbol{\theta}}_2$	$\mathbf{x}_k$	$\hat{\mathscr{H}}_{12}$	$\hat{\boldsymbol{\theta}}_1$	$\hat{\boldsymbol{\theta}}_2$
τ_{ck-1}	0.918	0.889	0.943	τ_{ck-1}	3.470	0.912	0.929	τ_{ck-1}	-2.250	1.275	1.196
τ_{ck-20}	-4.574	0.010	-0.079	τ_{ck-20}	-2.691	0.005	-0.105	τ_{ck-20}	4.274	0.001	0.006
TA_{k-17}	0.859	0.004	0.004	GA_{k-17}	0.681	0.006	0.021	GA_{k-19}	-0.805	-0.003	-0.001
GA_{k-20}	2.078	0.003	-0.017	GA_{k-20}	1.506	0.008	0.017	θ_{k-18}	1.755	-0.022	-0.002
θ_{k-12}	-2.472	0.005	-0.059	θ_{k-19}	-3.460	0.008	0.029	τ_{ck-4}	-0.960	-0.316	-0.238
1	1.235	0.043	0.085	1	-0.340	0.030	0.082	1	-0.003	0.028	0.021

Table 2.3: NMRSE fitting percentages obtained by the models identified for each experimental condition. The results are relative to three training-testing data split (70-30%, 60-40%, and 50-50%). S1,...,S10 indicate subjects.

Condition	S1	S2	S3	S4	S5	S6	S7	S8	S9	S10
	Training data							Testing data		
EO	97.1	95.9	96.2	94.3	93.6	90.8	91.2	91.2	87.5	91.6
EC	95.8	94.8	93.9	95.9	95.5	89.5	93.1	93.1	67.9	92.0
DT	97.9	97.9	96.3	97.2	97.5	97.5	98.1	98.1	95.7	97.4
	Training Data						Testing data			
EO	97.7	95.5	95.8	95.1	93.3	91.5	90.0	90.0	87.7	90.0
EC	96.0	94.5	93.3	96.4	96.0	89.9	92.1	92.1	69.4	91.7
DT	97.9	97.8	96.2	97.3	97.5	97.5	97.7	97.7	97.0	97.3
	Training Data					Testing data				
EO	97.1	96.3	97.2	95.4	94.4	87.9	91.2	91.1	85.4	92.3
EC	95.7	95.1	94.5	95.9	96.7	87.3	93.0	92.9	72.4	91.9
DT	97.5	97.7	96.3	97.5	97.6	96.6	97.7	97.7	97.1	97.3

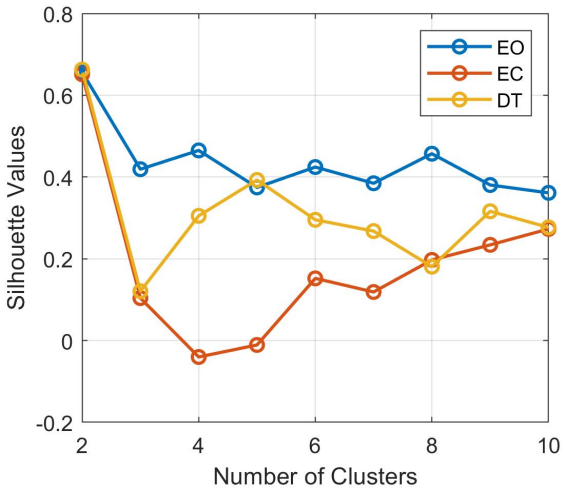

Figure 2.4: Silhouette spectral cluster evaluation for the three shrink regression spaces in EO, EC, and DT conditions. Note that the optimal numbers of clusters is given in correspondence to the maximum of the silhouette values.

The identified models present good fitting in training and testing steps, as highlighted by the value of the fit percentages for the three dataset partitioning (Table 2.3). However, it should be noted that subject 9 belonging to the testing data presented a moderate fit percentage value (about 70%) regarding the EC condition. All the other testing data

guaranteed high NRMSE (Table 2.3) [40].

2.4 Discussion

The study here reported aligns with the approach followed in the first chapter of this thesis. Indeed, despite the data driven techniques mentioned in 2.2 can be applied for a wide spectrum of data and processes, their use in the neural control modeling of the upright stance maintenance required a deep understanding of the mechanical quantities that challenge the balance in the case of support base translations. Indeed, although the experimental setup used for the study is commonly employed in the clinical scenario [4, 46], it produces coupling mechanical effects between the controlled variable and the disturbance, e.g. between the sway angle and the support base acceleration, that impacts on the generalization properties of the model one would identify [40]. Hence, rather than avoid this kind of experimental setup in favour of other devices like those employed in [33, 6], the present results encourage the development of ad-hoc procedures for the analysis and identification of neuromuscular models as emerged also from recent studies [7, 8, 20].

Moreover the findings confirm that a multi-source information analysis that accounts for kinematic, dynamic and EMG data can be used to infer the modalities through which CNS handles sensory information and cognitive load while the subject undergoes to sudden perturbations. Although the control action is a postural reflex and and can be mainly attributed to lower control structures, part of the response seems to be affected by higher level CNS control structures [4, 11, 7]. This aspect is supported by the criterion used to select the information and the time-lags of the input-output data used to identify the models for the three different experimental conditions. Results indicate that the information content markedly changed for the three tasks under the parsimonious selection criterion given by the mRMR (Table 2.1). For instance, all the exogenous information in the EO condition, can be used to obtain good fits in both the training and testing (Table 2.3). Moreover, the lag orders of the exogenous signals, i.e. θ, GA and TA, are always greater or equal to 12. This implies that the delays used to obtain a parsimonious model of the physiological control torque are of the order of 120-200 ms, aligning to the physiological values reported in the literature [1].

It deserves to be noted that both muscles play a relevant role in EO, whereas for EC and DT, the TA muscle activity was not ranked within the first five regressors considered for

the identification procedure. More precisely, in the EC and DT condition, two GA time-lags were identified to be meaningful in modeling the control action (Table 2.1) while TA did not appear, eventually supporting that sensory deprivation or cognitive loads can affects the CNS control responses also in the case of sudden compensatory balance maintenance mechanisms. A further reason for which mRMR did not rank TA in the first five significant regressor components may lie on the nature of the experiment as highlighted in [4]. In fact, moving backward with respect to the subject's visual field, the support base induces an inertial force to the COM that requires firstly the activation of the GA in order to prevent the subject from falling forward [4]. Following this line, the GA muscle activity may reflect a larger amount of control information with respect to TA, and it can be amplified in the more challenging conditions EC and DT, offering a more stiffening behavior with respect to what observed in EO [40].

The role of GA seems to be further enhanced in EC condition, where the presence of two time lags for the GA muscle activity indicates that the CNS employed the visual sensory information to regulate more efficiently the redundancy of the control structure [55]. This is in line with the findings of Albertsen et al.[10], where it is highlighted that postural adjustment in EC might be promoted by joint stiffening or increment of postural proprioceptive or vestibular reflex responses. On the contrary, with the presence of vision, the CNS could afford low degrees of muscle stiffness, which might no longer be possible in visual deprivation [10]. The predominant role of the GA with respect to TA in EC conditions seems to be confirmed also by the myoelectric activity of the two muscles within the time epoch considered in this study (Figures 2.5, 2.6).

Indeed, by using the ratio between GA and TA area under the curve as a metric of contraction prevalence [56], it resulted 2.48±0.43 (EO) and 5.02±0.55 (EC), averaged over all the participants. However, it deserves to be stressed that the the lack of TA for the identified models in EC and DT conditions does not mean that the role of tibialis is negligible for the physiology of balance recovery after the perturbation [57], but it simply means that under a modeling perspective the role of GA is an essential component in the description of the task considered.

The identified models for the EO and EC conditions showed a similar ARX structure, since the number of AR components were the same, incidentally the exogenous component changed its role passing form EO to EC (Table 2.1). A complete different situation was found for the DT model (Table 2.1), for which an increase in AR order is captured if compared to

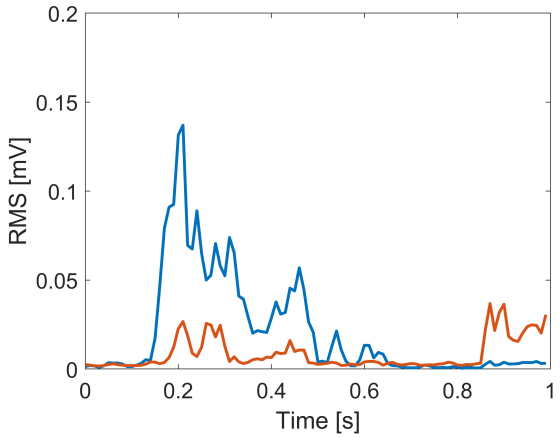

Figure 2.5: Root-mean-square value (RMS) of the myoelectric activity for the tibialis anterior (red line) and gastrocnemius (blue line) recorded during the EO trial, from a representative subject.

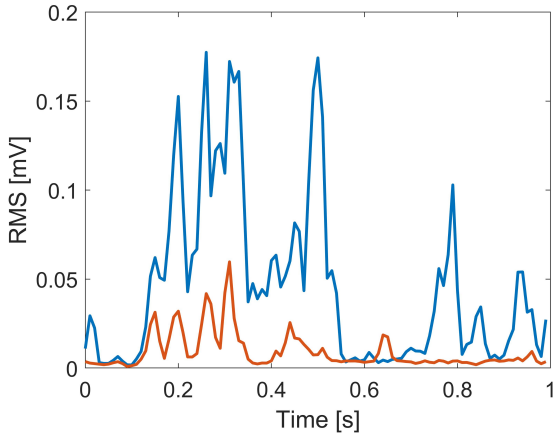

Figure 2.6: Root-mean-square value (RMS) of the myoelectric activity for the tibialis anterior (red line) and gastrocnemius (blue line) recorded during the EC trial, from a representative subject.

the other two experimental conditions. This structural change could be partially attributed to the involvement of higher CNS control centers in the cognitive task due to backward mental counting, hence promoting a more reflex-based control. Indeed, the additional AR term presented a lag order of 4, (40 ms), which indicated a sudden disturbance compensation. From a physiological point of view, this could be explained by greater involvement of the proprioceptive information to produce a postural adjustment (low level scheme), thus suggesting a control policy mainly driven by the peripheral information. This line holds also from a kinesiological perspective since previous studies demonstrated that the introduction

of torque related information for balance regulation in the feedback loop can provide more robust compensatory mechanism [16, 33].

An important aspect that deserves to be underlined regards the number of clusters, i.e. the sub-dynamics that silhouettes identified (see section 2.3). Such value was equal to two for all the three conditions (EO, EC, and DT) and for the different lagged signals, suggesting an akin control response between the considered perturbed conditions [40]. Albeit interpreting the two clusters subdivision of the five dimensional data is not straightforward, the identified models showed satisfactory autocorrelation properties of the residuals (Figure 2.7) in training and proper fitting percentage in both training and testing as shown in Table 2.3. These findings suggest that the identification procedure adopted in this work provided generalized models that did not report detrimental effects neither when the amount of testing data reached the 50%, with a consequent reduction of data available for training (Table 2.3). Such training-testing procedure permitted to verify the reliability of the identified control models in the three different experimental conditions. However, the use of leave-one-subject-out as validation scheme could provide models able to better highlight subject-specific characteristics rather than global population mechanisms. Indeed, S9 in Table 2.3 was not completely described by the identified models in EC condition, which were obtained with the data belonging to the first 7, 6 and 5 subjects respectively (Table 2.3). Indeed, the NMRSE for S9 was always not greater than 72.4% in the EC condition. Hence, a leave-one-subject-out scheme could be employed to highlight whether a behavior like the one above mentioned can be present also in one of the first 5 subjects never being used for testing. Although this point was beyond the aim of the present study, it could be potentially useful to characterize outliers or differences in the neuromuscular control strategy between healthy or pathological conditions.

To be noted, in section 2.2, the maximum time lag of any variable, e.g. sway angle, torque, GA and TA myoelectric activity, was set to 20 (corresponding to 200 ms), giving a total number of possible regressors equal to 80. Therefore, $n_d = 5$ was taken as a fixed value for two reasons: as first, it guaranteed a robust fitting of the testing data even when the size of the training set was reduced, promoting the identification of generalized models (Table 2.3). Secondly, the aforementioned choice allowed to obtain better explainable models if compared with other techniques such as neural networks or deep learning, for which the goodness of fitting is favored with respect the model interpretability [40, 58].

By analyzing the switching signals between the two sub-dynamics, it can be observed that

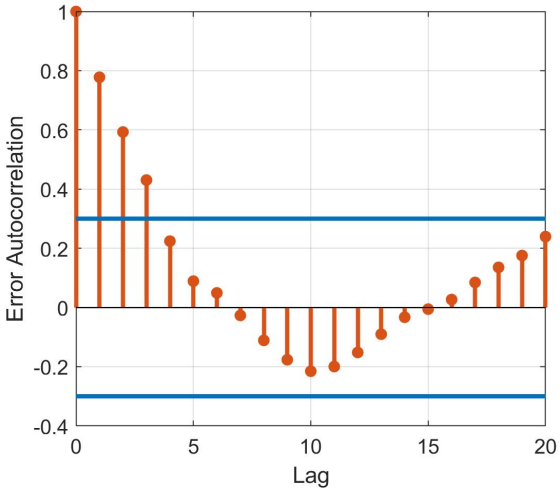

Figure 2.7: Error signal autocorrelation for a representative subject. The error signal was obtained as the difference between the output generated by the model and the measured torque.

the models present one switch (Fig. 2.8), which occurs at 210, 260, 230 ms for OA, OC, and DT respectively (median values among all the subjects). The aforementioned values are always lower than about 300 ms, which is the nominal time at which the platform stop to move. This suggests that the identified neuromuscular control models work with a certain control policy in the first part of the experiment, where the inertial force suddenly changes due to the presence of the support base acceleration (2.3), and switches to another policy when the inertia is reduced (after 300 ms), eventually confirming that the data partitions are consistent with the physics of the experiment. This suggests that the models made by two ARX components capture a significant amount of information, confirming the line proposed in [18] regarding the capability of black box modeling to be sensitive to balancing strategy changes. Hence, the approach here proposed can be employed in conjunction with more classical posturographic analyses to investigate the neural policies adopted for maintaining upright stance challenged by external disturbances [40].

Compering the IP model employed in the first chapter and the one proposed in section 2.2, it is possible to observe that the latter does not present any linearization even if the use of linearization is a common procedure in both unperturbed and perturbed posture modeling [12, 18, 6]. Nevertheless, the use of non-linear IP is justified by the nature of the experiment, since the perturbation magnitude delivered to the subject during the experiments were higher than the typical postural noise [2], thus rendering the linearization hypothesis

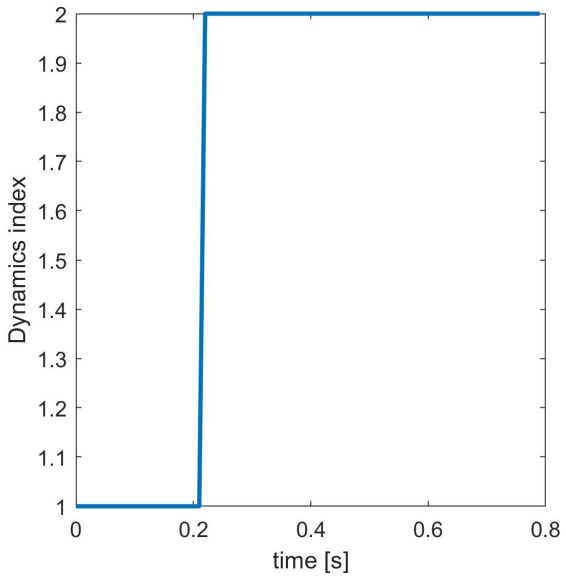

Figure 2.8: Switching signal of a representative subject in DT condition. Dynamic index i corresponded to the i-th ARX dynamic fitted with the i-th data cluster, for i=1,2. The signal shows one switch and in this case the second dynamic occurred at 230 ms.

an over-simplification of the problem. Such disturbance, at the same time, guaranteed a single-link IP description of the stance as observed in [45] where the same procedure was employed. This, together with the *first trial effect* avoidance due to trial repetition (see section 2.2), allowed to evoke ankle strategies from the subjects, eventually providing a set of data that effectively account for stereotyped responses of the CNS.

Confirmations regarding the non-linear properties of the process can be inferred also from the ARX sub-model coefficients: for a given regressor, either a change of the magnitude or the sign, or even of both were obtained (Table 2.2), indicating that unimodal linear controllers may be not adequate to fit postural data obtained through support base movement perturbation. Nevertheless, a piecewise approach seems to be adequate to successfully model the process when the final goal is the physiological interpretation. In fact, despite other kinds of models, such as nonlinear ARX (NARX) or PWNARX, could be applied, the potential benefits in terms of data fitting would be obtained at the cost of poorer and more difficult interpretability of the results, hindering their practical use in the clinical context [40, 18]. Moreover, it is noteworthy that despite the single-link inverted pendulum represents a simplified model of the human upright stance, it appears suitable for modeling stance maintenance in perturbed conditions. Indeed, many previous studies investigated balance

responses to external perturbations relying on single-link inverted pendulum model, where the ankle joint is the only actuated joint for counteracting the disruption [16, 59, 60, 61]. In addition, as also observed in unperturbed posture modeling, the single-link IP constitutes the core for the description of any balancing task, indeed, also in dynamical conditions, the multi-link structure employed can often be reduced to the COP-COM relation [62, 63, 64], hence basically to a single-link IP description.

It deserves to be pointed out that discontinuous systems [32] with multiple dynamics were employed to model upright maintenance in perturbed [21], and unperturbed conditions, with internal physiological noise sources [13, 14, 65]. The latter resulted in highly explainable models and constitute a great advance toward the understanding of neuromuscular control CNS actuates in posture maintenance. In the PWARX identification context, the idea of multiple dynamics with possible discontinuities is still preserved; thus, the high fits obtained in this study seem to confirm the hypothesis that neuromuscular control of upright stance can be modeled as a multi-dynamic process [14, 13]. The use of PWARX in modeling neuromuscular control merits further investigations and additional efforts will be devoted to the investigation of the entire body chain, whose employment would provide valuable additional insights regarding the dynamics of balance response to a sudden external perturbation [40]. These aspects should be taken into account in future studies, since they require the use of different system identification approaches, e.g. multi-input multi-output, and the acquisition of kinematics and myoelectric activity also from the upper segments of the human body [40]. Eventually, such kind of system identification framework can be also applied in posturographic data analysis and other motor tasks, e.g. gait, in relation to different experimental conditions or populations, such as elderly and pathological individuals.

2.5 Remarks and personal perspective

In these two chapters, it has been highlighted the line followed for the study of neuromuscolar control in human balance maintenance. An important aspect regarded the finding of a common ground between the more classical perspective of posturography and the use of model based approaches. Indeed very recent works in which data and models were used in conjunction for inferential purposes demonstrated their values in the assessment of the detrimental effects due to neurodegenerative disease [66]. However, this research line is well recognizable in previous works [18, 9]. Here, such research line was pursued having the

possibility of employing a large spectrum of newest techniques, which emerged from the control and data science theory. Moreover along this path, it was found another research perspective that aligns with the one above mentioned and confirmed in [67]. Indeed, despite the inferential purposes are of key importance, also the assessment of appropriate data analysis techniques are of great importance in the advancement of neuromuscular control modeling and analysis. To do this, one should start from physical models which demonstrated to be able in generating plausible physiological data [64, 67]. Thus, it was particularly important to give attention to the formalization of the human balance maintenance as a biomechanical problem.

In the next chapters the attention moves toward other problems related to the neuromuscular control, which are focused on voluntary movements and related to the electromyographic signal processing. Such research line constitutes the second part of this thesis, and it is motivated by the recent advancement in the field of biomechancs and neural engineering, which grounds the bases for new engineering applications.

Bibliography

[1] Pietro Morasso, Amel Cherif, and Jacopo Zenzeri. Quiet standing: The single inverted pendulum model is not so bad after all. *PloS one*, 14(3):e0213870, 2019.

[2] Silvia Conforto, Maurizio Schmid, Valentina Camomilla, Tommaso D'Alessio, and Aurelio Cappozzo. Hemodynamics as a possible internal mechanical disturbance to balance. *Gait & posture*, 14(1):28–35, 2001.

[3] Andrea Berencsi, Masami Ishihara, and Kuniyasu Imanaka. The functional role of central and peripheral vision in the control of posture. *Human movement science*, 24(5-6):689–709, 2005.

[4] Fay B Horak and Lewis M Nashner. Central programming of postural movements: adaptation to altered support-surface configurations. *Journal of neurophysiology*, 55(6):1369–1381, 1986.

[5] Mitesh Patel, S Gomez, D Lush, and Per-Anders Fransson. Adaptation and vision change the relationship between muscle activity of the lower limbs and body movement during human balance perturbations. *Clinical Neurophysiology*, 120(3):601–609, 2009.

[6] Denise Engelhart, Alfred C Schouten, Ronald GKM Aarts, and Herman van der Kooij. Assessment of multi-joint coordination and adaptation in standing balance: a novel device and system identification technique. *IEEE Transactions on Neural Systems and Rehabilitation Engineering*, 23(6):973–982, 2014.

[7] Akihiro Nakamura, Yasuyuki Suzuki, Matija Milosevic, and Taishin Nomura. Long-lasting event-related beta synchronizations of electroencephalographic activity in response to support-surface perturbations during upright stance: A pilot study associating beta rebound and active monitoring in the intermittent postural control. *Frontiers in systems neuroscience*, 15, 2021.

[8] Aiden M Payne and Lena H Ting. Worse balance is associated with larger perturbation-evoked cortical responses in healthy young adults. *Gait & posture*, 80:324–330, 2020.

[9] Alessandro Mengarelli. Balance and motor control in dynamic tasks. *Phd thesis, Università Politecnica delle Marche*, 2017.

[10] Inke Marie Albertsen, Mouna Ghédira, Jean-Michel Gracies, and Émilie Hutin. Postural stability in young healthy subjects–impact of reduced base of support, visual deprivation, dual tasking. *Journal of electromyography and kinesiology*, 33:27–33, 2017.

[11] JV Jacobs and FB Horak. Cortical control of postural responses. *Journal of neural transmission*, 114(10):1339, 2007.

[12] Robert J Peterka. Postural control model interpretation of stabilogram diffusion analysis. *Biological cybernetics*, 82(4):335–343, 2000.

[13] Yasuyuki Suzuki, Taishin Nomura, Maura Casadio, and Pietro Morasso. Intermittent control with ankle, hip, and mixed strategies during quiet standing: a theoretical proposal based on a double inverted pendulum model. *Journal of Theoretical Biology*, 310:55–79, 2012.

[14] Taishin Nomura, Shota Oshikawa, Yasuyuki Suzuki, Ken Kiyono, and Pietro Morasso. Modeling human postural sway using an intermittent control and hemodynamic perturbations. *Mathematical Biosciences*, 245(1):86–95, 2013.

[15] Hongbo Zhang, Maury A Nussbaum, and Michael J Agnew. Development of a sliding mode control model for quiet upright stance. *Medical Engineering & Physics*, 38(2):204–208, 2016.

[16] Robert J Peterka. Comparison of human and humanoid robot control of upright stance. *Journal of Physiology-Paris*, 103(3-5):149–158, 2009.

[17] Kamran Iqbal. Optimal time-varying postural control in a single-link neuromechanical model with feedback latencies. *Biological Cybernetics*, 114(4):485–497, 2020.

[18] Maria Letizia Corradini, Sandro Fioretti, Tommaso Leo, and Roberto Piperno. Early recognition of postural disorders in multiple sclerosis through movement analysis: a modeling study. *IEEE Transactions on Biomedical Engineering*, 44(11):1029–1038, 1997.

[19] Denise Engelhart, Tjitske A Boonstra, Ronald GKM Aarts, Alfred C Schouten, and Herman van der Kooij. Comparison of closed-loop system identification techniques to quantify multi-joint human balance control. *Annual reviews in control*, 41:58–70, 2016.

[20] Huawei Wang and Antonie J van den Bogert. Identification of the human postural control system through stochastic trajectory optimization. *Journal of neuroscience methods*, 334:108580, 2020.

[21] Andrea Tigrini, Alessandro Mengarelli, Stefano Cardarelli, Annachiara Strazza, Francesco Di Nardo, Sandro Fioretti, and Federica Verdini. Description of postural strategies through a variable structure control. In *2019 41st Annual International Conference of the IEEE Engineering in Medicine and Biology Society (EMBC)*, pages 4113–4116. IEEE, 2019.

[22] Andrea Tigrini, Alessandro Mengarelli, Stefano Cardarelli, Annachiara Strazza, Francesco Di Nardo, Sandro Fioretti, and Federica Verdini. Modeling perturbed posture through an adaptive sliding mode approach. In *2019 41st Annual International Conference of the IEEE Engineering in Medicine and Biology Society (EMBC)*, pages 5335–5338. IEEE, 2019.

[23] S Hanneton, Alain Berthoz, Jacques Droulez, and Jean-Jacques E Slotine. Does the brain use sliding variables for the control of movements? *Biological cybernetics*, 77(6):381–393, 1997.

[24] L Young and J Meiry. Bang-bang aspects of manual control in high-order systems. *IEEE Transactions on Automatic Control*, 10(3):336–341, 1965.

[25] Alessandra Bottaro, Youko Yasutake, Taishin Nomura, Maura Casadio, and Pietro Morasso. Bounded stability of the quiet standing posture: an intermittent control model. *Human movement science*, 27(3):473–495, 2008.

[26] Adam D Goodworth and Robert J Peterka. Identifying mechanisms of stance control: a single stimulus multiple output model-fit approach. *Journal of neuroscience methods*, 296:44–56, 2018.

[27] L Ljung. *System identification-theory for the user 2nd edition ptr prentice-hall*. 1999.

[28] Erwin de Vlugt, Alfred C Schouten, and Frans CT van der Helm. Closed-loop multivariable system identification for the characterization of the dynamic arm compliance

using continuous force disturbances: a model study. *Journal of neuroscience methods*, 122(2):123–140, 2003.

[29] Jasper E Visser, Mark G Carpenter, Herman van der Kooij, and Bastiaan R Bloem. The clinical utility of posturography. *Clinical Neurophysiology*, 119(11):2424–2436, 2008.

[30] Diana Dimitrova, Fay B Horak, and John G Nutt. Postural muscle responses to multidirectional translations in patients with parkinson's disease. *Journal of Neurophysiology*, 91(1):489–501, 2004.

[31] Antonio Nardone, Massimo Galante, Davide Pareyson, and Marco Schieppati. Balance control in sensory neuron disease. *Clinical neurophysiology*, 118(3):538–550, 2007.

[32] Yury V Orlov. *Discontinuous systems: Lyapunov analysis and robust synthesis under uncertainty conditions*. Springer Science & Business Media, 2008.

[33] Robert J Peterka. Sensory integration for human balance control. *Handbook of clinical neurology*, 159:27–42, 2018.

[34] Fabien Lauer and Gérard Bloch. Hybrid system identification. In *Hybrid System Identification*, pages 77–101. Springer, 2019.

[35] Simone Paoletti, Aleksandar Lj Juloski, Giancarlo Ferrari-Trecate, and René Vidal. Identification of hybrid systems a tutorial. *European Journal of Control*, 13(2-3):242–260, 2007.

[36] René Vidal, Yi Ma, and S Shankar Sastry. *Generalized principal component analysis*, volume 5. Springer, 2016.

[37] Hayato Nakada, Kiyotsugu Takaba, and Tohru Katayama. Identification of piecewise affine systems based on statistical clustering technique. *Automatica*, 41(5):905–913, 2005.

[38] Sergio Bittanti. *Model Identification and Data Analysis*. Wiley Online Library, 2019.

[39] N Fujisawa, Tadashi Masuda, Hidenori Inaoka, Yutaka Fukuoka, Akimasa Ishida, and Haruyuki Minamitani. Human standing posture control system depending on adopted strategies. *Medical and Biological Engineering and Computing*, 43(1):107–114, 2005.

[40] Andrea Tigrini, Federica Verdini, Marco Maiolatesi, Andrea Monteriù, Francesco Ferracuti, Sandro Fioretti, Sauro Longhi, and Alessandro Mengarelli. Neuromuscular control modelling of human perturbed posture through piecewise affine autoregressive with exogenous input models. *Frontiers in Bioengineering and Biotechnology*, 9, 2022.

[41] Alberto Leardini, Zimi Sawacha, Gabriele Paolini, Stefania Ingrosso, Roberto Nativo, and Maria Grazia Benedetti. A new anatomically based protocol for gait analysis in children. *Gait & Posture*, 26(4):560–571, 2007.

[42] W Nanhoe-Mahabier, JHJ Allum, S Overeem, GF Borm, LB Oude Nijhuis, and BR Bloem. First trial reactions and habituation rates over successive balance perturbations in parkinson's disease. *Neuroscience*, 217:123–129, 2012.

[43] Pietro Morasso, Taishin Nomura, Yasuyuki Suzuki, and Jacopo Zenzeri. Stabilization of a cart inverted pendulum: improving the intermittent feedback strategy to match the limits of human performance. *Frontiers in computational neuroscience*, 13:16, 2019.

[44] Naoya Yoshikawa, Yasuyuki Suzuki, Ken Kiyono, and Taishin Nomura. Intermittent feedback-control strategy for stabilizing inverted pendulum on manually controlled cart as analogy to human stick balancing. *Frontiers in computational neuroscience*, 10:34, 2016.

[45] HC Diener, FB Horak, and LM Nashner. Influence of stimulus parameters on human postural responses. *journal of Neurophysiology*, 59(6):1888–1905, 1988.

[46] JHJ Allum, K-S Tang, MG Carpenter, LB Oude Nijhuis, and BR Bloem. Review of first trial responses in balance control: influence of vestibular loss and parkinson's disease. *Human Movement Science*, 30(2):279–295, 2011.

[47] Min Han, Weijie Ren, Meiling Xu, and Tie Qiu. Nonuniform state space reconstruction for multivariate chaotic time series. *IEEE Transactions on Cybernetics*, 49(5):1885–1895, 2018.

[48] C Ding and H Peng. Minimum redundancy feature selection from microarray gene expression data. In *Computational Systems Bioinformatics. CSB2003. Proceedings of the 2003 IEEE Bioinformatics Conference. CSB2003*, pages 523–528. IEEE, 2003.

[49] Hanchuan Peng, Fuhui Long, and Chris Ding. Feature selection based on mutual information: criteria of max-dependency, max-relevance, and min-redundancy. *IEEE Transactions on Pattern Analysis and Machine Intelligence*, 27(8):1226–1238, 2005.

[50] Georges A Darbellay and Igor Vajda. Estimation of the information by an adaptive partitioning of the observation space. *IEEE Transactions on Information Theory*, 45(4):1315–1321, 1999.

[51] Oliver Nelles. *Nonlinear System Identification: From Classical Approaches to Neural Networks, Fuzzy Models, and Gaussian Processes*. Springer Nature, 2020.

[52] Rajiv Singh and Mario Sznaier. On identification of nonlinear arx models with sparsity in regressors and basis functions. *IFAC-PapersOnLine*, 54(7):720–725, 2021.

[53] Peter J Rousseeuw. Silhouettes: a graphical aid to the interpretation and validation of cluster analysis. *Journal of Computational and Applied Mathematics*, 20:53–65, 1987.

[54] Andrew Y Ng, Michael I Jordan, and Yair Weiss. On spectral clustering: Analysis and an algorithm. In *Advances in neural information processing systems*, pages 849–856, 2002.

[55] Alessandro Mengarelli, Stefano Cardarelli, Sandro Fioretti, Annachiara Strazza, Andrea Tigrini, Francesco Di Nardo, Laura Burattini, and Federica Verdini. Role of the visual feedback on balance responses to upright stance perturbations. In *World Congress on Medical Physics and Biomedical Engineering 2018*, pages 685–689. Springer, 2019.

[56] Adam Donald Campbell, Christopher J Dakin, and MG Carpenter. Postural responses explored through classical conditioning. *Neuroscience*, 164(3):986–997, 2009.

[57] Laura Perucca, Antonio Caronni, Gaj Vidmar, and Luigi Tesio. Electromyographic latency of postural evoked responses from the leg muscles during equitest computerised dynamic posturography: Reference data on healthy subjects. *Journal of Electromyography and Kinesiology*, 24(1):126–133, 2014.

[58] Lennart Ljung, Carl Andersson, Koen Tiels, and Thomas B Schön. Deep learning and system identification. *IFAC-PapersOnLine*, 53(2):1175–1181, 2020.

[59] Bradley S Davidson, Michael L Madigan, Steve C Southward, and Maury A Nussbaum. Neural control of posture during small magnitude perturbations: effects of aging and

localized muscle fatigue. *IEEE Transactions on Biomedical Engineering*, 58(6):1546–1554, 2010.

[60] Herman Van Der Kooij and Erwin De Vlugt. Postural responses evoked by platform pertubations are dominated by continuous feedback. *Journal of Neurophysiology*, 2007.

[61] IM Schut, JH Pasma, JMB Roelofs, V Weerdesteyn, H van der Kooij, and AC Schouten. Estimating ankle torque and dynamics of the stabilizing mechanism: no need for horizontal ground reaction forces. *Journal of Biomechanics*, page 109813, 2020.

[62] Christine Chevallereau, Dalila Djoudi, and Jessy W Grizzle. Stable bipedal walking with foot rotation through direct regulation of the zero moment point. *IEEE Transactions on Robotics*, 24(2):390–401, 2008.

[63] Pietro Morasso. Centre of pressure versus centre of mass stabilization strategies: the tightrope balancing case. *Royal Society open science*, 7(9):200111, 2020.

[64] Andrea Tigrini, Federica Verdini, Sandro Fioretti, and Alessandro Mengarelli. Center of pressure plausibility for the double-link human stance model under the intermittent control paradigm. *Journal of Biomechanics*, 128:110725, 2021.

[65] Alessandra Bottaro, Maura Casadio, Pietro G Morasso, and Vittorio Sanguineti. Body sway during quiet standing: Is it the residual chattering of an intermittent stabilization process? *Human Movement Science*, 24(4):588–615, 2005.

[66] Yasuyuki Suzuki, Akihiro Nakamura, Matija Milosevic, Kunihiko Nomura, Takao Tanahashi, Takuyuki Endo, Saburo Sakoda, Pietro Morasso, and Taishin Nomura. Postural instability via a loss of intermittent control in elderly and patients with parkinson's disease: A model-based and data-driven approach. *Chaos: An Interdisciplinary Journal of Nonlinear Science*, 30(11):113140, 2020.

[67] Andrea Tigrini, Federica Verdini, Sandro Fioretti, and Alessandro Mengarelli. Long term correlation and inhomogeneity of the inverted pendulum sway time-series under the intermittent control paradigm. *Communications in Nonlinear Science and Numerical Simulation*, 2022.

Chapter 3

Muscle Onset Detection

3.1 Introduction

Muscle onset detection (MOD) problem plays a fundamental role in different applications in the field of biomechanics and motor control. Indeed, knowing the instant at which a certain muscle passes from a relaxed to a contracted state, and vice versa, is a basic kind of information that can be extracted from surface electromyography (sEMG) signals through the use of many different algorithms [1, 2, 3, 4, 5, 6, 7, 8, 9, 10]. Before to enter into the technical details, it is important to give a perspective regarding the needs behind the development of such techniques and the role that the aforementioned information plays in the clinical and application scenario. Rhythmic movements, controlled voluntary or involuntary, such as gait or breathing, are just examples where the timing of muscle activation can characterize the physiological state of the subject [11, 12]. In neuro-physiology, the evaluation of muscles activation latency with respect to a given external perturbation, i.e. postural reflex, is commonly employed to characterize the pathological group versus the control group [13, 14]. In such clinical applications, automatic methods of MOD, can thus be employed to render the analysis more direct, possibly merging clinician experience with robust detection algorithms [15].

As literature highlights, sEMG has been widely employed in wearable robotics and MOD found application in different assistive technologies [16, 17]. In pattern recognition myoelectric control, for instance, the onset detection analysis plays a key role for automatizing the segmentation of sEMG epochs upon which signal features can be extracted [18]. Further, end-effector rehabilitation robots, exoskeletons, and assistance robots employed onset detection to trigger their assistive action [19, 20, 21, 22]. Other sensing technologies such as

electroencephalography (EEG) or inertial measurement unit, can be used to trigger assistive devices[23, 24, 25]. However as emerged in [26], even a simple threshold based detection algorithm constitute a viable alternative to more cumbersome solutions such as the EEG. Moreover the use of sEMG data is recommended in order to obtain accurate detection of the movement onset [25].

It is worth noticing that, threshold based or other detection algorithms, tend to degrade their performances when the signal to noise ration (SNR) decreases. Despite this can seem a trivial consideration, many practical circumstances present the aforementioned detrimental condition. Indeed, the weakness or alteration of muscle activity due to pathology affecting the neuromuscular system such as stroke, spinal cord injuries or Duchenne dystrophy could render more difficult the MOD [27, 28, 29, 30]. Since this can negatively impact on the design of assistive solutions based only on sEMG, literature reports studies in which information fusion paradigm, i.e. combining sEMG with other type of information, could be employed for managing the human-robot interaction [17, 25, 31, 32]. However, different linear and non-linear filtering solutions were proposed to mitigate the noise effect in MOD algorithms such as Wiener filter, wavelet transform, subspace approaches and Teager-Kaiser energy operator (TKEO) [28, 33, 7, 6]. Despite the signal processing techniques reported are just a limited portion of a continuous growing research field, it is well acknowledged that TKEO constitutes a preconditioning signal block used in many different detection schemes, ranging from threshold to statistic-based algorithms [34, 6, 4, 9]. Considering that, in this work, attention was given to the use of TKEO and its extended version, that is ETKEO, as tools for sEMG signal preconditioning [16]. The latter represents an attempt to generalize the definition of the TKEO by introducing three time-lag coordinates that can be tuned to cope with the intrinsic variability of the sEMG signal. Such extended version can improve the localization of changes of instantaneous amplitudes in the signal if compared to TKEO [35, 16]. Indeed, for highly corrupted sEMG signal, the TKEO in its simple version might not consistently improve the performances of the MOD algorithms taken into account [28, 4], even showing limited sensitivity to different SNR values [34].

Thus, in the Methods section of this chapter, state of the art and modern muscle onset detection methods are presented. More in detail, the MOD algorithms introduced are muscle onset detectors based on threshold (TP), and wavelet transform (WLT) [16, 1, 7]. Regarding the statistics-based algorithm used in this study, profile likelihood maximization (PLM) and its fast version are described [4, 9] and finally the well known CUSUM is reported

[36, 37, 10]. A further section of this chapter describes the TKEO and ETKEO signal preconditioning filters that can be applied before to use a specific MOD algorithms. A possible characterization of the ETKEO time-lag coordinates following [16] is also reported. Then, in the Results section, the comparisons between TKEO and ETKEO preconditioning using the algorithms cited above over a public available dataset containing sEMG signals SNR$\leq$8dB are shown.

3.2 Muscle onset detection algorithms

3.2.1 Threshold-based algorithm

The first MOD technique analyzed regards the threshold based method [3, 6, 4]. Such procedure presents the following steps. As first, the sEMG signal can be preconditioned through TKEO or ETKEO, then, it goes through rectification and thresholding steps [6, 4]. The threshold can be defined by the following equation:

$$\Gamma = \mu_{baseline} + h \cdot \sigma_{baseline} \tag{3.1}$$

where $\mu_{baseline}$ and $\sigma_{baseline}$ indicate respectively the mean and the standard deviation (STD) of the rectified signal baseline pattern [6, 4], while h is a scaling factor that can be selected in the interval $h \in [3; 7]$ without affecting the accuracy of the threshold-based detection algorithms [4], in this work $h = 5$ was fixed [16]. After the thresholding, a rough binary signal of 0 and 1 is obtained, giving 1 when the signal is greater or equal to the threshold, or 0 in the other case. Then, such sequence can be cleaned with a post-processor as that proposed in [1]. This should reduce the false transitions detected. Finally the vector $\hat{\mathbf{t}}_{tran}$ containing the estimated instants at which each transition occurred is obtained. In the rest of this chapter, the procedure above-described is referred as threshold and post-processor detection algorithm (TP).

3.2.2 WLT-based algorithm

The thresholding step is employed also in the formulation of the WLT algorithm proposed in [7]. A certain number of approximation levels a for the wavelet filter bank is selected [7].

Then, the threshold method is applied to the signal:

$$\eta(t) = \max_{a}\{WLT(a,t)\} \tag{3.2}$$

in other words, the max at any given time of the approximation levels of the filter bank is taken. As reported by the authors [7], given a portion off the noise baseline where no activation is present, it is possible to define:

$$\begin{cases} M = \max\{\eta(t)\} \quad \text{for } 0 < t < T_{noise} \\ th = \gamma \cdot M \end{cases} \tag{3.3}$$

where M is the maximum of the signal (3.2) taken from the baseline pattern lasting from for T_{noise} s. The threshold th is defined as the product between M and the adjusting constant $\gamma > 1$ [7]. Thus, the sEMG signal once preconditioned [16], undergoes trough the steps here reported. Additional details regarding the theory behind the methodological aspects of the wavelet transform and parameter selection can be found in [7].

3.2.3 Likelihood maximization algorithms

The two algorithms introduced until now work without any statistical assumption, since the decision of attributing to a signal sample the label 1 or 0 based on a threshold defined as in (3.1), (3.3) corresponds to label a portion of the empirical signal distribution as 1 or 0. However, it is worth noting that, the idea of using signal distribution as a model to include in a detection algorithm is widely used.The CUSUM or Maximum-Likelihood (ML) algorithms are typical examples of statistical detectors [36, 38, 4]. In general the latter class of detector provide robust and accurate performances, however, most of the ML algorithms reported in literature employ a gaussian distribution model for the sEMG signal [8, 38].

This can be a too restrictive assumption, indeed as highlighted in [4, 16], the use of energy operators such as TKEO or ETKEO should render the signal probability density function (PDF) far from a gaussian one, this was further confirmed analytically in [39]. For this reason a Profile Likelihood Maximization (PLM) approach that accounts for different data distributions can be a suitable choice when on deals with detection problems [4]. The working principle behind PLM for MOD assumes that two different PDF, respectively for the signal baseline and activation segments, are associated to the entire observations. An objective

function can be defined as follows:

$$\mathcal{L}_k(k) = \sum_{i=1}^{k} \log f_1(x[i]; \hat{\boldsymbol{\theta}}_1(k)) + \sum_{j=k+1}^{N} \log f_2(x[j]; \hat{\boldsymbol{\theta}}_2(k)) \tag{3.4}$$

where $x[i]$ is the i-th data point of the sEMG signal, which sample index is given by $k = 1 \dots N$. The $\hat{\boldsymbol{\theta}}_1(\cdot))$ and $\hat{\boldsymbol{\theta}}_2(\cdot))$ are the ML estimates of the parameters characterizing, in this case, the PDFs of the baseline and of the activation epoch, i.e., $f_1(\cdot;\cdot)$ and $f_2(\cdot;\cdot)$ respectively.

From what emerges by previous studies [4, 9], a good model for both baseline and activation segments, once energy operators are used to condition the sEMG signal is the Laplacian distribution [4, 16, 9], more formally:

$$f(x) = \frac{1}{2b} \exp\left(-\frac{|x-\mu|}{b}\right) \tag{3.5}$$

in this case, the two coefficients μ and b are the components of the vectors $\hat{\boldsymbol{\theta}}(k)$ in (3.4). Laplace distribution presents closed form estimates given by:

$$\hat{\mu} = \text{median}(\mathbf{x}); \quad \hat{b} = \frac{1}{N} \sum_{i=1}^{N} |x[i] - \hat{\mu}| \tag{3.6}$$

where $\mathbf{x}$ represents a given signal epoch.

Broadly speaking, PLM looks for the argument that maximizes the profile likelihood function (3.4), which represents the most likely instant where the signal, previously described by the baseline PDF, appears to be better represented by the PDF of the activation pattern. Thus, the k at which the maximum of the likelihood function is obtained, represents the detected muscle onset [4, 9, 16]. PLM-based algorithm presented in [4], compute an exhaustive research to find the maximum of the likelihood function. This aspect could introduce delay for real time applications that limits the usability of such technique. For this reason, a new version of the algorithm named PROLIFIC was presented in [9]. PROLIFC introduces the use of discrete Fibonacci search (DFS), which theoretically requires $\log N$ steps with respect to the N required by the exhaustive form. Since DFS does not constitute a key aspect for this work, the reader interested to the technical implementation of such searching procedure is referred to [9].

The last algorithm employed in this work is the CUSUM algorithm [10, 36], which found applications in many different detection problems [36]. Let consider the time-series $\mathbf{x} = (x[1], x[2], \dots, x[k], \dots, x[N])$ made by independent observations, and consider also

that the process can be modeled through a PDF characterized by the parameters vector $\boldsymbol{\theta}$. If a change occurs, the concept of stationarity drops and it is plausible that $\boldsymbol{\theta}$ assumes other values. To detect the point at which such change happens, the algorithm works in the following way: given the PDFs $f_0(x_k;\boldsymbol{\theta}_0)$ and $f_1(x_k;\boldsymbol{\theta}_1)$ of the hypothesis H_0 and H_1 (respectively related to the relaxed and contracted phase of the muscle [38], the log-likelihood ratio between them is given by

$$s_k = \log \frac{f_1(x_k;\boldsymbol{\theta}_1)}{f_0(x_k;\boldsymbol{\theta}_0)} \tag{3.7}$$

Thus, one can define the cumulative sum function as follows:

$$CS_k = \sum_{i=1}^{k} s_i \tag{3.8}$$

while the detection function is given by:

$$g_k = CS_k - \min_{1\leq j\leq k} CS_j \tag{3.9}$$

Then, a stopping time criterion can be defined by assuming a threshold over g_k:

$$k_a = \inf\{k \geq 1 : g_k \geq h\} \tag{3.10}$$

where k_a is the sample index, estimated by the CUSUM, for which the transition is occurred. Another possibility is to take the k for which the CS function presents a minimum. Additional information can be found in [10, 36, 37].

All of these technique accept a signal precondition phases, as previously reported. Thus, in this chapter, the effects of the TKEO and ETKEO over the methodologies proposed in terms of performances are analyzed. In the next sections an overview of the TKEO and ETKEO is presented. Moreover, for the latter filter, a time-leg selection criterion is presented.

3.3 Nonlinear signal energy operators

3.3.1 The TKEO in EMG signal preconditioning

The TKEO represents a widely used nonlinear filter in many detection problems and formally it is defined in both continuous and discrete form [40, 41, 39]. The latter is the most

popular for its applicability in digital signal processing applications [41]. Given the sampled time-series $x[\cdot]$, TKEO can be computed through the following equation:

$$\Psi[n] \triangleq x[n]^2 - x[n+1]x[n-1] \tag{3.11}$$

where $x[n]$ indicates the n^{th} signal sample. It can observed that for computing $\Psi[n]$ is required the information contained in a symmetric time-window $[n-1; n+1]$, with 1 representing a time lag. Thus $\Psi[n]$ spans three samples of the signal in a non-linear form, providing a local description of its energy content [41, 40]. Kumaresan et al. [42] introduced a different way to compute $\Psi[n]$ that makes possible to see at the energy operators as the determinant of random matrices. This can be referred as the matrix framework, and it was adopted in other works [43, 41]. Hence the TKEO is computed as:

$$\Psi[n] = \det\left(\begin{bmatrix} x[n] & x[n+1] \\ x[n-1] & x[n] \end{bmatrix}\right) \tag{3.12}$$

3.3.2 The extended TKEO

Based on the matrix framework, an extension of TKEO was presented in [35] and is named ETKEO. It is obtained through the determinant of a signal embedded matrix of dimension $(d \times d)$, computed by the following procedure [35]. The signal sequence $x[\cdot]$ is sliced in vectors of length d, as defined in (3.13):

$$\mathbf{x}_n = \begin{bmatrix} x[n] & x[n-m] & \dots & x[n-(d-1)m] \end{bmatrix}^T \tag{3.13}$$

where m and d are integer time-lag values, with d necessarily greater then 1. Thus, introducing a further embedding integer time-lag $s > 0$, it is possible to fix the sliced vectors in the matrix $\mathbf{X}_n$ [35]:

$$\mathbf{X}_n = \begin{bmatrix} \mathbf{x}_n & \mathbf{x}_{n+s} & \dots & \mathbf{x}_{n+s(d-1)} \end{bmatrix} \tag{3.14}$$

as previously highlighted, once $\mathbf{X}_n$ at time instant n is available, ETKEO is computed as the determinant of that matrix (3.15).

$$\Psi_{(d,m,s)}[n] = \det(\mathbf{X}_n) \tag{3.15}$$

$\Psi_{(d,m,s)}[\cdot]$ presents three degrees of freedom in terms of time-lag coordinates, namely d, m and s, that can be opportunely selected to characterize the nonlinear filter structure. To be noted, ETKEO generalizes TKEO when $d = 2$, $m = 1$ and $s = 1$ [35]. It should also be observed that the computation of ETKEO at time n requires a signal time-window of $[n - (d-1)m; n + (d-1)s]$ samples.

In this view, it is important to note that the ETKEO computational parameters can significantly affect its real-time practical feasibility in two main ways: the first one regards the computational load and buffering costs, while the second one involves boundary effects. Regarding the former, if one considers the structure of the embedded matrix for the ETKEO computation in (3.14), given a value of d equal to 33 as in [35], at any given time instant n, the dimension of such matrix is (33×33), thus leading to a computational cost for calculating the determinant much higher with respect to the case $d = 2$ (approximately 10 time greater with MATLAB software running on a MacBookPro IntelCore i5). Moreover, for computing a single ETKEO sample, a sEMG analysis window of length $(d-1)(s+m)$ is required. This means that even for limited increases of s and/or m, the above mentioned window would dramatically enlarge, leading to an increase in the buffering demands for the signal analysis and window shifting. As reported in a number of different studies [44, 45], the updating rate for motion intent recognition, based on myoelectric activation patterns, was typically 100 ms. Therefore, for large values of d the length of the analysis window could compromise real-time controllability of the triggered device, due to excessive control delays [46].

The second side effect related to the ETKEO computational parameters involves the ETKEO boundary description. Due to its formulation, for the n-th sample computation, the ETKEO requires a signal epoch equal to $[n - (d-1)m; n + (d-1)s]$. On one hand, this prevents the definition of the ETKEO at the tails of the original signal: for instance given a N-length signal, the ETKEO can not be defined for the first $(d-1)m$ samples, while the last sample for which the ETKEO can be defined is the $N - (d-1)s$ sample. This means the higher is d value, the higher is the number of samples where the ETKEO can not be computed, due to the fact that the ETKEO results not defined on a total of $(d-1)m+(d-1)s$ samples, located at the signal tails. On the other hand, as a secondary effect in a real-time scenario, the upper limit of the signal epoch needed for ETKEO computation requires to wait at least $(d-1)s$ samples for the forward computation of a single ETKEO sample. This could lead to an excessive increase of the average controller delay, making its real-time use a challenging issue [46]. Thus, an opportune tuning of the ETKEO time-lags necessarily has

to account to the signal properties and application in which the filter operates.

3.3.3 ETKEO Parameters Selection

Based on the considerations reported in the previous section, the problem of ETKEO lags selection can be thought as an optimization procedure with the objective of minimizing the detection error in sEMG transitions [16]. Concretely, the procedure constitutes of three steps:

- Generate synthetic sEMG signals with known SNR and transition instants.
- Employ a detection algorithm.
- Set an opportune cost function to be optimized.

In literature, many EMG signal models were developed due to the complex nature of the myoelectric signal, each of those methods took into account different physical and morphological properties of the EMG signal [47, 48, 49]. Due to the need for a controlled environment for algorithms prototyping, the use of synthetic signals in studies related to EMG onset detection is a common and widely used procedure [1, 7, 50, 51]. In this study, the surface EMG model originally formulated in [52], and modified accordingly with [1], was adopted. Such model was selected for two main reasons: firstly, it permits a simple tuning of the SNR parameter, secondly, despite it represents one of the first proposed method for sEMG data simulation, the model results still adopted in studies focused on testing feature extraction methods and onset detection algorithms [1, 50, 53].

According with [16], sEMG realizations of 1 s (1000 samples) with two transitions and SNR values: 1.4, 2.1, 3, 5 and 8 dB are generated. Regarding the detection procedure, the TP algorithm proposed in section 3.2 is taken into account during the lag selection procedure for estimating the $\mathbf{t}_{tran}$ of the synthetic sEMG signals. Based on what highlighted in 3.11, to ensure that ETKEO could be defined at the tails of the sEMG signals, d is fixed equal to 2, while m and s are kept free to be optimized [16]. In order to account for the different SNR values adopted, a cost function made by a smooth and non-smooth part is formulated. Such objective function is defined with respect to the integer vector $\Theta = \begin{bmatrix} m & s \end{bmatrix}^T$, whose components are the lag-coordinates in equation 3.15. The smooth behavior of the objective is defined through:

$$J = T_{a.e.}^2 + \boldsymbol{\lambda}^T \boldsymbol{\Theta} \tag{3.16}$$

where the first term accounts for the sample errors in detecting the transitions and is based on:

$$T_{a.e.} = ||\mathbf{t}_{tran} - \hat{\mathbf{t}}_{tran}||_1 \tag{3.17}$$

where $\mathbf{t}_{tran}$ and $\hat{\mathbf{t}}_{tran}$ are respectively the true and estimated vectors containing the instants at which each transition occurred. The second term of (3.16) represents a regularization component, which avoids a selection of a large value for both m and s. This has been obtained by the dot product between $\boldsymbol{\lambda}$ and $\boldsymbol{\Theta}$. To give at the regularization term an opportune weight within the optimization procedure, $\boldsymbol{\lambda} = \begin{bmatrix} 10 & 10 \end{bmatrix}^T$ is set.

The non-smooth behavior instead is generated by fixing the term M to large value, i.e. 10^5, allowing to penalize forbidden cases such as:

- the selection of large value for m and s with a consequent impossibility to describe the original signal through $\Psi_{(2,m,s)}$ at the tails.
- not guaranteed enough samples to describe the baseline through $\Psi_{(2,m,s)}$.
- number of detected transitions greater than the number of the actual ones.
- $\mathrm{T}_{a.e.} \geq \epsilon$, with $\epsilon = 5$ ms.

When all the forbidden cases have been avoided, the cost function drops in the smooth portion of the search space, returning the value J described in(3.16).

A variant of the genetic algorithm (GAL) proposed in [54] and implemented in MATLAB 2019a, Global Optimization Toolbox, is used to deal with the integer optimization and for each of the aforementioned SNR value, 100 GAL runs are performed. Each GAL run stop when the average relative change in the best fitness function value, over 400 generations, is less than or equal to a tolerance value of 10^{-6}.

Being $\boldsymbol{\Theta}$ made by m and s, their weighted averages m_{SNR} and s_{SNR}, for each SNR value were computed as:

$$\boldsymbol{\Theta}_{SNR}[k] = \frac{\sum_{i=1}^{100} \boldsymbol{\Theta}_i[k] \cdot T_{a.e.}(i)}{\sum_{i=1}^{100} \boldsymbol{\Theta}_i[k]} \qquad \text{for } k = 1, 2 \tag{3.18}$$

where k indicates the component of the vector $\boldsymbol{\Theta}$, while i is the index related to the optimization trial. The ETKEO time-lags selected by the optimization, i.e. the components

of $\boldsymbol{\Theta}_{SNR}$, are reported in Table 3.1.

Table 3.1: Optimal m and s obtained through the procedure above-reported with respect to the different signal SNR considered.

SNR (dB)	1.4	2.1	3	5	8
m_{SNR}	11	11	9	9	7
s_{SNR}	8	7	8	6	5

The lag coordinates reported in Table 3.1 can be used to characterize the ETKEO in different SNR conditions [16].

In order to study the preconditioning effects of ETKEO over the detection algorithm reported above with real data is important to consider sEMG signals with transitions annotation made by experts and possibly ranging a wide SNR range. Thus, for such purpose, in the next section the dataset employed and its partition are presented.

3.4 Real sEMG dataset for MOD

The dataset used in this study was originally presented by Tenan et. al [5]. It contains 103 sEMG signals for which muscle onset transition was labeled by three experts in a randomized and double blind fashion. Each expert visually determined the muscle onset transition in a given signal, repeating the labeling after 24 hours. While the inter-determination period was never longer than 7 days[5]. This dataset was also used in [4, 9] to compare among different detection algorithms.

Since the signals provided a large spectrum of SNR ranges, the sEMG signals with their respective true onset transitions are shunted following the SNR-based partition shown in Table 3.2, resulting in a total of 52 signals. To partition the dataset, knowing the instant at which transition occurred for each sEMG (see Figure 3.1), it was possible to distinguish baseline and activation epochs to compute the SNR; this permitted to exclude those signals having SNR $>$ 8 dB. Then, the selected signals were preprocessed with a second order, zero-phase, Butterworth band pass filter with cut-off frequencies at 30 Hz and 450 Hz.

The preconditioning effects of ETKEO with respect to TKEO were evaluated applying

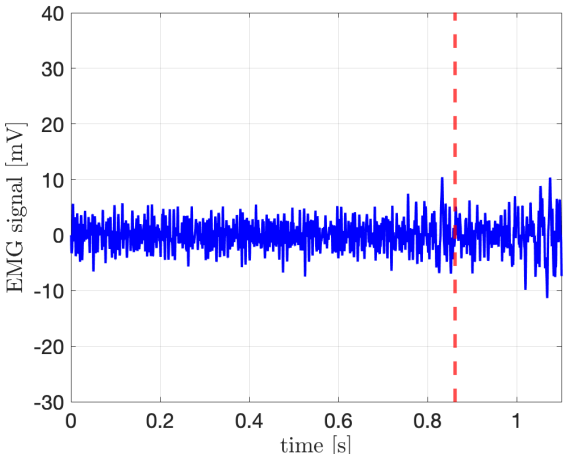

(a)

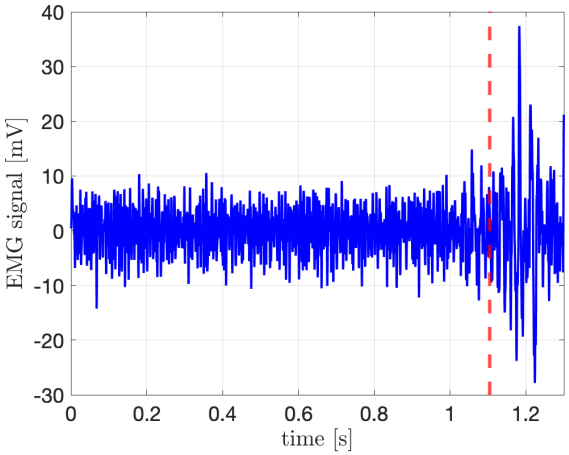

(b)

Figure 3.1: Example of raw sEMG signals extracted from [5] employed with different SNR values: for SNR= 1.4 dB (Panel 3.1a) and SNR= 7.2 dB (Panel 3.1b). The dashed red line indicates instant at which onsets occurred.

Table 3.2: Partitions of the testing dataset.

SNR Bands (dB)	n° of epochs
≤ 2	6
$2 \div 4$	10
$4 \div 6$	15
$6 \div 8$	21

both filter to a same sEMG signal and observing the performances for a given onset detection method [16]. For each SNR band the ETKEO filter was characterized according to the optimal values reported in Table 3.1. Absolute detection errors, in terms of mean and median

values were computed for each preconditioning method. To check the significance of the the improvements obtained by using ETKEO in substitution to the TKEO, the normality of error samples distributions was evaluated by means of the Kolmogorov-Smirnov test for all the dataset. Student's t-test or the signed variant of the Wilcoxon rank-sum test, were used when errors were respectively gaussian or not-gaussian distributed. Both tests are specifically suited for dealing with dependent (paired) samples [55]. Significance was set at 5%.

3.5 Results

Table 3.3 shows the detection errors comparison between the TKEO and ETKEO signal preconditioning. For each MOD algorithm, i.e., TP, WLT, CUSUM, PROLIFIC, the mean and median absolute errors are computed. Moreover, for completeness, also the standard deviation and the interquartile range are presented (Table 3.3). Finally the improvement carried by using ETKEO with respect to TKEO is additionally showed to facilitate the reader in the analysis of the results.

As one can observe in Table 3.3, the TP shows decreasing detection errors both in mean and median term for the two nonlinear filtering procedures employed when the SNR increases. However, despite this cannot clearly indicate the preference for a specific preconditioning filter, one can observe that, for each SNR range, the standard deviations obtained are always lower for ETKEO, suggesting a global increase in the detection accuracy also in highly detrimental conditions. The latter aspect is strengthened by the significantly lower ($p = 7.9 \cdot 10^{-4}$) detection error of ETKEO with respect to TKEO. Another element that confirm this aspect lies in the improvement magnitudes, which grows in relation to the decreasing of the. Thus the lower is the SNR the greater is the advantage of use ETKEO preconditioning.

Regarding the WLT algorithm, it shows a decreasing error trend in median terms. By compering the first and the last SNR bands, similar improvements of about 40% are obtained. In any case, the global improvement of the ETKEO with respect to the TKEO resulted statistically significant, with $p = 0.019$.

The CUSUM algorithm benefits from the use of the ETKEO signal preconditioning, showing a percentage improvements in all the cases not lower than 85%. Significance of the improvement is guaranteed by $p = 1.4 \cdot 10^{-7}$, showing the highest improvement of using ETKEO over TKEO among the four considering algorithms (91.8%). Finally, ETKEO

significantly decreases the detection error also for a robust algorithm as the PROLIFIC ($p = 5.3 \cdot 10^{-5}$), which appears to perform globally better than the other methods. Indeed it presents the lowest median error (54.9 ms) and an almost regular increase in percentage improvements, which follows the increase in the SNR value.

Table 3.3: Absolute onset detection errors for each considered SNR band in terms of mean, median, STD, 25-percentile and 75-percentile. All values are expressed in milliseconds. For each algorithm (TP, WLT, CUSUM and PROLIFIC) the last row reports the global detection behavior considering the whole dataset. In the last column the improvement of the optimized ETKEO over TKEO is shown, computed with respect to the median error values. Symbols ‡ and † indicate $p < 0.01$ and $p < 0.05$, respectively.

SNR range	Mean (ms)		SD (ms)		Median (ms)		25-Perc (ms)		75-Perc (ms)		Improvement (%)
	ETKEO	TKEO	ETKEO	TKEO	ETKEO	TKEO	ETKEO	TKEO	ETKEO	TKEO	
TP											
≤ 2	243.7	733.5	381.0	456.4	92.5	765.4	42.9	400.9	199.2	1042.9	87.9
$2 \div 4$	154.0	225.5	92.0	115.0	125.0	231.2	87.9	121.1	245.6	309.1	45.9
$4 \div 6$	101.3	201.3	106.2	266.9	58.6	104.0	27.6	47.8	146.6	231.9	43.7
$6 \div 8$	116.9	182.3	229.8	305.3	41.5	69.8	25.0	28.3	94.2	107.5	40.6
≤ 8	134.2	259.7	203.6	330.1	69.3	109.6	31.5	45.2	146.5	304.7	$36.7^{\ddagger}$
WLT											
≤ 2	139.8	504.5	66.9	578.5	133.3	208.3	126.5	127.4	197.7	861.3	35.9
$2 \div 4$	145.9	191.5	146.3	254.5	95.0	121.3	33.7	30.3	188.5	191.9	21.7
$4 \div 6$	165.2	248.5	272.5	335.4	104.9	122.6	31.7	71.2	128.5	223.4	14.4
$6 \div 8$	92.2	158.8	170.2	311.4	35.2	61.0	7.8	19.4	130.5	122.4	42.4
≤ 8	129.1	230.9	192.3	352.9	78.6	116.9	25.2	33.0	146.5	192.9	$32.8^{\dagger}$
CUSUM											
≤ 2	126.6	827.1	91.9	584.3	149.7	999.0	90.8	153.8	239.7	1182.1	85.0
$2 \div 4$	222.8	1143.8	170.4	489.2	148.7	1134.5	128.9	883.3	298.3	1483.9	86.9
$4 \div 6$	93.8	708.1	92.0	492.2	55.7	793.5	23.4	257.1	131.2	1124.8	93.0
$6 \div 8$	65.5	618.0	54.8	579.2	48.8	729.0	32.2	35.9	80.9	1115.2	93.3
≤ 8	115.5	769.2	114.8	558.7	78.6	958.0	40.3	100.3	152.6	1181.4	$91.8^{\ddagger}$
PROLIFIC											
≤ 2	303.4	357.9	519.4	534.6	104.0	111.1	56.6	57.6	157.7	409.2	7.2
$2 \div 4$	185.5	460.0	156.8	392.2	136.0	396.7	124.5	140.1	173.3	746.1	65.7
$4 \div 6$	123.4	371.4	249.6	453.3	50.8	93.8	20.7	40.4	88.6	680.9	45.8
$6 \div 8$	39.4	229.7	32.7	462.0	36.6	135.7	11.7	30.5	54.8	884.7	73.0
≤ 8	122.2	410.4	236.1	443.5	54.9	137.9	24.9	46.6	125.5	756.6	$60.2^{\ddagger}$

3.6 Discussion

In this work, the ETKEO and TKEO were employed for conditioning the sEMG signal before applying state of the art onset detection methods. This was done to verify whether ETKEO outperforms the commonly employed TKEO to enhance the change point detectability present in the signal. Since the ETKEO presented a more flexible structure with respect to TKEO, a characterization method to obtain time-lag coordinates has been proposed. Among the detectors employed, attention was given to TP and WLT since they are commonly employed [26, 7]. Moreover, two methods based on statistical modeling of the signal and time-series change point phenomenon were employed, i.e. PROLIFIC and CUSUM. As highlighted in literature [4, 38], the algorithms developed through the latter approach generally result in more accurate detectors with compared to threshold-based ones. However, effects of signal preconditioning step in statistical based methods were analyzed in [4, 9]. Thus, such investigation deserved an adequate analysisin order to assess the TKEO and ETKEO signal conditioning effects on the performance of the above mentioned detectors.

Regarding the use of TP algorithm combined with ETKEO, hereafter indicated as ETKEO-TP, it showed substantial improvements (Table 3.3) for all the considered SNR ranges with respect to TKEO (TKEO-TP). Results suggest a great advantage of using ETKEO-TP in highly noise conditions. Indeed, for SNR$\leq$2 dB the ETKEO-TP detection outperformed TKEO-TP of about 85%. On the other hand, for the other SNR ranges, the improvements remained still higher than 40%.

Despite its simplicity, the ETKEO-TP detection algorithm showed results (Table 3.3) comparable with more robust algorithms, such as Wavelet-based (WLT) and Bayesian-based change point detection methods [4]. In particular, ETKEO-TP applied over 52 signals with SNR $\leq$ 8 dB gave results comparable with Bayesian approach [4], while outperformed the WLT method both in mean (134 ms vs 235 ms) and median error terms (69 ms vs 209 ms). It should be highlighted that in [4] results were obtained considering the original entire dataset [5], where 51 additional signals having SNR $\geq$ 8 dB were included.For this reason, a direct comparison with respect to [4] cannot be done. However, the considerations stated above confirm the goodness of the improvements obtained in this work.

Moreover, for the whole dataset made by 52 signals with SNR $\leq$ 8 dB, ETKEO-TP globally outperform TKEO-TP of about 36%, showing significant differences over the detection errors distributions (Table 3.3). A possible interpretation behind such improvement could lie on

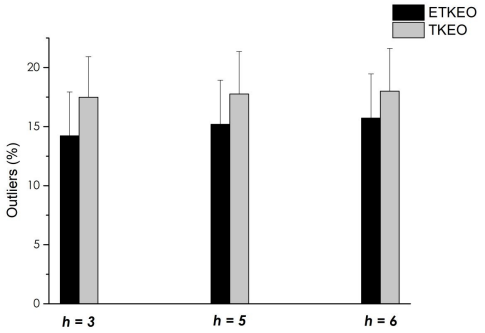

Figure 3.2: The figure shows the bar plots of the outliers percentage among all the epochs for the dataset analyzed, preconditioning the signal with TKEO and the ETKEO with optimal time lags. The three classes differs for the choice of h for computing the threshold.

the properties of the rough binary activation signal at the output of the thresholding step, which was post processed. By knowing the point at which the transition occurred, it was possible to count the number of outliers (O class), i.e. those samples that belonging to the baseline produce 1, or belonging to the activation pattern produce 0. By defining the post processor as in [1], it can be easily appreciated that the percentage of the samples belonging to the O class over their relative epoch length negatively affects the performances of the post processor.

To better explain this aspect, it is possible to observe that for the TP algorithm with h=5, the percentage of outliers with ETKEO remained lower with respect to TKEO preconditioning (figure 3.2), confirming once again that outliers percentage highly impacts on the post-processor output, and a low level of outliers can improve the accuracy of a threshold-based MOD procedure. Incidentally, it is worth noticing that, as highlighted in Figure 3.2, the outliers percentage did not depend on the specific h value used to threshold setting (see (3.1)), supporting that its choice was not crucial for the detection algorithm performances [4].

The WLT method showed the lowest percentage improvements for all the SNR bands and also for the whole dataset (Table 3.3). Nevertheless, the variability of the onset errors, mirrored by the SD values and the 25- and 75-percentile, seemed to greatly reduce with ETKEO preconditioning, leading to a more consistent onset detection measurements. For low SNR ranges, the percentage improvements remain in any case limited and below those obtained for the ETKEO-TP. This aspect underlines the intrinsic reliability of the WLT detector, which could be linked to the *a priori* assumptions on the sEMG signal, at the

base of the algorithm development [7]. However, the above mentioned reliability of the WLT method appeared to have a global less impact on its performances with respect to the ETKEO-TP, since the detection errors (mean and median values) remain comparable taking into account the whole dataset (SNR$\leq$ 8 dB, Table 3.3).

For what concerns the CUSUM algorithm, it appeared to improve in all the considered SNR bands (Table 3.3) with respect to the other methods, taking the highest advantages from ETKEO preconditioning. These significant improvements could be outlined bearing in mind that the CUSUM employed in the present study relies on the variance changes between baseline and activation patterns and that the energy operators basically increase the SNR, reducing the noise variance. The ETKEO, with its time-lags > 1, likely leads to weight more the uncorrelated nature of the noise, eventually lowering the baseline variance while the TKEO, being a more local descriptor of the signal, seems to be less suitable when used together with the CUSUM algorithm [37].

Regarding PROLIFIC algorithm, significant differences between ETKEO and TKEO errors were observed for the whole dataset (Table 3.3), considering that the improvements obtained through ETKEO signal preconditioning rather than TKEO is about 60%. However, for SNR$\leq$2 dB, the ETKEO carried out the lowest improvement of 7.2%. The latter underlines two relevant aspects: firstly, this supports the usefulness of ETKEO preconditioning when dealing with poor quality sEMG signals [29]. On the other hand, the use of ETKEO, originally tuned for a threshold detector, appears still able to enhance the performances of a robust and widely tested technique such as a PLM-like detector [9].

A possible partial explanation of this aspect could ground on the assumptions underling to PROLIFIC algorithm, where the PDFs of baseline and activation patterns were modeled as Laplace distribution [4, 9]. Therefore, comparing through Q-Q plot representation the Laplace distribution versus the PDF of both the baseline and activation patterns, for a representative sEMG signal (SNR range 4$\div$6 dB, Fig. 3.3), emerges that a more markable divergence from the straight line was presented when TKEO preconditioning is applied. This indicates that ETKEO provides a PDF with a shape closer to a Laplace distribution, and thus it better meets the assumptions behind the PROLIFIC algorithm [4, 9].

In particular, the PDF characteristics of the preconditioned signals seem to play a role also in the improvements of the TP algorithm, despite its different nature with respect to a PLM-based method. Since the former does not foresee any *a priori* knowledge of the signal PDF, in TP algorithm it is important to have a limited number of outliers in the

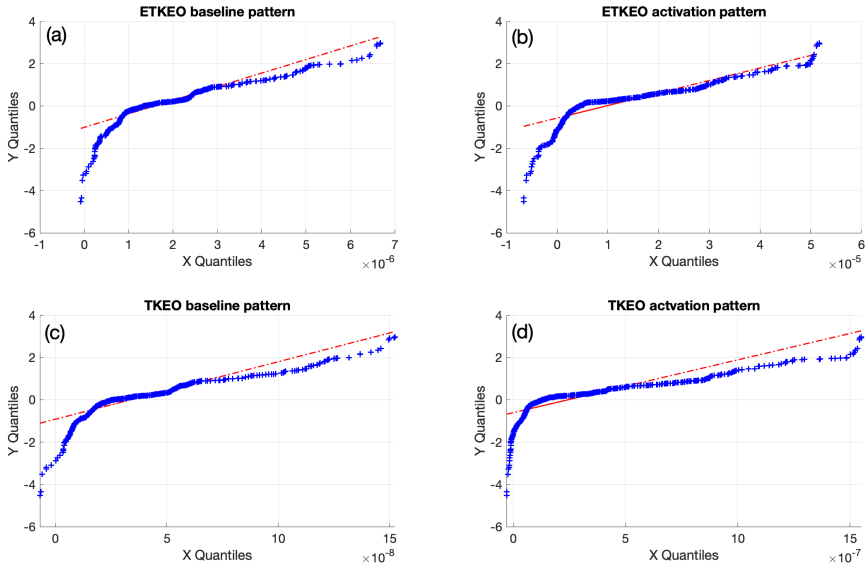

Figure 3.3: Q-Q plots of two patterns of a signal belonging to the range 4≤SNR≤6 preconditioned with TKEO and ETKEO against Laplace distribution. Plot (a) corresponds to the sEMG baseline preconditioned with ETKEO, plot (b) assumes the same signal precondition, but accounting for the activation pattern. Plot (c) and (d), instead consider the TKEO signal preconditioning procedure.

rough binary signal, in order to render the algorithm less prone to produce false transitions. Considering the PDF of a signal, a low number of outliers is mirrored by a reduced thickness of the tails. The latter feature of PDF was evaluated for the whole dataset and quantified by means of the kurtosis [56], an index related to the thickness of the tails of a distribution, i.e. the higher kurtosis is the heavier the tail is. The PDF relative to TKEO showed a slower decay with respect to the ETKEO (Fig. 3.4), and the average kurtosis resulted 23.3±11.2 for ETKEO and 33.1±20.9 for TKEO with a statistically significant difference ($p<10^{-6}$). This could partially account for the reduced outliers percentage of ETKEO (Fig. 3.2), supporting that the reason behind improvements grounds on a lower outliers percentage in the signal provided to the post-processor.

A tendency toward a reduction of outliers seems to guide the GAL logic, despite in the optimization procedure, a simple TP algorithm was employed, without any requirement regarding the properties of the signal PDF. However, some considerations about the searching procedure for the optimal ETKEO time-lags can be pointed out. Considering the aim of the study, searching the optimal ETKEO time-lags through an optimization based on the TP algorithm represented a natural option. However, given the results reported in Table 3.3, where the PROLIFIC method showed the best performance in terms of detection accuracy

for the whole dataset (54.9 ms), one can argue whether performing the optimization by the latter could lead to a more refined tuning. Therefore, as a representative case, the optimization of the $T_{a.e.}$ term (see Eq. (3.17)) was performed with respect to the ETKEO time-lags, by using 100 synthetic signals (SNR range 2÷4 dB) and the PROLIFIC algorithm in a different global optimization framework, i.e. a Bayesian approach [57]. From the 3D map of the expected improvement (Fig. 3.5) it is possible to appreciate that the parameters selected by using the thresholding method (Table 3.1) drop in a region of maximum expected improvement of the $T_{a.e.}$, i.e. $m = 10$ and $s = 9$. This seems to indicate that the optimal parameters obtained through PROLIFIC are in line with those obtained by the threshold method, highlighting that they were poorly affected by the particular detection algorithm and by the global optimization technique. It should also be noted that the $T_{a.e.}$ term could suffer from oscillations, presenting multiple regions of maximum (Fig. 3.5). The latter issue can be avoided or at least limited by introducing constraints and regularizations terms, as done for the optimization function adopted in the present study.

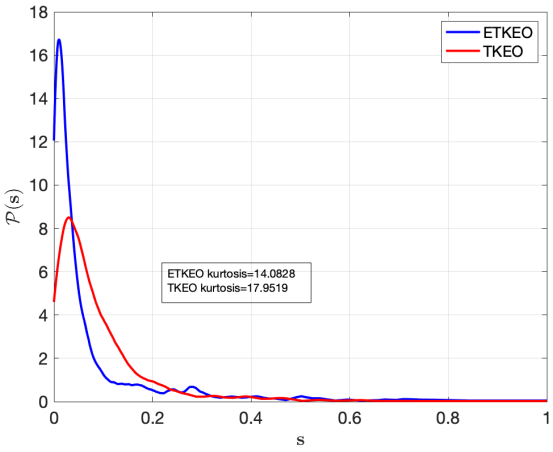

Figure 3.4: Figure shows the smoothed empirical PDF of one sEMG signal, belonging to the range 4 ≤SNR≤ 6dB after rectification, considering both ETKEO (blu line) and TKEO (red line) preconditioning. On the x-axes is reported the value of the scaled signal, on the y-axes the PDF value. Kurtosis of the two distribution are reported in the textbox.

As a final remark, it is important to underline that the ETKEO preconditioning appears able to improve the accuracy of different onset detection algorithms, also based on different approaches. In particular, the extended version of the TKEO enhanced the performances of a simple threshold detector, reaching accuracy results at least comparable with those provided by different algorithms, which rely conversely on stochastic or physical models of sEMG

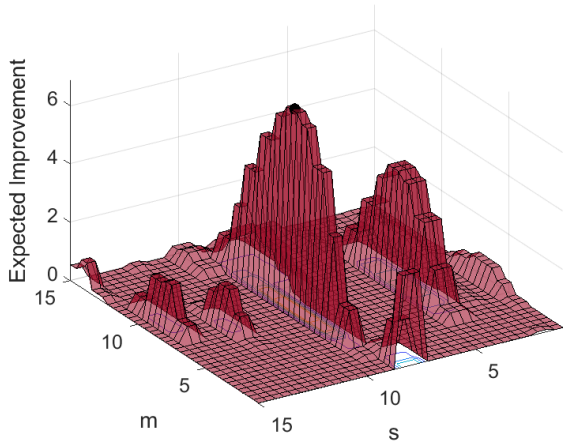

Figure 3.5: Representative case of expected improvement for the $T_{a.e.}$ term obtained with 100 synthetic data with SNR in the range $2 \div 4$ dB through Bayesian optimization framework and PROLIFIC algorithm used for onset detection.

signal and on *a priori* assumptions on signal distribution. This study entails some ways for possible future developments. As first, despite the d ETKEO parameter was set at a fixed value, it could be involved in the parameter selection procedure, representing a further degree of freedom in the preprocessing step. Eventually, few words deserve to be spent about the dataset sample size and its statistical value. Although the original dataset [5] encompassed 103 sEMG signals, the SNR band analysis led to an obvious reduction of the available data, particularly enhanced for the lower ranges. For this reason the statistical comparisons have been made taking into account the whole dataset with SNR<8 dB, i.e. 52 signals. Thus, future studies should evaluate the significance of the results using dataset with larger and possibly uniform sample size for each SNR band.

Bibliography

[1] Paolo Bonato, Tommaso D'Alessio, and Marco Knaflitz. A statistical method for the measurement of muscle activation intervals from surface myoelectric signal during gait. *IEEE Transactions on Biomedical Engineering*, 45(3):287–299, 1998.

[2] Marco Ghislieri, Giacinto Luigi Cerone, Marco Knaflitz, and Valentina Agostini. Long short-term memory (lstm) recurrent neural network for muscle activity detection. *Journal of neuroengineering and rehabilitation*, 18(1):1–15, 2021.

[3] Gerhard Staude, Claus Flachenecker, Martin Daumer, and Werner Wolf. Onset detection in surface electromyographic signals: a systematic comparison of methods. *EURASIP Journal on Advances in Signal Processing*, 2001(2):1–15, 2001.

[4] S Easter Selvan, Didier Allexandre, Umberto Amato, and Guang H Yue. Unsupervised stochastic strategies for robust detection of muscle activation onsets in surface electromyogram. *IEEE Transactions on Neural Systems and Rehabilitation Engineering*, 26(6):1279–1291, 2018.

[5] Matthew S Tenan, Andrew J Tweedell, and Courtney A Haynes. Analysis of statistical and standard algorithms for detecting muscle onset with surface electromyography. *PloS one*, 12(5):e0177312, 2017.

[6] Stanislaw Solnik, Patrick Rider, Ken Steinweg, Paul DeVita, and Tibor Hortobágyi. Teager–kaiser energy operator signal conditioning improves emg onset detection. *European journal of applied physiology*, 110(3):489–498, 2010.

[7] Andrea Merlo, Dario Farina, and Roberto Merletti. A fast and reliable technique for muscle activity detection from surface emg signals. *IEEE transactions on biomedical engineering*, 50(3):316–323, 2003.

[8] Qi Xu, Yazhi Quan, Lei Yang, and Jiping He. An adaptive algorithm for the determination of the onset and offset of muscle contraction by emg signal processing. *IEEE Transactions on Neural Systems and Rehabilitation Engineering*, 21(1):65–73, 2012.

[9] Easter S Suviseshamuthu, Didier Allexandre, Umberto Amato, Biancamaria Della Vecchia, and H Yu Guang. Prolific: A fast and robust profile-likelihood-based muscle onset detection in electromyogram using discrete fibonacci search. *IEEE Access*, 8:105362–105375, 2020.

[10] Brian J Wenzel, Joseph W Boggs, Kenneth J Gustafson, and Warren M Grill. Detecting the onset of hyper-reflexive bladder contractions from the electrical activity of the pudendal nerve. *IEEE transactions on neural systems and rehabilitation engineering*, 13(3):428–435, 2005.

[11] Luis Estrada, Abel Torres, Leonardo Sarlabous, and Raimon Jané. Onset and offset estimation of the neural inspiratory time in surface diaphragm electromyography: a pilot study in healthy subjects. *IEEE Journal of Biomedical and Health Informatics*, 22(1):67–76, 2017.

[12] Alessandro Mengarelli, Andrea Gentili, Annachiara Strazza, Laura Burattini, Sandro Fioretti, and Francesco Di Nardo. Co-activation patterns of gastrocnemius and quadriceps femoris in controlling the knee joint during walking. *Journal of Electromyography and Kinesiology*, 42:117–122, 2018.

[13] Antonio Nardone, Carlo Pasetti, and Marco Schieppati. Spinal and supraspinal stretch responses of postural muscles in early parkinsonian patients. *Experimental neurology*, 237(2):407–417, 2012.

[14] James G Colebatch and Sendhil Govender. Axial perturbations evoke increased postural reflexes in parkinson's disease with postural instability. *Clinical Neurophysiology*, 131(4):928–935, 2020.

[15] Usman Rashid, Imran Khan Niazi, Nada Signal, Dario Farina, and Denise Taylor. Optimal automatic detection of muscle activation intervals. *Journal of Electromyography and Kinesiology*, 2019.

[16] Andrea Tigrini, Alessandro Mengarelli, Stefano Cardarelli, Sandro Fioretti, and Federica Verdini. Improving emg signal change point detection for low snr by using extended

teager-kaiser energy operator. *IEEE Transactions on Medical Robotics and Bionics*, 2(4):661–669, 2020.

[17] Domen Novak and Robert Riener. A survey of sensor fusion methods in wearable robotics. *Robotics and Autonomous Systems*, 73:155–170, 2015.

[18] Thomas Lorrain, Ning Jiang, and Dario Farina. Influence of the training set on the accuracy of surface emg classification in dynamic contractions for the control of multifunction prostheses. *Journal of Neuroengineering and Rehabilitation*, 8(1):25, 2011.

[19] Xiu Zhang, Xingyu Wang, Bei Wang, Takenao Sugi, and Masatoshi Nakamura. Meal assistance system operated by electromyogram (emg) signals: Movement onset detection with adaptive threshold. *International journal of control, automation and systems*, 8(2):392–397, 2010.

[20] Laura Dipietro, Mark Ferraro, Jerome Joseph Palazzolo, Hermano Igo Krebs, Bruce T Volpe, and Neville Hogan. Customized interactive robotic treatment for stroke: Emg-triggered therapy. *IEEE Transactions on Neural Systems and Rehabilitation Engineering*, 13(3):325–334, 2005.

[21] Roberto Colombo and Vittorio Sanguineti. Assistive controllers and modalities for robot-aided neurorehabilitation. In *Rehabilitation Robotics*, pages 63–74. Elsevier, 2018.

[22] J Marvin Fernández García, Camila R Carvalho, Filipe O Barroso, and Juan C Moreno. Pseudo-online muscle onset detection algorithm with threshold auto-adjustment for lower limb exoskeleton control. In *International Symposium on Wearable Robotics*, pages 275–279. Springer, 2020.

[23] Mitra Soltani Mirzaee and Sahar Moghimi. Detection of reaching intention using eeg signals and nonlinear dynamic system identification. *Computer methods and programs in biomedicine*, 175:151–161, 2019.

[24] Ahmad Abdullah, Zareena Kausar, Aamer Hameed, Shakil R Shiekh, and Haroon Khan. Patient's intention detection and control for sit-stand mechanism of an assistive device for paraplegics. *Biomedical Signal Processing and Control*, 68:102627, 2021.

[25] Kieran Little, Bobby K Pappachan, Sibo Yang, Bernardo Noronha, Domenico Campolo, and Dino Accoto. Elbow motion trajectory prediction using a multi-modal wearable

system: A comparative analysis of machine learning techniques. *Sensors*, 21(2):498, 2021.

[26] Sivakumar Balasubramanian, Eliana Garcia-Cossio, Niels Birbaumer, Etienne Burdet, and Ander Ramos-Murguialday. Is emg a viable alternative to bci for detecting movement intention in severe stroke? *IEEE Transactions on Biomedical Engineering*, 65(12):2790–2797, 2018.

[27] Xu Zhang and Ping Zhou. Sample entropy analysis of surface emg for improved muscle activity onset detection against spurious background spikes. *Journal of Electromyography and Kinesiology*, 22(6):901–907, 2012.

[28] Jie Liu, Dongwen Ying, and Ping Zhou. Wiener filtering of surface emg with a priori snr estimation toward myoelectric control for neurological injury patients. *Medical Engineering & Physics*, 36(12):1711–1715, 2014.

[29] Joan Lobo-Prat, Mariska MHP Janssen, Bart FJM Koopman, Arno HA Stienen, and Imelda JM De Groot. Surface emg signals in very late-stage of duchenne muscular dystrophy: a case study. *Journal of Neuroengineering and Rehabilitation*, 14(1):86, 2017.

[30] WB McKay, AV Ovechkin, TW Vitaz, DGL Terson De Paleville, and SJ Harkema. Long-lasting involuntary motor activity after spinal cord injury. *Spinal cord*, 49(1):87–93, 2011.

[31] Anirban Chowdhury, Haider Raza, Yogesh Kumar Meena, Ashish Dutta, and Girijesh Prasad. An eeg-emg correlation-based brain-computer interface for hand orthosis supported neuro-rehabilitation. *Journal of Neuroscience Methods*, 312:1–11, 2019.

[32] Mads Jochumsen, Muhammad S Navid, Usman Rashid, Heidi Haavik, and Imran K Niazi. Emg-versus eeg-triggered electrical stimulation for inducing corticospinal plasticity. *IEEE Transactions on Neural Systems and Rehabilitation Engineering*, 27(9):1901–1908, 2019.

[33] Jie Liu, Dongwen Ying, William Zev Rymer, and Ping Zhou. Subspace based adaptive denoising of surface emg from neurological injury patients. *Journal of neural engineering*, 11(5):056025, 2014.

[34] Xiaoyan Li, Ping Zhou, and Alexander S Aruin. Teager–kaiser energy operation of surface emg improves muscle activity onset detection. *Annals of Biomedical Engineering*, 35(9):1532–1538, 2007.

[35] Meryem Jabloun. A new generalization of the discrete teager-kaiser energy operator-application to biomedical signals. In *2017 IEEE International Conference on Acoustics, Speech and Signal Processing (ICASSP)*, pages 4153–4157. IEEE, 2017.

[36] Michèle Basseville, Igor V Nikiforov, et al. *Detection of abrupt changes: theory and application*, volume 104. prentice Hall Englewood Cliffs, 1993.

[37] Wassim El Falou, A Khalil, and Jacques Duchêne. Adaptive approach for change detection in emg recordings. In *2001 Conference Proceedings of the 23rd Annual International Conference of the IEEE Engineering in Medicine and Biology Society*, volume 2, pages 1875–1878. IEEE, 2001.

[38] Silvestro Micera, Angelo M Sabatini, and Paolo Dario. An algorithm for detecting the onset of muscle contraction by emg signal processing. *Medical Engineering & Physics*, 20(3):211–215, 1998.

[39] Yves Préaux and Abdel-Ouahab Boudraa. Statistical behavior of teager-kaiser energy operator in presence of white gaussian noise. *IEEE Signal Processing Letters*, 27:635–639, 2020.

[40] Petros Maragos and Alexandros Potamianos. Higher order differential energy operators. *IEEE Signal Processing Letters*, 2(8):152–154, 1995.

[41] Abdel-Ouahab Boudraa and Fabien Salzenstein. Teager–kaiser energy methods for signal and image analysis: A review. *Digital Signal Processing*, 78:338–375, 2018.

[42] R Kumaresan, AG Sadasiv, CS Ramalingam, and JF Kaiser. Instantaneous non-linear operators for tracking multicomponent signal parameters. In *[1992] IEEE Sixth SP Workshop on Statistical Signal and Array Processing*, pages 404–407. IEEE, 1992.

[43] Balu Santhanam. On a matrix framework for the teager-kaiser energy operator. In *2013 IEEE Digital Signal Processing and Signal Processing Education Meeting (DSP/SPE)*, pages 69–73. IEEE, 2013.

[44] Zhiyuan Lu, Kai-yu Tong, Xu Zhang, Sheng Li, and Ping Zhou. Myoelectric pattern recognition for controlling a robotic hand: a feasibility study in stroke. *IEEE Transactions on Biomedical Engineering*, 66(2):365–372, 2019.

[45] Zhijun Li, Baocheng Wang, Fuchun Sun, Chenguang Yang, Qing Xie, and Weidong Zhang. semg-based joint force control for an upper-limb power-assist exoskeleton robot. *IEEE journal of biomedical and health informatics*, 18(3):1043–1050, 2014.

[46] Lauren H Smith, Levi J Hargrove, Blair A Lock, and Todd A Kuiken. Determining the optimal window length for pattern recognition-based myoelectric control: balancing the competing effects of classification error and controller delay. *IEEE Transactions on Neural Systems and Rehabilitation Engineering*, 19(2):186–192, 2011.

[47] Dario Farina and Roberto Merletti. A novel approach for precise simulation of the emg signal detected by surface electrodes. *IEEE transactions on biomedical engineering*, 48(6):637–646, 2001.

[48] Andrew Hamilton-Wright and Daniel W Stashuk. Physiologically based simulation of clinical emg signals. *IEEE Transactions on biomedical engineering*, 52(2):171–183, 2005.

[49] Konstantin Akhmadeev, Tianyi Yu, Eric Le Carpentier, Yannick Aoustin, and Dario Farina. Simulation of motor unit action potential recordings from intramuscular multi-channel scanning electrodes. *IEEE Transactions on Biomedical Engineering*, 2020.

[50] Giuseppe Vannozzi, Silvia Conforto, and Tommaso D'Alessio. Automatic detection of surface emg activation timing using a wavelet transform based method. *Journal of Electromyography and Kinesiology*, 20(4):767–772, 2010.

[51] Iman Akef Khowailed and Ahmed Abotabl. Neural muscle activation detection: A deep learning approach using surface electromyography. *Journal of biomechanics*, 95:109322, 2019.

[52] Foster B Stulen and Carlo J De Luca. Frequency parameters of the myoelectric signal as a measure of muscle conduction velocity. *IEEE Transactions on Biomedical Engineering*, (7):515–523, 1981.

[53] JA Guerrero and JE Macías-Díaz. An optimal bayesian threshold method for onset detection in electric biosignals. *Mathematical biosciences*, 309:12–22, 2019.

[54] Kusum Deep, Krishna Pratap Singh, Mitthan Lal Kansal, and C Mohan. A real coded genetic algorithm for solving integer and mixed integer optimization problems. *Applied Mathematics and Computation*, 212(2):505–518, 2009.

[55] Myles Hollander, Douglas A Wolfe, and Eric Chicken. *Nonparametric statistical methods*, volume 751. John Wiley & Sons, 2013.

[56] Robert V Hogg. More light on the kurtosis and related statistics. *Journal of the American Statistical Association*, 67(338):422–424, 1972.

[57] Michael A Gelbart, Jasper Snoek, and Ryan P Adams. Bayesian optimization with unknown constraints. In *30th Conference on Uncertainty in Artificial Intelligence, UAI 2014*, pages 250–259. AUAI Press, 2014.

Chapter 4

Motion Intention Detection through EMG

4.1 Introduction

In the previous chapter, an overview of the main methodologies employed for muscle onset detection were introduced. Such procedures allow to know when muscle pass from relaxed to contracted state, and vice versa, giving the basis for segmenting surface electromyography (sEMG) signal, eventually providing a rudimental form of information. Indeed, through signal change point detection techniques one can only take into account that muscle contraction/relaxation is occurring. However, many applications involving sEMG in medicine, assistive robotics, and virtual reality might require the extraction of a more refined form of information from the sEMG signals [1, 2, 3]. This should not be surprising, indeed sEMG constitutes a rich source of information upon which design smart human-machine interfaces in order to control or interact properly with machines or robots [4].

A typical example that guaranteed the growth of myoelectric interfaces for devices control is the prosthetic hand [5, 6, 7]. As literature highlights [8, 9], it is possible to recognize two main myoelectric control architectures: the first based on pattern recognition (PR) models, which can be trained in order to predict a set of gesture, movements that can be mapped at the lower control level through predefined actuation policies [7]. The second instead, works upon regression based logic. This latter is referred in general to proportional myoelectric control and employs sEMG data in order to predict the time course of joints kinematic quantities [9, 10]. These methodologies should be useful to make more natural and interactive the control of the external device [11].

However, proportional architectures may present issues due to the data acquisition step. Indeed, sEMG and kinetic data have to be acquired to generalize an input/output map

through training, testing and validation of a chosen regression architecture [9]. However, the level of patient disability could prevent the technical development of a proportional myoelctric control solution, since the patient could be as weak in certain muscles so that even starting a movement can be difficult [12, 13]. This aspect can be encountered in rehabilitation robotics [3], but also in prosthetic control for amputees, hampering the use of proportional myoelctric architecture [14, 15]. Moreover, the offline and online control performances of such architectures still present poor correlation. Thus, despite good performances of kinematic forecasting can be obtained from offline data, online performances are substantially different from the former [15]. For this reason, pattern recognition control (PRC) architectures results still appealing to eliciting assistive devices for the upper limb such as end-effector robots, exoskeletons or prosthesis [12, 16, 17, 18, 19].

PRC techniques permit to retrieve and handle a higher level of information from sEMG, that results fundamental for the purposes stated above. Indeed, in such framework the sEMG signals commonly undergo through features extraction step after preprocessing, then dimensionality reduction and model training can be consiquently perfromed [7, 6].

Despite the hand gesture recognition is one of the largest application field of myoelectric PRC, the latter can be employed also in motion intention detection (MID) problems. A crucial difference between MID and other myoelectric pattern recognition problems ground on the signal windowing used to extract the features, and on the type of application. Actually, MID problems are in general encountered in the assistive device triggering for rehabilitation robotics [16, 17, 3, 12], and transient sEMG signals epochs were employed to compute features [16, 17]. This opens different perspective regarding the assessment of PRC architecture specifically tuned for dealing with such kind of transient sEMG behavior [13]. Moreover, if compared to PRC used for hand gesture recognition, the signals epochs are shorter resulting in a limited amount of data points extracted for training and testing [16, 17, 13]. Indeed in the former case, windows that capture the sEMG signal in a steady-state condition is in general considered since transient data tends to be less prone to be easily classified [20]. However, literature highlights the importance of including dynamic data in the design of sEMG PRC in order to improve the performances of the architectures [21, 22, 23]. This can be further recognized in triggering assistive devices [17], where the real time applicability is a crucial aspect, and decision delay should be reduced as much as possible [24].

In this work, MID problems of the shoulder joint using PR approaches were taken into account. The main reasons behind the study grounds on the fact that the shoulder plays

a fundamental role for the development of assistive technologies involving the upper limb, ranging from the rehabilitation robotics to full-limb prosthesis [3, 17, 25]. However, if compared to other upper extremity joints, i.e. elbow and wrist, the shoulder was less studied under PR framework. A possible reason behind this could be found in the inherent complexity of the shoulder, which embodies a high number of degrees of freedom (DoF) to be decoded [26, 27]. Furthermore, translate the knowledge from classical myolectric PRC approaches to shoulder MID problems constitutes *per se* an aspect that deserves to be investigated and it was considered in this study. Indeed, several feature-sets involving time and frequency representation of sEMG signal have been employed through the hand gesture recognition literature [28, 19], however, the evaluation of the above reported features were not systematically performed for the shoulder joints as well as for MID problems involving dynamic data. In [26], for instance shoulder gesture recognition was performed employing steady-state portions of sEMG data for the feature extraction step. While in [25], a limited number of sEMG features were extracted from relatively long signal epochs.

On the contrary, in this work attention was given to the sEMG feature commonly used in pattern recognition problems, but extracted from transient EMG signals. Both time and frequency domains features have been investigated, firstly by analyzing their behavior for synergistic (latent) muscles pattern recognition in four kind of four shoulder movements. Then, time and frequency domain features were treated in a more complex MID problem involving eight shoulder movements. In case accounts also the study of the feature reduction step through principal component analysis (PCA) [7]. To deal with these experiments, a public available sEMG dataset was employed [29]. Thus, in the next section of the chapter the latter dataset is introduced. Then, some aspect related with sEMG signal windowing, feature extraction together with the PRC architectures employed are presented [30, 13]. The experiments and the metrics for assessing the feature stets and PRA performances have been accordingly described. Results are eventually reported and discussed.

4.2 Methods

4.2.1 Dataset presentation, signal preprocessing and segmentation

The dataset employed for this study was presented in [26] and public available at [29]. Authors recorded the sEMG signals and the shoulder angles of eight subjects (four males and four females) aged 25 $\pm$ 1.8 years underwent to eight shoulder movements, each of them

repeated ten times. In particular: shoulder flexion (FL) by 45°, 90°, 110°; hyperextension (HY) by −30°; abduction (AB) by 45° and 90° and shoulder elevation (EL) by 45° and 90° in a 45° externally rotated plane [26]. Electrodes were placed over the following muscles: clavicular and sternal heads of pectoralis major, serratus anterior, trapezius descendent, trapezius transversalis, trapezius ascendent, infraspinatus, and latissimus dorsi. Data were acquired with a sampling frequency of 1 kHz, the muscle taken into account are commonly recognized as crucial for synergistic activation and generation of the upper-limb movements [31]. Given the availability of kinematic data, the dataset resulted particularly useful for assessing shoulder MID [13]. Indeed, it is possible to take a sEMG signal epoch that fell within a MID window of 300 ms centered at the movement onset, thus spanning 150 ms before and after the beginning of the motion [16, 17, 13]. To be noted, the MID windows are essentially obtained starting by the knowledge of the movement onset [32], for this reason the kinematic data together with an accurate visual inspection of the sEMG signals is of great importance to capture the sense given by the synergistic patterns present in the transient data that generates the upper limb movements [23]. To better clarify these aspects, reader can refer to the example showed in figure 4.1. As said, the sEMG data present a dynamic

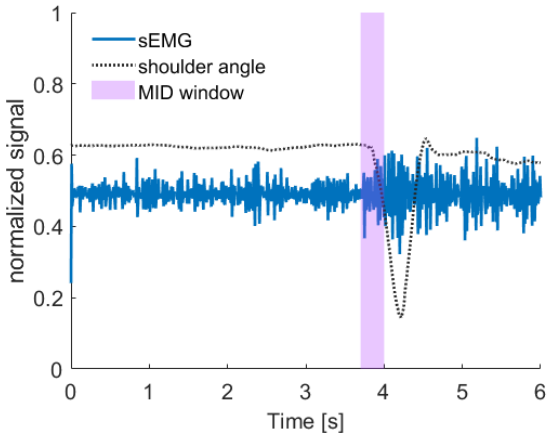

Figure 4.1: Example of sEMG signal windowing. First six seconds of shoulder angle (gray dashed line) and trapezius descendent sEMG signal (blue trace) for the first subject are represented. Both time-series were range-normalized for a better visualization. The MID window of 300 ms (violet box) is centered on the onset of the movement and it highlights the signal epoch taken in this case.

behavior during the MID window (figure 4.1) and muscles might not be in fully contracted state.

For each subject all the sEMG signals were band-pass filtered between 30 and 450 Hz with a fourth order zero-phase filter [13, 32]. After that, signal epochs can undergo through

feature extraction process. It could be helpful to realize that at this stage for each subject a number of 8 (muscles) × 8 (movements) × 10 (repetitions) of signal epochs were potentially available for extracting features.

4.2.2 sEMG feature extraction

In this section the sEMG feature employed in this study are reported, the literature highlights many different features used for myoelectric PR approaches [28, 33, 19]. Table 4.1 shows those that were analyzed and used for the study.

Table 4.1: Features extracted for both time and frequency domains. More information regarding their computation can be found in [33, 30, 34].

Type	Feature Name	Abbreviation
Time Domain features	Mean Absolute Value	MAV
	Variance of sEMG	VAR
	Root Mean Square	RMS
	Waveform Length	WL
	Difference Absolute Mean Value	DAMV
	Difference Absolute Standard Deviation Value	DASDV
	Zero Crossing	ZC
	Myopulse Percentage Rate	MYOP
	Willison Amplitude	WAMP
	Slope Sign Change	SSC
	Fuzzy Entropy	FuzEn
	Permutation Entropy	PermEn
	Histogram of EMG, 10-bins	HIST
	Auto-Regressive Coefficients, 4^{th} Order	AR
Frequency Domain features	Mean Frequency	MNF
	Median Frequency	MDF
	Peak Frequency	PKF
	Total Power	TTP
	1^{st} Spectral Moment	SM1
	2^{nd} Spectral Moment	SM2
	3^{rd} Spectral Moment	SM3
	Frequency Ratio	FR
	Power Spectrum Ratio	PSR
	Variance of Central Frequency	VCF

As one can observe in table 4.1 two domains of signal representation were taken into account, that is time and frequency domain (TD and FD respectively), this subdivision is recognized also in other studies as in [28, 19, 13], and it constitutes a robust framework in

order to highlight pattern in multi-channel sEMG data.

Let now introduce the TD features, which are commonly employed in medical and engineering applications since they are fast to be computed and they do not require any signal domain transformation [28, 33]. This was recognized in many different papers [17, 3, 23]. Despite non-stationarity of the signal in transient condition might lead to large variations, features of this group showed good classification performances [28], thus making their use a gold-standard in the field.

Given a discrete signal x_i of N samples, where N is related to the window time length used to compute the features, with reference to table 4.1 one can define the MAV as:

$$\text{MAV} = \frac{1}{N}\sum_{i=1}^{N}|x_i| \tag{4.1}$$

the VAR can be computed as an average of square values of the deviation of that variable. However, mean value of sEMG signal is in general close to zero, thus accordingly with [28] VAR can be defined as:

$$\text{VAR} = \frac{1}{N-1}\sum_{i=1}^{N}x_i^2 \tag{4.2}$$

RMS is modeled as amplitude modulated Gaussian random process whose give information related to constant force and non-fatiguing contraction [35, 28], formally it is defined as:

$$\text{RMS} = \sqrt{\frac{1}{N}\sum_{i=1}^{N}x_i^2} \tag{4.3}$$

the next feature is the WL, which is a measure of the sEMG epoch taken into account. It is defined as the cumulative length of the EMG signal over the time segment:

$$\text{WL} = \sum_{i=1}^{N-1}|x_{i+1} - x_i| \tag{4.4}$$

similar to the WL one can compute the DAMV [36], which introduces an averaging term that contribute to the feature stabilization, more formally:

$$\text{DAMV} = \frac{1}{N}\sum_{i=1}^{N-1}|x_{i+1} - x_i| \tag{4.5}$$

following the same line, Kim and colleagues [36] introduced also an RMS-like feature, namely DASDV, which is a standard deviation value of the wavelength the latter can be computed

as reported below:

$$\text{DASDV} = \sqrt{\frac{1}{N-1}\sum_{i=1}^{N-1}(x_{i+1}-x_i)^2} \tag{4.6}$$

another classical TD feature is the ZC [7, 6], it is basically a measure of the frequency information of the sEMG window considered. Its estimation can be obtained using time domain signal representation through two approaches. One way employs the estimation of spectral moments of second and fourth order [34]. The other, which was adopted in this study is the following:

$$\begin{aligned} \text{ZC} =& [\sum_{i=1}^{N-1} \text{f}(x_{i+1}\cdot x_i) \cap |x_{i+1}-x_i| \geq \text{threshold}]; \\ \text{f}(x) =& \begin{cases} 1, & \text{if} \quad x \geq \text{threshold} \\ 0, & \text{otherwise} \end{cases} \end{aligned} \tag{4.7}$$

in a similar fashion one can define the MYOP, WAMP and SSC, such features basically accounts for frequency information of the sEMG signal defied in time, their formal definitions are reported below:

$$\begin{aligned} \text{MYOP} =& \sum_{i=1}^{N} [\text{f}(x_i)] \geq \text{threshold}; \\ \text{f}(x) =& \begin{cases} 1, & \text{if} \quad x \geq \text{threshold} \\ 0, & \text{otherwise} \end{cases} \end{aligned} \tag{4.8}$$

$$\begin{aligned} \text{WAMP} =& \sum_{i=1}^{N-1} [\text{f}(|x_{i+1}-x_i|)] \geq \text{threshold}; \\ \text{f}(x) =& \begin{cases} 1, & \text{if} \quad x \geq \text{threshold} \\ 0, & \text{otherwise} \end{cases} \end{aligned} \tag{4.9}$$

$$\begin{aligned} \text{SSC} =& \sum_{i=2}^{N-1} [\text{f}(|x_{i+1}-x_i|)\cdot \text{f}(|x_{i-1}-x_i|)] \geq \text{threshold}; \\ \text{f}(x) =& \begin{cases} 1, & \text{if} \quad x \geq \text{threshold} \\ 0, & \text{otherwise} \end{cases} \end{aligned} \tag{4.10}$$

Literature showed different suitable values for the threshold employed in ZC, MYOP, WAMP, and SSC computation. Values range from 50 μV to 100 mV. However the threshold should be defined knowing the background noise properties. If the sEMG activation shows a magnitude

order much greater than noise, one can put the threshold value to 0.

In table 4.1 are reported also two features that deal with the estimation of the complexity of the given sEMG time-series. More specifically, FuzEn and SampEn were employed in this study [30, 13].The FuzEn was proposed as a measure of time-series complexity, providing the conditional probability that two vectors recognized similar for m samples remain similar also for the next $m+1$ samples [37]. Given the sEMG signal epoch $x_i \quad i = 1 \dots N$ and an embedding dimension m, $(N-m)$ embedding vectors are constructed as follows:

$$\mathbf{z}_i^m = \Big[x_i, x_{i+1}, \dots, x_{i+m-1}\Big] - x_0(i) \quad i = 1, \dots, N-m+1 \tag{4.11}$$

where $x_0(i)$ is a scalar value representing the baseline:

$$x_0(i) = \frac{1}{m} \sum_{j=0}^{m-1} x_{i+j} \tag{4.12}$$

Each embedding vector $\mathbf{z}_i^m$ contains m consecutive samples of the original time-series x_i and the distance value $d_{i,j}$ is computed as the distance between $\mathbf{z}_i^m$ and $\mathbf{z}_j^m$, using the Chebyshev metric [37]:

$$d_{i,j} = \max |\mathbf{z}_i^m - \mathbf{z}_j^m| \quad i \geq 1 \quad j \leq N-m+1 \tag{4.13}$$

The degree of similarity $\Gamma_{i,j}^m$ between $\mathbf{z}_i$ and $\mathbf{z}_j$ is derived through an exponential function $\psi(d_{i,j}, r, n)$:

$$\Gamma_{i,j}^m = \psi(d_{i,j}, r, n) = \exp\left(-\frac{(d_{i,j})^n}{r}\right) \tag{4.14}$$

Through $\Gamma_{i,j}^m$, the $\Phi_m(r,n)$ is defined as follows:

$$\Phi_m(r,n) = \frac{1}{N-m} \sum_{i=1}^{N-m} \left(\frac{1}{N-m-1} \sum_{j=1}^{N-m} \Gamma_{i,j}^m\right) \quad j \neq i \tag{4.15}$$

Then, constructing the embedding vectors for an embedding dimension of $m+1$, the $\Phi_{m+1}(r,n)$ function is derived according to (4.15) and the FuzEn is finally obtained as the natural logarithm of the ratio between $\Phi_m(r,n)$ and $\Phi_{m+1}(r,n)$:

$$FuzEn(m,r,n) = \ln \Phi_m(r,n) - \ln \Phi_{m+1}(r,n) \tag{4.16}$$

It is clear from (4.11) and (4.14) that the FuzEn depends upon three parameters: the embedding dimension m, which defines the length of the embedding vectors to be compared, the width, and the gradient of the $\psi(\cdot)$ function boundary [37], i.e. r and n.

The main difference between FuzEn and more classical time-series complexity measures (approximate and sample entropy) is the function used for assessing similarity, which in the latter case is the Heaviside step function [38], whereas for the FuzEn is the exponential function (4.14). The use of (4.14) allows to avoid abrupt changes in similarity, due to the continuous property of the exponential, ensuring to obtain the maximum degree of self-similarity, since the exponential function is convex [37].

The above mentioned entropy measures are all based on evaluating the distance between sub-series, using a certain distance metric. In more recent years, different measures for evaluating time-series complexity have been proposed, relying on a mapping on ordinal or probability patterns of neighboring points [39, 40]. In particular, the PermEn [39] uses ordinal descriptors instead of distance metrics. Considering a N-length time series x_i, its embedding representation has the following form:

$$\mathbf{z}_j^{d,\tau} = \left[x_j, x_{j+\tau}, \ldots, x_{j+(d-1)\tau} \right] \quad j = 1, 2, \ldots, (N - (d-1)\tau) \tag{4.17}$$

where d is the embedding dimension and must be ≥ 2 and $\tau \in \mathbb{N}$ is the embedding delay, i.e. the time separation between time-series samples and is commonly set to 1. The elements of each sub-series of length d are mapped into an ordinal pattern, based on their ranks. For instance, choosing $d = 3$ and with an embedding vector equal to $\begin{pmatrix} 7, & 2, & 9 \end{pmatrix}$, its ordinal pattern results $\begin{pmatrix} 1, & 0, & 2 \end{pmatrix}$. Then, the relative frequencies of all the possible permutations π_i are computed, obtaining an ordinal pattern probability distribution (note that the number of possible permutation is equal to $d!$):

$$\mathbb{P} = \{p(\pi_i)\} \quad i = 1, 2, \ldots, d! \tag{4.18}$$

Eventually, the PermEn can be obtained as a function of $\mathbb{P}$:

$$PermEn = -\sum_{i=1}^{d!} p(\pi_i) \ln \left(p(\pi_i) \right) \tag{4.19}$$

A common procedure is to normalize the PermEn value [41] by a factor equal to $\ln(d!)$, so

that it ranges within the set $\begin{bmatrix} 0, & 1 \end{bmatrix}$. Based on previous results [30], the triplet $\big(m, r, n\big) = (2, 0.2, 1)$ for the FuzEn computation was adopted, while for computing the SampEn the couple $\big(m, \tau\big) = (3, 1)$ was employed.

Up to now, all the features described present a dimension not greater than one. On the other hand, the last two TD features employed in this work are multidimensional features. The HIST and AR coefficients can be treated as ten and four-dimension feature vectors respectively. The HIST is an extension version of the ZC and WAMP features [35, 28]. While the above mentioned features applied a single threshold, the HIST equally space the sEMG data point in B number of bins and returning the number of samples per bin, here B=10 was employed. The AR coefficients instead try to model the sEMG epoch as an autoregressive process, this can also be appreciated in [42], where guidelines for modeling sEMG through AR process were discussed. Essentially the AR model describes each sample of the EMG signal as a linear combination of the previous samples x_{i-p} with an additive white noise term w_i. More precisely:

$$x_i = \sum_{k=1}^{p} a_k x_{i-k} + w_i \tag{4.20}$$

the term p indicates the order of the AR process, which in this study was set p =4 [19, 13]. The coefficient a_k instead constitute the feature vector to be estimated. To do this a classical linear method such as Yule-Walker estimation procedure can be applied.

Regarding the FD features, they are commonly employed for the characterization of muscle fatigue status, but also in the context of sEMG pattern recognition for hand gesture characterization where they provided good results [34, 19]. The first feature analyzed was the MNF which can be computed as follows:

$$\text{MNF} = \sum_{j=1}^{M} f_j P_j \Big/ \sum_{j=1}^{M} P_j \tag{4.21}$$

where f_j and P_j represent the frequency of the spectrum at frequency bin j and the power spectrum at frequency bin j, respectively. M is the length of frequency bin [28]. Another feature widely employed is the MDF, which can be computed considering its definition. MDF is the frequency at which the spectrum is divided into two regions wit equal amplitude. More precisely:

$$\sum_{j=1}^{\text{MDF}} P_j = \sum_{j=MDF}^{M} P_j = \frac{1}{2} \sum_{j=1}^{M} P_j \tag{4.22}$$

Another feature that was taken into account was the PKF defined as:

$$\text{PKF} = \max(P_j), \quad j = 1 \dots M \tag{4.23}$$

The next set of FD features related to the energy content of the signal, accounting also for the statistical properties of sEMG signal. They are the TTP (or Spectral moment of order 0), SM1, SM2, and SM3 and were analyzed in different papers [43, 28, 34]. It is also important to note that the even order moments can be directly computed without any change of signal domain by using Parseval's theorem [34]. Thy are defined as following:

$$\text{TTP} = \sum_{j=1}^{M} P_j \tag{4.24}$$

$$\text{SM1} = \sum_{j=1}^{M} P_j f_j \tag{4.25}$$

$$\text{SM2} = \sum_{j=1}^{M} P_j f_j^2 \tag{4.26}$$

$$\text{SM3} = \sum_{j=1}^{M} P_j f_j^3 \tag{4.27}$$

The last three FD features are defined as ratios between power spectral quantities, they are the FR, PSR and VCF. The former is computed as the ratio between the low and high frequency components of the EMG signal [44, 28], to select the upper and lower frequency bands MNF can be employed [28], thus resulting:

$$\text{FR} = \sum_{j=1}^{\text{MNF}} P_j \Big/ \sum_{j=\text{MNF}+1}^{M} P_j \tag{4.28}$$

The PSR can be viewed as an extension version of the PKF and FR [28]. The PSR is defined as the ratio between P_0 wich is the sum pf the signal power content closed to the maximum value of the sEMG power spectrum and the TTP:

$$\text{PSR} = \sum_{j=f_0-n}^{f_0-n} P_j \Big/ \text{TTP} \tag{4.29}$$

here n is set to 20 according with [28]. Finally the VCF is an important characteristic of the

EMG power spectral density [43], it can be defined using the spectral moments of order 0,1 and 2:

$$\mathrm{VCF} = \frac{\mathrm{SM2}}{\mathrm{SM0}} - \left(\frac{\mathrm{SM1}}{\mathrm{SM0}}\right)^2 \tag{4.30}$$

Another aspect that deserves to be mentioned regards the time window and window overlapping length used to extract the above mentioned features. The milestone study provided by Smith and colleagues [24] highlighted that an optimal window length of sEMG signal for feature extraction ranges between 150 to 250 ms. Thus in this study, the MID sEMG epochs underwent to sub-windowing through windows of 150 ms with an increment of 75 ms (50% overlap) [13, 19]. This should increase the amount of data for estimating the decision boundaries and reducing the delay of the PRA [24, 19].

4.2.3 Models for myoelctric pattern recognition architectures

In this section, the three machine learning models employed for training the PRA used in this thesis are introduced. In particular, attention was given to three commonly used PR schemes that are currently adopted in practical scenarios, that is:

- linear discriminant analysis (LDA);
- support vector machine (SVM);
- multiclass logisitc regression (MLR);

Despite nonlinear techniques based on neural-network (NN) approaches are widely used for research applications [45, 46, 47], linear architectures such those above mentioned result widely used in the practice [24]. That choice grounds on the fact that within-subject classification problems involving EMG PR approaches showed good levels of accuracy when faced with LDA, SVM and MLR. Moreover, a non significant advantage of using NN architectures with respect to LDA was observed in terms of external device controllability [48, 24]. This rendered linear PRA still used for assistive technology design and analysis [3, 12, 49, 19]. However, for completeness, it should be mentioned that deep-learning techniques, such as adaptive domain NN [50], seem to be suitable when dealing with cross-user myoelectrc control problems. Hence, since cross-usability remains a key aspect for the enhancement of sEMG based human-machine interfaces, deep learning or more in general NN architectures should not be completely disregarded, although their investigation was beyond the scope of this work of thesis.

In order to design multi-class LDA, SVM and logistic regression classifiers, the error-correcting output codes method (ECOC) was used [51]. Such methodology implies the treatment of a multiclass classification problem through a specific number of binary classifiers opportunely aggregated [52, 53]. Hence, ECOC is here introduced since it constituted the basis for building multi-class PRA used in this work. LDA, SVM and MLR binary classifiers then characterized the ECOC structure above mentioned. In general ECOC methodologies work in two steps [52, 54]:

1. The coding step, in which a set of B different bipartitions (groups of classes) of the class set $\{c_1, c_2, \dots c_L\}$ are constructed. Then B binary classifiers $h_1, h_2, \dots, h_B$ are trained over the partitions.

2. The decoding step, where given an instance of the dataset, a code-word is generated using the outputs of the B binary classifiers. Then, the code-word is compared with the base code-word of each class, and based on a similarity function (distance), the instance is attributed to the class with the most similar code-word.

Essentially two coding design frameworks are recognized, that is, the binary or the ternary ECOC coding schemes [52, 54]. For the binary coding, the partitions of class set are specified by a coding matrix $M \in \{-1, +1\}^{L \times B}$. In the ternary scheme the element 0 is introduced to mean that for a certain classifier a particular class is not considered. Hence the class set are mapped in a coding matrix of the form $M \in \{-1, 0, +1\}^{L \times B}$. One can intuitively infer that one-versus-all class partitioning ground the basis for a binary coding, while the one-versus-one is commonly considered for the ternary coding [52, 54]. However, it should be noted that the framework of ECOC multi-class classifiers accepts other binary or ternary coding schemes. Regarding this aspect, the interested reader can find further information in [54].

Concerning the decoding schemes, literature highlights different strategies that can be applied respectively for binary and ternary coding schemes [52, 54]. For the ECOC models employed in this work, the one-versus-one ternary coding scheme with a loss-weighted decoding strategy was employed since it should improves classification accuracy [54, 55]. The predicted class (for a given observation) $\hat{k}$ can thus be decoded trough:

$$\hat{k} = \arg\min_{k} \frac{\sum_{j=1}^{L} |m_{kj}| g(m_{kj}, s_j)}{\sum_{j=1}^{L} |m_{kj}|} \tag{4.31}$$

where m_{kj} is the (k, j) element of the coding matrix M, that is the code corresponding to class k of the binary learner j, s_j is the score given by the $j-$th binary classifier for an observation, while $g(\cdot, \cdot)$ is a loss function [55]. For ternary coding matrices many different loss functions were potentially available [55, 56]. For the binary learners employed the *hinge* loss function $g(m_{kj}, s_j) = \max(0, 1 - m_{kj}s_j)/2$ was considered [56].

4.2.4 The LDA

As previously introduced, linear binary classifiers were aggregated through ECOC. However it is important to stress the meaning of the term "linear" used for PR applications [57]. Let suppose a binary classification problem between two classes $\mathcal{C} = \{c_1, c_2\}$, here one has to find a decision surface that permits to attribute at any given data point $\mathbf{x}$ the class it belongs to. In this case with "linear" is meant that the decision surface is a linear function of the input vector $\mathbf{x}$ and hence is defined by $(D - 1)$ dimensional hyperplane, where D is the dimension of the input space. For binary classification classes should be represented in discrete forms within the mathematical formulation of the problem. A common procedure is to represent the classes with a target variable $t \in \{0, 1\}$ that code the classes, namely $t = 1$ represent class c_1, while $t = 0$ represents class c_2. In this way it is possible to interpret the value of t as the probability that the class of $\mathbf{x}$ is c_1, with the values of probability taking only the extreme values of 0 and 1. Then, by approaching the problem through a probabilistic perspective, one can infer the probability distribution $p(c_k|\mathbf{x})$ and use the inferred such probability and use the model to make prediction [53, 57]. A possibility is to employ a parametric model for the aforementioned conditioned probability $p(c_k|\mathbf{x})$, for which its parameters are learnt (optimized) from the training data. To predict a discrete class, one would infer a posterior probability that lie in the range of $(0, 1)$, this can be achieved introducing a link function of the form[57]:

$$y(\mathbf{x}) = f\left(\mathbf{w}^T\mathbf{x} + w_0\right) \tag{4.32}$$

where $\mathbf{w}$ are the parameter vector, w_0 is a bias term, and $f(\cdot, \cdot)$ is a selected function to model the conditioned probability. In any case, the decision surface correspond to $y(x) = \text{constant}$, such that $\mathbf{w}^T\mathbf{x} + w_0 = \text{constant}$, and thus the decision surface are linear function of $\mathbf{x}$ even if the $f(\cdot, \cdot)$ is nonlinear, For this reason the models described by (4.32) are called generalized linear models [57]. In the following it is possible to observe that the *linear discriminant* trained for the LDA binary classifier is a particular case of (4.32). The *discriminant* is

defined as a function that takes input vector $\mathbf{x}$ and assigns it to a certain class within the set $\mathcal{C}$, the simplest for of a liner discriminant is a function of the form

$$y(\mathbf{x}) = \mathbf{w}^T\mathbf{x} + w_0 \tag{4.33}$$

one can note that (4.33) is a specific case of (4.32), the term w_0 is the bias and its negative value is called a threshold and it determines the location of the decision surface in the feature space [57]. It is easy to demonstrate that the weighted vector $\mathbf{w}$ characterizes the orientation of the decision surface since it is orthogonal to every data point lying on surface itself [57]. Based on these concepts, Fisher developed the LDA, which is essentially a dimensionality reduction tool that can be thought as a classifier. Let consider a binary classification problem, then let tale the D-dimensional input vector and project it down to one dimension by the following relation:

$$y = \mathbf{w}^T\mathbf{x} \tag{4.34}$$

if a threshold on y and classify $y \geq -w_0$ as class c_1, and otherwise c_2 one obtain the classifier described above. However, the projection onto a one dimension generally implies a considerable loss of information. Hence, classes that were easily separable in the D-dimensional feature space may become strong overlapping in one dimension. In, any case, it is possible to tune the vector $\mathbf{w}$ so that the projection maximizes the class separation [57]. If one consider a problem in which N_1 points belong to c_1 and N_2 to c_2, so that the mean vectors of the two classes are given by

$$\mathbf{m}_1 = \frac{1}{N_1}\sum_{n\in c_1}\mathbf{x}_n, \qquad \mathbf{m}_2 = \frac{1}{N_2}\sum_{n\in c_2}\mathbf{x}_n. \tag{4.35}$$

Thus, the simplest way is to find $\mathbf{w}$ such that maximize the distance:

$$m_2 - m_1 = \mathbf{w}^T(\mathbf{m}_2 - \mathbf{m}_1) \tag{4.36}$$

however the simple measure given in the last equation results in an ill-posed formulation for the reason reported in [57]. Fisher proposed a better formalization of the problem, that is, find the $\mathbf{w}$ that guarantee the largest separation between projected class mean while

minimizing the class overlapping. The functional to be minimized hence results

$$J(\mathbf{w}) = \frac{\mathbf{w}^T \mathbf{S}_B \mathbf{w}}{\mathbf{w}^T \mathbf{S}_W \mathbf{w}} \tag{4.37}$$

where S_B and S_w are the *between-class* and the *within-class* covariance matrix respectively. They can be computed as follows:

$$\begin{cases} \mathbf{S}_B = (m_2 - m_1)(m_2 - m_1)^T \\ \mathbf{S}_w = \sum_{n \in c_1} (\mathbf{x}_n - \mathbf{m}_1)(\mathbf{x}_n - \mathbf{m}_1)^T + \sum_{n \in c_2} (\mathbf{x}_n - \mathbf{m}_2)(\mathbf{x}_n - \mathbf{m}_2)^T \end{cases} \tag{4.38}$$

By deriving the (4.37) with respect to $\mathbf{w}$ is possible, through mathematics, to obtain the following result[57]:

$$\mathbf{w} \propto \mathbf{S}_w^{-1}(\mathbf{m}_2 - \mathbf{m}_1) \tag{4.39}$$

Such result is known as *Fisher's linear discriminant*, though actually it is a specific projection direction rather than a discriminant in the sense previously reported. It is important to note that up to now no hypothesis related to the gaussianity of the data for the development of the LDA was required [53, 57]. However the introduction of gaussianity of the data eventually permits to model the class-conditional density $p(c_k|\mathbf{x})$. Indeed by using the maximum likelihood approach, it is possible to estimate in closed form the parameters characterizing the distribution and the optimal threshold for the LDA classifier[57, 53].

4.2.5 The SVM

The second binary classification algorithm employed is the SVM, such technique was introduced by Vapnik as a kernel based ML algorithm, and it found application in many classification and regression problems [57, 58]. Due to its strong mathematical foundations and its good generalization capacity [58], such learning machine resulted extremely useful in the filed of pattern recognition, and it was constantly cited in the filed of sEMG myoelectric control[7, 19, 18]. Differently from other machine learning techniques, SVM formulation makes an extensive use of the Lagrange multipliers in order to translate the learning problem to a convex optimization problem, which can be solved to determine the model parameters [57]. The approach is thus different with respect to more classical statistical learning techniques such as LDA or logistic regression, although a common perspective behind such different methods exists [53, 57].

In the following the SVM is introduced for the binary classification problem as kernel machine with linear kernel since the latter was used in many different studies [18, 16, 19]. Indeed, for the problems commonly encountered in sEMG patter recognition, the feature space dimension generally results quite large that the data points are linearly separable, or can be separated consistently through soft margin hyperplanes. However, for completeness, the reader interested to a more general formalization of kernel machines is remanded to [57, 58]. To begin with, let consider the simplest case of linearly separable data as reported in figure 4.2. As one can observe, several hyperplanes can perfectly separates the two classes of

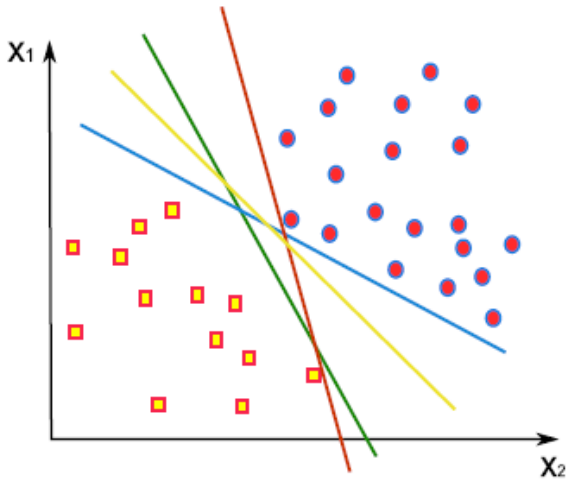

Figure 4.2: Example of 2D feature space presenting linearly separable data. Figure has been taken from [58]

points. However, the generalization properties of the machine depends on the location of the decision hyperplane and on the margin [58]. The latter represent the distance between the hyperplane and the training data closed to the hyperplane [57]. SVM based its formulation upon the margin maximization. To better formalize the problem let assume the training data comprising N data point $\mathbf{x}_1, \ldots, \mathbf{x}_N$, each corresponding to a certain target value $t_1, \ldots, t_N$ where $t_N \in \{-1, 1s\}$ and a linear model of the form:

$$y(\mathbf{x}) = \mathbf{w}^T \boldsymbol{\phi}(\mathbf{x}) + b \tag{4.40}$$

where $\boldsymbol{\phi}(\mathbf{x})$ denotes a fixed feature space transformation and b is the bias term. Note that $\phi(\cdot)$ should also be the identity multiplied by$\mathbf{x}$, making (4.40) in the same form of (4.33). This corresponds to eventually assume a linear kernel for the SVM [57]. The data points discrimination can be based on the sign of $y(\mathbf{x})$, hence having assumed linear separable

data points, there exist at least one choice of the parameters $\mathbf{w}$ and b so that (4.40) satisfy $y(\mathbf{x}_n) > 0$ for the points labelled with $t_n = +1$ and $y(\mathbf{x}_n) < 0$ for those points having $t_n = -1$ [57].

As previously said, there may exist many solutions that perfectly separate the two classes (see figure 4.2). If there are multiple hyperplanes, then it is possible to find the one that will give the smallest generalization error. The SVM face such problem by maximizing the margin. In figure 4.3, it is reported a sketch of the described situation. Given the decision hyperplane

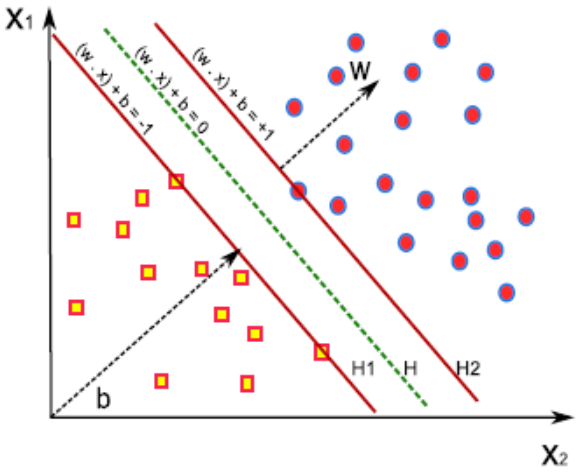

Figure 4.3: Hyperplane selection through margin maximization. Support vectors lie on H1 ans H2 hyperplanes parallel to the decision boundary H. Figure has been taken from [58]

made by $y(x) = 0$, the distance of the point $\mathbf{x}$ from such plane is given by $|y(\mathbf{x})|/\|\mathbf{w}\|$ [57]. Moreover, considering a perfect classification, for all data points the inequality $t_n y(\mathbf{x} > 0)$ holds. Thus the distance of a point $\mathbf{x}_n$ to the decision surface assume the following expression

$$\frac{t_n y(\mathbf{x}_n)}{\|\mathbf{w}\|} = \frac{t_n(\mathbf{w}^T \boldsymbol{\phi}(\mathbf{x}) + b)}{\|\mathbf{w}\|} \tag{4.41}$$

The margin is given by the perpendicular distance to the closest point $\mathbf{x}_n$, thus it is required to find a solution to the following problem:

$$\arg\max_{\mathbf{w},b} \left\{ \frac{1}{\|\mathbf{w}\|} \min_n [t_n(\mathbf{w}^T \boldsymbol{\phi}(\mathbf{x}) + b)] \right\} \tag{4.42}$$

where the factor $1/\|\mathbf{w}\|$ has been taken outside of the optimization over n since it does not depend on n. As highlighted in [57], a direct solution of the aforementioned problem would be very complex. Thus it should be converted in an equivalent problem easier to handle.

This can be done by rescaling the parameter $\mathbf{w}$ and b so that for all the points in the dataset the following inequality holds:

$$t_n(\mathbf{w}^T\boldsymbol{\phi}(\mathbf{x}_n) + b) \geq 1 \quad \forall n = 1 \dots N \tag{4.43}$$

This is referred in literature as the canonical representation of the decision hyperplane [57, 59] (see figure 4.3). For those points for which the equality in (4.43) holds, the constraints are said to be active while for the other points they are said to be inactive. By definition there is always one active constraint, because there is always a closest point to the hyperplane, and when the margin is maximized there are at least two points that satisfy the active constraint. In this way it is possible to reduce the problem stated in (4.42) to the maximization of $1/\|\mathbf{w}\|$ which is equivalent to minimizing $\|\mathbf{w}\|^2$ [57]. This can be pointed out more formally through the following *quadratic programming* problem [58, 57]:

$$\begin{aligned} &\underset{\mathbf{w}, b}{\text{minimize}} && \|\mathbf{w}\|^2 \\ &\text{subject to} && t_n(\mathbf{w}^T\boldsymbol{\phi}(\mathbf{x}_n) + b) \geq 1, \quad n = 1 \dots N \end{aligned}$$

Lagrange multipliers $a_n \geq 0$ can be introduce to solve the above mentioned problem. Thus, the following Lagrangian function can be used:

$$L(\mathbf{w}, b, a_n) = \frac{1}{2}\|\mathbf{w}\|^2 - \sum_{n=1}^{N} a_n \Big[t_n(\mathbf{w}^T\boldsymbol{\phi}(\mathbf{x}_n) + b) - 1 \Big] \tag{4.44}$$

The *dual representation* can be obtained in two steps [57, 58]. First by taking the derivative with respect to $\mathbf{w}$ and b and put them equal to zero, obtaining:

$$\mathbf{w} = \sum_{n=1}^{N} a_n t_n \boldsymbol{\phi}(\mathbf{x}_n) \tag{4.45}$$

$$0 = \sum_{n=1}^{N} a_n t_n \tag{4.46}$$

then, substituting back in (4.44), $\mathbf{w}$ and b are cancelled out obtaining the dual problem:

$$\begin{aligned} \underset{a_n}{\text{maximize}} \quad & \sum_{n=1}^{N} a_n - \frac{1}{2}\sum_{n=1}^{N}\sum_{m=1}^{N} a_n a_m t_n t_m \mathcal{K}(\mathbf{x}_n, \mathbf{x}_m) \\ \text{subject to} \quad & a_n \geq 0, \quad n = 1, \ldots, N, \\ & \sum_{i=1}^{N} a_n t_n = 0 \end{aligned}$$

where $\mathcal{K}(\cdot,\cdot)$ is is the kernel function defined as the dot product $\mathcal{K}(\mathbf{x}_1, \mathbf{x}_2) = \boldsymbol{\phi}(\mathbf{x}_1)^T \boldsymbol{\phi}(\mathbf{x}_2)$. Kernel functions have to respect certain mathematical properties as reported in [58], the linear kernel is simply the dot product between the two vectors. Despite the dual problem could appear disadvantageous, it allows to reformulate the initial problem making use of kernels, thus maximum margin classifiers can be applied efficiently to feature spaces whose dimensionality exceeds the number of data points[57].

To be noted the optimization problem proposed satisfies the Karush-Khun-Tucker conditions, that in this case resulted in:

$$\begin{cases} a_n \geq 0 \\ t_n y(\mathbf{x}_n) - 1 \geq 0 \\ a_n\{t_n y(\mathbf{x}_n) - 1\} = 0 \end{cases} \tag{4.47}$$

Such conditions permit to highlight a practical important aspect for the SVM in terms of application, indeed only those data points that in the sum of the dual problem presented a corresponding $a_n > 0$ contributed to the identification of the decision hyperplane and those points are called *support vectors* (see figure 4.3). Hence, once the model is trained a consistent portion of the data can be discharged, limiting the the memory and computation burden to predict new data point. In fact, the prediction can be performed by evaluating the sign of the model (4.42), the latter parametrized with respect to the learnt a_n of the support vectors as reported in [57]. Linear SVMs were trained and aggregated through ECOC procedure as previously reported, state-of-the art training procedures were employed, further details regarding the dual problem solution can be found in [56, 60].

4.2.6 The Logistic Regression

The latter architecture employed is the logistic regression for binary classification. Similar to LDA, such technique approaches the PR problem in a probabilistic discriminative way[53, 57]. Let consider the two class problem stated for the LDA, It is possible to model directly the class-conditional density $p(\mathbf{x}|c_k)$, as well as the class priors $p(c_k)$ and use theme to compute the posterior probabilities $p(c_k|\mathbf{x})$ through Bayes' theorem [53, 57]. Thus for the class c_1 one can write:

$$p(c_1|\mathbf{x}) = \frac{p(\mathbf{x}|c_1)p(c_1)}{p(\mathbf{x}|c_1)p(c_1) + p(\mathbf{x}|c_2)p(c_2)} \tag{4.48}$$

defining

$$a = \ln \frac{p(\mathbf{x}|c_1)p(c_1)}{p(\mathbf{x}|c_2)p(c_2)} \tag{4.49}$$

it is possible to rearrange (4.48) in he following way:

$$p(c_1|\mathbf{x}) = \frac{1}{1 + \exp(-a)} = \sigma(a) \tag{4.50}$$

where $\sigma(a)$ is named *logistic sigmoid* function. The inverse of the logistic sigmoid function is the *logit* and can be expressed through:

$$a = \ln \left(\frac{\sigma}{1 - \sigma} \right) \tag{4.51}$$

the latter represents the log of the ratio of the probabilities $ln[p(c_1|\mathbf{x})/p(c_2|\mathbf{x})]$ for the two classes, also known as the *log odds* [57]. What is convenient now is to model a as a linear function of x, this grounds the base for the logistic regression model. Let thus consider

$$a(\mathbf{x}) = \mathbf{w}^T\mathbf{x} + w_0 \tag{4.52}$$

if the bias term w_0 would be characterized it is possible, just for convenience, to extend each vector $\mathbf{x_n}$ with the last term equal to 1. Hence, the idea is to employ a maximum likelihood based estimation procedure to learn the parameters of the model.

Let consider the dataset with the target used for describing the LDA. The likelihood function can be written as following:

$$p(\mathbf{t}|\mathbf{w}) = \prod_{n=1}^{N} y_n^{t_n}\{1 - y_n\}^{1-t_n} \tag{4.53}$$

where $y_n = p(c_1|\mathbf{x_n}) = \sigma(\mathbf{w}^T\mathbf{x}_n)$ where $\sigma(\cdot)$ is the logistic sigmoid function. Using the cross-entropy error function:

$$E(\mathbf{w}) = -\ln p(\mathbf{t}|\mathbf{w}) = -\sum_{i=1}^{N}\{t_n \ln \sigma(\mathbf{w}^T\mathbf{x}_n) + (1-t_n)\ln(1-\sigma(\mathbf{w}^T\mathbf{x}_n)\} \tag{4.54}$$

taking the gradient of the error function and using the following property:

$$\frac{\mathrm{d}\sigma(a)}{\mathrm{d}a} = \sigma(1-\sigma) \tag{4.55}$$

one eventually obtains that the gradient of E is of the form:

$$\boldsymbol{\nabla} E(\mathbf{w}) = \sum_{i=1}^{N}(y_n - t_n)\mathbf{x}_n = \mathbf{X}^T\mathbf{X}\mathbf{w} - \mathbf{X}\mathbf{t} \tag{4.56}$$

where $\mathbf{X}$ is the matrix which rows correspond to the data points $\mathbf{x}_n^T$. It deserves to be noted that such gradient takes the same form of the gradient of the sum of square error function for the linear regression model [57]. Indeed, Bishop demonstrated that the cross-entropy error function (4.54) is still convex, thus admit an unique minimum [57]. Moreover, despite a closed form solution in the case of logistic regression cannot be found, an efficient iterative *Newton-Raphson* optimization scheme can be used to obtain a solution, as well as learn the model parameters $\mathbf{w}$. Such procedure makes use of a local quadratic approximation of the log-likelihood function $E(\mathbf{w})$ by introducing its Hessian. The updating equation can be synthetically expressed in this way:

$$\mathbf{w}^{(\text{new})} = \mathbf{w}^{(\text{old})} - \mathbf{H}^{-1}\boldsymbol{\nabla} E(\mathbf{w}) \tag{4.57}$$

where the matrix H is the Hessian of E, and can be computed using the derivative rule for σ, previously used also for getting $\boldsymbol{\nabla} E$:

$$\mathbf{H} = \boldsymbol{\nabla}\boldsymbol{\nabla} E(\mathbf{w}) = \sum_{i=1}^{N} y_n(1-y_n)\mathbf{x}_n\mathbf{x}_n^T = \mathbf{X}^T\mathbf{R}\mathbf{X} \tag{4.58}$$

where $\mathbf{R}$ is a $N \times N$ diagonal matrices whose R_{nn} element corresponds to $y_n(1-y_n)$. The equation (4.57) can thus be rewritten making explicit use of (4.56) and (4.58):

$$\mathbf{w}^{(\text{new})} = (\mathbf{X}^T\mathbf{R}\mathbf{X})^{-1}\mathbf{X}^T\mathbf{R}\mathbf{z} \tag{4.59}$$

where $\mathbf{z}$ is an N-dimensional vector with elements

$$\mathbf{z} = \mathbf{X}\mathbf{w}^{(\text{old})} - \mathbf{R}^{-1}(\mathbf{y} - \mathbf{t}) \tag{4.60}$$

It emerges from (4.59) that the $\mathbf{R}$ matrix is not constant, but it depends on the parameters vector $\mathbf{w}$. Hence, at each step of iteration such matrix need to be renewed, this is the reason why that this form of Newton-Raphson method is also named as *iterative reweighted least squares* (IRLS), and it is particularly useful for fitting logistic regression classifiers [53, 57]. IRLS results useful to understand the mathematics behind the learning of logistic regression model, however software libraries available in MATLAB or Python make an extensive use of stochastic gradient descent (SGD) to train logistic regression classifiers since it results fast and reliable [56]. Thus, in this study the SGD is adopted to train the binary logistic regression models.

4.2.7 Description of the myoelectric pattern recognition experiments performed

The first objective of the work is to highlight which features among that reported in 4.1 presented reliable properties of class-separability for the early recognition of shoulder MID. For this reason, four basic movements classes are considered disregarding the different degrees of motion highlighted in paragraph 4.2.1. In particular, shoulder FL by 45°, HY by −30°, AB by 45° and EL by 45° are considered at this stage. As first, feature-sets made by the same feature over the eight muscles are min-max normalized and their class separability is assessed [19, 35]. Then, MLR and SVM models are trained by splitting the same feature-sets in 70% of data for training and 30% for testing. Within-subject classification accuracy (WSA) obtained in testing is used as another metric for quantify the goodness of the feature spaces taken into account [19, 28].

In the second experiment those features that presented a mean accuracy among the subjects greater than 90% for both PRA are selected. For such features, multiple models are trained by successively holding out 40%, 50%, 60%, and 70% of the data for the testing phase. This experiment aims to asses the robustness of the selected features in order to train classifiers when few training data are available. This mirrors cases that occur in real practice, when patients cannot undergo to long lasting trials for data acquisition [16]. Also in this case, WSA obtained in test is used to investigate the effects of reducing the amount of training

data. For both experiments, hyper-parameter tuning of MLR and SVM architectures were performed through Bayesian optimization using MATLAB 2020b [19, 32]. Kruskal-Wallis non-parametric test is employed to evaluate whether changes among the WSA for the same PRA are statistically significant (significance set at 0.05).

The first two experiments are set to highlight the role of the features and their robustness in terms of pattern recognition. However, it may be interesting to understand how TD and FD features work as ensambles in more challenging MID problems. This can be encountered when, within each shoulder motion, a different final arm configuration would be reached by the subjects [26]. To do this, in the third experiments, all the eight shoulder movements previously presented (see section 4.2.1) are taken into account. Rather than SVM, in this case LDA is used since it seems one of the preferred choice in the real practice [12, 3, 61]. As reported in [13], WSA is evaluated for both classifiers by a five-fold validation method, using four different feature sets. In the first and second case, the classifiers were fit employing TD and FD features and their average accuracy is statistically (t-test). PCA retaining 95% of explained variance (PCA95) is applied to the whole feature set (TD+FD) to assess how a common feature reduction technique can impact on both LDA and MLR classifiers.

For completeness, the class separability metrics and the role of PCA in myoelectric pattern recognition are defined respectively in the next two sections. They are widely encountered in the literature, thus they deserve to be at least properly introduced in this thesis. Moreover, these tools are also employed in the next chapter, when the problem of handwriting recognition is faced through sEMG.

4.2.8 Class separability metrics

In myoelectric based pattern recognition, goodness of the feature spaces can be evaluated *a priori* by means of opportune metrics [62, 16, 49]. A well acknowledged indicator is the DB index, which is generally used to quantify how significantly a cluster overlaps its neighbors [16], representing a measure of movement class separability [19, 16]. Following [35], to compute such index one should proceed by defining the cluster similarity measure as:

$$R_{i,j} = \frac{S_i + S_j}{D_{i,j}} \tag{4.61}$$

where S_i and S_j represent the dispersion of the i_{th} and j_{th} cluster respectively, and D_{ij} is the distance between their mean values [35]. The dispersion of a general cluster k can be

computed as the standard deviation of the distance of cluster samples with respect to their cluster center [16, 62]. More formally:

$$S_k = \left\{ \frac{1}{N_k} \sum_{l=1}^{N_k} (x_l - m_k)^T (x_l - m_k) \right\}^{\frac{1}{2}} \tag{4.62}$$

where N_k is the number of data points (vectors) in the cluster k, x_l is the l-th data point in the cluster, while m_k is the cluster centroid. The last term, namely, the distance between two cluster centroids k and p can be computed through the euclidean distance, hence:

$$D_{k,p} = \left\{ (m_k - m_p)^T (m_k - m_p) \right\}^{\frac{1}{2}} \tag{4.63}$$

Thus, the DB index is defined as the mean of the similarity measures of each cluster with its most similar cluster [16]:

$$DB = \frac{1}{K} \sum_{i=1}^{K} \max(R_{i,j}) \quad \text{with} \quad i \neq j \tag{4.64}$$

From the measure definition it follows that the greater is the class separability in a given feature space, the lower is the DB index [19].

Although the DB index represents one of the main employed metrics, literature highlight other type of descriptors able to quantify the data clustering properties in a given feature space. In particular, the separability index (SI) has been employed to quantify the distance between different movement classes within an EMG feature space, such metric can be computed as in [49]: given the covariance matrix of class j, namely Σ_j, and the covariance matrix of its most conflicting class, Σ_{Cj}, we can compute Σ as:

$$\Sigma = \frac{\Sigma_j + \Sigma_{Cj}}{2} \tag{4.65}$$

then, the SI is obtained as follows:

$$\text{SI} = \frac{1}{K} \sum_{j=1}^{K} \left(\frac{1}{2} \left\{ (m_j - m_{Cj})^T \Sigma^{-1} (m_j - m_{Cj}) \right\}^{\frac{1}{2}} \right) \tag{4.66}$$

where K is the number of cluster as for the DB formulation, m_j represents the mean of the jth cluster data points and m_{Cj} is the mean of the most conflicting cluster data points with respect to the jth cluster [49]. It deserves to be noticed that the SI metric reflects the

distances between classes in the feature space, hence the greater is the SI the better is the mapping of the different movements in the given EMG feature space.

The last metric considered is the mean-semi-principal axis (MSA), which was introduced to quantify the intra-class variability [49]. Each cluster is modeled as a hyper-ellipsoid in the feature space. Thus, the size of the cluster can be approximated through the singular value decomposition of the data within each cluster and then averaged by the geometric mean of the singular values:

$$\text{MSA} = \frac{1}{K}\sum_{j=1}^{K}\left(\prod_{p=1}^{P} a_{jp}\right)^{\frac{1}{P}} \tag{4.67}$$

where a_{jp} is the p^{th} singular value of cluster j and P is the dimension of feature space. The MSA mirrors the agglomeration properties of each cluster and by definition the lower is MSA, the more the cluster are compact.

4.2.9 Principal Component Analysis: applications in sEMG pattern recognition

The PCA is a linear feature projection method which is commonly employed in the human movement analysis to reveal patterns in data of various kinds, including kinematics, kinetics, electroencephalography and EMG data [63]. In principle PCA aims to compute a smaller set of basis vectors,namely the principal components (PCs), that defines a low-dimensional space in which the original data can be projected, preserving most of the relevant initial properties in terms of variance. Indeed, by means of PCA, the axes of the original feature space are rotated such that the new coordinate system targets to the directions of highest data variance [63, 64]. Furthermore, from a practical point of view, the use of dimensionality reduction allows to simplify the design of the PRA, significantly reducing the computational cost [63, 65].

As highlighted in [63], there are two commonly used procedures to perform PCA: the first way is to compute the *eigenvalue decomposition* of the data covariance matrix, alternatively one can undergo to the *singular value decomposition* (SVD) of the centered data matrix, where centered here means that the mean of each variable is equal to 0.

Let thus consider the $m \times n$ centered data matrix $\mathbf{X}$, where m is the number of observations an n is the number of variables, with $m > n$. The covariance matrix of $\mathbf{X}$ is given by the $n \times n$ symmetrical matrix $\mathbf{C} = \mathbf{X}^T\mathbf{X}/(m-1)$. The first method above mentioned diagonalizes $\mathbf{C}$ to yeld $\mathbf{V}\mathbf{\Lambda}\mathbf{V}^T$, where the columns of $\mathbf{V}$ and the diagonal elements $\lambda_i, \quad i = 1 \ldots n$ of $\mathbf{\Lambda}$ are

respectively the eigenvectors and the eigenvalues of the covariance matrix. Note that the eigenvalues of $\mathbf{C}$ are arranged in a decreasing order along the main diagonal of $\mathbf{\Lambda}$ and each of them are in correspondence with a column vector of $\mathbf{V}$. This induces a natural ordering of the PCs the are expressed as the column of $\mathbf{XV}$, whose variances are in the decreasing order as well [63].

On the other hand, the use of SVD of $\mathbf{X}$ allows to obtain the decomposition $\mathbf{X} = \mathbf{USV}^T$, the main diagonal elements $s_i, \quad i = 1 \dots n$ of $\mathbf{S}$ are named singular values. A relation between $\mathbf{C}$ and $\mathbf{S}$ can be pointed out considering that $\lambda_i = s_i^2/(n-1)$, the PCs instead can be obtained as in the previous case, thus $\mathbf{USV^TV} = \mathbf{US}$.

It is important also to notice that PCA, can be used to give a measure of the features importance in terms of how much each feature impacts on the PCs [13]. Indeed, each PC presents a vector size equal to the dimension of the original feature space since it can also be interpreted as a projection with respect to the original axes. The higher the value of such projection, the more is the original feature important to determine the PCA component under consideration. Thus, if PCA components altogether have little projection on one of the original feature axis, then this one would be considered less important than other axes for which the overall projection is higher [13]. To formalize this concept, it is reasonable to consider the absolute value of all PCs components, and then make their vector sum. Indeed, by taking the modulus allows to highlight coordinates with both positive and negative projections, preventing such quantities to cancel out. Therefore, the outcome of these operations is a single vector containing the overall projections. In order to assign to the latter an importance score, each of them is divided by the total sum of all overall projections. This would allow to quantify feature importance as a percentage. These aspects can be better understood in the example shown in figure 4.4.

Such approach based on PCA is used to evaluate the feature importance when all the TD+FD features are employed in the eight-class shoulder MID problem described in section 4.2.7.

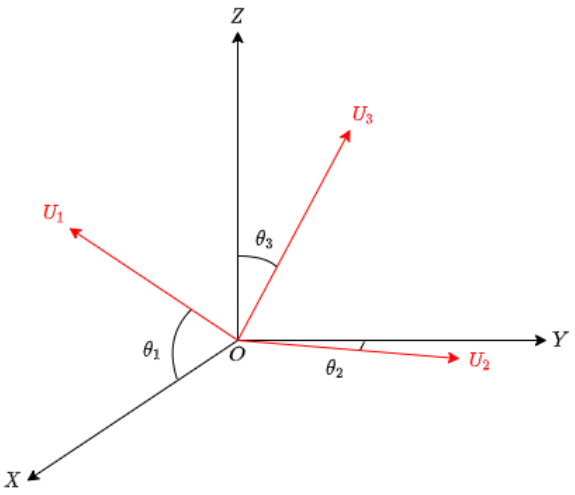

Figure 4.4: Assume that $\{\hat{\mathbf{u}}_1, \hat{\mathbf{u}}_2, \hat{\mathbf{u}}_3\}$ are the PCA components of the new reference frame $O-U_1U_2U_3$, starting from the initial reference frame $O-XYZ$ (each axis underlines a feature). In this case, the angles between the original and new reference axes are respectively: $\theta_1 = 45°$, $\theta_2 = 5.06°$ and $\theta_3 = 45.25°$. As such, PCA components with respect to the initial reference frame are $\hat{\mathbf{u}}_1 = (0.71, 0.06, -0.70)$, $\hat{\mathbf{u}}_2 = (0, 0.99, 0.09)$ and $\hat{\mathbf{u}}_3 = (0.71, -0.06, -0.70)$.The overall projection vector is $(0.35, 0.28, 0.37)$. From this outcome, Y has the least importance in defining PCA components. This is quite intuitive, since 2 out of 3 components project mainly on X and Z axes, making these latter two the more relevant features.

4.3 Results

4.3.1 TD and FD features reliability in the four-class shoulder MID problem

Table 4.2 summarizes the results relative to the first experiment in 4.2.7 together with the DB, SI and MSA values obtained for the considered feature-sets. Among the TD features, MAV, RMS, WLm DAMV and DASDV showed good clustering properties (Table 4.2). However, only DAMV and DASDV overcame the median WSA threshold of 90% for both SVM and MLR (see 4.2.7). On the other hand, AR showed greater DB values among the subjects, but it revealed good performances with both PRA. Thus the TD features selected for the second experiment were the DAMV, DASDV and AR.

Concerning the FD features, SM3 presented the best clustering properties (table 4.2), while SM2, SM1 and TTP showed a slightly superior DB index, indicating a sparser representation of the clusters. However, the latter mentioned features showed good performances in terms of classification for both MLR and SVM. Furthermore SM1 and SM2 presented the two lowest interquartile ranges (IQR) in terms of accuracy, hence confirming a certain degree

of repeatability among the subjects. Following the criterion reported in section 4.2.7, three features for the FD were selected, that is, TTP, SM1 and SM2.

Table 4.2: Table shows the DB, SI, MSA, and the accuracy for the TD and FD features considered. WSA percentage (median and interquartile range (IQR)) for both SVM and MLR referred to the first experiment in section (4.2.7). In bold we highlighted the six features that presented a median WSA% greater than 90%.

Feature Name	**DB**		**SI**		**MSA**		**MLR** (WSA%)		**SVM** (WSA%)	
	median	IQR	median	IQR	median	IQR	median	IQR	median	IQR
MAV	2.07	0.57	1.54	0.51	0.78	0.21	90.39	7.29	89.89	5.05
VAR	2.27	0.45	1.38	0.34	0.58	0.27	86.40	17.01	86.27	16.51
RMS	2.05	0.52	1.59	0.47	0.77	0.23	88.06	8.27	85.93	8.43
WL	2.02	0.52	1.72	0.40	0.77	0.28	88.96	5.62	90.73	9.00
DAMV	**2.02**	**0.52**	**1.72**	**0.40**	**0.77**	**0.28**	**91.07**	**6.37**	**92.67**	**7.19**
DASDV	**2.05**	**0.52**	**1.73**	**0.39**	**0.76**	**0.27**	**94.38**	**6.94**	**93.64**	**11.23**
ZC	3.34	0.79	0.97	0.27	1.30	0.11	69.83	13.08	68.18	16.52
MYOP	2.48	0.88	0.78	0.25	0.12	0.02	72.84	18.82	72.04	12.06
WAMP	3.28	2.72	0.56	0.32	0.14	0.01	54.36	17.07	55.58	18.05
SSC	2.87	0.71	1.11	0.39	1.27	0.15	73.34	8.00	71.66	8.85
PermEn	2.92	0.49	1.01	0.35	1.27	0.17	70.69	12.31	69.24	12.20
FuzEn	2.84	0.71	1.10	0.41	1.24	0.10	70.48	18.10	71.36	15.60
HIST	5.70	0.99	3.42	2.17	0.97	0.11	65.11	6.58	64.87	5.21
AR	**3.19**	**0.50**	**3.66**	**0.90**	**0.41**	**0.08**	**92.52**	**8.82**	**91.71**	**9.20**
MNF	2.79	1.13	1.17	0.46	1.20	0.20	69.96	16.31	70.87	17.58
MDF	3.67	1.34	0.92	0.35	1.25	0.35	64.30	22.50	59.50	27.52
PKF	2.84	0.36	1.00	0.21	0.55	0.22	80.91	8.58	80.91	10.58
TTP	**2.27**	**0.48**	**1.39**	**0.34**	**0.58**	**0.27**	**90.33**	**11.39**	**91.27**	**12.72**
SM1	**2.29**	**0.70**	**1.51**	**0.35**	**0.57**	**0.29**	**91.14**	**3.95**	**90.61**	**4.28**
SM2	**2.20**	**0.56**	**1.48**	**0.32**	**0.60**	**0.35**	**90.62**	**4.75**	**91.35**	**4.56**
SM3	2.18	0.80	1.32	0.37	0.66	0.33	86.92	8.46	86.89	7.02
FR	4.56	2.44	0.67	0.27	1.26	0.07	54.69	22.47	53.20	20.38
PSR	4.61	1.24	0.66	0.18	1.33	0.13	46.68	14.92	46.41	15.85
VCF	2.73	0.53	1.25	0.35	1.30	0.14	75.43	7.91	75.43	12.28

Figure 4.5 is showed how the WSA varied reducing the training data (increasing the holdout percentage). Any significant drop of accuracy using the three FD descriptors with the same PRA was detected (figure 4.5b, 4.5d, 4.5f). The same can be observed for DAMV and DASDV (figure 4.5a, 4.5c). On the contrary, AR showed significant accuracy drops passing from 40% to 70% holdout percentage in the case of MLR classifier (p= 2.1·10^{-2}). On the other hand, SVM significantly dropped the accuracy passing from 40% to 60% (p= 2.7·10^{-2}) and from 40% to 70% (p= 3.3·10^{-3}) of holdout percentage.

4.3.2 Performance of TD and FD feature in the eight-class shoulder MID problem

Table 4.3 reports the WSA obtained in the third PR experiment, where eight shoulder movements were considered. Both LDA and MLR provided good classification performances exception made for the LDA in the TD+FD case. The latter architecture presented poor accuracy scores with high variance (12.9%) among the subjects. By comparing both PRA models, it emerged that MLR outperformed LDA within each dataset considered (table 4.3). In addition, it is interesting to highlight that the dimensionality reduction of the TD+FD feature set in the PCA95 set permitted to significantly boost the performances of the LDA classifier, on the other hand, no significant drop or boost in the MLR was observed when PCA95 was employed with respect TD+FD.

Table 4.3: Table reports the within-subject accuracy in percentage averaged among the eight subjects. † symbol indicates p<0.01.

Classifier	Feature Domain			
	TD	FD	TD+FD	PCA95
LDA	86.9 ± 4.9	82.7 ± 5.0	63.8† ± 12.9	88.8† ± 3.3
MLR	91.8 ± 3.0	87.0 ± 5.3	93.0 ± 3.1	91.8 ± 3.4

Regarding the features importance (see section 4.2.9), they were averaged over channels in order to obtain mean features importance on the core 36 features from the TD+FD set (Fig. 4.6).

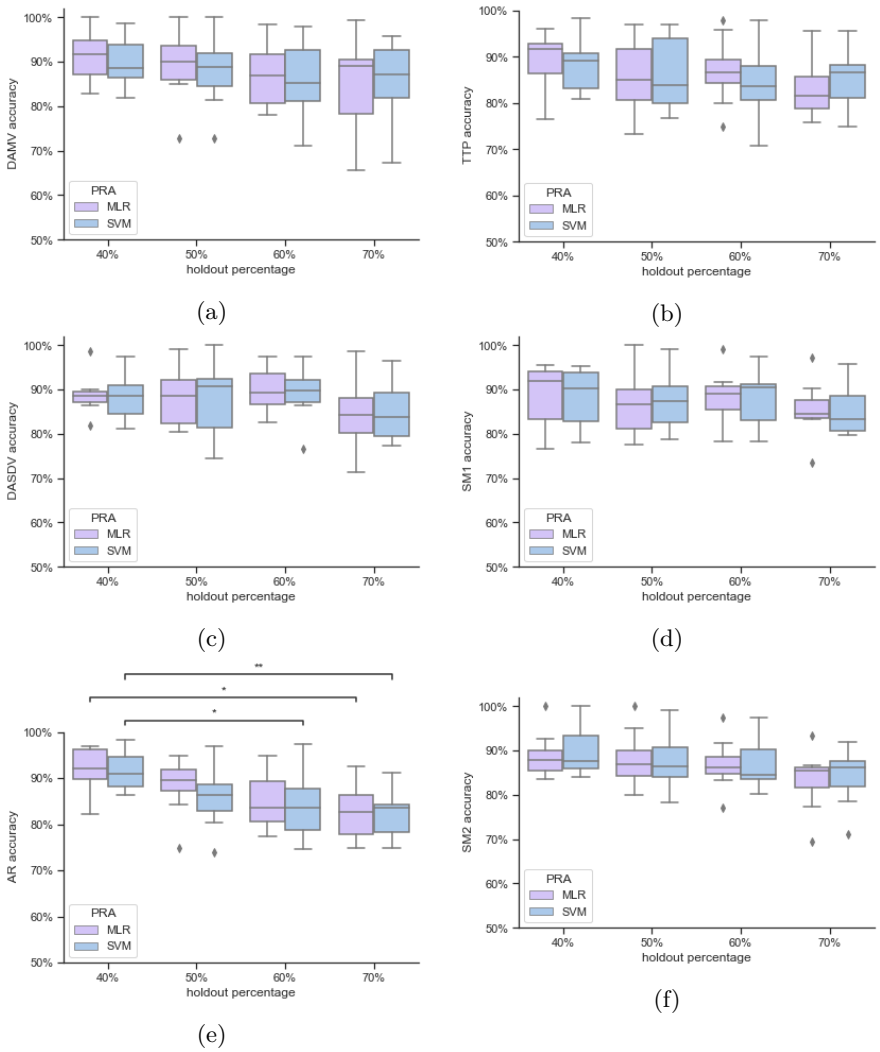

Figure 4.5: Figure shows how WSA, for both SVM and MLR, varied holding out an increased amount of data retained for testing (see section 4.2.7). DAMV, DASDV and AR feature-space (panel 4.5a, 4.5c, 4.5e respectively) are reported on the left side. Right side reported the remained three FD features selected in the experiment 2, namely TTP, SM1 and SM2 (panel 4.5b, 4.5d, 4.5f). Significant comparison obtained through Kruskal-Wallis are indicated with * ($0.01 < p < 0.05$) and with ** ($p < 0.01$)

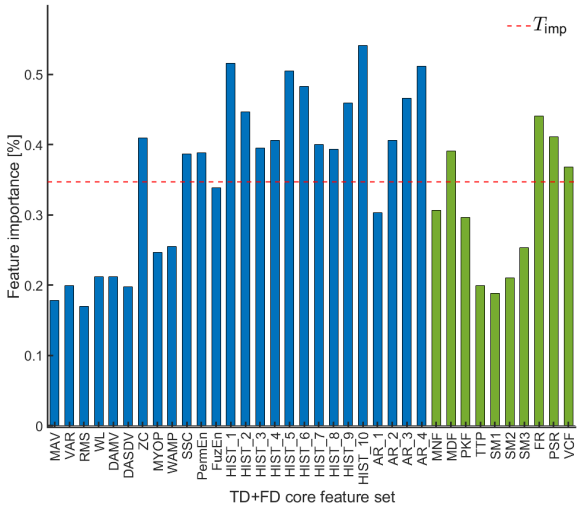

Figure 4.6: Feature importance, averaged over channels, for TD (in blue) and FD (in green) features.

4.4 Discussion

4.4.1 Role of TD and FD features in myoelectric MID

In this work, the problem of detecting the subject movement intention of the shoulder joint was faced. Such joint resulted less studied in literature from a myoelectric control viewpoint if compared for instance with the distal segments of the upper-limb, i.e. elbow, wrist, and the hand [26, 25]. However, shoulder plays a key role in many motor tasks, such as reaching or grasping, since it is sinergistically involved by the central nervous system to cooperate with the other proximal joints [31]. This justifies the increasing interest in the development of myoelectric control solutions either to guide rehabilitation robots and exoskeleton, or to study possible control solutions for full-limb prosthetic replacement [18, 3, 26, 25]. Thus, in this context, the problem of upper limb MID was further analyzed since it constitute a key step in the real rehabilitation scenarios [16, 17]. Indeed, particular importance was given to those movements, namely shoulder FL, HY, AB and EL that involve joint degrees of freedom that are naturally accounted in robotic-based therapeutic contexts [66, 67].

To be noted, differently from other studies where only TD features where considered for the upper limb MID [17, 16, 3], the possible role of a wide range of FD features was here investigated[13, 33]. The main reason behind the preference of TD features over FD ones in such kind of problems lies on the computational cost of changing the signal representation domain [28].However, for many FD features, it is not required to change signal domain by

computing FFT [34, 68]. This is of great importance in real time application scenario, where fast feature computation is required to reduce the global decision delay of the PRA for working on-line [17, 24]. Moreover, the investigation of FD featured for the shoulder MID problem seemed to be partially justified also by the results reported in table 4.2 (section 4.3.1), where DB index highlight clustering properties of the FD features comparable to those expressed in the TD. This is also strengthened by the SI and MSA obtained, which support the goodness of data clustering of the aforementioned features.

Concerning the first experiment, six features, three in TD and three in the FD, overcame the median accuracy threshold set at 90% for both PRA. Among the TD features, only DAMV and DASDV presented the requirement needed to be further analyzed in the second experiment. In particular DASDV exhibited the best performances in terms of accuracy among the other features (table 4.2). The strength of this feature in myolectric PR was confirmed in many different works, where architectures trained with DASDV resulted among the best performing [36, 28, 19]. This suggested that the DASDV can be a valuable feature also in the field of shoulder MID, where few but significant features have to be retrieved for each sEMG channel in order to fast the computation. The last feature that filled the requirement to be analyzed in the second experiment was the 4-th order AR coefficients, which is also largely employed alone or with other TD features in works facing MID problems [16, 3]. Despite this feature worked fine in the above mentioned studies, it tends to generate large feature space due to four coefficients obtained for each employed sEMG channel. This aspect can be an issue when the amount of sEMG data is limited as could happen in MID. In fact, when one reduces the windowing of sEMG data in the transient stage, a lower amount of data points in the feature space can be retrieved if compared to the static phase of muscle activity, where 3 to 5 seconds of signal epochs can be employed[13, 21, 69]. The reduction of the signal epoch may lead to small amount of data for training and testing entailing poor generalized and over-fitted models [70].

Furthermore, it should be noted that, within the TD feature set, MAV, VAR, RMS, and WL presented remarkable clustering properties (DB < 2.3) and classification performances (not below 85%), highlighting once more the expediency of TD features in myoelectric based MID, and in general for EMG pattern recognition [12, 18, 33].

4.4.2 TD and FD feature reliability for pattern recognition

Also the second experiment provided confirmation on the FD features suitability and reliability. As one can appreciate in figure 4.5, TTP, SM1, and SM2 (panel 4.5b, 4.5d, 4.5f) were able to maintain a good inter-class distinction by reducing the amount of trained data for both MLR and SVM. As a matter of fact, the accuracy obtained presented median values always greater than 85%. Here, it is important to highlight that the WSA were computed upon the holdout percentage of data, while the remaining part was used to train the PR models. The features that did not present any significant drop of accuracy (Figure 4.5) can be ascribed as robust. Indeed, in practical scenarios, small datasets for training PRA are generally available, since patients cannot undergo through prolonged data acquisition sessions [16].

In the same way one can observe that DAMV and DASDV (panel 4.5a and 4.5c respectively) did not present any significant drop of accuracy, while AR showed significant drops of WSA (panel 4.5e) which can be attributed to over-fitted models. In fact, the sub-fold division of the AR training set, during the hyperparameter tuning, led to folds that presented an amount of data comparable with the dimension of the AR feature spaces. This produced detrimental effects that grew with the increase of the hold out percentage. This can be explained also as follows: the dimension of the AR feature space remained invariant (4 coefficients $\times$ 8 channels) but the amount of fold data was progressively reduced, eventually providing poorer generalized models [70].

The other descriptors analyzed in the second experiment presented feature-spaces dimension equal to 8 (one feature for each channel) and the trained models did not report over-fitting. This indicates that a multichannel sEMG approach with smaller dimension feature-spaces made by reliable features are preferable when it is not possible to collect a large amount of data. Indeed, the hold-out testing performed aimed to assess the performances of the features in a real scenario, since it is a common procedure to carry out hyper-parameters optimization, splitting the training dataset through k-fold validation [19].

4.4.3 Features ensambles evaluation

Let now consider the third experiment,in which all the eight shoulder movement classes reported in the public available dataset were considered [29]. As already mentioned in section 4.2.1, the dataset comprises shoulder movements that offered a certain range of motion for the final limb configuration. For instance, concerning the shoulder AB, it was performed

by 45° and by 90°, potentially resulting in two additive classes for PR problem [26]. In the first two experiments this aspect was not considered, since the primary aim was to verify the feasibility of using TD and FD features for solving shoulder MID. Thus, with the third experiment, an additive level of complexity was added to investigate whether one can recognize finer intention the final limb configuration from transient sEMG data.

To be noticed, this tends to steer the MID problem toward the more classical myoelectric PR problems encountered in the literature. Indeed, the number of classes involved are comparable with those one can find in hand gesture recognition [19, 33, 23]. Thus, the motion intention could be viewed as a particular synergistic muscle activation pattern that can be recognized in an opportune feature space with an adequate dimension, that can be obtained through a proper sEMG spatial covering [13]. Thus, rather then facing this aspect with the "each-feature" approach taken in the past experiments, the entire TD, FD and TD+FD domains where considered, since the whole amount of data (number of instances) was grater due to the eight movement classes taken into account. Moreover, when possible, computing more features permits to avoid possible loss of information *a priori*, which can be instead preserved by using ad-hoc dimensionality reduction schemes such as PCA [7]. This justifies the methodological choice of use wider ensambles of features as done in [13]. Further, although the use of the aforementioned feature sets (TD,FD, TD+FD and PCA95) on transient data might negatively impact on the classification accuracy [26, 20], both LDA and MLR classifiers reported good WSA, supporting the use of such models for solving MID problems [12, 16, 17, 3].

The feature importance assessed by means of the methodology proposed in section 4.2.9, seems to be in contrast to the single feature evaluation provided in the second experiment (see figure 4.6 and table 4.2). Indeed, the feature that obtained the best classification accuracy when used by themselves, both in TD and FD, contributed less in the PC95. The latter instead was particularly affected by the HIST components for the TD, whereas for FD the most important features identified were the MDF, FR, PSR and VCF. However, this result should be read under the metric employed for assessing the feature importance which is the variance of the feature. However, a feature that shows great variance does not imply that it is able by itself to provide good classification performances. On the contrary, the results suggest that such features can be mixed or "fused" through PCA. In this case feature variance can be exploited to retrieve a compressed and meaningful representation of the data, whereas feature such as DAMV, DASDV, AR and TTP, SM1, SM2 seem to be able in

highlighting myolectric patterns through spatial muscle covering.

Thus, despite the results pointed out through experiment two and three seem to be competing, they reveal two different strategies to develop myolectric pattern recognition architectures. From one side, one can approach the problem with features that map in distinct patterns the multiple muscles without the need of data compression. On the other hand, one can proceed by initially extracting a variety of features and leave to an opportune dimensionality reduction procedure the burden of collapsing the useful information. The latter way of reasoning can be particularly suitable when no *a-priori* knowledge of the process is available or when a myolectric PRA works in an inter-subject scenario. Despite this was beyond the aim of this study, one can recognize such processing pipeline in different studies [7, 71, 72].

From a neuromuscular control perspective, the results provided by the third experiment may indicate the presence of a fine selective anticipatory action in the upper limb control. Indeed, despite only transient data features were used, the PR architectures were able to successfully predict a class that characterize the final limb configuration. This suggests that a consistent amount of motor planning information can be retrieved from sEMG data slightly before the start of the arm movements. This agrees with the aspects pointed out in [21], where the use of transient data in conjunction with static sEMG windows boosted the performance of the classifiers involved in hand gesture recognition for prosthetic control. Confirmations of the above-stated aspect can be observed from the neurophysiology of the motor planning, where evidences suggests that in time-windows of 150 ms are enough for the nervous system to perform both action selection and movement specification [73].

Bibliography

[1] Nihal Fatma Güler and Sabri Koçer. Classification of emg signals using pca and fft. *Journal of medical systems*, 29(3):241–250, 2005.

[2] Nadia Nasri, Sergio Orts-Escolano, and Miguel Cazorla. An semg-controlled 3d game for rehabilitation therapies: Real-time time hand gesture recognition using deep learning techniques. *Sensors*, 20(22):6451, 2020.

[3] Craig G McDonald, Jennifer L Sullivan, Troy A Dennis, and Marcia K O'Malley. A myoelectric control interface for upper-limb robotic rehabilitation following spinal cord injury. *IEEE Transactions on Neural Systems and Rehabilitation Engineering*, 28(4):978–987, 2020.

[4] Miguel Simão, Nuno Mendes, Olivier Gibaru, and Pedro Neto. A review on electromyography decoding and pattern recognition for human-machine interaction. *IEEE Access*, 7:39564–39582, 2019.

[5] Mahmoud Tavakoli, Carlo Benussi, and Joao Luis Lourenco. Single channel surface emg control of advanced prosthetic hands: A simple, low cost and efficient approach. *Expert Systems with Applications*, 79:322–332, 2017.

[6] Silvestro Micera, Jacopo Carpaneto, and Stanisa Raspopovic. Control of hand prostheses using peripheral information. *IEEE reviews in biomedical engineering*, 3:48–68, 2010.

[7] Micera Zecca, Silvestro Micera, Maria C Carrozza, and Paolo Dario. Control of multifunctional prosthetic hands by processing the electromyographic signal. *Critical Reviews™ in Biomedical Engineering*, 30(4-6), 2002.

[8] Silvestro Micera, Jacopo Carpaneto, and Stanisa Raspopovic. Control of hand prostheses using peripheral information. *IEEE Reviews in Biomedical Engineering*, 3:48–68, 2010.

[9] Janne M Hahne, Felix Biessmann, Ning Jiang, Hubertus Rehbaum, Dario Farina, Frank C Meinecke, K-R Müller, and Lucas C Parra. Linear and nonlinear regression techniques for simultaneous and proportional myoelectric control. *IEEE Transactions on Neural Systems and Rehabilitation Engineering*, 22(2):269–279, 2014.

[10] Lizhi Pan, Dustin L Crouch, and He Huang. Comparing emg-based human-machine interfaces for estimating continuous, coordinated movements. *IEEE Transactions on Neural Systems and Rehabilitation Engineering*, 27(10):2145–2154, 2019.

[11] Qin Zhang, Te Pi, Runfeng Liu, and Caihua Xiong. Simultaneous and proportional estimation of multijoint kinematics from emg signals for myocontrol of robotic hands. *IEEE/ASME Transactions on Mechatronics*, 25(4):1953–1960, 2020.

[12] Joseph V Kopke, Michael D Ellis, and Levi J Hargrove. Determining user intent of partly dynamic shoulder tasks in individuals with chronic stroke using pattern recognition. *IEEE Transactions on Neural Systems and Rehabilitation Engineering*, 28(1):350–358, 2019.

[13] Andrea Tigrini, Luca Alberto Pettinari, Federica Verdini, Sandro Fioretti, and Alessandro Mengarelli. Shoulder motion intention detection through myoelectric pattern recognition. *IEEE Sensors Letters*, 5(8):1–4, 2021.

[14] Ning Jiang, Johnny LG Vest-Nielsen, Silvia Muceli, and Dario Farina. Emg-based simultaneous and proportional estimation of wrist/hand kinematics in uni-lateral transradial amputees. *Journal of neuroengineering and rehabilitation*, 9(1):1–11, 2012.

[15] Agamemnon Krasoulis, Sethu Vijayakumar, and Kianoush Nazarpour. Effect of user practice on prosthetic finger control with an intuitive myoelectric decoder. *Frontiers in neuroscience*, 13:891, 2019.

[16] Benedetta Cesqui, Peppino Tropea, Silvestro Micera, and Hermano Igo Krebs. Emg-based pattern recognition approach in post stroke robot-aided rehabilitation: a feasibility study. *Journal of neuroengineering and rehabilitation*, 10(1):1–15, 2013.

[17] Emilio Trigili, Lorenzo Grazi, Simona Crea, Alessandro Accogli, Jacopo Carpaneto, Silvestro Micera, Nicola Vitiello, and Alessandro Panarese. Detection of movement onset using emg signals for upper-limb exoskeletons in reaching tasks. *Journal of neuroengineering and rehabilitation*, 16(1):1–16, 2019.

[18] Siqi Cai, Yan Chen, Shuangyuan Huang, Yan Wu, Haiqing Zheng, Xin Li, and Longhan Xie. Svm-based classification of semg signals for upper-limb self-rehabilitation training. *Frontiers in neurorobotics*, 13:31, 2019.

[19] Fady Botros, Angkoon Phinyomark, and Erik Scheme. Emg-based gesture recognition: Is it time to change focus from the forearm to the wrist? *IEEE Transactions on Industrial Informatics*, 2020.

[20] Kevin Englehart, B Hudgin, and Philip A Parker. A wavelet-based continuous classification scheme for multifunction myoelectric control. *IEEE Transactions on Biomedical Engineering*, 48(3):302–311, 2001.

[21] Thomas Lorrain, Ning Jiang, and Dario Farina. Influence of the training set on the accuracy of surface emg classification in dynamic contractions for the control of multifunction prostheses. *Journal of Neuroengineering and Rehabilitation*, 8(1):25, 2011.

[22] Dapeng Yang, Jingdong Zhao, Li Jiang, and Hong Liu. Dynamic hand motion recognition based on transient and steady-state emg signals. *International Journal of Humanoid Robotics*, 9(01):1250007, 2012.

[23] Gunter Kanitz, Christian Cipriani, and Benoni B Edin. Classification of transient myoelectric signals for the control of multi-grasp hand prostheses. *IEEE Transactions on Neural Systems and Rehabilitation Engineering*, 26(9):1756–1764, 2018.

[24] Lauren H Smith, Levi J Hargrove, Blair A Lock, and Todd A Kuiken. Determining the optimal window length for pattern recognition-based myoelectric control: balancing the competing effects of classification error and controller delay. *IEEE Transactions on Neural Systems and Rehabilitation Engineering*, 19(2):186–192, 2011.

[25] Ejay Nsugbe and Ali H Al-Timemy. Shoulder girdle recognition using electrophysiological and low frequency anatomical contraction signals for prosthesis control. *CAAI Transactions on Intelligence Technology*, 2021.

[26] Diletta Rivela, Alessia Scannella, Esteban E Pavan, Carlo A Frigo, Paolo Belluco, and Giuseppina Gini. Analysis and comparison of features and algorithms to classify shoulder movements from semg signals. *IEEE Sensors Journal*, 18(9):3714–3721, 2018.

[27] Patrick Goetti, Patrick J Denard, Philippe Collin, Mohamed Ibrahim, Pierre Hoffmeyer, and Alexandre Lädermann. Shoulder biomechanics in normal and selected pathological conditions. *EFORT Open Reviews*, 5(8):508–518, 2020.

[28] Angkoon Phinyomark, Pornchai Phukpattaranont, and Chusak Limsakul. Feature reduction and selection for emg signal classification. *Expert systems with applications*, 39(8):7420–7431, 2012.

[29] Giuseppina Gini, Esteban Pavan, Carlo Frigo, Diletta Rivela, Alessia Scannella, and Paolo Belluco. semg shoulder. 2018.

[30] Alessandro Mengarelli, Andrea Tigrini, Sandro Fioretti, Stefano Cardarelli, and Federica Verdini. On the use of fuzzy and permutation entropy in hand gesture characterization from emg signals: Parameters selection and comparison. *Applied Sciences*, 10(20):7144, 2020.

[31] S Micera, J Carpaneto, F Posteraro, L Cenciotti, Mirjana Popovic, and P Dario. Characterization of upper arm synergies during reaching tasks in able-bodied and hemiparetic subjects. *Clinical Biomechanics*, 20(9):939–946, 2005.

[32] Andrea Tigrini, Alessandro Mengarelli, Stefano Cardarelli, Sandro Fioretti, and Federica Verdini. Improving emg signal change point detection for low snr by using extended teager-kaiser energy operator. *IEEE Transactions on Medical Robotics and Bionics*, 2(4):661–669, 2020.

[33] Angkoon Phinyomark, Franck Quaine, Sylvie Charbonnier, Christine Serviere, Franck Tarpin-Bernard, and Yann Laurillau. Emg feature evaluation for improving myoelectric pattern recognition robustness. *Expert Systems with applications*, 40(12):4832–4840, 2013.

[34] Rami N Khushaba, Maen Takruri, Jaime Valls Miro, and Sarath Kodagoda. Towards limb position invariant myoelectric pattern recognition using time-dependent spectral features. *Neural Networks*, 55:42–58, 2014.

[35] Reza Boostani and Mohammad Hassan Moradi. Evaluation of the forearm emg signal features for the control of a prosthetic hand. *Physiological measurement*, 24(2):309, 2003.

[36] Kang Soo Kim, Heung Ho Choi, Chang Soo Moon, and Chi Woong Mun. Comparison of k-nearest neighbor, quadratic discriminant and linear discriminant analysis in classification of electromyogram signals based on the wrist-motion directions. *Current applied physics*, 11(3):740–745, 2011.

[37] Weiting Chen, Zhizhong Wang, Hongbo Xie, and Wangxin Yu. Characterization of surface emg signal based on fuzzy entropy. *IEEE Transactions on Neural Systems and Rehabilitation Engineering*, 15(2):266–272, 2007.

[38] Weiting Chen, Jun Zhuang, Wangxin Yu, and Zhizhong Wang. Measuring complexity using fuzzyen, apen, and sampen. *Medical Engineering & Physics*, 31(1):61–68, 2009.

[39] Christoph Bandt and Bernd Pompe. Permutation entropy: a natural complexity measure for time series. *Physical Review Letters*, 88(17):174102, 2002.

[40] Mostafa Rostaghi and Hamed Azami. Dispersion entropy: A measure for time-series analysis. *IEEE Signal Processing Letters*, 23(5):610–614, 2016.

[41] Luciano Zunino, Felipe Olivares, Felix Scholkmann, and Osvaldo A Rosso. Permutation entropy based time series analysis: Equalities in the input signal can lead to false conclusions. *Physics Letters A*, 381(22):1883–1892, 2017.

[42] Dario Farina and Roberto Merletti. Comparison of algorithms for estimation of emg variables during voluntary isometric contractions. *Journal of Electromyography and Kinesiology*, 10(5):337–349, 2000.

[43] Sijiang Du and Marko Vuskovic. Temporal vs. spectral approach to feature extraction from prehensile emg signals. In *Proceedings of the 2004 IEEE International Conference on Information Reuse and Integration, 2004. IRI 2004.*, pages 344–350. IEEE, 2004.

[44] Jeong-Su Han, Won-Kyung Song, Jong-Sung Kim, Won-Chul Bang, Heyoung Lee, and Zeungnam Bien. New emg pattern recognition based on soft computing techniques and its application to control of a rehabilitation robotic arm. In *Proc. of 6th international conference on soft computing (IIZUKA2000)*, pages 890–897, 2000.

[45] Wentao Wei, Qingfeng Dai, Yongkang Wong, Yu Hu, Mohan Kankanhalli, and Weidong Geng. Surface-electromyography-based gesture recognition by multi-view deep learning. *IEEE Transactions on Biomedical Engineering*, 66(10):2964–2973, 2019.

[46] Miguel Simão, Pedro Neto, and Olivier Gibaru. Emg-based online classification of gestures with recurrent neural networks. *Pattern Recognition Letters*, 128:45–51, 2019.

[47] Miguel Simao, Pedro Neto, and Olivier Gibaru. Improving novelty detection with generative adversarial networks on hand gesture data. *Neurocomputing*, 358:437–445, 2019.

[48] BA Lock, Kevin Englehart, and Bernard Hudgins. Real-time myoelectric control in a virtual environment to relate usability vs. accuracy. Citeseer, 2005.

[49] Andreas W Franzke, Morten B Kristoffersen, Vinay Jayaram, Corry K van der Sluis, Alessio Murgia, and Raoul M Bongers. Exploring the relationship between emg feature space characteristics and control performance in machine learning myoelectric control. *IEEE Transactions on Neural Systems and Rehabilitation Engineering*, 29:21–30, 2020.

[50] Evan Campbell, Angkoon Phinyomark, and Erik Scheme. Deep cross-user models reduce the training burden in myoelectric control. *Frontiers in Neuroscience*, 15, 2021.

[51] Thomas G Dietterich and Ghulum Bakiri. Solving multiclass learning problems via error-correcting output codes. *Journal of artificial intelligence research*, 2:263–286, 1994.

[52] Zhi-Hua Zhou. *Ensemble methods: foundations and algorithms*. Chapman and Hall/CRC, 2012.

[53] Trevor Hastie, Robert Tibshirani, and Jerome Friedman. *The elements of statistical learning: data mining, inference, and prediction*. Springer Science & Business Media, 2009.

[54] Sergio Escalera, Oriol Pujol, and Petia Radeva. On the decoding process in ternary error-correcting output codes. *IEEE transactions on pattern analysis and machine intelligence*, 32(1):120–134, 2008.

[55] Erin L Allwein, Robert E Schapire, and Yoram Singer. Reducing multiclass to binary: A unifying approach for margin classifiers. *Journal of machine learning research*, 1(Dec):113–141, 2000.

[56] Matlab 2020b, statistics and machine learning toolbox, 2020. The MathWorks, Natick, MA, USA.

[57] Christopher M Bishop. Pattern recognition. *Machine learning*, 128(9), 2006.

[58] Jair Cervantes, Farid Garcia-Lamont, Lisbeth Rodríguez-Mazahua, and Asdrubal Lopez. A comprehensive survey on support vector machine classification: Applications, challenges and trends. *Neurocomputing*, 408:189–215, 2020.

[59] Christopher JC Burges. A tutorial on support vector machines for pattern recognition. *Data mining and knowledge discovery*, 2(2):121–167, 1998.

[60] Vojislav Kecman, T-M Huang, and Michael Vogt. Iterative single data algorithm for training kernel machines from huge data sets: Theory and performance. In *Support vector machines: Theory and Applications*, pages 255–274. Springer, 2005.

[61] Rami Khushaba and Kianoush Nazarpour. Decoding hd-emg signals for myoelectric control-how small can the analysis window size be. *IEEE Robotics and Automation Letters*, 2021.

[62] David L Davies and Donald W Bouldin. A cluster separation measure. *IEEE transactions on pattern analysis and machine intelligence*, (2):224–227, 1979.

[63] Ganesh R Naik, Suviseshamuthu Easter Selvan, Massimiliano Gobbo, Amit Acharyya, and Hung T Nguyen. Principal component analysis applied to surface electromyography: a comprehensive review. *IEEE Access*, 4:4025–4037, 2016.

[64] Giulia C Matrone, Christian Cipriani, Emanuele L Secco, Giovanni Magenes, and Maria Chiara Carrozza. Principal components analysis based control of a multi-dof underactuated prosthetic hand. *Journal of neuroengineering and rehabilitation*, 7(1):1–13, 2010.

[65] Neta Rabin, Maayan Kahlon, Sarit Malayev, and Anat Ratnovsky. Classification of human hand movements based on emg signals using nonlinear dimensionality reduction and data fusion techniques. *Expert Systems with Applications*, 149:113281, 2020.

[66] Min-Su Kim, Sung Hoon Kim, Se-Eung Noh, Heui Je Bang, and Kyoung-Moo Lee. Robotic-assisted shoulder rehabilitation therapy effectively improved poststroke hemiplegic shoulder pain: a randomized controlled trial. *Archives of physical medicine and rehabilitation*, 100(6):1015–1022, 2019.

[67] Ruthber Rodríguez Serrezuela, Mauricio Torres Quezada, Marcia Hernández Zayas, Arquímedes Montoya Pedrón, Daily Milanés Hermosilla, and Roberto Sagaró Zamora.

Robotic therapy for the hemiplegic shoulder pain: a pilot study. *Journal of neuroengineering and rehabilitation*, 17:1–12, 2020.

[68] Rami N Khushaba, Ali H Al-Timemy, Ahmed Al-Ani, and Adel Al-Jumaily. A framework of temporal-spatial descriptors-based feature extraction for improved myoelectric pattern recognition. *IEEE Transactions on Neural Systems and Rehabilitation Engineering*, 25(10):1821–1831, 2017.

[69] Itzel Jared Rodríguez Martínez, Andrea Mannini, Francesco Clemente, and Christian Cipriani. Online grasp force estimation from the transient emg. *IEEE Transactions on Neural Systems and Rehabilitation Engineering*, 28(10):2333–2341, 2020.

[70] Janne Mathias Hahne, Bernhard Graimann, and Klaus-Robert Muller. Spatial filtering for robust myoelectric control. *IEEE Transactions on Biomedical Engineering*, 59(5):1436–1443, 2012.

[71] Rami N Khushaba. Correlation analysis of electromyogram signals for multiuser myoelectric interfaces. *IEEE Transactions on Neural Systems and Rehabilitation Engineering*, 22(4):745–755, 2014.

[72] Francesco Riillo, Lucia Rita Quitadamo, Francesco Cavrini, Emanuele Gruppioni, Carlo Alberto Pinto, N Cosimo Pastò, Laura Sbernini, Lorenzo Albero, and Giovanni Saggio. Optimization of emg-based hand gesture recognition: Supervised vs. unsupervised data preprocessing on healthy subjects and transradial amputees. *Biomedical Signal Processing and Control*, 14:117–125, 2014.

[73] Aaron L Wong, Adrian M Haith, and John W Krakauer. Motor planning. *The Neuroscientist*, 21(4):385–398, 2014.

Chapter 5

Myoelectric-based handwriting recognition

5.1 Introduction

The problem of motion intention detection faced through surface electromyographic signals (EMG) allows to better appreciate the potential role that myoelectric-based pattern recognition architectures (PRAs) can have in many different fields. As already mentioned, robotics and prosthesis are affine fields over which the EMG signals can be used to retrieve the neuromuscular information useful for control purposes [1, 2]. As a matter of fact, the literature involving myoelectric control is currently receiving many attentions, as also confirmed by the increasing number of publications per year [3].

A further field in which EMG signals are finding application is the human-machine interaction (HMI), indeed, the use of such signals permit the user to interact with a certain program, also in a virtual or augmented reality scenario [4, 5, 6, 7], for gaming or medical diagnosis aims [3, 8]. Despite simple hand gesture can be used to interact with a machine in a satisfactory way [9], it is desirable to enlarge the range of commands making more reach the HMI experience. This opens to the possibility to include more fine gestures of the hand in addition to the commonly used set of grasps, fingers, and wrist movements [10, 11, 12]. Such tendency can be observed in recent studies where a a large number of gestures and multiple dataset were taken into account [13, 3].

The recent technological advancement observed in the field of consumer devices have given the attention to wearable devices i.e. Myo armband, Gforce+ [3, 10], that can be placed either on the forearm, or on the wrist which appeared to be promising for HMI, so much that Facebook has recently developed a wrist-armband that acquires also myoelectric activity. The interest to change the focus from forearm to wrist in the development of EMG-based HMI

was confirmed in [3]. Indeed, the PRAs trained on wrist data provided similar or superior performances with respect to PRAs designed upon forearm EMG signals, considering a number of seventeen gestures in the global case [3]. The aforementioned change of perspective from forearm to wrist can be justified not only by the goodness of the results obtained, but also by the needs behind the development of minimally cumbersome interfaces [3]. Hence, the assessment of PRAs based on wrist EMG data deserves to be further investigated to get a deeper awareness of the potential role that such joint, with its muscular structures, can play for the above mentioned purposes.

To understand whether the wrist can be a reliable landmark for EMG based PRA it is important thus to consider also challenging motor tasks that can be encountered in daily life activity and that can be useful for HMI. For this reason, in this thesis, the assessment of EMG-based handwriting recognition was taken into account. Indeed, the handwriting constitutes, among all human gestures, one of the most complex task to be accomplished, since it requires a hierarchical activation of the forearm and hand muscles [14, 15]. As observed in [14, 16], the central nervous system integrates visuo-spatial information and regulates all the fine contractions of muscles in order to adjust the movement to finally map a graphical sign into a 2D orthographic representation. As a matter of fact, it has been observed that the handwriting requires the synergistic activation of different brain areas in order to coordinate muscles for writing and performing other classical actions that go along with writing, such as reading, elaborating sentences and understanding the meaning of phrases [15, 16]. For this reason, it is difficult to establish which specific brain area is responsible for the pure writing. Indeed, one can observe through brain imaging techniques that the more common areas activated during writing are the left superior frontal sulcus/middle frontal gyrus area, left intraparietal sulcus/superior parietal area and right cerebellum, whereas others zones are related to non-specific motor (primary motor and sensorimotor cortex, supplementary motor area, thalamus, and putamen) or linguistic processes (ventral premotor cortex, posterior/inferior temporal cortex) [14, 17].

A further aspect that deserves to be pointed out regards the intrinsic variability in handwriting styles over individuals, which can depend on the writing method picked up as a kid, but also on personal preference, the copying of style variants from peers in adolescence, and later in age, by the amount of writing experience [18], in any case such variability encompasses static and dynamic properties. A static variation may occur in the size or in the shape of written symbols, thus same letters may present different height or width, while a

dynamic variation can occur in sequence of strokes or in writing pattern. Indeed, the degree of variation depends on the style and speed of writing, with fast writing usually showing less legibility and greater variation [19, 20]. Moreover, although the highest variability is mostly observed between different subjects, the handwritten track can significantly vary also intra-subject [18]. Indeed, personal writing style is strongly affected by external environment conditions e.g. light conditions and location, and internal condition such as emotional state [18]. These aspects unavoidably affect the characteristics of the EMG signals of the upper limb, showing pattern differences among subjects, but also within each subject [21]. The latter point found a physiological interpretation by considering the redundancy of the human musculoskeleltal system [21].

From a biomechanical point of view, one can recognize three main muscle groups that actuate the movement of the pen during handwriting [22, 23]. As first the muscles in the superior part of the forearm, e.g. Extensor Carpi Radialis Brevis, Extensor Carpi Ulnaris, Extensor/Flexor Digitorum and Flexor Carpi Radialis; Radial Abduction and Ulnar Abduction of the wrist joint are commonly used in giving letters width [23]. Moreover it should be noted that, in the case of left-handed writers, those writing with the hand in a hooked position above the line of writing exchange the roles of thumb/finger and wrist movements, so that the latter is responsible for letter height [23]. The second muscle group encompasses the muscles of the hand: Opponens Pollicis, First Dorsal Interosseus, Medial Slip/Lateral Slip, Abductor Pollicis Brevis. Flexion and extension of thumb, index, and second fingers are usually used to give letters their height. The last group involves large upper limb muscles closed to the shoulder, these muscles are for instance responsible of large movements of the pen across the pages [23]. However, it is difficult to treat each muscle group separately when one deal with the hand movements during the handwriting task since the muscles of the hand are intimately connected with the wrist and the forearm muscles, so that it is reasonable to approach the study of the aforementioned motor task through the muscles synergy perspective [24]. On the other hand, from a practical point of view, the use of a limited number of sEMG probes are unavoidably necessary if one would to render the user experience, and thus the movements, as much as possible fluent. For this reason, a typical spatial covering of the forearm and the wrist can be adopted as observed in the literature inherent to the hand gesture recognition [3, 25, 26].

This also permits to test possible limits that the typical sensing approaches used in myoelectric-based hand gesture recognition can carries in a complex motor task such as the

handwriting. Indeed, the problem of automatic recognition of hand-wrote characters was faced using architecture which inputs are traces images [27], or kinematic data [28, 29], whereas, the use of sEMG pattern recognition architectures is new and deserves to be substantially investigated since only two solutions were found in the literature when sEMG signals have to be used for solving problems related to the handwriting recognition. The first technique proposed by [30] consists in creating a template (averaging the EMGs over all detected epochs yielding a generic template) that is entered in the template matching analysis where a sliding window is moved along the EMG recordings. In this way the EMGs and the template are continuously correlated in order to refine the EMG epochs, that are further recognized using proper classification algorithms such as the linear discriminant analysis (LDA). On the other side, in [31] a novel sEMG based handwriting recognition method was proposed. Dynamic time warping (DTW) algorithm was introduced to align two sEMG time series in the time axis. Two timeseries, which have approximately the same overall waveforms, are not close to each other in Euclidean distance. To overcome constraints imposed by geometric distance, they used DTW algorithm to warp one time series non-linearity and calculate the distance with the other time series in a more accurate way. These distance values represent discriminating features extracted from the signal. DTW algorithm is particularly addicted when dealing with sequences in which individual components have characteristics that largely vary over time, and for which the simple linear expansion or compression of the two sequences does not bring satisfactory results.

However, both previous two architectures based on a template matching are consistently different with respect to the classical approaches employed in the hand gesture recognition literature [25, 3]. In a more recent study [21], it was proposed a new approach where deep learning (DL) architectures for feature extraction and sequence recognition are used. However, despite the application of such architectures carried out promising results (94.8% overall classification accuracy), DL approaches resulted more computationally expensive than typical myoelectric based PRA, thus it might be practically more difficult to be applied in a practical scenario [32].

Thus, a first aspect of this study is to understand whether it is possible to detect the character wrote by a subject by means of pattern recognition architectures used in EMG based hand gesture recognition [3, 25, 10], extending the methodologies already present in the literature toward a not fully investigated motor-task. Moreover, for the reasons highlighted above, a second crucial point is the evaluation of the role that the wrist have in the usege of

new wearable EMG technologies. For these purposes, an opportune dataset was collected taking into account 11 subjects that wrote the ten digits matching a given template.

Myoelectric activity was recorded through 8 sEMG channels and considering a good spatial covering of the forearm and wrist as indicated in [3]. Further, a total of 27 features belonging to the time, frequency and time-frequency domains were extracted. Similarly to what done in the previous chapter, focused evaluations were conducted taking into account datasets made by the same type of feature computed over the eight channels. In such experiment, the clustering properties of the features and the accuracy obtained by gold-standard myoeoectric PRAs were evaluated.

Then, in a second experiment features have been aggregated in order to study how feature sets commonly employed in the literature behaves in the present context [33], thus investigating PRA that can be potentially implemented in the real practice. In the following, the Methods section introduces the experimental protocol and the signal processing steps employed in this study, in particular the latter shares many aspect already reported in the previous chapter, thus when possible, some concepts will be recalled briefly, whereas the description of the classification experiments concludes the section. The results and the discussion naturally follow.

5.2 Methods

5.2.1 Experimental protocol and signals preprocessing

Eleven healthy subjects, six men and five women aged between 21 and 50, took part to this experiment. Two of them were left-handed, all the others were right-handed. Each subject' s wrist and forearm were instrumented with BTS Bioengineering FREEEMG surface electrodes. Such probes trasduce myoelectric signal generated by muscle contraction into electric digital signal that are digitalized and transferred to a computer through Wi-Fi technology. In this way, connection cables are avoided, hence handwriting can be performed in a more comfortable way. The EMG signals were acquired with a sampling frequency of 1000 Hz. A total of 8 electrodes were placed in such a manner that 4 probes were located in the superior part of the forearm, surrounding its whole circumference, and the other 4 probes were positioned at the level of the wrist, hence following the spatial covering proposed in [3] (see Figure 5.2).

Forearm electrodes 1,2,3,4 were positioned circumferentially around the proximal forearm

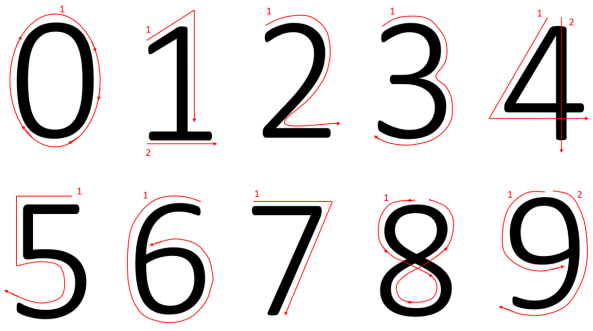

Figure 5.1: Number template. Red arrows indicate writing direction, small red numbers indicate strokes, hence digit 1, digit 4 and digit 9 are double stroke (pen lifts once), all other digits are single stroke (pen keeps attached to the sheet for all the writing phase).

(Figure 5.2a). In detail, electrodes 1 and 2 were placed over the extensor digitorum (ED) and flexor carpi radialis (FCR) respectively, proximal to the elbow joint, consistent with the locations of maximum EMG signals from these muscles. The other two electrodes, 3 and 4, were equidistantly located between 1 and 2, covering brachioradialis and flexor carpi ulnaris respectively, in order to achieve the widest spatial coverage. This forearm electrode configuration was selected to be in line with common practices in literature [34, 35, 36]. Wrist electrodes 5, 6, 7, 8 were positioned in such a way that electrodes 5 and 7 cover extensor digitorum minimi and extensor digiti respectively (Figure 5.2a), on the posterior side of the wrist proximally to the ulnar styloid process, and electrodes 6 and 8 were placed equally but on the opposite anterior side of the wrist, over distal ending of flexor carpi radialis in correspondence of the deep flexor pollicis longus and over flexor digitorum superficialis respectively. Such wrist configuration facilitates the recording of EMG signals from bellies of deep layer muscles, involved in the control of fine finger motion, coming to the surface at the wrist level [37, 38]. The experimental EMG setup used within the Movement Analysis Laboratory (UNIVPM) is reported in Figure 5.3.

All participants were asked to write numbers from 0 to 9 with their dominant hand, sitting in a comfortable position and leaning the arm against desk to not feel fatigue during the task. In order to standardize the writing pattern of every digit and facilitate the writer, a template of numbers (Figure 5.1) was followed. As estabilished by pre-graphism rules, each number was written 10 times. Subjects were asked to alternate a writing phase of 3 seconds and a resting phase of 5 seconds for every number repetition. Approximately 80 seconds were necessary to write down one single number, for a total duration of the task of about 15 minutes.

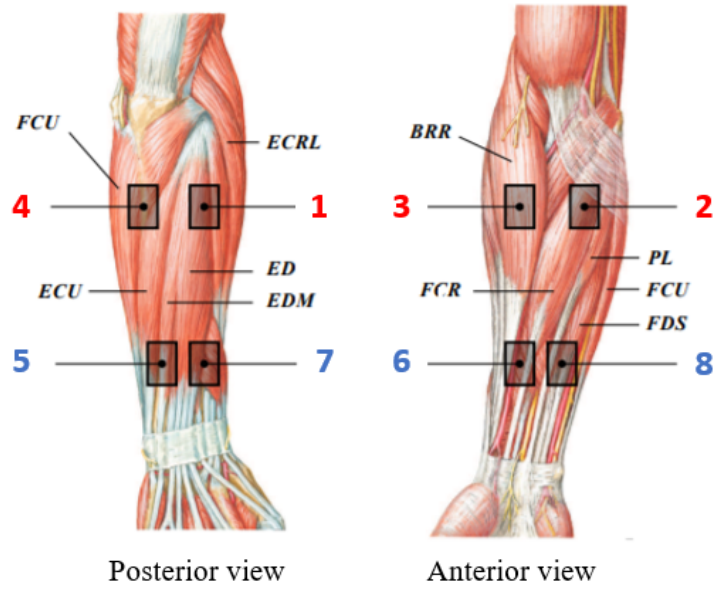

(a)

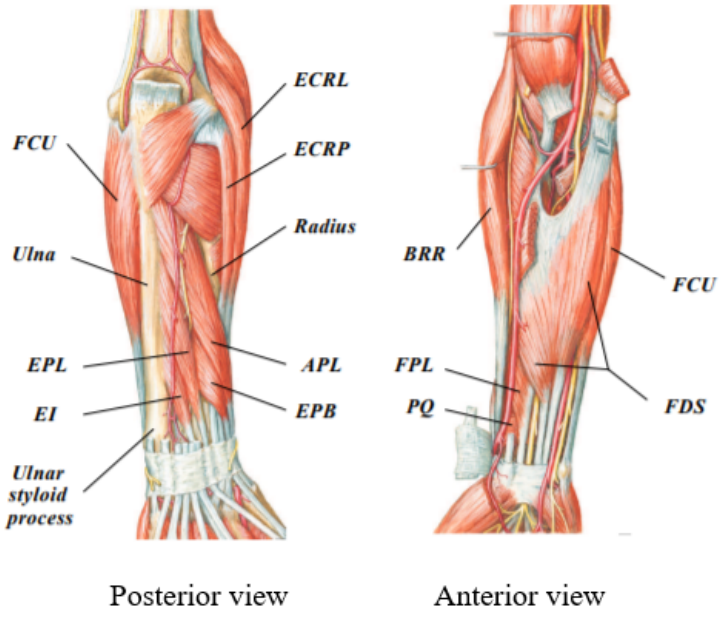

(b)

Figure 5.2: Locations of forearm (1,2,3,4) and wrist (5,6,7,8) electrodes with anatomical references of superficial (a) and deep (b) muscles. *APL: abductor pollicis longus; BRR: brachioradialis; ECRB: extensor carpi radialis brevis; ECRL: extensor carpi radialis longus; ECU: extensor carpi ulnaris; ED: extensor digitorum; EDM: extensor digiti minimi; EI: extensor indicis; EPB: extensor pollicis brevis; EPL: extensor pollicis longus; FCR: flexor carpi radialis; FCU: flexor carpi ulnaris; FDS: flexor digitorum superficialis; FPL: flexor pollicis longus; PL: palmaris longus; PQ: pronator quadratus.* Figure adopted by [3].

Signals were band-pass filtered between 30 Hz and 450 Hz[39] with a second order, zero phase Butterworth filter. Then, signals amplitude was normalized with respect to the

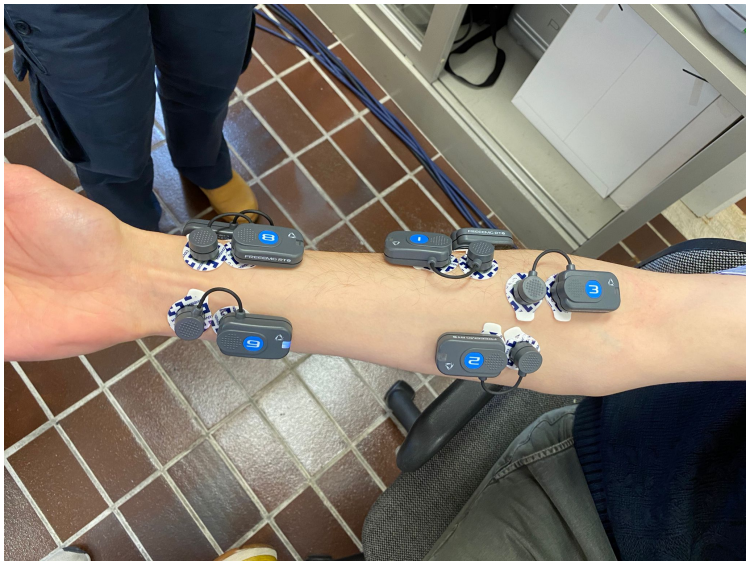

(a)

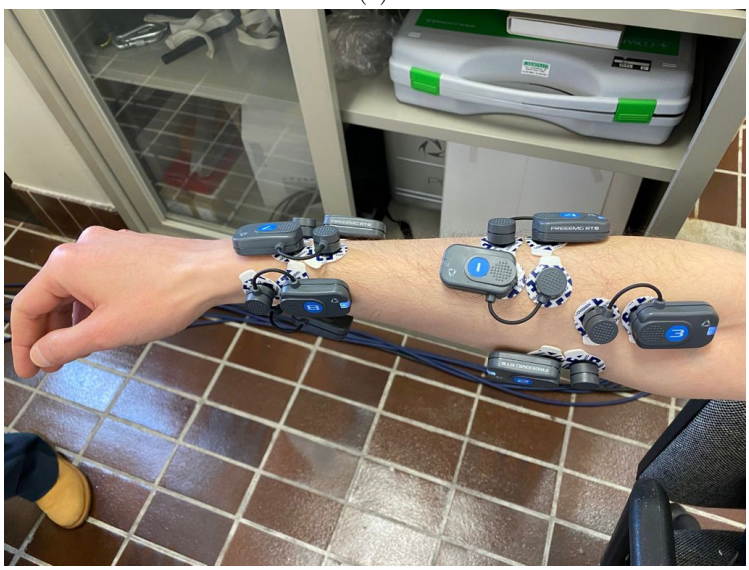

(b)

Figure 5.3: Figure shows the EMG setup employed in the experiment for a representative subject. All the experimental data were recorded in the Movement Analysis Laboratory at Università Politecnica delle Marche.

maximum amplitude value detected during period of contraction. Each new signal has a shape identical to the original one, but resulting in an amplitude scaled to a reduced range of 0 and 1. This method, namely *peak dynamic method*, is commonly adopted in EMG data processing as observed in [40, 41]. After that, signals underwent to ON-OFF segmentation in order to extract the ON segments related to the handwriting task, this was done to obtain reliable signal epochs upon which extract features for pattern recognition. More precisely, for every digit writing task, a total of 8 raw recordings is observed and, among them, the

cleanest signal is chosen. From this signal, 10 successive ON values were extracted. The OFF times were obtained adding 3 s to the ON times and checking that each portion of the signals within such windows corresponded effectively to a true ON state of the muscle. In this way, ten 3000 samples long windows (3 seconds) were extracted from a single signal. The previously defined ON-OFF signals were used to cut the remaining 7 signals in order to obtain activation windows for all the remaining channels (see Figure5.4). At the end of this process, for each subject and for each class of handwriting movement, the signal epochs of the active muscles were organized in a 10 repetitions × 8 channels array.

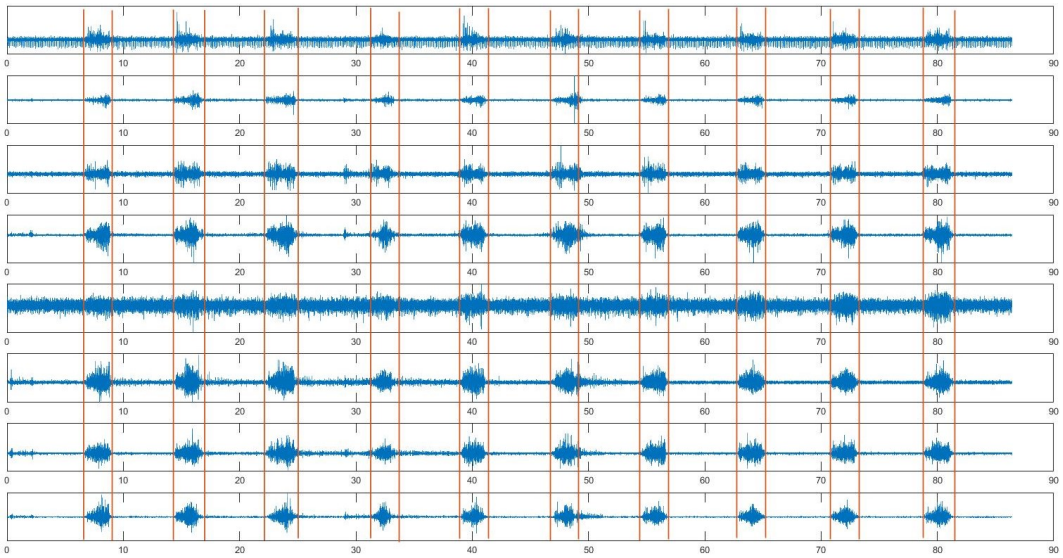

Figure 5.4: Example of segmented signals for a class of handwriting task

5.2.2 Feature extraction and datasets aggregation

Similarly to what done in the previous chapter, for each subject, sEMG features were computed taking into account the signal epochs previously segmented (see 5.2.1). A total of 26 features were taken into account, in particular 16 and 10 features were computed in the time and frequency domain, respectively [3, 26, 42]. Moreover, in this case, also features in the time-frequency domain were considered taking into account the extraction method proposed by [43]. A list of the features employed in this case was reported in Table 5.1.

Table 5.1: Features extracted for time, frequency, and time-frequency domains. More information regarding their computation can be found in [25, 43, 42].

Type	**Feature Name**	**Abbreviation**
Time Domain	Integrated EMG	IEMG
	Mean Absolute Value	MAV
	Variance of sEMG	VAR
	Root Mean Square	RMS
	Waveform Length	WL
	Difference Absolute Mean Value	DAMV
	Difference Absolute Standard Deviation Value	DASDV
	Zero Crossing	ZC
	Myopulse Percentage Rate	MYOP
	Willison Amplitude	WAMP
	Slope Sign Change	SSC
	Fuzzy Entropy	FuzEn
	Permutation Entropy	PermEn
	Histogram of EMG, 10-bins	HIST
	Auto-Regressive Coefficients, 4^{th} Order	AR
	Cepstrum coefficients of the 4^{th} Order AR process	CC
Frequency Domain	Mean Frequency	MNF
	Median Frequency	MDF
	Peak Frequency	PKF
	Total Power	TTP
	1^{st} Spectral Moment	SM1
	2^{nd} Spectral Moment	SM2
	3^{rd} Spectral Moment	SM3
	Frequency Ratio	FR
	Power Spectrum Ratio	PSR
	Variance of Central Frequency	VCF
Time-Frequency Domain	third-level approximation coefficient	cA3
	first-level detail coefficient	cD1
	second-level detail coefficient	cD2
	third-level detail coefficient	cD3

It should be noticed that the integrated EMG (IEMG) and the cepstrum coefficnets (CC) of the signals were added as features in the time domain with respect what employed in the previous chapter [44, 25]. Just for conciseness, in this section is reported the description of the features that has not been yet encountered, in particular the IEMG is defined as a summation of absolute values of the EMG signal amplitude, which can be expressed as:

$$IEMG = \sum_{i=1}^{N} |x_i| \tag{5.1}$$

where x_i represents the EMG signal sample at a given time $i$and N denotes length of the EMG signal window considered. On the other hand, the CC provide information about the rate of change in different frequency spectrum bands of a signal and they can be computed from the AR coefficients of the signal as shown in [44, 42]:

$$c_1 = -a_1 \tag{5.2}$$

$$c_i = -a_i - \sum_{n=1}^{i-1} \left(1 - \frac{n}{i}\right) a_n c_{i-1} \tag{5.3}$$

where a_i is the i-th AR coefficient, c_i is the i-th cepstrum coefficient and i is the order of the AR process. It deserves to be highlighted that, the estimation of CC here described is notably faster with respect to those methodologies that require fast Fourier transform [42]. Indeed, it does not require FFT application [45], and it is performed by not linearly combining the AR coefficients as in (5.2). For such reason CC are commonly referred to be time domain features [25, 44].

Regarding the time-frequency domain features, they were computed on the basis of the analysis proposed in [43]. In particular, EMG signal epochs underwent to three levels of decomposition using a discrete wavelet transform approach with *Coiflet 5* as the mother wavelets [43, 46, 47]. Then, the maximum absolute values of the detail coefficients at the first, second and third level of decomposition (cD1, cD2, cD3 in Table 5.1), together with the absolute maximum value of the third level approximation coefficients (cA3 in Table 5.1) were considered as features [43].

When all the features were computed, they can be aggregated in datasets made by the same feature for a certain set of channels, but also considering aggregation of different descriptors as commonly done in the literature. Indeed, the latter presents different way to combine features in order to train reliable PRA [33]. For this study, six state of the art feature sets have been employed:

- **Hudgin's Feature Set (Hudgins)**[48]: Mean Absolute Value (MAV), Waveform Length (WL), Slope Sign Change (SSC) and Zero Crossing (ZC).
- **Du Feature Set (Du)** [49]: Integrated EMG (IEMG), Variance (VAR), Wilson Amplitude (WAMP),WL, SSC, ZC.
- **Phinyomark Feature Set 1 (Phinyomark 1)** [50]: MAV, WL, WAMP, ZC, Auto-regressive Coefficients (ARs), Mean Frequency (MNF) and Power Spectrum Ratio

(PSR).

- **Phinyomark Feature Set 2 (Phinyomark 2)** [25]: Permutation entropy (PermEn), Cepstrum Coefficients (CC), RMS and WL.
- **Time Domain features combined with Autoregressive model coefficients (TDAR)** [51]: MAV, SSC, WL, VAR, WAMP, ARs, and ZC.
- **Discrete Wavelet Transform Coefficients (DWTC)** [43]: cA3, cD1, cD2, cD3.

It should be noticed that, based on the results obtained in [10], the sample entropy feature in Phinyomark 2 was substituted with PermEn.

As introduced in the previous chapter, the class separability of each dataset can be quantified through metrics that evaluate the clusters separability properties in the given feature space. For this reason, the Davies-Bouldin (DB) index [52], the separability index (SI) and the mean-semi-principal axis (MSA) were employed [32].

5.2.3 Pattern recognition experiments

The first experiment considered in this study regards the evaluation of the clustering properties of each single feature. For this reason, feature sets made by the same feature computed over the eight channels underwent through the DB, SI and MSA metrics computation. This kind of evaluation was also performed for the aggregated datasets reported in the previous section.

In the second experiment, the aggregated datasets were used for training three PRAs with a five-fold cross validation approach: support vector machine (SVM) with quadratic kernel (QSVM), linear discriminant analysis (LDA), and random forest (RF). In addition, aggregated datasets were further considered in relation to the forearm and wrist channels. This was done to understand whether the wrist can be a viable alternative with respect to the forearm for training robust EMG-based PRAs.

The SVM and LDA algorithms were already mentioned in the previous chapter and they do not need further explanations. On the other hand, the RF has not yet been introduced and it deserves to be pointed out. Such PRA is an ensamble method which is constructed through decision tree models, hence, the RF predicts by taking the average of the output from various trees that compounds the forest [53]. A given decision tree consists of split nodes and leaf nodes, as shown in Figure 5.5. Each split node performs a split decision and routes a data sample x_i to the left child node or to the right child node. To let the tree

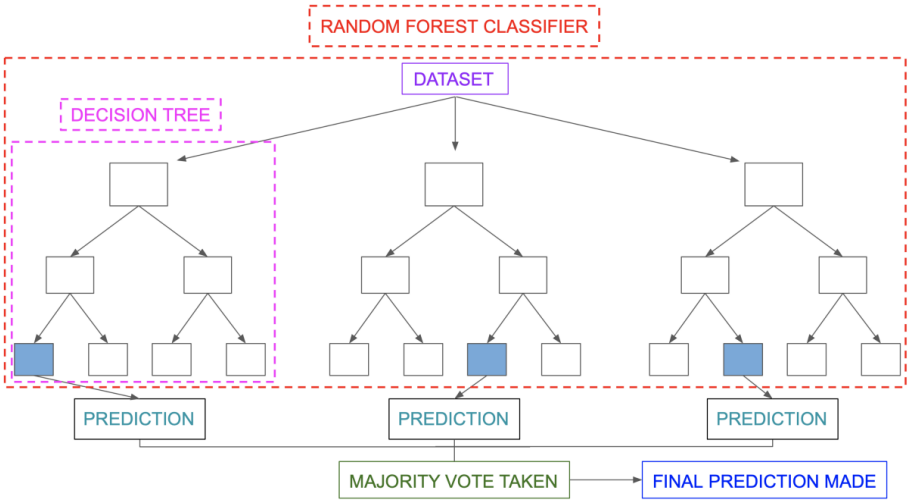

Figure 5.5: Block scheme of Random Forest algorithm [53].

know where to address the decision, a set of rules is necessary. Rules are under the form of numerical thresholds. The data sample x_i is routed to the left child node if the value of feature of x_i is smaller than a threshold and to the right child node otherwise. All leaf nodes store votes for the classes. Starting at the root node, the data is recursively split into subsets. In each step the best split is determined according specific criteria, like Gini index or entropy level, determining the information gain reached at the leaves of the tree [53]. Classification in random forests employs an ensemble methodology to attain the outcome. The training data is fed to train various decision trees. This dataset consists of observations and features that will be selected randomly during the splitting of nodes. In this case, the output chosen by the majority voting of the decision trees becomes the final output of the model. An important advantage of using RF lies on the fact that it does not need any assumption of linearity of the data, thus resulting in a good approach when facing with features presenting non-gaussian distributions [54].

5.3 Results

5.3.1 Features class separability properties

Table 5.2 shows the clustering metrics calculated for each time-domain feature as average of all 11 subjects. In bold are highlighted the features that presented the best class separability properties. It should be noticed that MAV, RMS, WL, DAMV, DASDV and IEMG show SI values higher than 1, hence indicating a great separation among classes. The same was done

	MSA	SI	DB
MAV	$\mathbf{0.0074 \pm 0.0015}$	$\mathbf{1.06 \pm 0.15}$	$\mathbf{0.72 \pm 0.16}$
VAR	0.0058 ± 0.0017	0.78 ± 0.11	0.58 ± 0.12
RMS	$\mathbf{0.0084 \pm 0.0014}$	$\mathbf{0.99 \pm 0.13}$	$\mathbf{0.73 \pm 0.16}$
WL	$\mathbf{0.0068 \pm 0.0012}$	$\mathbf{1.15 \pm 0.19}$	$\mathbf{0.73 \pm 0.15}$
DAMV	$\mathbf{0.0067 \pm 0.0017}$	$\mathbf{1.15 \pm 0.18}$	$\mathbf{0.73 \pm 0.16}$
DASDV	$\mathbf{0.0075 \pm 0.0014}$	$\mathbf{1.09 \pm 0.16}$	$\mathbf{0.73 \pm 0.15}$
IEMG	$\mathbf{0.0074 \pm 0.0014}$	$\mathbf{1.06 \pm 0.15}$	$\mathbf{0.71 \pm 0.17}$
ZC	0.0143 ± 0.0025	0.32 ± 0.14	0.71 ± 0.06
MYOP	0.0077 ± 0.0056	0.25 ± 0.15	0.65 ± 0.09
WILSON	0.0078 ± 0.0062	0.26 ± 0.16	0.63 ± 0.11
SSC	0.0119 ± 0.0041	0.30 ± 0.15	0.67 ± 0.10
PERMEN	0.0110 ± 0.0046	0.30 ± 0.16	0.66 ± 0.11
FUZZYEN	0.0113 ± 0.0021	0.35 ± 0.13	0.67 ± 0.08
HIST	0.0121 ± 0.0022	0.88 ± 0.21	1.22 ± 0.16
AR	0.0062 ± 0.0017	0.62 ± 0.18	1.36 ± 0.11
CC	0.0068 ± 0.0017	0.63 ± 0.24	1.33 ± 0.12

Table 5.2: Mean and standard deviation of MSA, SI and DB value of 11 subjects calculated for time-domain features.

for the frequency and time-frequency domains, the results were reported in Table 5.3 and 5.4, respectively. In frequency domain, the first three spectral moments presented the best separability properties among the ten writing tasks. On the other hand, in the time-frequency domain the maximum absolute value of the first level detail coefficients seem to be the more suitable to highlight class differences. Table 5.5 reports the metrics calculated for each

	MSA	SI	DBI
MNF	0.0120 ± 0.0030	0.39 ± 0.12	0.68 ± 0.15
MDF	0.0155 ± 0.0031	0.34 ± 0.18	0.75 ± 0.19
PKF	0.0044 ± 0.0016	0.56 ± 0.21	0.43 ± 0.08
TTP	0.0058 ± 0.0017	0.78 ± 0.14	0.57 ± 0.19
SM1	$\mathbf{0.0056 \pm 0.0016}$	$\mathbf{0.83 \pm 0.16}$	$\mathbf{0.59 \pm 0.15}$
SM2	$\mathbf{0.0051 \pm 0.0013}$	$\mathbf{0.89 \pm 0.19}$	$\mathbf{0.58 \pm 0.11}$
SM3	$\mathbf{0.0047 \pm 0.0012}$	$\mathbf{0.92 \pm 0.22}$	$\mathbf{0.56 \pm 0.16}$
FR	0.0087 ± 0.0035	0.23 ± 0.21	0.58 ± 0.09
PSR	0.0069 ± 0.0044	0.34 ± 0.14	0.51 ± 0.08
VCF	0.0092 ± 0.0017	0.41 ± 0.29	0.64 ± 0.05

Table 5.3: Mean and standard deviation of MSA, SI and DB value of 11 subjects calculated for frequency-domain features.

feature set. Note that a fair comparison is guaranteed if two feature set with equal dimensions are to be compared.Hence, It is thus meaningful to compare TDAR with Pninyomark 2 set, Hudgins with DWTC set and Du with Phinyomark 1 set. In such comparisons, TDAR, Hudgins and Phinyomark 1 presented respectively the best separability properties.

	MSA	SI	DB
cA3	0.0083 ± 0.0015	0.53 ± 0.11	0.55 ± 0.12
cD1	$\mathbf{0.0084 \pm 0.0009}$	$\mathbf{0.70 \pm 0.13}$	$\mathbf{0.61 \pm 0.10}$
cD2	0.0092 ± 0.0016	0.64 ± 0.19	0.63 ± 0.09
cD3	0.0099 ± 0.0021	0.59 ± 0.09	0.64 ± 0.08

Table 5.4: Mean and standard deviation of MSA, SI and DB value of 11 subjects calculated for time-frequency domain.

	MSA	SI	DB
Hudgins	$\mathbf{0.0039 \pm 0.0006}$	$\mathbf{1.60 \pm 0.28}$	$\mathbf{1.37 \pm 0.20}$
Du	0.0027 ± 0.0007	1.88 ± 0.38	1.57 ± 0.22
Phinyomark 1	$\mathbf{0.0025 \pm 0.0006}$	$\mathbf{1.89 \pm 0.29}$	$\mathbf{2.00 \pm 0.23}$
Phinyomark 2	0.0042 ± 0.0008	1.90 ± 0.31	1.89 ± 0.21
TDAR	$\mathbf{0.0029 \pm 0.0007}$	$\mathbf{2.15 \pm 0.24}$	$\mathbf{1.87 \pm 0.23}$
DWTC	0.0059 ± 0.0009	1.02 ± 0.19	1.20 ± 0.18

Table 5.5: Mean and standard deviation of MSA, SI and DB value of 11 subjects calculated for all the aggregated feature sets.

5.3.2 Pattern recognition on aggregated datasets

Table 5.6 shows the results obtained for the classification of the aggregated datasets considering all the eight channels of the forearm and wrist. The dataset presenting the best performances among the three different architectures was TDAR. However, although made by few features, Hudgins dataset presented results slightly inferior with respect to TDAR. However, it should be highliighted that also Du, Phinyomark 1, Phinyomark 2, showed comparable results with respect to TDAR, wheras DWTC dataset showed the lowest accuracy althugh it results always greater than 90%. This aspect is confirmed also through the avarege precision obtained among the PRAs and the dataset employed. Indeed, in Figure 5.11 is better highlighted that DWTC provided less accurate PRA models if compared with the other sets.

		Hudgins	Du	Phinyomark 1	Phinyomark 2	TDAR	DWTC
QSVM	Accuracy	96.9 ± 1.6	97.0 ± 1.6	97.0 ± 1.5	97.1 ± 1.5	97.2 ± 1.5	94.1 ± 1.3
	Precision	84.0 ± 7.7	85.0 ± 8.2	84.6 ± 0.7	84.9 ± 7.5	85.3 ± 7.6	69.2 ± 6.8
	Recall	83.8 ± 7.8	84.7 ± 8.2	84.3 ± 7.7	84.6 ± 7.6	85.6 ± 7.2	69.3 ± 6.8
	Specificity	98.3 ± 0.8	98.3 ± 0.9	98.4 ± 0.9	98.4 ± 0.9	98.2 ± 0.8	97.2 ± 0.7
	F1	83.9 ± 7.8	84.8 ± 8.1	84.4 ± 7.5	84.8 ± 7.6	84.9 ± 7.6	69.3 ± 6.8
LDA	Accuracy	96.0 ± 1.5	96.7 ± 1.5	96.6 ± 1.4	96.5 ± 1.5	97.3 ± 1.4	92.6 ± 1.1
	Precision	80.2 ± 7.8	83.6 ± 7.8	83.2 ± 7.4	82.7 ± 7.9	86.2 ± 7.3	61.5 ± 5.8
	Recall	80.2 ± 7.7	83.6 ± 7.7	83.1 ± 7.4	82.7 ± 7.8	86.7 ± 7.3	62.4 ± 5.7
	Specificity	97.8 ± 0.8	98.2 ± 0.9	98.1 ± 0.8	98.1 ± 0.9	98.2 ± 0.8	96.5 ± 0.6
	F1	80.2 ± 7.8	83.6 ± 7.8	83.2 ± 7.4	82.7 ± 7.8	86.5 ± 7.3	62.8 ± 5.7
RF	Accuracy	95.6 ± 1.5	95.7 ± 1.6	94.8 ± 1.6	95.2 ± 1.7	95.3 ± 1.5	92.9 ± 1.4
	Precision	79.8 ± 9.5	78.6 ± 8.0	74.7 ± 8.0	76.5 ± 8.3	78.7 ± 7.6	62.8 ± 7.5
	Recall	78.0 ± 7.6	78.5 ± 8.0	74.4 ± 8.1	76.3 ± 8.5	77.1 ± 7.7	62.8 ± 7.3
	Specificity	97.5 ± 0.8	97.6 ± 0.9	97.1 ± 0.9	97.3 ± 0.9	97.5 ± 0.8	96.7 ± 0.7
	F1	83.2 ± 7.6	83.5 ± 8.0	80.8 ± 8.0	81.9 ± 8.4	83.1 ± 7.6	71.4 ± 7.4

Table 5.6: Performance parameters of the PRAs used in the second experiment. Accuracy, precision, recall, specificity and F1 score calculated as mean and standard deviation among the 11 subjects. Values are reported for all the aggregated feature sets.

To better contextualize the metrics obtained in Table 5.6, in the following it is shown an explanatory example of six confusion matrices using QSVM, which generally outperforms the other PRAs (Table 5.6). In particular, the best and the worst subject cases are reported for 3 representative feature sets, Hudgins (Figure 5.6,5.7), TDAR (Figure 5.8, 5.9), and DWTC (Figure 5.10, 5.11). Notice in Figures 5.7,5.9,5.11, one can appreciate the results of a misclassification between task 0 and task 9, that is repeated whichever feature sets are used to train the QSVM classifier.

Actual \ Predicted	Task 0	Task 1	Task 2	Task 3	Task 4	Task 5	Task 6	Task 7	Task 8	Task 9
Task 0	97.4	0	0.5	0	0.7	0.5	1.8	0	0.7	0
Task 1	0	96.2	0.7	0.5	6.3	0	0	0	0.5	0
Task 2	0.3	0.3	91.2	0.8	1.7	1.3	0.5	0	0	0
Task 3	0	0.3	1.5	97.6	2.2	0	0.3	0	0	0
Task 4	0.3	3	2.5	1	85.1	1	0	0	1.5	0
Task 5	0.5	0	3.2	0	1	96.1	0.8	0	0	0
Task 6	0.8	0	0.2	0	0	1	94.4	0	2.5	0
Task 7	0.5	0	0.2	0	1.2	0	0	100	0	0
Task 8	0.3	0	0	0	1.7	0	0.5	0	92.2	1.1
Task 9	0	0.3	0	0	0.2	0	1.8	0	2.7	98.9

Figure 5.6: Classification accuracy of Hudgins feature set for the best subject case.

Actual \ Predicted	Task 0	Task 1	Task 2	Task 3	Task 4	Task 5	Task 6	Task 7	Task 8	Task 9
Task 0	17.4	0	0.3	0	0	0.3	0.3	0	0.3	83.6
Task 1	0.5	94.5	0.8	0.5	2.2	0.5	0.8	0	1.3	0
Task 2	0	0.3	93.7	0.5	1	1.3	1	0	1.3	0
Task 3	0.5	0.5	0	93	3.5	1	0.3	0	1.3	0.5
Task 4	0.5	2.3	0.3	2.8	86.1	1.8	1	0	1.3	1.3
Task 5	0.5	0.3	0.3	1	4.5	89.8	0.5	0	5	0.3
Task 6	1.2	1.1	3	0.5	1	1.6	92.4	0	0.3	0.5
Task 7	0	0	0	0	0.7	0	1	100	0	0
Task 8	0.5	1	1.5	1.6	1	3.4	2.3	0	89	1.3
Task 9	79.1	0	0.3	0	0	0.3	0.3	0	0.3	12.4

Figure 5.7: Classification accuracy of Hudgins feature set for the worst subject case.

Finally, a key step regards the performances of the PRAs when using only the information coming from the forearm or the wrist. Table 5.7 reports precision values when only forearm channels are used to extract features from EMG signals of each subject, while Table 5.8 when only wrist channels are considered. It deserves to be noticed that the performances of the aggregated feature sets are unsatisfactory, whichever architecture is adopted. When only

Figure 5.8: Classification accuracy of TDAR feature set for the best subject case.

Figure 5.9: Classification accuracy of TDAR feature set for the worst subject case.

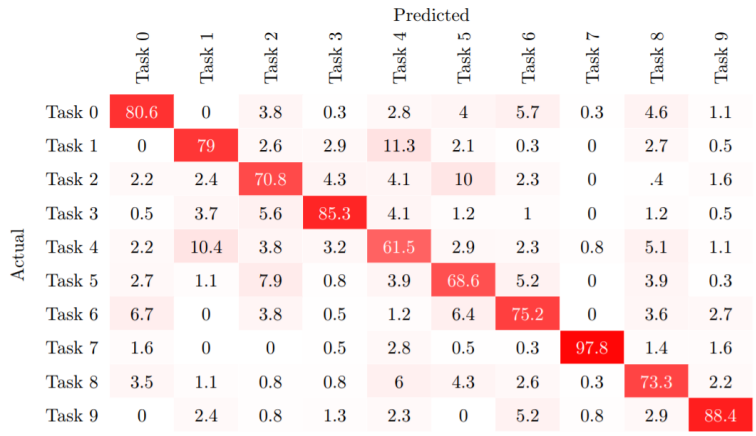

Figure 5.10: Classification accuracy of DWTC feature set for the best subject case.

forearm or wrist channels are considered, a minor amount of information is retrieved, thus translating into poor level of classification precision (at most 64.7% in forearm channels and 70.8% in wrist channel case).

Actual \ Predicted	Task 0	Task 1	Task 2	Task 3	Task 4	Task 5	Task 6	Task 7	Task 8	Task 9
Task 0	14.1	0.8	0.5	3.2	1.3	0.5	1.8	0	2.7	71.2
Task 1	2.5	76.7	4.9	4.1	6.1	3.4	1.3	0	2.2	2
Task 2	1.6	5.1	77.9	1.5	1.3	3.9	3.9	0	4.4	1
Task 3	3	2.1	2.3	73.5	3.2	3.4	2.6	0	3	3
Task 4	2.3	5.6	1.3	5.6	71.8	4.4	4.2	0.8	4.6	1.5
Task 5	1.4	3.5	4.4	4.4	5.5	71	3.1	0	6	1.7
Task 6	2.3	2.7	2.8	1.9	4.2	4.9	76.2	0	3.5	2.7
Task 7	0	0.8	0	0	2.6	0.5	0.8	98.9	0	0
Task 8	3.2	1.9	5.1	3.6	2.6	7.8	3.9	0.3	71.4	4
Task 9	69.5	0.8	0.8	2.2	1.3	0.3	2.1	0	2.2	12.9

Figure 5.11: Classification accuracy of DWTC feature set for the best subject case.

	QSVM	LDA	RF
Hudgins	59.1 ± 3.1	52.3 ± 4.2	58.0 ± 6.2
Du	60.2 ± 4.2	56.2 ± 6.2	58.8 ± 4.3
Phinyomark 1	64.3 ± 2.5	57.1 ± 5.0	56.6 ± 3.9
Phinyomark 2	63.2 ± 3.4	57.1 ± 3.6	56.8 ± 3.7
TDAR	64.7 ± 5.7	60.8 ± 6.5	57.4 ± 6.1
DWTC	45.8 ± 0.3	40.7 ± 2.8	43.9 ± 1.7

Table 5.7: Mean and standard deviation of precision values in the case in which EMG signals acquired by the four forearm channels are exploited.

	QSVM	LDA	RF
Hudgins	67.2 ± 3.2	60.2 ± 6.5	64.0 ± 5.6
Du	68.2 ± 2.4	64.3 ± 5.6	64.6 ± 7.0
Phinyomark 1	69.4 ± 4.3	63.5 ± 4.7	63.5 ± 6.5
Phinyomark 2	70.5 ± 2.4	64.3 ± 4.0	63.4 ± 7.1
TDAR	70.8 ± 5.7	67.2 ± 5.9	63.9 ± 6.9
DWTC	49.0 ± 1.6	44.9 ± 2.4	49.4 ± 2.3

Table 5.8: Mean and standard deviation of precision values in the case in which EMG signals acquired by the four wrist channels are exploited.

5.4 Discussion

5.4.1 Feature class separability properties

The first aspect analyzed regards the class separability properties of time (TD), frequency (FD)and time-frequency (TFD) domain features. This aspect plays a fundamental step when aggregated feature sets are constructed. In the TD, six features (see Table 5.2) appeared to be particularly able in highlighting differences among the ten classes, although part of them shared similar meaning. Indeed, as already observed in the previous chapter, DAMV

is calculated exactly as WL, but averaging the latter by the number of window samples [25], and the same consideration can be pointed out for DASDV and RMS. Hence, using DAMV and WL (or DASDV and RMS) together in the same feature set is not properly recommended since it would increase redundancy without supplying additional information. On the contrary, using either WL and RMS, or DAMV and DASDV within an aggregated feature set could be a valuable choice since their combined effect provides energy (RMS, DASDV) and complexity (WL, DAMV) information contemporaneously [50, 25].

The separability properties showed by MAV and IEMG (Table 5.2) are not completely surprising since they are commonly present in aggregated featurests [33, 25]. On the other hand, it is interesting to observe the behavior of the multidimensional features such as HIST, AR and CC. The first presents clusters with poor aggregation properties as indicated by the relatively high MSA and DB. This seems to be in agreement with what reported in [50], although some works highlighted that HIST is a feature robust with respect to electrode location stability, providing good results in myoelectric pattern recognition problems[32, 55]. A similar line hold for CC and AR since the inclusion of these two features in an aggregated feature set seems to add meaningful information which generally increases the overall recognition accuracy [25, 50]. Indeed, TDAR feature set combines AR coefficients with 6 other time-domain features while Phyniomark 2 feature set mixes cepstral coefficient with 3 time-domain features [25, 50]. Nevertheless, being CC and AR multidimensional features, their inclusion in a feature set tends to increase the dimensionality of feature space, which eventually enhances the complexity of the classifier and the computational burden for real-time applications.

Among the 10 FD features, the first three spectral moments showed the best class separability properties. This confirms that such features presented a great capability of mapping EMG signal epochs in well defined patterns as observed also in the previous chapter when shoulder motion intention detection problem was faced. Hence, although less investigated and used in aggregated datasets, such features deserves to be further studied also in relation to time domain features following the line proposed by [56]. Similar considerations can be pointed out for the TFD features, where only cD1 reported good clustering properties. This supports the preference of using TD features in myoelectric pattern recognition [33, 55, 1], also confirmed by the higher SI values observed in Table 5.5. Indeed, all the aggregated datasets characterized by a high number of TD features, presented a greater capability in separating handwriting classes.

As one can observe in Table 5.6, such separability was confirmed by the high degree of accuracy when trained with all six features sets. An average accuracy of 92.6% was obtained in the worst performing classifier-feature set combination (RF with DWTC) while 97.3% in the best case (QSVM-TDAR). Regarding the classification precision, a decreasing in its average value can be observed for all feature sets. The same held for the recall and F1 score. These three parameters are strictly correlated each other. Hence, in order to make a performance analysis, besides accuracy, one can rely on precision value. Among the six aggregated sets, TDAR was the one that presents the highest degree of precision. When it was used with LDA classifier, it carried out an average precision of 86.2%. In a similar manner, QSVM classifier could correctly predict as well, with an overall precision of 85.3%. On the other hand, one can observe that the precision of the RF classifiers with TDAR was consistently lower if compared to the others, with an overall precision of 78.7%. Despite the solid performances and reliable results obtained using TDAR, it should be noted that such set generated the largest feature space (along with Phinyomark 1 set). Indeed, TDAR is composed by 9 features for channels, since AR coefficients carries 4 descriptors each. Thus, its larger dimensionality could be a drawback for real time applications due to higher computational burden if compared for instance with the Hudgins set. However, the results confirm that TDAR is one of the most suitable set to adopt when an offline handwriting recognition problem has to be faced. As a matter of fact, TDAR guaranteed a very high class separation, e.g SI index was 2.15 for TDAR, whereas Phinyomark 1 reached 1.90 (Table 5.5).

An important aspect regards the results obtained for Hudgins set, confirming its relevance in many EMG classification studies [57, 58, 48, 35]. Its widespread use is due to the trade off between discriminating performance and low feature space dimensionality. Indeed, the use of only 4 time domain features for channels ensures application when dealing with online pattern recognition problems. In this study, Hudgins feature set gave the best classification precision when used in conjunction with QSVM algorithm (84%), whereas the lower values were observed for LDA (80.2%) and RF (79.8%) (Table 5.6). The performances showed by Du feature set were similar to Hudgins (Table 5.6). Also in this case, the involvement of a QSVM classifier guaranteed higher degree of precision (85%). Anyway, even LDA and RF showed good performances, achieving 83.6% and 78.6% respectively. Although Du set showed a slight increase with respect to Hudgins in the overall performances, it should be highlighted that the former set is made by 6 features each channel, hence resulting more computational expensive. The QSVM predictions were more precise even when the classifier was fed through

Phinyomark 1 and Phinyomark 2, reaching 84.6% and 84.9% of mean precision, respectively.

Regarding the DWTC feature set, it presented the worst performances. Even if accuracy value for this set was satisfying (QSVM 94.1%, LDA 92.6%, RF 92.9%), in terms of precision and recall, DWTC showed serious deficits. DWTC set achieves higher precision (and recall) when non-linear classification algorithms are used for predicting data. In particular, QSVM classifier could achieve at most 69.2% of overall precision with this set. It is still a too poor result to rely on, but it is higher with respect to LDA (61.5%) and RF (62.8%) which showed to be not suitable at all when using DWTC. This confirms what reported in [59], namely that TFD features can achieve higher accuracy for a properly tuned SVM classifier in a pattern recognition contest [50, 59]. The possible non-linear relationships among data points inside feature space of DWTC set seems to not affect too much the SVM algorithm, which essentially does not use any prior assumption on the data distribution. Other type of classifiers that are less sensitive to non-linearity could perform better, as demonstrated in [60], where a deep learning convolutional neural network approach was adopted to solve hand gesture recognition problem.

The presented results suggest that DWTC features were not recommended in combination with simple but largely employed machine learning algorithms used for EMG-based PRAs. Indeed, it may be useful to supply DWT coefficients by additional time domain feature for a major robustness of feature set [61]. The class separability metrics support such aspect, indeed the mean SI index is 1.02, which results much lower than Hudgins set (1.60). MSA index underlines a high variability of data, while DB index value is low(1.20), smaller than that computed for Hudgins set (1.60). This latter result might be misleading, as one should expect that DB would increase in DWTC set. This is due to the fact that DB index takes into account only geometrical distances between clusters, i.e. it relies on euclidean distances between centroids of each class group, without considering any statistical difference among them. Indeed, euclidean distances can distort the metrics to the scale of the larger magnitude features [32]. In this case a more reliable result is provided by SI index that calculates distinctness of classes passing through calculation of the covariance matrix.

The general behavior described up to now was confirmed also by investigating the confusion matrices provided for the classifiers in relation to the best and worst subjects. In Figures 5.6-5.11, one can observe the classification performances of QSVM trained with best and worse subject case for Hudgins, TDAR and DWTC respectively. In Figure 5.6, Hudgins feature set showed to be excellent in terms of accuracy: it distinguished correctly all 10 classes

of handwriting task. Indeed, values in the diagonal of matrix represents the percentage accuracy of correct associations between target values (vertical axis) and predicted values (horizontal axis). In the worst subject case (Figure 5.7) a strong misclassification occurred between first and last class. Classifier were not able to distinguish 0 from 9. This is due to the fact that number 0 and number 9 share a similar writing pattern. Despite of that, all the other classes were brilliantly predicted.

The last important aspect that deserves to be pointed out regards the study of the wrist as an alternative to the forearm for the development of EMG based human machine interfaces. As already observed the use of forearm and wrist EMG probes together permitted satisfying classification performances, indicating that a certain degree of spatial covering is required for developing adequate myoelectric PRAs when the motor task presents fine coordination properties (Table 5.6). On the contrary, when used separately, wrist channels and forearm channels did not provide reliable results, indeed as one can observe from Table 5.7 and and Table 5.8, the average precision of the three classifiers for all feature set did not overcome 64.7% in the case of forearm channels and 70.8% for wrist channels. In the worst case, if predictions are made with a linear classifier (LDA) trained with DWTC dataset, precision fell down to 40.7 %, thus demonstrating the infeasibility of this approach. Thus, in handwriting recognition problems, the complexity and fineness of the task suggest the use of larger setups, where the information of both wrist and forearm have to be accounted for guaranteeing the necessary amount of information required for the identification of the handwritten digits. This seems to be in contrast to what recently observed in the hand gesture recognition literature, where it has been demonstrated that the wrist can be a valid alternative to the forearm for acquiring trusty EMG information [3].

To summarize, in this chapter, EMG-based PRAs were developed to solve the handwriting recognition problem of the ten digits. Such point constitutes a remarkable element of novelty in the field of hand gesture recognition through EMG since the latter commonly takes into account hand movements that presented a lower level of neuromuscular control if compared with respect to handwriting. However, the increasing demand of EMG based human-machine interfaces in the fields of motor rehabilitation and robotic, motivated the investigation of using myoelectric control techniques for studying the handwriting task. A first aspect that can be pointed out regards the possibility to transfer procedures commonly encountered in the hand gesture recognition in the field of handwriting recognition, hence extending the number of ways to interact with a machine by adapting, without great efforts, the technical

solutions already presented in the literature. Concerning this point, the use of few electrodes located only on the forearm or on the wrist seems to provide unreliable information for the development of PRAs. This opens to the possibility of further investigations. Indeed, future research can focus on the use of different type of probes, i.e. high density EMG electrodes, which permit to extract a large amount of information and limiting, at the same time, the high number of anatomical landmarks upon which to place the standard EMG electrodes.

Bibliography

[1] Craig G McDonald, Jennifer L Sullivan, Troy A Dennis, and Marcia K O'Malley. A myoelectric control interface for upper-limb robotic rehabilitation following spinal cord injury. *IEEE Transactions on Neural Systems and Rehabilitation Engineering*, 28(4):978–987, 2020.

[2] Miguel Simão, Nuno Mendes, Olivier Gibaru, and Pedro Neto. A review on electromyography decoding and pattern recognition for human-machine interaction. *IEEE Access*, 7:39564–39582, 2019.

[3] Fady Botros, Angkoon Phinyomark, and Erik Scheme. Emg-based gesture recognition: Is it time to change focus from the forearm to the wrist? *IEEE Transactions on Industrial Informatics*, 2020.

[4] Ulysse Côté-Allard, Gabriel Gagnon-Turcotte, Angkoon Phinyomark, Kyrre Glette, Erik Scheme, François Laviolette, and Benoit Gosselin. A transferable adaptive domain adversarial neural network for virtual reality augmented emg-based gesture recognition. *IEEE Transactions on Neural Systems and Rehabilitation Engineering*, 29:546–555, 2021.

[5] A Sharmila. Hybrid control approaches for hands-free high level human–computer interface-a review. *Journal of Medical Engineering & Technology*, 45(1):6–13, 2021.

[6] Yongje Kwon, Anany Dwivedi, Andrew J McDaid, and Minas Liarokapis. Electromyography-based decoding of dexterous, in-hand manipulation of objects: Comparing task execution in real world and virtual reality. *IEEE Access*, 9:37297–37310, 2021.

[7] Tommy Sugiarto, Chun-Lung Hsu, Chi-Tien Sun, Wei-Chun Hsu, Shu-Hao Ye, and Kuan-Ting Lu. Surface emg vs. high-density emg: Tradeoff between performance and usability for head orientation prediction in vr application. *IEEE Access*, 9:45418–45427, 2021.

[8] Marco Recenti, Carlo Ricciardi, Romain Aubonnet, Ilaria Picone, Deborah Jacob, Halldór ÁR Svansson, Sólveig Agnarsdóttir, Gunnar H Karlsson, Valdís Baeringsdóttir, Hannes Petersen, et al. Toward predicting motion sickness using virtual reality and a moving platform assessing brain, muscles, and heart signals. *Frontiers in Bioengineering and Biotechnology*, 9:132, 2021.

[9] Nadia Nasri, Sergio Orts-Escolano, and Miguel Cazorla. An semg-controlled 3d game for rehabilitation therapies: Real-time time hand gesture recognition using deep learning techniques. *Sensors*, 20(22):6451, 2020.

[10] Alessandro Mengarelli, Andrea Tigrini, Sandro Fioretti, Stefano Cardarelli, and Federica Verdini. On the use of fuzzy and permutation entropy in hand gesture characterization from emg signals: Parameters selection and comparison. *Applied Sciences*, 10(20):7144, 2020.

[11] Manfredo Atzori, Arjan Gijsberts, Claudio Castellini, Barbara Caputo, Anne-Gabrielle Mittaz Hager, Simone Elsig, Giorgio Giatsidis, Franco Bassetto, and Henning Müller. Electromyography data for non-invasive naturally-controlled robotic hand prostheses. *Scientific data*, 1(1):1–13, 2014.

[12] Stefano Pizzolato, Luca Tagliapietra, Matteo Cognolato, Monica Reggiani, Henning Müller, and Manfredo Atzori. Comparison of six electromyography acquisition setups on hand movement classification tasks. *PloS one*, 12(10):e0186132, 2017.

[13] Rami Khushaba and Kianoush Nazarpour. Decoding hd-emg signals for myoelectric control-how small can the analysis window size be. *IEEE Robotics and Automation Letters*, 2021.

[14] Samuel Planton, Mélanie Jucla, Franck-Emmanuel Roux, and Jean-François Démonet. The "handwriting brain": a meta-analysis of neuroimaging studies of motor versus orthographic processes. *Cortex*, 49(10):2772–2787, 2013.

[15] Marieke Longcamp, Jean-luc Velay, Virginia Wise Berninger, and Todd Richards. Neuroanatomy of handwriting and related reading and writing skills in adults and children with and without learning disabilities: French-american connections. *Pratiques. Linguistique, littérature, didactique*, (171-172), 2016.

[16] Leisi Pei, Marieke Longcamp, Frederick Koon-Shing Leung, and Guang Ouyang. Temporally resolved neural dynamics underlying handwriting. *NeuroImage*, 244:118578, 2021.

[17] Zhaoqi Zhang, Qiming Yuan, Zeping Liu, Man Zhang, Junjie Wu, Chunming Lu, Guosheng Ding, and Taomei Guo. The cortical organization of writing sequence: evidence from observing chinese characters in motion. *Brain Structure and Function*, 226(5):1627–1639, 2021.

[18] Lambert Schomaker. *Handling within-writer variability and between-writer variation in the recognition of on-line handwriting.* PhD thesis, Citeseer, 1995.

[19] Charles C. Tappert, Ching Y. Suen, and Toru Wakahara. The state of the art in online handwriting recognition. *IEEE Transactions on pattern analysis and machine intelligence*, 12(8):787–808, 1990.

[20] Moussa Djioua and Réjean Plamondon. Studying the variability of handwriting patterns using the kinematic theory. *Human movement science*, 28(5):588–601, 2009.

[21] Jose Guadalupe Beltran-Hernandez, Jose Ruiz-Pinales, Pedro Lopez-Rodriguez, Jose Luis Lopez-Ramirez, and Juan Gabriel Avina-Cervantes. Multi-stroke handwriting character recognition based on semg using convolutional-recurrent neural networks. *Mathematical Biosciences and Engineering*, 17(5):5432–5448, 2020.

[22] Cristina Carmona-Duarte, Rafael de Torres-Peralta, Moises Diaz, Miguel A Ferrer, and Marcos Martin-Rincon. Myoelectronic signal-based methodology for the analysis of handwritten signatures. *Human movement science*, 55:18–30, 2017.

[23] Alan M Wing. Variability in handwritten characters. *Visible Language*, 13(3):283–298, 1979.

[24] Seyed Safavynia, Gelsy Torres-Oviedo, and Lena Ting. Muscle synergies: implications for clinical evaluation and rehabilitation of movement. *Topics in spinal cord injury rehabilitation*, 17(1):16–24, 2011.

[25] Angkoon Phinyomark, Franck Quaine, Sylvie Charbonnier, Christine Serviere, Franck Tarpin-Bernard, and Yann Laurillau. Emg feature evaluation for improving myoelectric pattern recognition robustness. *Expert Systems with applications*, 40(12):4832–4840, 2013.

[26] Silvestro Micera, Jacopo Carpaneto, and Stanisa Raspopovic. Control of hand prostheses using peripheral information. *IEEE reviews in biomedical engineering*, 3:48–68, 2010.

[27] Rohini Salunke, Dipali Badhe, Vanita Doke, Yogeshwari Raykar, and Bhushan S Thakare. The state of the art in text recognition techniques. 2015.

[28] Ayushman Dash, Amit Sahu, Rajveer Shringi, John Gamboa, Muhammad Zeshan Afzal, Muhammad Imran Malik, Andreas Dengel, and Sheraz Ahmed. Airscript-creating documents in air. In *2017 14th IAPR International Conference on Document Analysis and Recognition (ICDAR)*, volume 1, pages 908–913. IEEE, 2017.

[29] Prasun Roy, Subhankar Ghosh, and Umapada Pal. A cnn based framework for unistroke numeral recognition in air-writing. In *2018 16th international conference on frontiers in handwriting recognition (ICFHR)*, pages 404–409. IEEE, 2018.

[30] Michael Linderman, Mikhail A Lebedev, and Joseph S Erlichman. Recognition of handwriting from electromyography. *PLoS One*, 4(8):e6791, 2009.

[31] Gan Huang, Dingguo Zhang, Xidian Zheng, and Xiangyang Zhu. An emg-based handwriting recognition through dynamic time warping. In *2010 Annual International Conference of the IEEE Engineering in Medicine and Biology*, pages 4902–4905. IEEE, 2010.

[32] Andreas W Franzke, Morten B Kristoffersen, Vinay Jayaram, Corry K van der Sluis, Alessio Murgia, and Raoul M Bongers. Exploring the relationship between emg feature space characteristics and control performance in machine learning myoelectric control. *IEEE Transactions on Neural Systems and Rehabilitation Engineering*, 29:21–30, 2020.

[33] Wentao Wei, Qingfeng Dai, Yongkang Wong, Yu Hu, Mohan Kankanhalli, and Weidong Geng. Surface-electromyography-based gesture recognition by multi-view deep learning. *IEEE Transactions on Biomedical Engineering*, 66(10):2964–2973, 2019.

[34] Lauren H Smith, Levi J Hargrove, Blair A Lock, and Todd A Kuiken. Determining the optimal window length for pattern recognition-based myoelectric control: balancing the competing effects of classification error and controller delay. *IEEE Transactions on Neural Systems and Rehabilitation Engineering*, 19(2):186–192, 2011.

[35] Kevin Englehart and Bernard Hudgins. A robust, real-time control scheme for multifunction myoelectric control. *IEEE transactions on biomedical engineering*, 50(7):848–854, 2003.

[36] Nathan E Bunderson and Todd A Kuiken. Quantification of feature space changes with experience during electromyogram pattern recognition control. *IEEE Transactions on Neural Systems and Rehabilitation Engineering*, 20(3):239–246, 2012.

[37] E Van Oudenaarde and RA Oostendorp. Functional relationship between the abductor pollicis longus and abductor pollicis brevis muscles: an emg analysis. *Journal of anatomy*, 186(Pt 3):509, 1995.

[38] Marc A Maier and Marie-Claude Hepp-Reymond. Emg activation patterns during force production in precision grip. *Experimental Brain Research*, 103(1):108–122, 1995.

[39] Andrea Tigrini, Luca Alberto Pettinari, Federica Verdini, Sandro Fioretti, and Alessandro Mengarelli. Shoulder motion intention detection through myoelectric pattern recognition. *IEEE Sensors Letters*, 5(8):1–4, 2021.

[40] Lars Arendt-Nielsen, Thomas Graven-Nielsen, Heine Svarrer, and Peter Svensson. The influence of low back pain on muscle activity and coordination during gait: a clinical and experimental study. *Pain*, 64(2):231–240, 1996.

[41] HJA Van Hedel, L Tomatis, and R Müller. Modulation of leg muscle activity and gait kinematics by walking speed and bodyweight unloading. *Gait & posture*, 24(1):35–45, 2006.

[42] Micera Zecca, Silvestro Micera, Maria C Carrozza, and Paolo Dario. Control of multifunctional prosthetic hands by processing the electromyographic signal. *Critical Reviews™ in Biomedical Engineering*, 30(4-6), 2002.

[43] Feng Duan, Lili Dai, Wennan Chang, Zengqiang Chen, Chi Zhu, and Wei Li. semg-based identification of hand motion commands using wavelet neural network combined with discrete wavelet transform. *IEEE Transactions on Industrial Electronics*, 63(3):1923–1934, 2015.

[44] Dennis Tkach, He Huang, and Todd A Kuiken. Study of stability of time-domain features for electromyographic pattern recognition. *Journal of neuroengineering and rehabilitation*, 7(1):1–13, 2010.

[45] Erdem Yavuz and Can Eyupoglu. A cepstrum analysis-based classification method for hand movement surface emg signals. *Medical & biological engineering & computing*, 57(10):2179–2201, 2019.

[46] Martin Vetterli and Jelena Kovacevic. *Wavelets and subband coding*. Prentice-hall, 1995.

[47] Stéphane Mallat. *A wavelet tour of signal processing*. Elsevier, 1999.

[48] Bernard Hudgins, Philip Parker, and Robert N Scott. A new strategy for multifunction myoelectric control. *IEEE transactions on biomedical engineering*, 40(1):82–94, 1993.

[49] Yi-Chun Du, Chia-Hung Lin, Liang-Yu Shyu, and Tainsong Chen. Portable hand motion classifier for multi-channel surface electromyography recognition using grey relational analysis. *Expert Systems with Applications*, 37(6):4283–4291, 2010.

[50] Angkoon Phinyomark, Pornchai Phukpattaranont, and Chusak Limsakul. Feature reduction and selection for emg signal classification. *Expert systems with applications*, 39(8):7420–7431, 2012.

[51] Hu Huang, Hong-Bo Xie, Jing-Yi Guo, and Hui-Juan Chen. Ant colony optimization-based feature selection method for surface electromyography signals classification. *Computers in biology and medicine*, 42(1):30–38, 2012.

[52] David L Davies and Donald W Bouldin. A cluster separation measure. *IEEE transactions on pattern analysis and machine intelligence*, (2):224–227, 1979.

[53] Anne-Laure Boulesteix, Silke Janitza, Jochen Kruppa, and Inke R König. Overview of random forest methodology and practical guidance with emphasis on computational biology and bioinformatics. *Wiley Interdisciplinary Reviews: Data Mining and Knowledge Discovery*, 2(6):493–507, 2012.

[54] Vijay Kotu and Bala Deshpande. *Predictive analytics and data mining: concepts and practice with rapidminer*. Morgan Kaufmann, 2014.

[55] Benedetta Cesqui, Peppino Tropea, Silvestro Micera, and Hermano Igo Krebs. Emg-based pattern recognition approach in post stroke robot-aided rehabilitation: a feasibility study. *Journal of neuroengineering and rehabilitation*, 10(1):1–15, 2013.

[56] Rami N Khushaba, Maen Takruri, Jaime Valls Miro, and Sarath Kodagoda. Towards limb position invariant myoelectric pattern recognition using time-dependent spectral features. *Neural Networks*, 55:42–58, 2014.

[57] Guanglin Li, Aimee E Schultz, and Todd A Kuiken. Quantifying pattern recognition—based myoelectric control of multifunctional transradial prostheses. *IEEE Transactions on Neural Systems and Rehabilitation Engineering*, 18(2):185–192, 2010.

[58] Guanglin Li, Yaonan Li, Long Yu, and Yanjuan Geng. Conditioning and sampling issues of emg signals in motion recognition of multifunctional myoelectric prostheses. *Annals of biomedical engineering*, 39(6):1779–1787, 2011.

[59] Thomas Lorrain, Ning Jiang, and Dario Farina. Influence of the training set on the accuracy of surface emg classification in dynamic contractions for the control of multifunction prostheses. *Journal of Neuroengineering and Rehabilitation*, 8(1):25, 2011.

[60] Ulysse Côté-Allard, Cheikh Latyr Fall, Alexandre Drouin, Alexandre Campeau-Lecours, Clément Gosselin, Kyrre Glette, François Laviolette, and Benoit Gosselin. Deep learning for electromyographic hand gesture signal classification using transfer learning. *IEEE Transactions on Neural Systems and Rehabilitation Engineering*, 27(4):760–771, 2019.

[61] M Hariharan, CY Fook, R Sindhu, Bukhari Ilias, and Sazali Yaacob. A comparative study of wavelet families for classification of wrist motions. *Computers & Electrical Engineering*, 38(6):1798–1807, 2012.

Chapter 6

Concluding remarks

In this work of thesis, the modeling of neuromuscular control was taken into account from different perspectives and for different motor tasks. The first two chapters were developed upon the idea of merging data analysis techniques, based on time-series analysis, to the mechanical modeling approaches used to model the human upright stance and the neuromuscular control involved in the balance maintenance. An important element that justifies such research line lies on the intermittent motor control paradigm used to model the neural controller. Indeed, it has been showed in [1], that under such motor control paradigm, the single-link inverted pendulum, used to model the upright stance, was able to generate center of pressure (COP) timeseries that showed complex patterns like those observed in real data. This puts the focus on the physical interpretation of the controller parameters, which poses the basis for the employment of the the aforementioned models in the well-established field of posturography. Thus, rather than focus on kinematic quantities such as the sway angle, in this work, focus was given to COP time course since mainly involved in research and clinical practice.

Such research line was followed and enlarged when the stance was modeled through a double link inverted pendulum as reported in [2, 3]. The introduction of a second joint that mechanically models the hip required an appropriate formalization of the COP for a multi-link structure. This allowed to observe that COP fluctuations are intimately connected to passive and active control actions, that are developed at the joints. Moreover, it has been observed that certain COP descriptors can be used together with the mechanical model to infer possible differences in the neuromuscular control policies actuated by two different groups of subjects [2]. This offers another opportunity for exploiting the mechanical modeling framework in posturography, aligning with what reported in [4, 5], although in the latter,

parameters inference was performed through kinematic quantities.

The idea of using multiple dynamics for describing the role of the neuromuscular control was further developed through the use of data driven models in the context of perturbed posture. Indeed, the use of variable structure control policies such as the intermittent control in quiet stance can be a valuable example that can be transferred in the context of perturbed posture. However, rather than employing a specific model structure for the modeling of the neural control, in [6] a system identification approach was used. This allowed to build parsimonious models that took into account not only the kinematic and dynamic variables, but also the myoelectric activities of the gastrocnemius and tibialis anterior, which are mainly involved in the actuation of the disturbance rejection policy generated by the central nervous system. The family of models used in the above mentioned system identification scheme have a hybrid system structure, which effectively allowed to describe the entire process of balance maintenance through sub-dynamics. This constitutes an element of novelty in the field of neural control characterization under perturbed posture tasks. Indeed, up to now it has been observed in the literature the tendency of approximating the mechanics and the control of the stance through linear hypothesis assumptions that can be restricting when nonlinear phenomena appears in the data, as it happens during impulsive events like sudden support base translations [6].

From chapter three to chapter five, it has been reported the aspects related to the second core of research, which regards the modeling and characterization of neuromuscular control based on surface electromyography (sEMG). This line of research was motivated by the increasing needs behind the modern technologies. Indeed, sEMG can be used to design human-machine interfaces useful to guide machines during rehabilitation tasks controlling robot and software. As reported in [7], a first level of characterization of a motor task can require the knowledge of time instant at which the muscles activate, that is, the muscle onset detection (MOD). These aspects were used to realize even simple but trustful human-robot interactions [8]. In this study MOD was investigated when sEMG signals are characterized by low signal to noise ration (SNR). The latter represents a significant case that can be encountered for instance when subject's muscle activity is poor. This can be due for many different reasons commonly associated to pathological states or bad electrodes placement. Thus, based on recent literature the role of signal preconditioning through energy operators was investigated. In particular, in [7] the extended Teager-Kaiser operator was employed to boost state of the art MOD detection algorithms, providing a useful framework for

highlighting the muscle activity also in very low SNR conditions.

Although the muscle onset represents a fundamental source of information, many applications require more structured level of knowledge, that is, the prediction through an ensamble of EMG signals of which movement the subject is undergoing to perform. This can be referred as the motion intention detection (MID), and in this work of thesis, the latter was investigated under the myoelectric pattern recognition approach [9]. Specifically, a MID problem related to the identification of the shoulder movements has been taken into account by studying not only time domain features as commonly appears in literature, but also including the less studied frequency domain features, which demonstrated to be particularly suitable for such kind of applications. However, it deserves to be stressed that an important element of novelty lies on the implementation of such approaches for solving MID of the shoulder since the motion intention detection related to this joint results poorly studied in the literature. Moreover, as reported in chapter four, it was found that methodologies used in the hand gesture recognition can be transferred for solving MID problems that involve a relatively large set of movements.

Finally, the last chapter extended the studies related to the hand gesture toward the handwriting recognition. Indeed, despite EMG based pattern recognition architectures demonstrated to be appealing for many different applications [10, 11], they were commonly trained and tested over a well acknowledged set of gestures. Moreover, the common anatomical landmark taken into account for the extraction of sEMG signal is the forearm. In this study, based on the literature suggestion [11], the role of the wrist as a possible landmark for the sEMG acquisition was investigated in an extremely fine motor task: the digit handwriting. Similarly to what done for MID problems many different features in time, frequency and time-frequency domain were extracted and evaluated. Then, they have been aggregated in feature sets commonly used for the study of hand gesture recognition. A first evidence found in this work regards the opportunity to recognize handwriting digit from EMG signal. This is a new aspect that grounds the basis for future studies related to the EMG based hand writing recognition. Findings suggest that a complete change of perspective from forearm to wrist deserves to be further investigated since for a fine motor task like the handwriting, the pattern recognition architectures did not show satisfactory performances when only forearm wrist electrodes were used.

Bibliography

[1] Andrea Tigrini, Federica Verdini, Sandro Fioretti, and Alessandro Mengarelli. Long term correlation and inhomogeneity of the inverted pendulum sway time-series under the intermittent control paradigm. *Communications in Nonlinear Science and Numerical Simulation*, 2022.

[2] Andrea Tigrini, Federica Verdini, Sandro Fioretti, and Alessandro Mengarelli. Center of pressure plausibility for the double-link human stance model under the intermittent control paradigm. *Journal of Biomechanics*, 128:110725, 2021.

[3] Andrea Tigrini, Alessandro Mengarelli, Sandro Fioretti, and Federica Verdini. Anterior-posterior center of pressure analysis for the dip/vip balance maintenance model: Formalization and preliminary results. In *2021 10th International IEEE/EMBS Conference on Neural Engineering (NER)*, pages 832–835. IEEE, 2021.

[4] Yasuyuki Suzuki, Akihiro Nakamura, Matija Milosevic, Kunihiko Nomura, Takao Tanahashi, Takuyuki Endo, Saburo Sakoda, Pietro Morasso, and Taishin Nomura. Postural instability via a loss of intermittent control in elderly and patients with parkinson's disease: A model-based and data-driven approach. *Chaos: An Interdisciplinary Journal of Nonlinear Science*, 30(11):113140, 2020.

[5] A Tietäväinen, MU Gutmann, E Keski-Vakkuri, J Corander, and E Hæggström. Bayesian inference of physiologically meaningful parameters from body sway measurements. *Scientific reports*, 7(1):1–14, 2017.

[6] Andrea Tigrini, Federica Verdini, Marco Maiolatesi, Andrea Monteriù, Francesco Ferracuti, Sandro Fioretti, Sauro Longhi, and Alessandro Mengarelli. Neuromuscular control modelling of human perturbed posture through piecewise affine autoregressive with exogenous input models. *Frontiers in Bioengineering and Biotechnology*, 9, 2022.

[7] Andrea Tigrini, Alessandro Mengarelli, Stefano Cardarelli, Sandro Fioretti, and Federica Verdini. Improving emg signal change point detection for low snr by using extended teager-kaiser energy operator. *IEEE Transactions on Medical Robotics and Bionics*, 2(4):661–669, 2020.

[8] Laura Dipietro, Mark Ferraro, Jerome Joseph Palazzolo, Hermano Igo Krebs, Bruce T Volpe, and Neville Hogan. Customized interactive robotic treatment for stroke: Emg-triggered therapy. *IEEE Transactions on Neural Systems and Rehabilitation Engineering*, 13(3):325–334, 2005.

[9] Andrea Tigrini, Luca Alberto Pettinari, Federica Verdini, Sandro Fioretti, and Alessandro Mengarelli. Shoulder motion intention detection through myoelectric pattern recognition. *IEEE Sensors Letters*, 5(8):1–4, 2021.

[10] Alessandro Mengarelli, Andrea Tigrini, Sandro Fioretti, Stefano Cardarelli, and Federica Verdini. On the use of fuzzy and permutation entropy in hand gesture characterization from emg signals: Parameters selection and comparison. *Applied Sciences*, 10(20):7144, 2020.

[11] Fady Botros, Angkoon Phinyomark, and Erik Scheme. Emg-based gesture recognition: Is it time to change focus from the forearm to the wrist? *IEEE Transactions on Industrial Informatics*, 2020.